

The Segmentation of Reflectances from Moderate Resolution Remote Sensing Data for the Retrieval of Land Cover Specific Leaf Area Index

Dissertation

an der Fakultät für Geowissenschaften
der Ludwig-Maximilians-Universität München



vorgelegt von:

Marko Braun

aus Augsburg

Eingereicht im März 2007

- | | |
|---------------|-----------------------------|
| 1. Gutachter: | Prof. Dr. Wolfram Mauser |
| 2. Gutachter: | Prof. Dr. Friedrich Wieneke |

Tag der mündlichen Prüfung: 19. Juli 2007

Freedom from the desire for an answer is essential to the understanding of a problem.

Jiddu Krishnamurti (1895-1986)

Summary

Moderate resolution optical remote sensing sensors bare the potential of imaging the entire globe multiple times a day. They provide one of the most fundamental tools to monitor the earth's surface on a regular, operational basis as their measurements are used to derive surface properties such as albedo, surface cover and leaf area. With spatial resolution of a few hundred meters to a kilometer they capture the vital signs of the earth and provide insight into processes and changes of an ever more changing planet. While this type of monitoring devices deliver invaluable information on regional and global scales, many facets of ecosystem dynamics take place on spatial extent smaller than what these devices may capture. Thus, remote sensing instruments of much higher resolution have been established to be able to focus on the exploration of the finer structures of surface features and take a closer look. This closer look, however, is achieved only by surrendering the advantage of dense temporal coverage and is due to narrower swaths of the instruments and subsequently less frequent overpasses of the spaceborne instrument. While at moderate resolution a mid latitude central European site will be observed multiple times a day on every cloud free occasion, the matching of overpass and non-cloudiness can be expected to occur about 3-6 times per season for today's operational high resolution sensors. It is the objective of this thesis to tackle this dilemma of optical satellite remote sensing data of scarce high-resolution spatial information on the one hand and abundant coarser resolution data on the other. It presents a method that aims at linking bits of information of both available data sources. These data from the two sources are combined with a priori expert knowledge. The method is implemented as a value adding chain to provide leaf area index (LAI) as a surface parameter in improved form to be used in the driving of numerical environmental process models in the wake of global change research.

Along with the implementation of the method field measurements were carried out in order to achieve a better understanding of LAI and its temporal development. The Licor LAI-2000 optical sampling device was used for the measurement of in situ leaf area. During the growing seasons of 2002 through 2004 field campaigns were conducted to sample maize, rape and wheat fields on a biweekly basis. Additionally, deciduous and coniferous forest types were sampled on an irregular basis. The irregularity is due to the great dependency on weather conditions when sampling forest sites.

The layout of the algorithm connects to concepts of the GLOWA-Danube project (Global Change of the water cycle) by which this research was initiated and funded. The principal goal of this project is the development of the integrated decision support system DANUBIA. This system is a raster based, object-oriented compound of interacting expert numerical models capable of describing the processes involved in the hydrologic cycle. Static and dynamic land surface parameters are key quantities in these process descriptions. Remote sensing data are apt to be used as an input source for DANUBIA and other environmental models alike.

The study area for this thesis is located within the upper Danube catchment, which is the test site for the GLOWA-Danube project and DANUBIA. The area is a 144km square that includes the variety of the major natural environments represented in the encompassing upper Danube catchment. It stretches from lower river valley plains in its northern part through the alpine foreland to the Alps in the south. The area covers approximately 21.000 km² and includes fertile agriculturally used plains, large forested areas of different type as well as extended urban areas.

Data of two remote sensing instruments of high and low resolution are applied: the Moderate Resolution Imaging Spectroradiometer MODIS delivers data at up to 250m spatial resolution. It is used as the device capable of frequent monitoring. The Landsat Thematic Mapper (TM) instrument takes measurements at 30m spatial resolution. It is used to derive information on static land surface properties at high spatial resolution. Together with the target resolution of 1km of the DANUBIA raster three different scales are addressed. Further, within DANUBIA the concept of geocomplexes was developed to account for the heterogeneities observed on 1 km grid cells. It is used as a scaling instrument and common ground to bring the three scales of the two sensors and the model together. Due to the ambiguity of the scale term and its implications for remote sensing and environmental modeling, the study expands upon some relevant perspectives of scale for clarification.

With geocomplexes a single grid cell is conceptualized as an area composed of a set of fractions with homogeneous properties rather than a single homogeneous entity. Each square raster cell is thought to be made up of a number of geocomplexes that describe homogeneous properties of a fraction of the cell. This approach of maintaining land cover types fractions on a pixel has proven to be of great benefit to the quality of environmental model results when the model is run for each of the homogeneous subscale fractions. The fact that the generation of geocomplexes relies on land cover type as the prime criteria of separation of homogeneous fractions harmonizes with the fact that land cover type is also fundamental in the derivation of many land surface properties. This raises the question if also the retrieval of surface parameters from remote sensing can be based on these subscale homogeneous fractions.

When applying parameter retrieval algorithms to moderate resolution remote sensing data, usually the full pixel is assigned a land cover type. However, in many natural environments pixels at moderate scale will rarely represent homogeneous land cover. In the study area, an investigation of the areal fraction of majority cover types on 250m pixel results in the observation that on half of the pixels that majority land cover type represents less than 65% of the pixels area. In some cases it may even be lower than 20%. This makes it obvious that the generalization of the pixel as homogeneously covered introduces substantial error to any parameter retrieval that relies on pixel land cover type.

The method that is being developed tries to overcome the error resulting from the assumption of pixel homogeneity and seeks a better answer to the question of the true leaf area on a raster cell of heterogeneous surface. The reliable quantification of LAI is coupled to the knowledge of the land cover type producing the leaf area. At the same time the use of subscale fractional land cover information is valuable and in practice in environmental modeling. Therefore a method was developed to determine LAI for fractions of equal land cover on a pixel. However, a paradox lies within the notion of splitting up a moderate resolution raster cell's LAI to a set of different underlying land cover fractions: If the deduction of an LAI value requires land cover type information, such a value may not be broken up to other land cover types. Because of this paradox the endeavor of focusing on segments of the pixel has to be broken down to the most basic input for the retrieval algorithm: the pixel reflectance. The charming effect of this necessity is the fact that such segmented reflectances would be available for other application than LAI retrieval as well.

The segmentation of moderate scale pixel reflectances is achieved based on three inputs. First, there are the reflectances obtained from the measurements of the moderate scale sensor (MODIS). Second, there is information on fractional land cover type within the moderate resolution pixels. This information is deduced from land cover type raster data of spatial resolution exceeding the moderate scale to a degree that allows the computation of reasonable precision of the fractions. It is achieved by the classification of land cover types from Landsat TM data at fine spatial resolution. The third input for the algorithm for reflectance segmentation is of fuzzy nature. It is based on the fact that good knowledge exists about what kind of reflectance properties can be expected from land surfaces as a function of time. For example, it is well explored and to a certain degree predictable of how for instance a maize field or a deciduous forest will reflect radiance at a certain time of the year. This information is formalized as reflectance probabilities in functions that correspond to the time of acquisition of the first input, the moderate resolution reflectances.

The subscale land cover type information of a pixel connects to the fuzzy formalization of each land cover types possible reflectance that is expectable for the day of the year of the moderate resolution satellite measurement. Constrained by that measurement the algorithm is set out to determine an optimized distribution of reflectance for each pixels subscale land cover types. It is based on the multi-dimensional Newton-Raphson method and is implemented in the Java programming language. As the result, each land cover type present on the pixel will be assigned the most probable segment of the observed total reflectance. These reflectances of land cover types are used in the retrieval of LAI.

In remote sensing, geometric and radiometric preparation of data is a prerequisite for its use. In order to prototype and test the algorithm and to derive the fuzzy input data, satellite imagery of MODIS and Landsat TM are carefully prepared and analyzed. Two datasets are sought. One consists of coincident data of MODIS and TM and dates to June 19th 2001. This dataset is used in the development and prototyping of the algorithm. The other is a time series of MODIS imagery acquired during the growing season of 2003. It consists of the 19 best cloud free scenes of that season and is used to apply the algorithm. After the geocoding of the imagery, surface reflectances are derived from the data and atmospheric smearing is removed. It is shown that reflectances derived from both sensors agree well when comparing data of the temporally close acquisitions. Angular effects in the wide swath MODIS data however may seriously deteriorate the quality of the imagery.

Prototyping of the algorithm is performed on aggregated data of Landsat TM. In combination with the land cover type classification the high-resolution TM reflectances are used to derive the characteristics of 12 land cover types reflectances at the time of the TM acquisition. Additionally, a bidirectional canopy spectral reflectance model is used to develop an understanding of temporal reflectance behavior of the dynamic vegetation cover types. Fuzzy descriptions of expectable reflectances are deduced. It is shown that Gaussian functions suffice for a fuzzy description of the probabilities of reflectances for the land cover types. The algorithm is tested and thoroughly analyzed on the consistent set of input data derived from one data source. Because high-resolution reflectances are available for the aggregated synthetic moderate scale data, the land cover specific reflectances obtained from the reflectance segmentation algorithm can be compared to a reference dataset derived from this original high-resolution data. Reflectance segmentation is performed for the red (RED) and near infrared (NIR) bands of the data. In a second step, the land cover specific reflectances are used to derive LAI for the homogeneous fractions of pixels. Approved regression equations that relate LAI to normalized difference vegetation index (NDVI) computed from RED and NIR reflectances are applied to obtain LAI estimates.

The results from the prototyping are presented for the segmented reflectances and for the LAI derived from the reflectances. In the reflectances assigned to the 12 land cover types, a

tremendous reduction of variance can be observed as opposed to the reference data. The segmented reflectances are closely dispersed around mean land cover types reflectances. The reference data are only modestly reproduced. Maximum error of up to 50% in reflectance occurs. Error analysis, however, shows that the cover types area fraction plays a role in the deviation from the reference data with the smallest fractions exhibiting the largest error.

Despite rather discouraging results in the reflectance segmentation, the subsequent production of LAI values from the reflectances reveals some interesting results. LAI was elaborated for all land cover types fractions and then lumped to produce a single LAI value for the moderate scale pixel. While the fractional LAI can only be compared to the reference data set to assess error, the lumped single value is also compared to the alternative of deriving LAI using the majority land cover type. The data are analyzed for three agriculturally dominated sites in the northern part of the study area and one site in the alpine part.

In the fractional LAI results the extreme error observed in the segmented reflectances is preserved. When removing the 5% of the fractions with the largest error that needs to be judged as unacceptable, a 25% mean relative error remains in the data of the agricultural sites. Here, mean absolute error is around 0.65 units of LAI (m^2/m^2). In the alpine area mean relative error is as high as 50% and mean absolute error is 1.36 units of LAI.

For the moderate scale LAI, it is shown that the LAI produced separately for each land cover type and then summed to the pixel area correlates slightly better with the reference dataset than the LAI derived from majority land cover. This is the case despite the extreme error on some fractions that is introduced by the segmentation method. The statistical analysis reveals that mean absolute error computed against the reference data is lower when deriving LAI from reflectance segments for all tested sites outside the alpine environment. This applies to the full data without the removal of the 5% most extreme error. With the largest 5% errors removed, mean relative error on the lumped mesoscale pixel is 12.9% with a mean absolute error amounting to 0.26 units of LAI in the worst case observed. With these results of the prototyping experiment, the hypothesis can be confirmed that LAI retrieval will benefit from accounting for subscale pixel heterogeneities.

After the prototyping with synthetic data the method is applied to operational MODIS data in two experiments. First, MODIS reflectance data of two consecutive days are segmented and compared to reference data derived from coincident Landsat acquisitions on the second day. Then, the time series of MODIS reflectance data from 2003 is segmented. Both these experiments revealed that the presented implementation of the method is not ready for application. In the first application experiment it is discovered that the randomness in the produced reflectance segments is very large. While the regression coefficient of 0.75 between the original consecutive MODIS scenes is high in both the RED and NIR bands, pixel fractions accordance in the land cover types reflectances is equivocal. However, agreement with the reference dataset is commensurate for both scenes. The same applies to the LAI derived from the reflectance segmentation results. When LAI is derived for the MODIS time series data erroneous up- and downturns of the leaf area development are contained in the results. These fluctuations are strong in the fractional LAI and are little mitigated in the LAI time series lumped to the pixel area. With this finding the miscarriage of the second application experiment needs to be reported. The derivation of LAI time series for homogeneous land cover fractions of pixels is not feasible in the state of development of the approach.

The study concludes that the concept to derive land surface parameters based on fractional land cover type is auspicious and promising but with the presented method for reflectance segmentation not ready for application. In its current form it can be useful in the case where a surface feature like LAI is desired for a single instance in time. Although estimates for

subscale fractions of land cover types may contain large error, the leaf area estimate for the mesoscale pixel shows improvement when compared to the conventional majority type alternative. The current implementation will not be beneficial for the retrieval of temporally continuous land surface properties and their propagation.

Acknowledgements

you can imagine the opposite read the hardly decipherable lines of blue fluorescent tubes of an artwork on the outside wall of a Munich museum. During the work for this thesis I was a passerby there every day on my way to my workplace next door in the geoscience building of the Ludwig-Maximilians-University. Only after quite some time the lights had ceded for me to be but the familiar blue shimmer in snow flurry or a summer dawn and unraveled to a phrase. Even after being able to read it, I remained rather clueless of the artists intention of his linguistic play, but gleefully decided that occasionally considering the thought of the sentence seemed to be a worthwhile effort also for the natural philosopher. A bunch of those, at least, daily gathered in the opposite building. No need to imagine. I entered the building with a smile at most times, sometimes supported by a little distraction by some opposite imagination. The place was always a good place to be, in spite of hardships and privation experienced during work. The supportive and friendly atmosphere was constant inspiration and helpful in all ambitions followed. Hence, in this case I would easily refrain from even trying to imagine the opposite of the surroundings for the work on my thesis, as it was a pleasure just as that.

The person who made this time possible for me was Prof. Dr. Wolfram Mauser, holder of the Chair of Geography and Geographical Remote Sensing at the Ludwig-Maximilians-Universität in Munich. He not only provided excellent working conditions and equipment at his chair, but also was the initiator and driving force in the GLOWA-Danube initiative funded by the Federal Ministry of Education and Research (BMBF). As a postgraduate member, I was able to gain profound insight into the numerous activities of this exciting interdisciplinary project and did take part in various meetings, workshops and discussions. For me, Mr. Mausers wit in giving concise explanations and finding analogies has often dropped the penny. As my Ph.D. advisor he afforded me the freedom to develop my own ideas and readily left many opportunities to prosper and learn. His help and constructive criticism I could not have gone without. I cordially would like to thank him for the trust he placed in me and the patient guidance and support I received.

Many fruitful discussions with Dr. Ralf Ludwig had a significant stake in the progression of my work. His scientific knowledge and his hints on all kinds of smaller and larger problems and questions were invaluable at many times. As laughter was a frequent sound perceived on these occasions, many thanks go to him for contributing while being such a cheerful professional.

Especially I am indebted to Dr. Roswitha Stolz who took indispensable effort in the preparation of the land use classification used in this study. With her readiness to share her scientific knowledge on plant physiology and spectral remote sensing classification I greatly made profit from teaming up with her for this task.

With the obliging help of Dr. Heike Bach I was able to conduct the inverse transfer modeling with the GeoSAIL model. She gave me the opportunity to use her software and advised me in its application. My cordial thanks go to her for sharing her expertise and for her support not only with all questions concerning the radiative transfer model but also in the calibration of remote sensing data.

I would like to express my gratitude to Prof. Dr. Friedrich Wieneke and Dr. Florian Siebel for patiently answering all of my mathematical questions and for their encouragement to implement my ideas. I would also like to thank Mr. Markus Probeck for supplying me with PROMET-V model knowledge and data and for his constant help in conducting the field campaigns during three years. The many students involved in the campaigns are thanked for their constant commitment even at awkward schedules.

I am grateful for the helping hand of Mrs. Anja Colgan who was there when GIS problems occurred and could always help out with GLOWA data and their projection. Many thanks also go to Mrs. Doris Reichert who endured my moods all along the time we spent in the same office. She also shared her knowledge on Geocomplexes with me and was always a supportive companion in the doctoral struggle.

I cordially thank all unnamed colleagues of the scientific team of the remote sensing and hydrology working group at the Chair of Geography and Geographical Remote Sensing for their commitment, the great teamwork spirit and the friendly atmosphere they created. It was a pleasure to work with you.

Special thanks are due to Dr. Peter Fiener of the University of Cologne who carefully checked through the manuscript and provided me with valuable criticism and hints. His friendship and scientific enthusiasm were a great motivation in many stages of this work.

To all my dear friends I would like to say thank you for standing by me at all times by word and deed throughout the years I spent working on this thesis. Your support was bliss many times when the going got tough.

Finally, my deep gratitude goes to my parents and my family who encouraged me to prepare this work. As they never lost faith they gave me the confidence to complete this work. I could not have gone without them.

The MODIS data used in this study were acquired as part of the NASA's Earth Science Enterprise. The algorithms were developed by the MODIS Science Teams. The data were processed by the MODIS Adaptive Processing System (MODAPS) and Goddard Distributed Active Archive Center (DAAC), and are archived and distributed by the Goddard DAAC.

Table of Contents

Summary	iv
Acknowledgements.....	ix
Table of Contents	xi
List of Figures.....	xv
List of Tables.....	xxi
List of Acronyms	xxiii
1 Introduction	1
1.1 GLOWA Danube – Global Change in the Hydrologic Cycle.....	2
1.2 Scientific Objective and Outline of the Thesis.....	3
2 Study Area	6
2.1 The upper Danube catchment.....	6
2.2 Delineation of study area and test sites	11
3 Perspectives of Scale.....	15
3.1 What is Scale? – A Definition of scale terms.....	16
3.1.1 Scale	16
3.1.2 Scaling.....	18
3.2 Implications of Scale.....	19
3.2.1 Scaling Data	20
3.2.2 Scaling Environmental Models.....	21
3.2.3 Measuring and Description of Scale	22
3.3 Methods of data representation	23
3.3.1 Raster Data	24
3.3.2 Subscale Gridded Data.....	25
3.3.3 Geocomplexes	27
3.4 Scale in GLOWA-Danube	29
3.5 Scales of Leaves and Leaf Area	31
3.6 Scale in Remote Sensing Data	31
3.7 Scaling by Reflectance Segmentation.....	34
4 Remote Sensing Data and Data Preparation	37
4.1 Sensors	37
4.1.1 MODIS.....	37
4.1.2 Landsat Thematic Mapper.....	42

4.2 Data Formats	44
4.2.1 HDF and HDF-EOS Format.....	44
4.2.2 FAP Format	46
4.3 Geometric Correction.....	46
4.3.1 MODIS	47
4.3.2 Landsat	51
4.4 Radiometric Correction.....	53
4.4.1 Methodology	54
4.4.2 MODIS	55
4.4.3 Landsat	56
4.4.4 Validation of the Reflectance Calibration.....	57
4.5 Land Cover Classification derived from Landsat data.....	63
4.6 Datasets	65
4.6.1 MODIS Calibrated, Geolocated Radiances (MOD02).....	65
4.6.2 MODIS Geolocation Data Set (MOD03).....	66
4.6.3 MODIS Surface Reflectance: Atmospheric Correction Algorithm Product (MOD09).....	67
4.6.4 MODIS Land Cover Type (MOD12).....	67
4.6.5 MODIS Leaf Area Index Product (MOD15)	68
4.6.6 MODIS Cloud Mask (MOD35)	69
4.6.7 Landsat Data.....	69
5 Plant Leaves, Leaf Area and Leaf Area Index - LAI.....	71
5.1 Defining Leaf Area Index	71
5.2 Leaf Area as an agent in the Environment	73
5.3 Optical Properties of Vegetation	74
5.3.1 Leaf Optical Properties.....	74
5.3.2 Canopy Optical Properties	76
5.4 Measuring Leaf Area and Leaf Area Index.....	79
5.4.1 Ground based estimates.....	79
5.4.2 Remote Sensing based estimates.....	80
5.5 Leaf Area in Environmental Modeling	81
5.6 LAI Data.....	83
5.6.1 LAI Measurements using Li-Cor LAI-2000	84
5.6.2 Modeled LAI	86
5.6.3 LAI from the Literature.....	87
5.6.4 LAI derived from Remote Sensing Data.....	88
5.7 Discussion of available LAI data	89
5.7.1 Applicability of data.....	89
5.7.2 The paradox in scaling LAI from remote sensing.....	89
6 A Method for Reflectance Segmentation	91
6.1 Conception of the Algorithm.....	92
6.2 Methods.....	94
6.2.1 Optimization of land cover specific reflectances on pixels of multiple land cover	95
6.2.2 Fuzzy Representation of Reflectance Properties of Land Cover Types.....	100
6.2.3 Subscale Land Cover.....	106
6.2.4 LAI Algorithm.....	106
7 Application of the Algorithm	109
7.1 Prototyping of the Algorithm	110
7.1.1 Simulation of possible Results	110

7.1.2 Application to a synthetic data pyramid.....	111
7.1.3 Results of reflectance segmentation at 240m.....	114
7.1.4 Results of LAI retrievals based on reflectance segments at 240m.....	123
7.1.5 Visual Interpretation of results at 240m.....	133
7.1.6 Effects of varying scale.....	140
7.2 Application to coincident data of high and low resolution.....	141
7.2.1 Reflectances.....	143
7.2.2 Leaf Area Index.....	144
7.3 Application to a time series of the 2003 growing season.....	148
8 Discussion.....	151
9 Conclusion.....	157
10 References.....	159
Appendix.....	175
Appendix 1: MODIS Data Levels.....	175
Appendix 2: Software.....	176
Codec FapPicIO.....	176
Reflectance Segmentation.....	177
Converter HDF2FAP/HDF2PIC.....	179
Appendix 3: LAI Measurements.....	180
Appendix 4: Generalized Seasonal Development of LAI.....	185
Appendix 5: Reflectance Probability Functions.....	191
Appendix 6: Pixel by Pixel Analysis of LAI from reflectance segmentation.....	197
Appendix 7: Gallery of results from reflectance segmentation / LAI algorithm.....	204
Reflectances.....	204
LAI.....	217
Curriculum Vitae.....	223

List of Figures

Figure 1.1: The proxel concept of DANUBIA for raster based modeling (Ludwig, et al., 2003a).....	3
Figure 2.1: The location of the catchment area of the upper Danube in relation to the whole river system.	7
Figure 2.2: Satellite image with map overlay of the upper Danube catchment area.....	8
Figure 2.3: Location of the study area within the catchment of the upper Danube.	12
Figure 2.4: Location of the test areas Landsberg, Wetterstein, Gut Huell and Hochstadt within the study area.....	13
Figure 3.1: Physical and ecological phenomena tend to maintain a constant ratio in their spatial and temporal scale (Wu, 1999)	17
Figure 3.2: Elements to be addressed in scaling environmental and remote sensing models (Pelgrum, 2000, Kellenberger, 2001, modified)	22
Figure 3.3: The concept of quadtree data representation. An area is repeatedly subdivided into quarters until a subscale feature can be captured (left). The highest and the lowest level in the example are marked with numbers, the moderate level is marked with letters. In a regular raster capable of capturing a feature like the area marked dark, 8x8 raster cells would be stored. In the quadtree (right) only values for the 19 squares need to be stored (Bernhardsen 2002, modified).	26
Figure 3.4: Subscale information on a pixel. The properties 2,3,5 and 6 are present on the pixel. Their attributes are stored in the corresponding layers. The other properties are not present on this pixel but may be on others. A prominent example would be the property “land cover type” with the attribute “area fraction”	26
Figure 3.5: The concept of geocomplexes. Derived from high-resolution input, each of n geocomplexes on a mesoscale resolution cell is ingested in a run of a hydrologic model. Mesoscale results are generated by areal weighting of geocomplex based model output.....	28
Figure 3.6: Example of the deviation of mesoscale model results from microscale results using geocomplexes (red) and on regular mesoscale data (blue). The plot shows the evapotranspiration of a mixed forest modeled for 1996 (courtesy of D. Reichert)	29
Figure 3.7: Frequencies of the number of land cover types on 240m resolution pixels of the study area cutout of the DANUBIA catchment.....	30

- Figure 3.8: Discrepancy between actual measured area of a sensor and the abstraction as pixels. The small circles and squares correspond to a high-resolution sensor; the large circle and square correspond to a low-resolution sensor. The pale shapes in the background illustrate dislocation of a measurement and pixel in data from another orbit for the low-resolution sensor. 32
- Figure 3.9: Effect of viewing angle on resolution in MODIS imagery; left: close to nadir viewing image; right: off nadir view of the same area at a scan angle of $\sim 40^\circ$ 33
- Figure 3.10: Schematic of the scaling of moderate resolution remote sensing data to geocomplexes using reflectance segmentation. LAI algorithms may be applied to fractional reflectances of land cover types. The approach is detailed in Chapter 6. 35
- Figure 4.1: Relative spectral response functions of MODIS, ETM+ and TM in the VIS to SWIR region..... 40
- Figure 4.2: Levels of interaction with HDF files (from: NCSA HDF User Guide 2003)..... 45
- Figure 4.3: Schematic illustration of the ground projection of MODIS scans. The central scan (scan 2, gray) is overlapping with the previous (scan 1) and following scan as the scan angle increases (Wolfe et al. 2002). 48
- Figure 4.4: Coastline near Mont St. Michel, France as seen by MODIS under high scan angle (approx. 50°) in three consecutive scans at 250m resolution. A scan has 40 rows in 250m MODIS imagery. 48
- Figure 4.5: Tile coordinate system for MODIS products of Level 2G, Level 3 and Level 4 (Image taken from the National Snow and Ice Data Center (NSIDC) web page, http://nsidc.org/data/docs/daac/mod10_modis_snow/landgrid.html) 49
- Figure 4.6: Three cases of overpass times and orbit ground tracks for coverage of the upper Danube catchment (red circle) by Terra/MODIS (descending). Best geometric conditions are present when the overpass is intersecting with the catchment around 10:20 UTC (left), moderate conditions for orbits close to the catchment (about 10:05 UTC, center), unfavorable conditions are met around 11:25 UTC with an orbit far to the west of the catchment (right). Note that daytime descending orbits run in a NE to SW direction (Space science and Engineering data center, <http://www.ssec.wisc.edu/datacenter/terra/>, modified)..... 50
- Figure 4.7: Overview of the Landsat TM scenes to cover the GLOWA-Danube catchment. . 51
- Figure 4.8: Schematic illustration of the terrain induced effect in scanner imagery: Viewing at large angles in scanning direction, a scanner will record a mountaintop T at T' on the image plane. The true location of T is viewed in the direction of P and is mapped to P' on the image plane. The distance T'P' is the terrain induced displacement in scanner imagery. 52
- Figure 4.9: Artifacts in the data derived from the DTM. The images show a visualization of the cosine of the local solar incidence in an area where the 75m DTM of Tyrol (southeast section) abuts the 30m resolution DTM of Bavaria (northwest section). In the left image, the calculation was performed on interpolated data at 30m. In the right image the calculation was performed on the 75m data and the local solar incidence angle was interpolated and merged with the 30m data. 57
- Figure 4.10: Spectra of surfaces in the six images compared in the validation of the reflectance calibration. The spectra are averaged from 3x3 boxes of homogeneous land cover. 59

Figure 4.11: Correlations of MODIS reflectances for band 1-7 from PULREF corrected imagery versus the reflectances from the MOD09 reflectance product on DOY 170 year 2000	62
Figure 4.12: Classification of land covers for the study area and detail. Unclassified pixels are shown in black. The little black square in the detail indicates an area of 1km by 1km.....	64
Figure 5.1: Parameters determining the reflectance properties of plant leaves (taken from Oppelt, 2002).....	75
Figure 5.2: Relationship between leaf single scattering albedo (ω =reflectance+transmittance) and canopy reflectance with A) changing LAI and B) changing mean leaf angle of an ellipsoidal distribution. The best translation of leaf optical properties to the canopy level occurred when $\omega > 0.9$ which corresponds to NIR reflectance (taken from Asner, 1998)	77
Figure 5.3: Temporal development of four sites sampled in the LAI field measurement campaign.	85
Figure 5.4: Seasonal development of LAI as modeled by PROMET-V for six cover types. Mean values of model results including standard deviation are in black, maximum values in green and minimum values in red.	86
Figure 5.5: Field estimates of LAI from the literature (Demircan, 1995, Kneubühler, 2002).	87
Figure 5.6: Seasonal development of LAI derived from the MOD15 LAI Product 2000-2004 for four cover types/biomes. Plots are based on averages from 3x3 boxes of homogeneous land cover.	88
Figure 6.1: Schematic view of a set of land covers contributing to the reflectance value of a moderate resolution spectral measurement. For the algorithm, fractions of land covers are known and a fuzzy description of each land cover types current reflectance properties is provided. The blue upward pointing arrows indicate the unknown reflectance of the land cover types.	94
Figure 6.2: Inputs and outputs of the algorithm for reflectance segmentation	95
Figure 6.3: Multiple differentiable functions ψ_i for fuzzy description of the probability of the degree of reflectance in the NIR region for three surface types on June 18: Urban (red), Maize (green) and grassland (blue)	97
Figure 6.4: A graphical representation of the function ψ_{total} (psi). The optimization using the Newton-Raphson iteration will find the position of the peak of the surface. In the example shown a pixel with the land covers grassland, maize and urban fabric was simulated. The urban fabric land cover type is contained in the constraint of ψ_{total}	100
Figure 6.5: Histograms of NIR Reflectances of similar cover types. For comparison a differing land cover (deciduous forest, rock) is provided in each plot. The similar classes were combined to a class “needleleaf forest” and “grassland”.....	101
Figure 6.6: Histograms of the RED reflective Landsat band and fitted modified Gaussian function and Gaussian function for the 12 land cover types.	102
Figure 6.7: Histograms of the NIR reflective Landsat band and fitted modified Gaussian function and Gaussian function for the 12 land cover types.	103

- Figure 6.8: Approximations of mean (blue), maximum (green) and minimum (red) leaf area index derived from hosts of available measurements of LAI (black) for maize and winter grain..... 105
- Figure 6.9: Reflectance probability functions generated from GeoSAIL model results. Possible reflectance values change with the temporal development of the vegetated surfaces..... 106
- Figure 7.1: The surface formed by possible NDVI values viewed from two angles (the graph to the right is rotated 90° to the right as compared to the graph on the left). The solid green part of the surface is the NDVI that may result from valid ranges of RED and NIR reflectances of maize on June 19th. A horizontal plane intersecting the surface would cut along equal values of NDVI obtained from different combinations of RED and NIR reflectances. 110
- Figure 7.2: Illustration of the truth dataset for a single reflective band. It allows the comparison of information contained in high-resolution 30m data (left) and results from reflectance segmentation (right). 113
- Figure 7.3: Histograms of the RED and NIR reflectances of each of the 12 land cover types. Histograms are for the full test site at 240m resolution. Results from the reflectance segmentation are shown as dotted lines, the histograms from the truth dataset are the solid lines..... 115
- Figure 7.3 (continued)..... 116
- Figure 7.3 (continued)..... 117
- Figure 7.4: Area fractions of the 12 land cover types for the frame of the entire study area derived from the 30m land cover classification. 118
- Figure 7.5: Scatter plots on a pixel by pixel basis of the 12 land cover types comparing the RED reflectances obtained from the reflectance segmentation (RED RefSeg) to the true RED reflectances obtained from the high resolution Landsat TM image (RED Truth). Data are from the full test area at 240m resolution. The diagonal dotted line is the 1:1 line. 119
- Figure 7.6: Scatter plots on a pixel by pixel basis of the 12 land cover types comparing the NIR reflectances obtained from the reflectance segmentation (NIR RefSeg) to the true NIR reflectances obtained from the high resolution Landsat TM image (NIR Truth). Data are from the full test area at 240m resolution. The diagonal dotted line is the 1:1 line. 120
- Figure 7.7: Absolute error between land cover types 240m RED reflectances in the truth dataset and the reflectance segmentation result depending on the area fraction of the land cover type. 121
- Figure 7.8: Absolute error between land cover types 240m NIR reflectances in the truth dataset and the reflectance segmentation result depending on the area fraction of the land cover type. 122
- Figure 7.9: Correlation of the two options of generating a reference dataset for land cover type specific LAI at 240m. LAI micro is the 30m resolution LAI averaged per land cover type. LAI truth is derived from average reflectances of land cover types. 124
- Figure 7.10: Test areas Hochstadt (left) and Gut Huell (right) used in the investigation of LAI values obtained from reflectance segmentation. The images show the land cover types at 30m resolution with a 240m grid superimposed..... 124

- Figure 7.11: Test areas Landsberg (above) and Wetterstein (below) used in the investigation of LAI values obtained from reflectance segmentation. Size: 640x640 pixel at 30m resolution; 19.2x19.2 km. Legend see Figure 7.10. 125
- Figure 7.12: Results from regression analysis of all fractional LAI values for all land cover types in the four test areas. LAI from reflectance segmentation (LAI refseg) is plotted against LAI from the truth dataset (LAI truth). Spatial resolution is 240m. 129
- Figure 7.13: Regressions of the lumped values of LAI on 240m pixels. The left column compares the area-weighted sums of different land cover types LAI from reflectance segmentation (LAI sum refseg) to the area-weighted sums of LAI from the truth dataset (LAI sum truth). The right column compares the LAI obtained from the homogeneity method (LAI majority) to the truth dataset. 130
- Figure 7.14: Reflectances of the NIR band of the land cover types needleleaf forest (this page), winter grain (next page left) and urban fabric (next page right). Top to bottom: majority dataset, reflectance segmentation result, truth dataset. 135
- Figure 7.15: LAI of the land cover types mixed forest (this page), grassland (next page left) and maize (next page right). Top to bottom: majority LAI, LAI derived from reflectance segmentation result, LAI derived from the truth dataset. 137
- Figure 7.16: MODIS imagery from doy 170 (left) and doy 171 (right) of year 2000 acquired under different viewing angles. The images shown are NIR band cutouts of the northwestern quarter from the study area. Images are displayed without a reduction factor..... 142
- Figure 7.17: Reflectance of the RED and NIR MODIS bands of doy 170 and doy 171 in the Landsberg test area..... 143
- Figure 7.18: Distribution of results from the segmentation of NIR reflectances of the two MODIS images from doy 170 and doy 170, 2000 in the Landsberg test area. The regression lines and coefficients of correlation are equivocal. 144
- Figure 7.19: Results from the regression analysis of land cover type specific fractional LAI versus the truth dataset of the Landsberg test area of the two MODIS scenes of doy 170 and doy 171, 2000. 145
- Figure 7.20: Regression of the fractional land cover type specific LAI deduced from the reflectance segmentation of MODIS images of doy 170 and 171 146
- Figure 7.21: Results from the regression analysis of the lumped LAI derived from reflectance segmentation and the majority LAI produced from MODIS data of doy 170 (upper row) and doy 171 (lower row) versus the lumped LAI from the truth dataset.... 147
- Figure 7.22: Time scale indicating the dates of acquisition (doy) of the 19 MODIS scenes of the time series of 2003..... 148
- Figure 7.23: Temporal development of LAI on four pixels derived from the time series of reflectance segments of the 19 MODIS scenes. 149
- Figure 7.24: Seasonal development of LAI at the 250m scale. LAI from the area weighted sum of fractional land cover type specific LAI (left) and LAI derived based on the majority land cover type (right). Pixel coordinates: Maize (188,305), winter grain (190,305), mixed forest (190,205), grassland (190,200)..... 150
- Figure A1: UML Class diagram of the FapPicIO codec, Iterators and Visitors. 176

Figure A2: UML Class diagram of the algorithm for reflectance segmentation implemented as <code>ReflectanceSegmentationPEV</code>	178
Figure A3: HDF2FAP converter, surface reflectance bands 1-7 of a MOD09 Reflectance file selected for conversion.	179
Figure A4: HDF2PIC converter, help displayed when no arguments are provided.	179

List of Tables

Table 3.1: Scale terms used in this study and the dimensions attributed	18
Table 4.1: MODIS Technical Specifications (NASA, http://modis.gsfc.nasa.gov , King et al., 2004).....	38
Table 4.2: MODIS data products (NASA, http://modarch.gsfc.nasa.gov/data/dataproduct , King et al., 2004).....	41
Table 4.3: Landsat Thematic Mapper Technical Specifications (NASA, 2006, King and Greenstone, 1999, Lillesand and Kiefer, 2000).....	43
Table 4.4: Data types available for data stored in a FAP image file.....	46
Table 4.5: Parameters used in the reprojection of MODIS data	50
Table 4.6: Vertical and horizontal RMS of the geometric correction over all corrected TM images.....	52
Table 4.7: Average absolute vertical and horizontal deviation in [m] from the topographic map within each of the three Landsat paths.	53
Table 4.8: Parameters set for all images in the processing of MODIS imagery for atmospheric correction.....	55
Table 4.9: Datasets compared in the validation of the atmospheric correction	58
Table 4.10: Formulae for predicting MODIS reflectances (R_i) from Landsat TM reflectances (r_i) (Liang et al., 2002)	58
Table 4.11: Coefficient of determination, mean difference and standard deviation of mean difference for the seven bands comparing MODIS simulated from TM to MODIS reflectances of PULREF corrected imagery and MOD09 product on DOY 171..	60
Table 4.12: Coefficient of determination, mean difference and standard deviation of mean difference for the seven bands comparing MODIS simulated from TM on DOY 171 to MODIS reflectances of PULREF corrected imagery and MOD09 product on DOY 170	61
Table 4.13: File naming conventions for MODIS products of production Level 1 and 2 (swath geometry) and production Level 2G, 3 and 4 (SIN projected grids).....	65
Table 4.14: Table of dates of year 2003 MODIS imagery time series.....	66
Table 4.15: Land Cover Type 3 from MOD12 Land Cover Types. This is the classification scheme used in the production of the MOD15 LAI/FPAR dataset (Strahler et al., 1999, HDF-EOS metadata)	68

Table 5.1: Sites of leaf area index measurement campaign 2002-2004.....	85
Table 6.1: Coefficients of determination of the regression of land cover types histograms with the peak distribution functions.	104
Table 6.2: Land cover type specific functions to derive LAI from arNDVI.....	107
Table 7.1: Statistics of LAI values obtained when possible NDVI are applied in land cover specific LAI algorithms of Table 6.2.	111
Table 7.2: Corner Coordinates (UL, UR, LR, LL) of the test areas used in the analysis of LAI results from reflectance segmentation.....	126
Table 7.3: Examples of the results on single 240m pixels from the Hochtstadt and the Gut Huell areas. The table lists fractional (left) and aggregated values (right). Majority land cover types on a pixel are in bold type. Date: June 19, 2000, doy 171 (full tables see Appendix 6)	127
Table 7.4: Statistics of the relative and absolute error in the land cover type specific fractional LAI from reflectance segmentation for the four test areas. Error was assessed against the truth dataset.	131
Table 7.5: Statistics of the relative and absolute error in the summed LAI from reflectance segmentation on 240m pixels and the LAI from the majority data for the four test areas. Error was assessed against the sums of LAI from the truth dataset.....	132
Table 7.6: Statistics of relative and absolute error of fractional LAI derived at different scales and aggregations of fractional LAI in the Landsberg test area.	140
Table 7.7: Statistics of relative and absolute error of lumped single value LAI on different scales and the error of the majority method for LAI retrieval.....	141
Table 7.8: Statistics of the error of LAI derived from reflectance segments for the MODIS imagery of doy 170 and doy 171, 2000 compared to the truth dataset.	146
Table 7.9: Statistics of the error of LAI at 250m in the Landsberg test area. Data were lumped from the fractional LAI and derived from majority data and compared to lumped LAI of the truth dataset.	147

List of Acronyms

asl	-	Above Sea Level
ASTER	-	Advanced Spaceborne Thermal Emission and Reflection Radiometer
AVHRR	-	Advanced Very High Resolution Radiometer
BRDF	-	Bidirectional Reflectance Distribution Function
BRF	-	Bidirectional Reflectance Factor
CERES	-	Clouds and the Earth's Radiant Energy System
CZCS	-	Coastal Zone Color Scanner
DAAC	-	Distributed Active Archive Center (The DAACs process, archive, document, and distribute data from NASA's past and current Earth Observing System (EOS) satellites and field measurement programs)
DEM	-	Digital Elevation Model
DFCB	-	Data Format Control Book
DOY	-	Day Of the Year
DTM	-	Digital Terrain Model
EDC	-	Earth Resources Observation System Data Center, South Dakota
ENPOC	-	Environmental Possibility Classifier
EOS AM	-	Earth Observing System Ante Meridiem (morning satellite); later named "Terra"
EOS	-	NASA's Earth Observing System
EOSDIS	-	Earth Observing System Data and Information System
EROS	-	National Center for Earth Resources Observation & Science, Earth Resources Observation System (both so on web page!)
ESDIS	-	Earth Science Data and Information System, organization implementing EOSDIS
ETM+	-	Enhanced Thematic Mapper Plus
FAP	-	Flächendaten Analyse Programm
FPAR	-	Fraction of Photosynthetically Active Radiation
GCP	-	Ground Control Point
GES DAAC	-	Goddard Earth Sciences Distributed Active Archive Center
GES DISC	-	Goddard Earth Sciences Data and Information Services Center
GIS	-	Geographic Information System
HDF	-	Hierarchical Data Format
HDF-EOS	-	Hierarchical Data Format - Earth Observation System
HIRS	-	High-Resolution Infrared Sounder
HKM	-	Half Kilometer
IFOV	-	Instantaneous Field Of View

IGGF	-	Institut für Geographie und Geographische Fernerkundung
LAD	-	Leaf Angle Distribution
LAI	-	Leaf Area Index
LP DAAC	-	Land Processes Distributed Active Archive Center http://edcdaac.usgs.gov/main.asp
LWIR	-	Long-Wave Infrared
MERIS	-	Medium Resolution Imaging Spectrometer
MIR	-	Middle infrared range of the electromagnetic spectrum (1300-2500nm)
MISR	-	Multi-Angle Imaging Spectroradiometer
MLA	-	Mean Leaf Angle
MODARCH	-	http://modarch.gsfc.nasa.gov mirrors http://modis.gsfc.nasa.gov
MODIS	-	MODERate Resolution Imaging Spectroradiometer
MODLAND	-	MODIS Land Science Team
MOPITT	-	Measurements of Pollution in the Troposphere
MWIR	-	Mid-Wave Infrared
MSB	-	Most Significant Bit
NASA	-	National Aeronautics and Space Administration
NCSA	-	National Center for Supercomputing Applications
NDVI	-	Normalized Difference Vegetation Index
NIR	-	Near infrared range of the electromagnetic spectrum (700-1300nm)
NOAA	-	National Oceanic and Atmospheric Administration
NPOESS	-	National Polar Operational Environmental Satellite System
NPV	-	NonPhotosynthetic Vegetation
NPVAD	-	NonPhotosynthetic Vegetation Angle Distribution
NPVAI	-	NonPhotosynthetic Vegetation Area Index
PAI	-	Plant Area Index
PAR	-	Photosynthetically Active Radiation
PGE	-	Program Executable
PROMET	-	Process Oriented Modular Environment and Vegetation Model
QKM	-	Quarter Kilometer
SAIL	-	Scattering of Arbitrary Inclined Leaves
SeaWiFS	-	Sea-viewing Wide Field-Of-View Sensor
SLC	-	Scan Line Corrector
SWIR	-	Short-Wave Infrared
TM	-	Thematic Mapper
TOA	-	Top Of Atmosphere
TOC	-	Top Of Canopy
USGS	-	U. S. Geological Survey
UTC	-	Coordinated Universal Time
UTM	-	Universal Transverse Mercator
VI	-	Vegetation Index
VIS	-	Visible range of the electromagnetic spectrum (400-700nm)
WRS	-	Worldwide Reference System for Landsat TM

1 Introduction

Only recently the beauty of imagery produced by remote sensing instruments has become readily available to everyone through easily accessible public Internet tools. Images collected from all over the globe are gathered to bring the layman the pleasure of the view from above, a sense of flight over his country, city and even backyard. Zooming in and out of the scene is but a click away and seems dead easy. For a simple *view* of a scenery this may today be veritable, for the vast information that is actually contained in the data sources of those images it is not.

Remote sensing science has emerged with a variety of instruments that not only produce much more than simply colorful pictures but covers a large quantum of different resolutions or scales. This “resolution” already is an ambiguous term (Quattrochi and Goodchild, 1997, Wu and Li, 2006). It may connect to what the user of the Internet tool sees as a zoom factor, that is, a *spatial* resolution. In the context of remote sensing data, however, it may also be interpreted as a *temporal* resolution or repetition of data collection and, additionally, the number and characteristics of simultaneous measurements made is addressed as *spectral* resolution. Also, the zooming in and out on the scientific datasets alone is by far a more complicated task in remote sensing and the environmental scientists use of such data (Quattrochi and Goodchild, 1997). Furthermore, such a change of spatial resolution is not independent of a temporal resolution factor.

The work presented in this study is concerned with some of the difficulties that occur when the information of satellite imagery shall be utilized for more than beautiful pictures. Remote sensing data has long been a major source for environmental data that is available for the entire surface of the earth on a regular and consistent basis. One of the prominent applications of the data is their use to derive land surface parameters (Asrar, 1989, Myneni and Ross, 1991, Lillesand and Kiefer, 2000). These parameters, that can be produced for large areas and at different resolutions have been a major source for the input requirements of many types of environmental models (Bach and Mauser, 2003). Especially in the field of global change research, outstanding contributions have been made by remote sensing in both, the detection of changes of the environments on this planet as well as in the fields of modeling future development scenarios and in decision support. Environmental modeling and remote sensing have become intertwined scientific activities and the handling of the interfaces of the two fields is a challenging task to both (Schultz and Engman, 2000). What data do the models need? How can these be produced? What benefit of modeling environmental processes emerges for the remote sensing scientist? What needs to be done for the possibilities and requirements of the two to harmonize? In many cases these questions have been answered successfully and the synergies have been proven repeatedly (Schultz and Engman, 2000, Lakshmi et al. 2001, Schneider, 2003). Nevertheless, questions remain unanswered. It is the attempt in this thesis to bridge a gap between spatial and temporal resolution requirements of

an environmental research model and the propositions of a new generation of remote sensing satellites.

The model that this work is focused on is the model developed in the framework of the GLOWA-Danube project (Mauser, 2000, Mauser and Ludwig, 2002, Ludwig et al., 2003a). The project and the DANUBIA model developed in the project are briefly described in the next section. The remote sensing instrument in focus of this work is the Moderate Resolution Imaging Spectroradiometer MODIS (Justice et al., 1998, Justice and Townshend, 2002, NASA, <http://modis.gsfc.nasa.gov/>). The model as well as the satellite sensor operate at intrinsic scales. Bringing together the spatial and temporal characteristics and requirements of the model and the remote sensing instrument is trivial when considering their identical spatial resolution capabilities of 1km. However, the DANUBIA model as well as other environmental models are laid out to enhance their performance by processing information that is maintained below this resolution (Mauser and Schädlich, 1998). MODIS on the other hand, provides some of its information at higher resolution as well. Thus, both systems have a potential of moving to a state of higher information content. The model thereby improves its representation of processes. The remote sensing imagery reveals more detail.

The methods of how this greater detail is introduced to the model and the remote sensing imagery, however, are different. The remote sensing device of higher resolution simply produces more pixels, where each pixel represents a smaller area of the surface sensed. It refines the scale. The model, in contrast, conceptualizes the pixel of the same size as a composite of different characteristics. The scale remains the same, but subscale characteristics are taken into account. It is this antagonism in data storage concepts that shall be tackled by the method for reflectance segmentation developed in this study.

One of the key parameters in environmental process models like DANUBIA is the area of leaves produced by plants. It plays a vital role in numerous processes such as evapotranspiration, radiative transfer, gas exchange, biomass production and generation of runoff (Schultz and Engman, 2000, Lakshmi et al. 2001). Leaf area is processed as leaf area index (LAI) in environmental models. LAI is also a parameter that can be derived from the surface reflectances obtained from remote sensing imagery (Asrar, 1989, Campbell, 1996, Lillesand and Kiefer, 2000, Myneni et al. 1997). It was chosen as the quantity to test and validate the method for reflectance segmentation.

1.1 GLOWA Danube – Global Change in the Hydrologic Cycle

The background and trigger for this thesis study was the GLOWA-initiative (Global Change of the water cycle), funded by the German Ministry of Research and Education (BMBF). Within this framework the GLOWA-Danube project focuses on the temperate mid-latitude catchment of the upper Danube area (see chapter 2). It serves as a test site for the development and testing of the integrated decision support system DANUBIA. This system is a distributed, web based, object-oriented and raster based compound of expert numerical modeling systems involved in the processes of the hydrologic cycle. Its objective is to identify, examine and develop new techniques of coupled integrated modeling. The system includes models from fields of natural and socio-economic sciences that are coupled to investigate the sustainability of future water use on an exhaustive scientific basis. It is developed by a network of experts from water related sciences. Integration of natural and socio-economic research is a key issue in the project, which is addressed by an integration concept based on the industry standard of the unified modeling language UML (Booch et al., 2005). This standard unites all contributors on a common platform-independent notation of

computational methods and data exchange procedures. The dialog with stakeholders in water resource management is sought to assure practical issues and future water related problems to be addressed (Ludwig, et al. 2003a).

The basic object in the system is the “proxel” (process-pixel) on which processes are described. A proxel is connected to its environment and may be adjusted in size for the system to operate on different scales. The 1km scale was agreed upon for the current development and testing of DANUBIA. The processes interconnect on the proxel and include atmospheric impact, energy exchange at the surface, plant growth, runoff formation, soil water movement, snowmelt, water uptake by water suppliers, household water use as well as economic, tourism and farming activities. All proxels are organized in a raster grid that defines the spatial context of the proxels (see Figure 1.1). The proxel itself is not assumed as an homogeneous entity, but may be subdivided into homogeneous static units of land cover type, soil type, topography etc. by the concept of geocomplexes (see chapter 3)

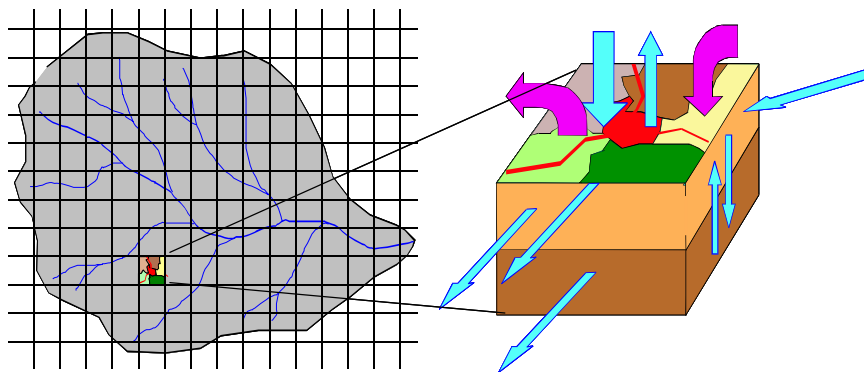


Figure 1.1: The proxel concept of DANUBIA for raster based modeling (Ludwig, et al., 2003a)

A standardized framework is set up to manage the connectivity of the individual models and to spatially and temporally control the interaction of the model compounds. This framework is open to plug in individually maintained models as well as new components. The system is implemented in the Java programming language using standards for data exchange and method invocation.

The use of remote sensing data is an important integrative component in the project. The possibilities of remote sensing to monitor processes and supply data and parameters at a range of scales play a major role for all project partners. The multiscale nature of remote sensing data make it an important matter of research within the project in terms of run-time assimilation of up to date information and improvement of parameter retrieval (Ludwig et al., 2003a). The latter is the subject of this research.

1.2 Scientific Objective and Outline of the Thesis

The MODIS sensor provides spectral measurements at 250m, 500m and 1km spatial resolution. With two instruments in orbit and the coverage of the scanner, multiple observations are available per day. Alternative sensors with higher spatial resolution such as Landsat Thematic Mapper cannot compete with this data rate and coverage. However, at any of its resolutions, MODIS will mostly capture heterogeneous surfaces on a pixel in a diversified area like the upper Danube catchment. The majority of the pixels are mixed pixels.

The application of remote sensing signals to derive parameters like leaf area index (LAI) is closely tied to the type of vegetation producing a pixels signal. Thus, land cover type is an important input in the retrieval algorithm for LAI from satellite data. This holds for other algorithms as well, and also applies to many processes described in land surface models. In either case land cover heterogeneity on a pixel greatly disturbs the applicability of the algorithms.

Like in DANUBIA, this problem of heterogeneity has led to the stratification of the pixel into units of homogeneous character. Stratification by land cover type has been explored earlier at the Department of Geography of the University of Munich (Mauser and Schädlich, 1998, Ludwig et al. 2003c, Reichert et al., 2004b). Such subdivision of the pixel contradicts with a straightforward use of remote sensing data that delivers a measurement that integrates over the homogeneous units contained in the area of the pixel. However, by introducing ancillary knowledge, two kinds of information may be provided for the remote sensing pixels measurement. The first is a land cover classification at higher resolution than the satellite sensors scale. It will give evidence of the surfaces that contributed to produce the signal collected by the sensor. The second is a reasonable guess about the spectral properties of the surfaces under concern. In respect of the knowledge about various surfaces and their spectral reflectance behavior, reasonable expectancies about different surfaces reflectance can be brought forward. From the expertise and experience in remote sensing it is at least roughly known how surfaces reflect radiation and how they change their reflectance characteristics over time. In other words, prior to a spectral measurement, a fuzzy statement can be made about what the signal will look like. This especially applies to the seasonal progression of vegetation surfaces of different types. A forested or agriculturally used surface is well known to exhibit different reflectance properties at different times of the growing season.

It is the objective of this thesis to explore the possibilities of producing this ancillary knowledge and using it to decompose a pixels remote sensing signal into the underlying land cover types specific contributions. A method to achieve this goal is developed and presented. It is an approach for scale independent derivation of subscale land surface reflectances from mesoscale remote sensing data. The procedure is tested and investigated on different datasets from a range of scales. It is used to stratify the reflectance on a moderate scale remote sensing pixel and assign the obtained segments to the land cover types that produced it. As a result, reflectances of the homogeneous units that a pixel is composed of are obtained. Based on these results, for the homogeneous fractions of the pixel LAI can be derived. Both, reflectances and LAI are validated against a reference dataset deduced from higher resolution imagery of the Landsat Thematic Mapper sensor. The fractional values of LAI are compared to the conventional approach of ignoring pixel heterogeneity in the production of the LAI parameter. The investigation makes use of the advantage of coincident data from the MODIS and the Thematic Mapper remote sensing instruments.

The chapter following this introduction provides insight into the characteristics of the upper Danube catchment. A brief overview of the natural and socio-economic features is given and the study area used in the testing of the method for reflectance segmentation is delineated.

In chapter 3 the issue of scale is discussed in detail and the consequences of scale for data and modeling are explored. Because scale is directly connected to data storage, ways of data representation are viewed in relation to scale. The chapter then casts a view on the factor of scale in GLOWA, in remote sensing data and how scale connects to the LAI parameter. The final section argues about the benefit for scaling that lies in the method for reflectance segmentation.

The 4th chapter introduces the sensors that collected the data used in this study and describes the preparation of the data. After the geocoding of the imagery, a localized atmospheric correction was applied to data of both images. The results are presented and compared to the operational atmospheric correction product (MOD09) issued by the MODIS Land Science Team (MODLAND). The chapter concludes with a presentation of all MODIS and Thematic Mapper data sought for this work.

As stated above, leaf area index is an important process variable in the environment. It is discussed in chapter 5. A thorough definition of the quantity is given and a summary of the role of leaf area in the environment is sought. The difficulties of determining canopy optical properties as opposed to leaf optical properties is addressed. Both play a vital role when optical remote sensing measurements shall be used to derive leaf area index. Alternatives and difficulties of determining leaf area index are subsequently highlighted. The chapter concludes with a presentation and critical discussion of available LAI data.

In chapter 6 the method for reflectance segmentation is introduced. The conception of the algorithm is outlined before the methods for the optimization of fractional reflectances are described.

The application of the method to the MODIS data is described in chapter 7. The algorithm was first prototyped on a synthetic dataset. A detailed analysis illuminates the characteristics and capabilities of the approach. Then it is used on actual MODIS data. It is applied to segment the reflectances of two MODIS scenes that coincide with high resolution Landsat Thematic Mapper data. Finally, the effects of applying the algorithm to a time series of MODIS data are shown.

Chapter 8 discusses the observations from the prototyping and the application of the method. A critical view is cast on the results and the usability of the method.

The thesis concludes in chapter 9 with a summary of the findings made and an outlook to possible improvements and future research in conjunction with the presented method.

2 Study Area

The issues addressed in this study are aimed at the requirements and the objectives of the GLOWA-Danube project. It focuses on the upper part of the river Danube catchment. This area was chosen for various reasons including its diversity in terms of natural environment and socio-economic characteristics. The investigations in the scientific context pursued in this thesis, however, were performed on an area that covers somewhat more than a third of the full GLOWA Danube catchment. Nevertheless this third exhibits most of the properties and characteristics observed in the whole of the catchment. The hydrologic aspect of the GLOWA Danube project called for a hydrologic entity as a test area. The remote sensing aspect of this study neglects this hydrologic demand but retains the diversity of the area in a subset. In order to support this approach, first the characteristics of the upper Danube catchment are described in the following. The subsequent section delineates the study area within the catchments area. It was used in all the following and localizes a number of test sites that were investigated in detail in order to evaluate the method presented.

2.1 The upper Danube catchment

Among the great rivers of Europe, the Danube has the distinct feature of flowing over a great distance in an east-west direction. Its great historic and economic significance are due to this outstanding characteristic. Being the second largest river in Europe with a length of 2,857km from wellspring to mouth it extends from 8°09'E to 29°45'E. In a total area of 817,000km² it unites a variety of landscapes including large parts of the Alps including glaciated mountains, forested low mountain ranges, hill countries and vast plains. The full catchment stretches across 18 European countries (RZD, 1986).

The upper part of the catchment, called the “upper Danube” in the following, is delineated at the gauge at Achleiten (287m asl) shortly below the city of Passau and the mouths of the tributaries of the Inn and the Ilz (see Figure 2.1 and Figure 2.2). The catchment above this point covers an area of 76,653km² with a river length of some 580km (BLfW, 1999). The larger parts of the landscapes in the area are the Black Forest to the west, the Swabian and the Franconian Alb to the north, the Bavarian and Bohemian Forest in the east and the Alpine Foreland and the Alps in the south. In the center part some of the large Basins are found, such as the Donauried, the Donaumoos and the Dungau.

The upper Danube encompasses territories of five European countries. The largest part is situated in Germany in the states of Bavaria (62%) and Baden-Württemberg (11%). The headwaters of the Inn are located in Austria (24%) with minor parts in Switzerland and Italy. Additionally, a small part in the east of the catchment belongs to Czech Republic (BLfW,

1999). The divides of the basin border to the river Rhine in the west and north, to the Elbe to the north, and the rivers Po and Etsch in the Italian Alps towards the south. The eastern basins belong to the center part of the Danube catchment itself. Within the basin, the main sinistral tributary rivers include the Wörnitz, the Altmühl, the Naab and the Regen and the dextral comprise the Iller, the Lech, the Isar and the Inn. The latter is the largest of the feeders to the Danube, covering 26,130km². It is this part of the catchment that reaches farthest into the Alps to include high alpine territory including the highest point at Piz Bernina at 4,049m asl (RZD, 1986, BLfW, 1999). An overview of the location of the catchment in the context of central Europe is given in Figure 2.1. The catchment itself is shown in Figure 2.2.

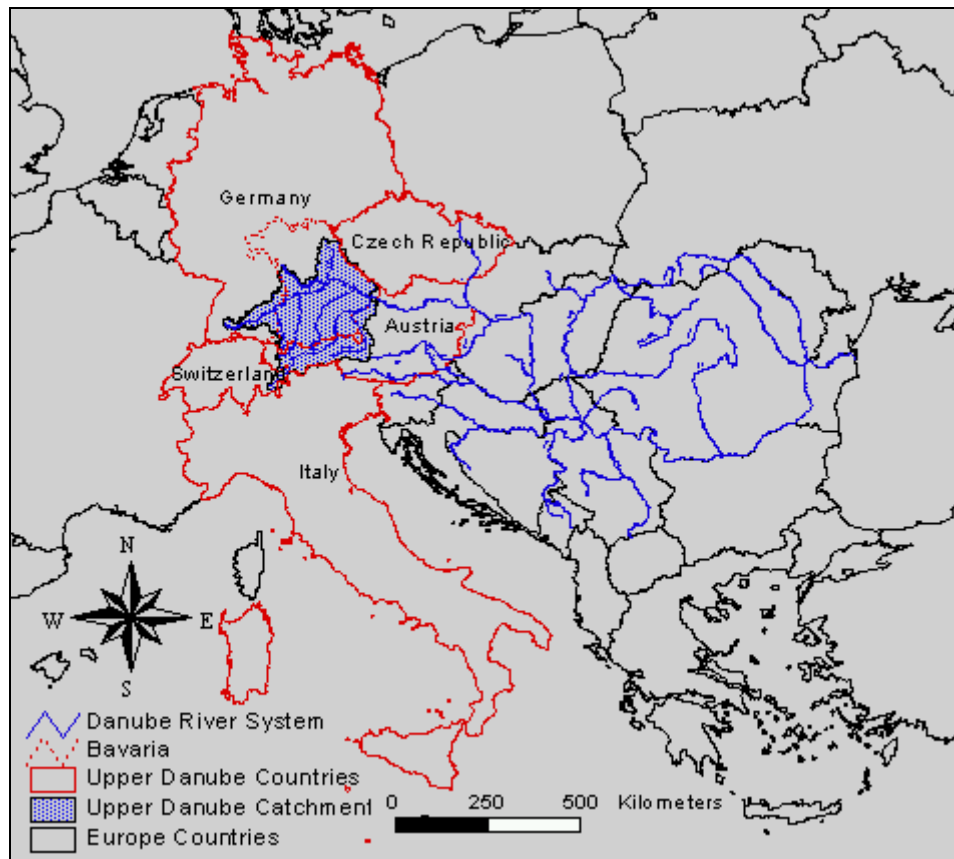


Figure 2.1: The location of the catchment area of the upper Danube in relation to the whole river system.

Geology and Geomorphology

A simple geographical breakdown of the area, which is marked by a multitude of geological media, would divide it into an alpine part, the alpine foreland and the region of the low mountain ranges of the Swabian and Franconian Albs. Crystalline shale and granite mostly form the central part of the Alps, the northern rim is made up of limestone with typical carst formations. At the outskirts of the mountains follow the clastic sedimentations of the flysch zone and a narrow band of the helvetic nappes. The southern alpine foreland is formed by the large deposits of the folded molasse sediments, mainly covered by quarternary sediments of the Würm glacial period and in parts by unconsolidated loess. The melting ice cover left it with the typical fluvial and fluvio-glacial landforms. The large lakes Ammersee and Starnberger See are some of the more outstanding remainders of that period. To the north of the terminal moraines the molasse basin continues forming the tertiary hill country, partially divided by gravel plains of the larger rivers. The valley of the Danube river takes its course between these tertiary deposits and the Jurassic plateaus of the Swabian Jura and the

Franconian Jura to the north and the crystalline mountains of the Bavarian Forest in the northeast (Jerz, 1993).

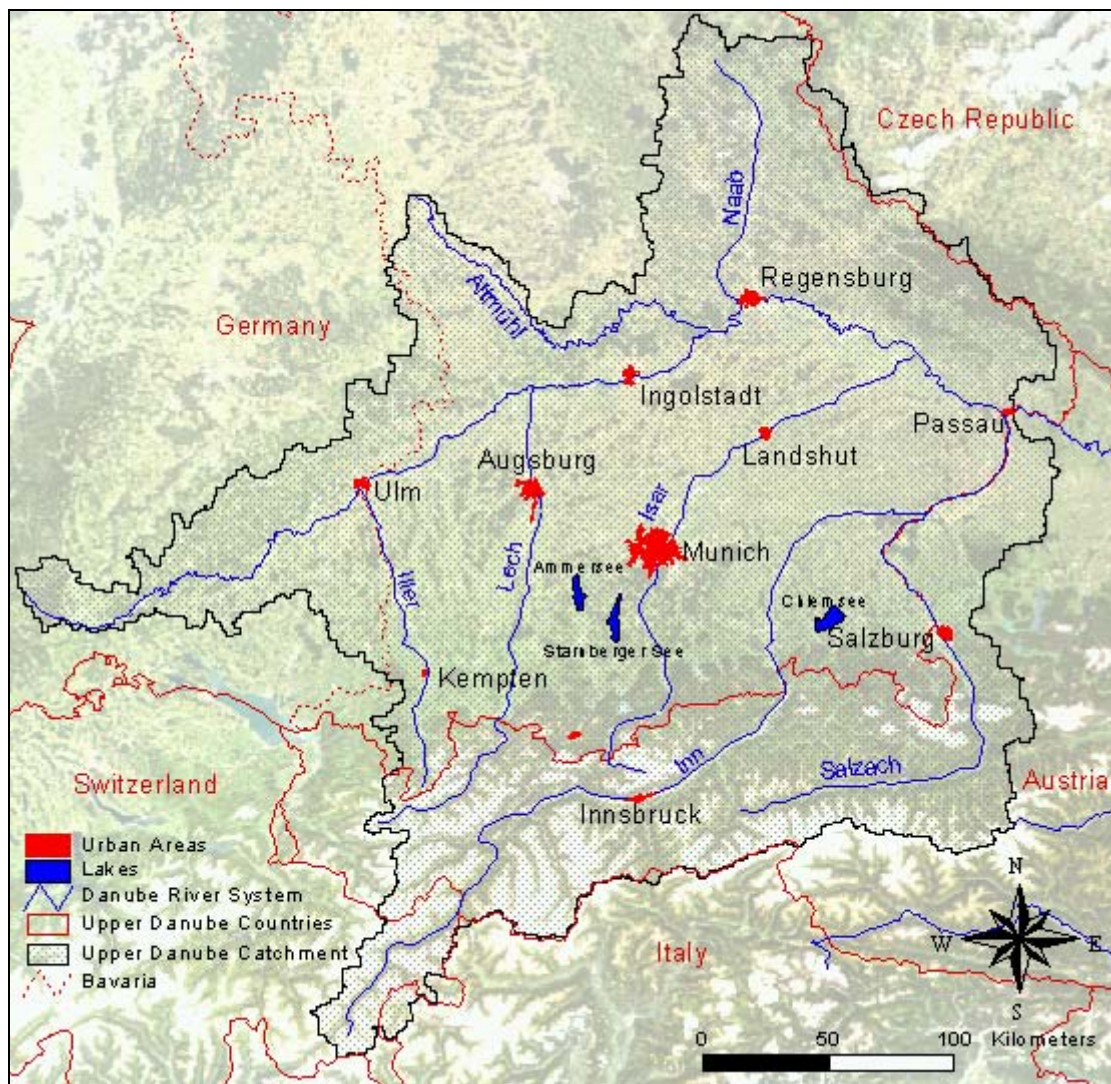


Figure 2.2: Satellite image with map overlay of the upper Danube catchment area.

Climate

Located in the northern mid-latitude temperate zone, the weather in the entire upper Danube area is dominated by the prevailing westerlies. The summer is characterized by northwesterly and westerly winds that turn to mostly southwestern winds in the winter. Advection currents originating in the northern Atlantic tend to bring enduring and yielding precipitation. In the lee of the Alps, during southerly winds foehn is a common feature in the area's weather that may reach as far north as the Danube valley.

Mean annual precipitation ranges from approximately 700mm in the valley of the Danube to 1500mm at the northern rim of the Alps. In the mountain areas, peaks notably above 2000mm are reached at higher elevations. Accumulation during northerly meteorological conditions along the mountain range greatly contributes to this increase from north to south. The more elevated parts of the Black and the Bavarian forest will also reach annual precipitation up to 1500mm. While the plateaus of the Swabian and Franconian Albs tend to exceed 1000mm/a

the lowest precipitation are recorded in some of the basins of Altmühl, Naab and the Miocene impact crater of the Nördlinger Ries (Bundesministerium für Umwelt, Naturschutz und Reaktorsicherheit, 2003). Also, some of the central alpine valleys report quite low annual rainfall. The overall mean of the German part of the catchment, which amounts to 73% of the total area, reaches 950mm with a maximum in the summer. Especially in the alpine foreland, extreme events may bring up to 200mm of precipitation per day (RZD, 1986).

Another important climatic factor is the duration of snow cover. While large parts of the catchment area are reported to have 40-60 days of annual snow cover it may exceed 100 days in the higher elevations of the mountainous parts. In the Alps at elevations of 2000m asl snow cover may last around six to eight months of the year. With a rise from the rim to the central Alps, the elevation of perennial snow cover lies between 2900-3200m asl (RZD, 1986).

Mean annual temperatures in the upper Danube region again are greatly influenced by the orography of the area. While means in large portions of the alpine foreland reside around 7-8°C, favored locations along the Danube River and in the lower parts of its tributaries may have mean annual temperatures between 8 to 10°C. In the mountains annual means below freezing are common. In July the highest monthly mean at 16-18°C is observed, in the coldest month January mean temperatures are between -2 to -3°C. Temperatures in the mountainous parts of the catchment decline with altitude at a rate of 0.5-0.7K/100m in the summer and due to frequent atmospheric inversion at 0.2-0.4 in the winter (RZD, 1986). In the Alps, pronounced small-scale variations in climate often occur due to local radiation budget, air temperature, cloud cover, wind conditions and precipitation.

Hydrology

With its route parallel to the mountain range of the Alps, the Danube is the receiving watercourse for a large number of rivers exiting the eastern Alps to the north. However, since its formation in the Pliocene, it had to release numerous tributary rivers and streams to the faster and stronger eroding Rhine river system. This surrendering of territory is ongoing along the northern rim of the Swabian and Franconian Jura in the north of the basin.

The Danube's flow regime is greatly influenced by the many tributaries. It changes several times due to the influences of the flow regimes of its affluents. While the rivers coming from the north exhibit a pluvial regime type with maxima in the winter, the tributaries coming from the Alps are characterized by strong influences of snow melt and glacier runoff with maximum discharge in the summer. High precipitation along the northern rim of the Alps in the early summer leads to frequent floods during that time of the year. Somewhat more than half of the mean runoff of 1420m³/s gauged at Achleiten near Passau is contributed by the Inn's catchment that reaches far into the Alps (BLfW, 1999). Many rivers have been regulated by dams and hydropower stations so that a natural condition of discharge and sediment transportation is rarely present in today's watercourses of the basin.

An important factor in the water balance of the catchment are the numerous lakes that mitigate the dynamics of the runoff by their retention effect. They are almost exclusively located to the south of the Danube and are formations of the Pleistocene glaciation of the area.

Soils

Due to the great differences in the factors and processes of soil formation a multitude of soils may be found in the area of the upper Danube. Regional variations in bedrock, terrain, climate, vegetation and time for soil formation result in soil types ranging from weakly developed leptosols in the mountain regions to fertile luvisols that formed on loess sediments. Soil texture ranges from loamy clays to grainy sand. In the Alps, the young soils are organized according to climatic factors and the type of bedrock. Lithics, rendzic and umbric leptosols make up the soils of the slopes of the mountains. In the forested altitudinal belts,

regosols and some chromic cambisols developed on carbonate rocks while umbric leptosols and albic luvisols are found in the crystalline bedrock regions of the central Alps. Locally, eutric leptosols, luvisols, cambisols as well as gleyic luvisols and gleysols occur, especially along the valley floors.

In the alpine foreland, mainly luvisols are developed on coarse permeable gravel-sheeted plains and on moraines. In the large basin around Munich some rendzic leptosols are found. Luvisols and cambisols are also predominant on the loess eolian sediments in the tertiary hill country, and, depending on the substrate and ground water level, gleyic luvisols and gleysols are frequent. Fluvisols are found throughout the upper Danube area along the numerous watercourses. Extended bog lands with peaty soils are also common, especially along the northern rim of the Alps.

On the Jurassic bedrock of the Swabian and Franconian Alps, rendzic leptosols and chromic cambisols are predominant on the upper Jurassic, while vertisols and gleyic luvisols are found on brown and lower Jurassic. On the crystalline rock formations of the Bavarian, Bohemian and the Black Forest, umbric leptosols and fertile cambisols dominate which tend to podzolize on granite and gneissic rock (Kuntze, et al., 1994, Hintermaier-Erhard and Zech, 1997).

Vegetation

Vegetation in the basin of the upper Danube is a product of the climatic, geologic and geomorphologic properties of the catchment and the anthropogenic influence over the centuries. The potential natural vegetation would be forest in almost all of the area (RZD, 1986). Under undisturbed natural conditions, deciduous forests dominated by beech (*fagus silvatica*) and oak (*quercus robur* and *quercus petraea*) would inhabit the land, excluding those elevated zones where climatic conditions inhibit the spread of the species. However, today man has claimed most of the territory that may be used agriculturally, repelling forest stands to unfavorable sites. Only few pure deciduous forests remain for forestry has substituted the natural vegetation by large plantings of spruce (*picea abies*). Unique and rich in species remain the extrazonal alluvial forests that stretch along the Danube and its tributaries wherever lack of human impact allows for a natural development of these biomes.

In the more elevated montane and subalpine altitudinal belts of the mountainous areas, mixed mountain forests and coniferous forests are situated. The mixed forests are made up of spruce (*picea abies*), white fir (*abies alba*) and beech (*fagus silvatica*). Due to anthropogenic influence spruce is the dominating tree in these surroundings as well and it is spruce that is found at the timberline at about 1800-1900m. In the climatically dryer central part of the Alps, the mixed forests are replaced by spruce in the lower stands while larch (*larix decidua*) and more scarcely Swiss stone pine (*pinus cembra*) and mountain pine (*pinus mugo*) reach up to the somewhat higher timberline at 2400m. Above this altitude grasses (*carex curvula*) and ericaceae (*calluna vulgaris*) are the native species adapted to that environment (Ellenberg, 1996). In the south of Bavaria, some of once widespread moorlands have been preserved in their natural state.

Socio-economic aspects

The area of the upper Danube catchment has been greatly formed and influenced by the activity of man. Intensely used and densely populated it is the home to about 8 Mio people. The largest settlements of the area are the agglomerations of Munich, Augsburg and Ingolstadt. Important industries have been established here and wherever feasible, the land is cultivated or used as pastures, even in the high and remote areas of the mountains. Common crops include winter and summer grains (mainly *triticum L.*, *hordeum vulgare L.*, *secale cereale L.*) maize (*zea mays L.*), sugar-beet (*beta vulgaris*), potatoes (*solanum tuberosum L.*), canola (*brassica napus L.*) as well as specialized crops like hops (*humulus L.*) and asparagus

(*asparagus L.*) are grown. Preferred sites are the low and climatically favorable basins along the river Danube itself. Above the climatic limits of agricultural productivity extended pastures and grasslands are extensively used. Many areas in the upper Danube, especially in the region of the Alps and the Bavarian forest, are attractive to tourism, which has developed into an economic branch of substantial size.

Various public and private institutions pursue water management in the catchment of the upper Danube. Besides the water supply for the people, trade and industries, it includes flood protection, low water management, operation of hydropower facilities and navigation. The necessities emerging from these tasks have early led to profound transfigurations of watercourses by measures of hydraulic engineering. Reclaiming land for settlements and farming as well as flood protection and hydro power production have led to river regulations and the construction of dams and storage reservoirs throughout the catchment area. This implies substantial shortening of river courses and loss of retention basins. Today, the Danube and its tributaries are vastly regulated with numerous flow and reservoir power stations. The Danube is navigable below the mouth of the Altmühl and is connected to the Rhine-Main river system via the Rhine-Main-Danube-Channel. It is through this system that water is exported from the Danube basin to the Rhine-Main basin (Ludwig et al., 2003a).

2.2 Delineation of study area and test sites

For the purposes of this study a subarea of the upper Danube catchment was selected as the study area. Concerning the dataset, it was chosen as a square area that does not intersect with the border of the catchment, i.e. that is a true subset that lies fully within the catchment area. This not only yields a dataset that is filled with data over the entire cutout but also avoids a number of difficulties in data processing that occur when parts of a rectangular raster dataset are filled with invalid or missing values. The size of the square was chosen such that it will evenly divide by a number of different spatial resolutions. This will assure that the dataset could easily be worked with at different pixel sizes without conflicting with pixel fractions at either edge of the area. It also provides the possibility to work with a hierarchical scaling pyramid where each coarser resolution pixel will divide up into an integer number of higher resolution pixels (see chapter 3).

Concerning the location and extent of the area, the square was positioned such that it would include most of the natural and man made features observed in the whole of the basin of the upper Danube. Only a short section of the Danube itself cuts through the square, nevertheless different environments such as fertile agriculturally used plains, forests of different type, mountainous terrain with forests and pastures, water bodies and urban areas are contained in the subset of the upper Danube. The extend of the cutout includes most of the variation in climate, vegetation, soils, terrain and land cover that is observed in the whole of the upper Danube catchment. The location, size and characteristics of this study area are illustrated in Figure 2.3.

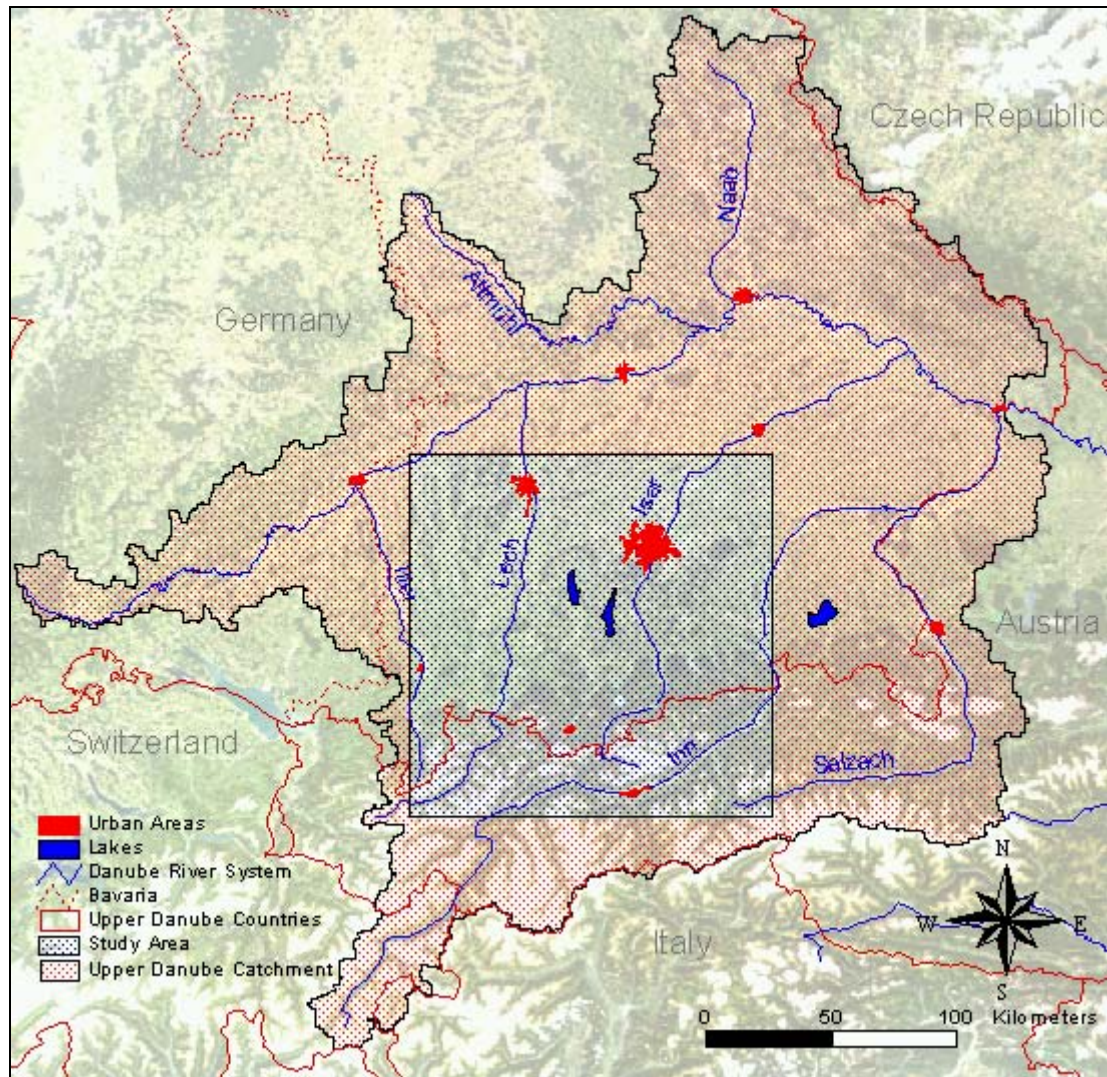


Figure 2.3: Location of the study area within the catchment of the upper Danube.

While the preparation of data (chapter 4) was carried out for the entire upper Danube area, all processing of data in the context of this study was performed on this subset area described above. The area has the additional advantage of being a cloud free part of the applied satellite imagery. Furtherly, by focusing on this sub area, data amounts are kept at reasonable size and computational cost is reduced.

For the analysis of data four test areas were chosen within the study area. For reasons of scaling of the data and capturing the sites at different scales, again these areas were selected to be square cutouts of the study areas frame. Two smaller areas, Gut Huell and Hochstadt, were selected in the southwest of Munich. Two larger areas, Landsberg and Wetterstein were selected to investigate a lowland and a mountainous cutout of the area. The location of these test areas is illustrated in Figure 2.4. Further detail on these sites along with the analysis is provided in chapter 6.

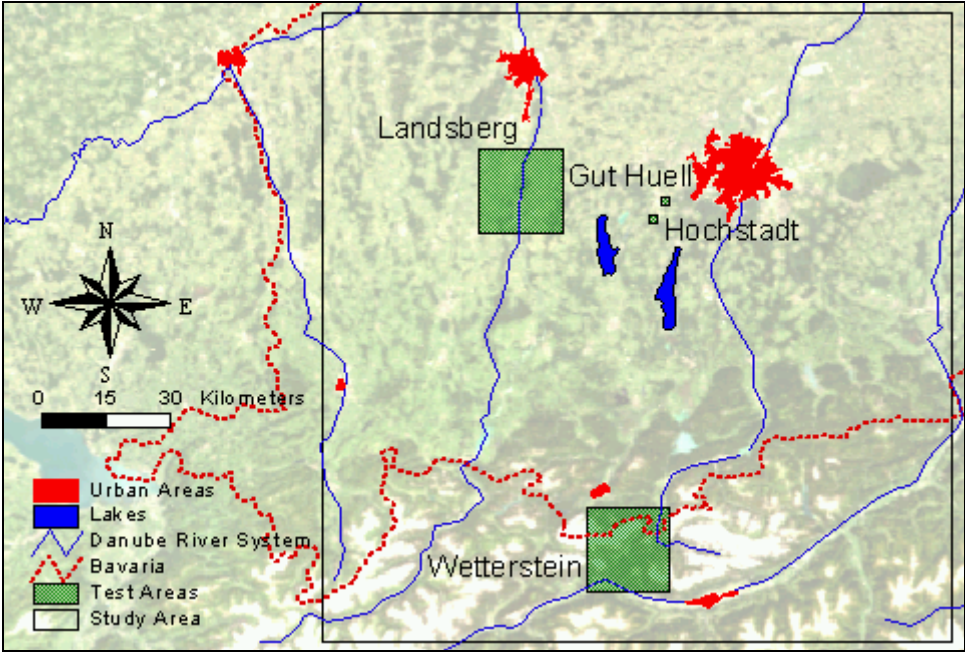


Figure 2.4: Location of the test areas Landsberg, Wetterstein, Gut Huell and Hochstadt within the study area.

3 Perspectives of Scale

The method presented later in this study is an approach to address scale in the context of remote sensing and environmental modeling. This chapter is to address issues connected to scale and to the method developed.

The general term of *scale* is widely used but it is highly ambiguous. It appears across scientific fields such as economic sciences (“economy of scale”), computer sciences (“scalability of hardware and software systems”) or social sciences, where the term “scale” is often associated with groups of individuals and their sizes. Any measured value such as temperature or length is referenced to some type of ordered system of marks of fixed intervals and this system is referred to as a scale (Stevens, 1946). A general theory on scaling, measurements, and scaling methods has been provided by Torgerson, 1958. However, in many scientific fields scale is linked to location, position, space, area or time period (Curran et al., 1997). This notion of scale is addressed more precisely by geographic information scale. It is specifically associated with all sorts of spatially distributed information.

Geographic information scale plays a vital role in all applications in geosciences. Its significance in ecological process modeling, GIS applications and remote sensing has been widely discussed (Woodcock and Strahler, 1987, Quattrochi and Goodchild, 1997, Van Gardingen et al., 1997, Tate and Atkinson, 2001, Lam et al. 2004, Wu et al., 2006). Scientists from a number of geographic and other disciplines have ventured into the scale issue. Wu and Qi, (2000) revealed an exponential increase of studies on the topic in ecological sciences and that this increase can be observed across disciplines. A variety of studies have evaluated methods of scaling, the impact of scale on data information content and quality and the role of scale in process description and modelling (see also chapter 5). However, even within the field of geosciences the terms scale and scaling remain ambiguous. The same term may be used to describe varying aspects of scale while a ubiquitous definition of scale does not exist (Schneider, 1994, Quattrochi, 1993, Blöschl and Sivapalan, 1995, Bian, 1997, Lam et al., 2004). The following sections will cast a light on the significance of the scale term for this study, how the term scale is used and discuss the ways scales interfere with the methods and data presented.

The method for contextual segmentation of land surface reflectances presented in chapter 6 is designed and developed to ingest data of different scales and data models and can produce information content of scale invariant type. Bringing together various aspects of scale triggered and drove the development of the present study. Finding a way for a sophisticated representation of remote sensing data on arbitrary scales is a key issue in this work.

3.1 What is Scale? – A Definition of scale terms

In order to avoid confusion of terms related to scale in the subsequent chapters it is necessary to clarify the different conceptions of scale and scaling. The conceptualizations given below are linked to the meaning of scale and scaling in geographic information science, environmental and ecological studies. The terms and explanations are derived from more profound discussions on the issue by Lam et al. (2004) and Wu and Li (2006).

3.1.1 Scale

Based on earlier work by Lam and Quattrochi (1992) and Cao and Lam (1997), Lam et al. (2004) propose four major meanings of scale that address different aspects of the matter: *observational* scale, *operational* scale, *measurement* scale and *cartographic* scale. All four are prevalent in the topics discussed in this thesis and shall provide a guideline to the issues related to scale. According to the authors, they apply to both the spatial and temporal domain as well as spatial-temporal domains.

Observational scale or geographic scale refers to the spatial extend or size of a geographic area under investigation. With this notion a large scale study encompasses a larger study area, a small-scale study focuses on a smaller area. In this study, the area under investigation is a subsection of the larger study area of the GLOWA-Danube catchment of the upper Danube (see section 2.1).

The *operational* scale is the scale at which processes or natural phenomena operate in the environment. It denotes the distance (or time span) at which spatial patterns exhibit maximum variability. Knowing the operational scale of a phenomenon is important for researchers as determining appropriate observational scale is dependent on the extend of the action of the object under study. Measuring and Modelling LAI requires some thought on the operational scale of LAI and is discussed in chapter 5.

Measurement scale refers to the size of sampling intervals and is commonly called *resolution*. In applications involving uniform raster data it is equivalent to grid size or pixel (proxel) size. Due to storage and computational capacities, measurement scale is often connected to observational scale: A large-scale study sets a limit to the number of individual samples that can be stored or processed. Usually, the smaller the observational scale, the finer a grid or resolution of samples can be deployed. Decreasing cost and increasing efficiency of computer facilities however, allow for an increase of measurement scale in relation to observational scale. Measurement scale is also related to the operational scale. In order to assess a phenomenon the sampling interval needs to be smaller than the operational scale of the phenomenon.

The *cartographic* scale or map scale refers to the size of objects on a map in relation to the real world size of the objects. A large-scale map usually covers a smaller area and exhibits more detail than a small-scale map. Other than the previous denotations of scale, which refer to data characteristics, cartographic scale is coupled to graphical data representations. It provides information on how data is displayed. Any depiction of spatial data should provide information on the cartographic scale it is presented at.

The four meanings of scale are closely related. In the context of a spatial or temporal study, they can be ordered: The observational scale is largest, so that it can cover the operational scale of the phenomenon under study. Data on the subject should be sampled at intervals with a smaller scale than the operational scale. Presentation of the data will finally be at some

cartographic scale, which people will rely on for interpretation, conclusion or policy making (Lam et al., 2004).

The above definitions stem from authors with a strictly geographical background. They appear to be focused on GIS and remote sensing applications with an emphasis on rastered information. A different notion of the issue of defining scale was presented by Wu and Li (2006). They propose a three-tiered conceptualization of scale that organizes scale definitions into a conceptual hierarchy that consists of the *dimensions*, *kinds*, and *components* of scale. It encompasses the four meanings given above, but emphasizes related terms and points out synonymically used perceptions of scale. From their perspective of ecological sciences, some additional meaningful concepts shall be presented here.

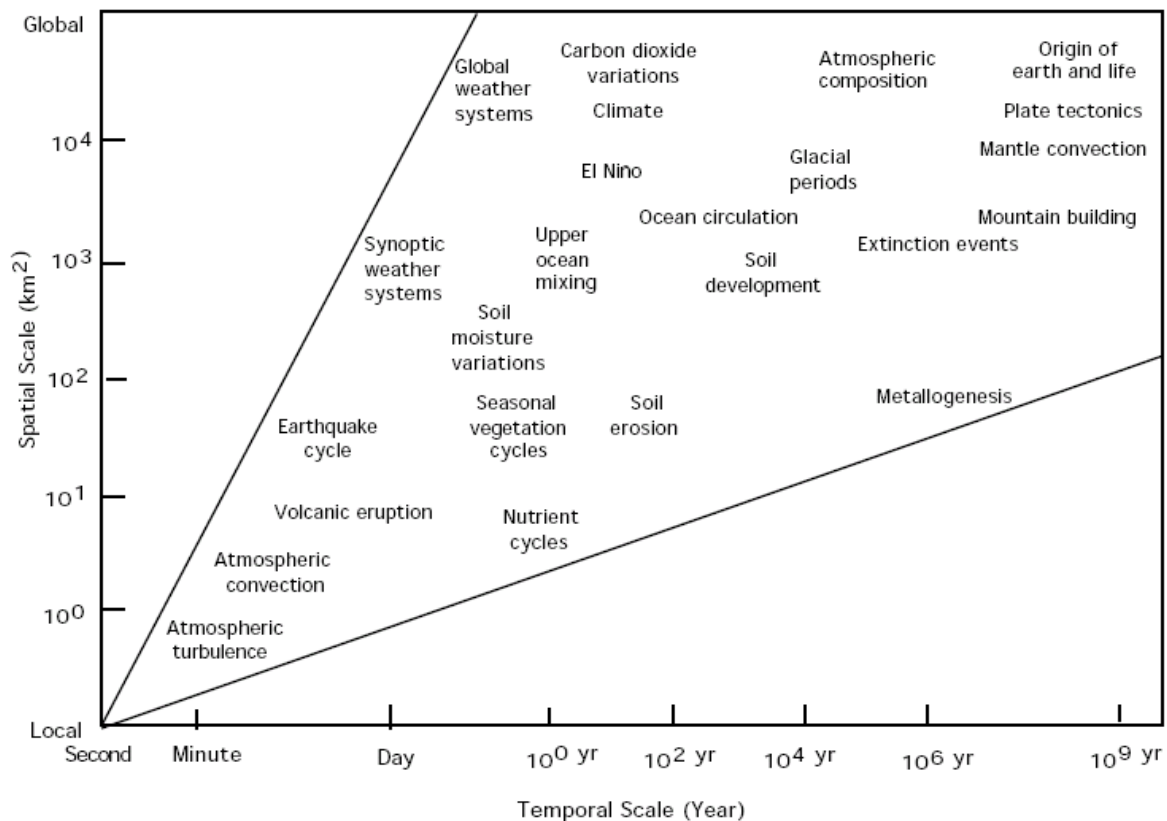


Figure 3.1: Physical and ecological phenomena tend to maintain a constant ratio in their spatial and temporal scale (Wu, 1999)

Scale is defined in terms of time and space. It is well understood, that the characteristic scales of many physical and ecological phenomena are related in space versus time. The ratio between temporal and spatial scales of phenomena tends to be invariant over a range of scales, which is illustrated for a number of different natural processes in Figure 3.1 (Wu, 1999). Together with an organizational level, time and space make up the three *dimensions* of scale (Wu and Li, 2006).

The *kinds* of scale encompass the observational and operational scales defined above. Wu and Li use the term *intrinsic* scale to address the scale at which a pattern or process actually operates. It expresses the same notion of a scale immanent to a phenomenon as *operational* scale. Yet, they award intrinsic scale a broader notion than the term *process* scale. The two notations are used synonymically in this study.

Confusion arises with observational scale. Wu and Li use observational scale as a synonym of measurement scale and *sampling* scale. While sampling scale denotes the same as the measurement scale, the separation of observational scale and measurement scale as defined above seems more adequate and is pursued in the following.

More kinds of scale are given by the *experimental* scale referring to the extend of experimentation, the *analysis* or *modeling* scale which refers to statistical analysis and modeling and the *policy* scale which is influenced by economic, political and social factors. Policy scale arises in the context of management and planning and is dependent on regional and national legislation. Although important differentiations of the definition of scale, these scale terms are not relevant in the presented study. In the wake of general definitions, the author thinks that these latter scale terms are contained in the definitions above. Any experiments scale is encompassed by an observational scale; analysis and modeling depend on the data's scale, which is defined by the above notions of scale. When policy scale plays a role in a research it will provide one notion of operational scale and set rules for observational or measurement scale as defined above.

The *components* of scale defined by Wu and Li (2006) are cartographic scale, *grain*, *extend*, *coverage* and *spacing*. Their concept of cartographic scale agrees with the definition given above. Grain is what has been termed resolution or measurement scale earlier in this section. Extend is equivalent to the observational scale defined by Lam et al. (2004). Yet, coverage and spacing add two more terms in relation to scale. *Coverage* is the intensity of sampling in space and time. *Spacing* refers to the interval between two adjacent samples or lag (Wu and Li, 2006).

The four definitions by Lam et al. (2004) suffice for the conceptualizations of scale in this study. Important aspects and clarification of terms were added from the hierarchical definition by Wu and Li (2006). Still, other lexical meanings of scale and related terms may exist and be defined, yet it has been stressed repeatedly, that for a progress of a "science of scale" agreement on scale terms is a fundamental step (Quattrochi, 1993).

The dimension of a scale is often roughly classified by terms like micro, meso, macro, moderate, continental or the like. In the context of this study, the term micro scale is understood as a dimension smaller than 100m. The terms moderate and meso scale refer to scales of 100m to 1000m, which contains the three resolutions of the MODIS sensor (Table 3.1). The items are mainly used to describe the resolution of data.

Table 3.1: Scale terms used in this study and the dimensions attributed

Scale	Dimension
micro	< 100m
meso, moderate	100 to 1000m
macro	> 1000m

3.1.2 Scaling

The item *scaling* is closely related to scale and just as the scale term may have different signification in different scientific disciplines. In the context of geographical information and earth science and in connection with the above definitions scaling is the translation of information between or across temporal or spatial scales (Turner et al. 1989, Blöschl and Sivapalan, 1995, Curran et al., 1997, Marceau 1999, Wu 1999, Wu and Li, 2006). A lot of research has been completed on the question of how scaling or the transfer across scales can be achieved. The question may apply to data on the one hand and to the description and definition of processes on the other. Scaling may be further distinguished by the direction the

transformation is performed in. In the GLOWA-Danube community agreement was achieved that *upscaling* or *scaling-up* is the process of moving from a small scale to a large scale. In connection with process descriptions, the term *bottom-up* is linked to the transfer from a small scale to a large scale. Upscaling of data usually goes along with *aggregation* and data reduction. Conversely, *downscaling* or *scaling-down* is associated with moving from a large scale to a small scale. Transferring a process in that direction is referred to as *top-down*. Downscaling of data will require *disaggregation* of parameters or data values and will increase data amounts.

3.2 Implications of Scale

Scales and scaling cover a large range. From the point in space and microscopic dimensions to micro, meso and macro scales up to global consideration of environmental phenomena research may be conducted. Focusing in on one particular scale of interest will reveal a distinct picture and perception of a topic (Levin, 1992). Changing scales impacts on data as well as on process description models and numerical models that reproduce environmental processes.

Looking at the same subject at a different scale may result in a significantly altered impression of the subject. Changing the scale of data will pose questions on whether the data at the new scale will be commensurate with the original dataset. Using data at different resolutions as input to a numerical model begs the question if the model valid at one scale will still provide useful results at another. Yet, the process of changing scales itself imposes continual asking on how this can be done. Both, scaling of information and scaling of processes are subject to scientific interest. Once different scales have been established and transgression of scales is feasible, instrumentality is desirable to measure and describe what we gain or loose along the way. These implications of scale and scaling have been addressed in numerous studies in earth system sciences with strong recommendations for establishing a *science of scale* (Quattrochi and Goodchild, 1997, Quattrochi, 1993, Wu and Li, 2006)

The following highlights aspects of scaling data and process models and discusses methods of how scale of spatial data and the scaling process can be described. In scaling data and models, all of the definitions of scale given above may layout the sense of scaling. Changing extent (observational scale) and changing resolution (measurement scale) denote different senses of modifying scale. Intrinsic scales of patterns and processes are reflected in the data or described by a model. Changing the extent or the resolution of data may result in the recognition of a different process or pattern but might shroud them as well. Applying a model on a different area or resolution may yield different results and may call for changes to the model or process description (VanGardingen et al., 1997, Mauser and Schädlich, 1998, Marceau and Hay, 1999). Finally the scale of processes themselves, i.e. the operational scale, may be changed dramatically (Wu and Li, 2006).

Cartographic scale of course may be changed and has a loose tie to the other aspects of scaling. It is connected to the form of graphic output of information. Changing the scale of a map is a particular issue and is discussed extensively in the literature (Hake and Grünreich, 1994, Kraak and Ormeling, 2003). Maps are used in this work, nevertheless changes of map scale and their implications for graphic output are not detailed on.

3.2.1 Scaling Data

When transforming data in a way that the new dataset has a different scale than the original, some form of aggregation or disaggregation is applied. It will change the grain or resolution size by fine- or coarse-graining and will involve the processes of interpolation or extrapolation (Wu and Li, 2006).

Disaggregation of data requires a method for finding estimates of information on a scale smaller than the original. This process requires careful assessment as it involves the difficult issue of deriving information for spaces where no information is available. Methods for finding good estimates for these spaces have been investigated (Lam 1983, Friedl, 1997, Atkinson, 1997).

Aggregation of data reduces the original data to a smaller number of data units. The method of aggregation plays a vital role in the effects of the lumping of data. Mean and median values are usually retained in the scaling process, but standard deviation and variance in the data may change significantly (Bian, 1997, Bian and Butler, 1999).

Techniques and methods for scaling or resampling data are numerous in the literature. Yet, many are not readily available to the user and judgement of appropriateness to an application is difficult. Simple aggregation or disaggregation procedures derived from classical image processing are most likely to be applied (Hay et al. 1997). Lam et al. (2004) stress that in existing scale studies that heavily rely on resampling methods to generate multiscale data layers, the observations made may be attributable to the resampling rather than scale.

The difficulties that occur when data at different scales is sought, has early been identified as the modifiable areal unit problem or MAUP (Openshaw, 1984, Cao and Lam, 1997, Marceau 1999). It is endemic to all spatially aggregated data and states that variations occur when data from one scale of areal units is aggregated into more or less areal units. It is a “problem arising from the imposition of artificial units of spatial reporting on continuous geographical phenomenon resulting in the generation of artificial spatial patterns” (Heywood et al. 1998). The MAUP is divided into two components: the *scale effect* and the *zonation* or *aggregation effect*. The former is the variation in results that may be observed when data collected at one scale are progressively aggregated into fewer larger units for analysis. The latter is the variation in results generated by the use of alternative combinations of areal units at the same scale (Marceau 1999).

The MAUP applies to both vector and raster data. However, the context of this study as well as the conception of the DANUBIA model of the GLOWA Danube project has a strong focus on rastered data both from the modelling perspective as the remote sensing side (see section 3.4). The acquisition of remote sensing data has been identified as a particular case of the modifiable areal unit problem (Marceau et al. 1999). Information on units that form a uniform spatial sampling grid is subject to the same above-mentioned problems when different scales are addressed. A number of solutions to the MAUP have been suggested in the literature. A review of approaches to tackle the MAUP is provided by Marceau and Hay (1999).

When analyzing data of different aggregation levels, relationships that can be observed at a coarse scale may not be brought forward to finer scale. This observation has been termed the *ecological fallacy* problem (Cao and Lam, 1997, Marceau, 1999). It stresses the urge to carefully select the scale at which analysis results are produced and suggests expanding analysis to a host of scales in order to dodge the ecological fallacy.

A stack of data at different measurement scales (resolutions) has been described as a data pyramid or scaling ladder (Csillag, 1997, De Cola, 1997, Wu, 1999). A data pyramid is a nested hierarchy in which each level precisely covers the other by a multiple of its raster cells.

Along such a data pyramid or scaling ladder the data amount on each level changes. In the case of square nested raster cells, doubling resolution results in a quadratic reduction of data volume. This aspect of scaling is often an important argument in selecting a scale as storage capacities and computational cost play a vital role in the realization of a study (DeFries et al. 1997, Mauser and Schädlich, 1998).

3.2.2 Scaling Environmental Models

The issue of scaling has a profound impact on the applicability of environmental models. On the one hand the scaling of data impacts directly on the feasibility of a model. The differences in data on different scales will reflect in the results a model can provide (Marceau and Hay, 1999). Often the application of a model is simply limited by the availability of data with sufficient detail or extent at a different scale than the scale the model was developed at (Russel and Van Gardingen, 1997, Mauser and Schädlich, 1998).

On the other hand the process described by a model may apply to a distinct scale and may not be applicable on another (Bian, 1997, Marceau et al. 1999). The non-linear response of environmental processes prohibits a simple transfer of a model to a new scale. Meteorological variables, fluxes of water and gases as well as vegetation canopy attributes cannot readily be averaged to represent a new scale. Computing average fluxes from mean or average surface conditions commonly results in significant bias (Lammers et al. 1997) and can be formalized as:

$$E(p(x)) \neq p(E(x)) \quad (3.1)$$

where x is a vector of surface parameters and p is a process model at a fine spatial scale. $E(p(x))$ expresses the averaging of results of the model at the fine scale or small area. To obtain an unbiased estimate of a larger area some functional relationship needs to be established to account for non-linearities. With $f(x)$ as a joint distribution function of x , a solution to $E(p(x))$ could be

$$E(p(x)) = \int_x p(x) f(x) dx \quad (3.2)$$

Finding the distributional information is a key problem in migrating environmental models across scales (Lammers et al., 1997).

Taking a validated model to a different environment may result in inaccurate predictions because processes are omitted or inadequately represented (Russel and Van Gardingen, 1997). This may be the case by merely changing the extent of the model. By encompassing previously unpresent conditions into the modeled area, model results may be tampered.

The elements to be addressed when a model is applied on high and low resolution data are summarized in Figure 3.2. The illustration applies to both environmental models as well as remote sensing models. On the level of input data as well as on the model level questions of scaling are prevalent. If the problems are not adequately addressed the resulting parameters at different scales will not be commensurate.

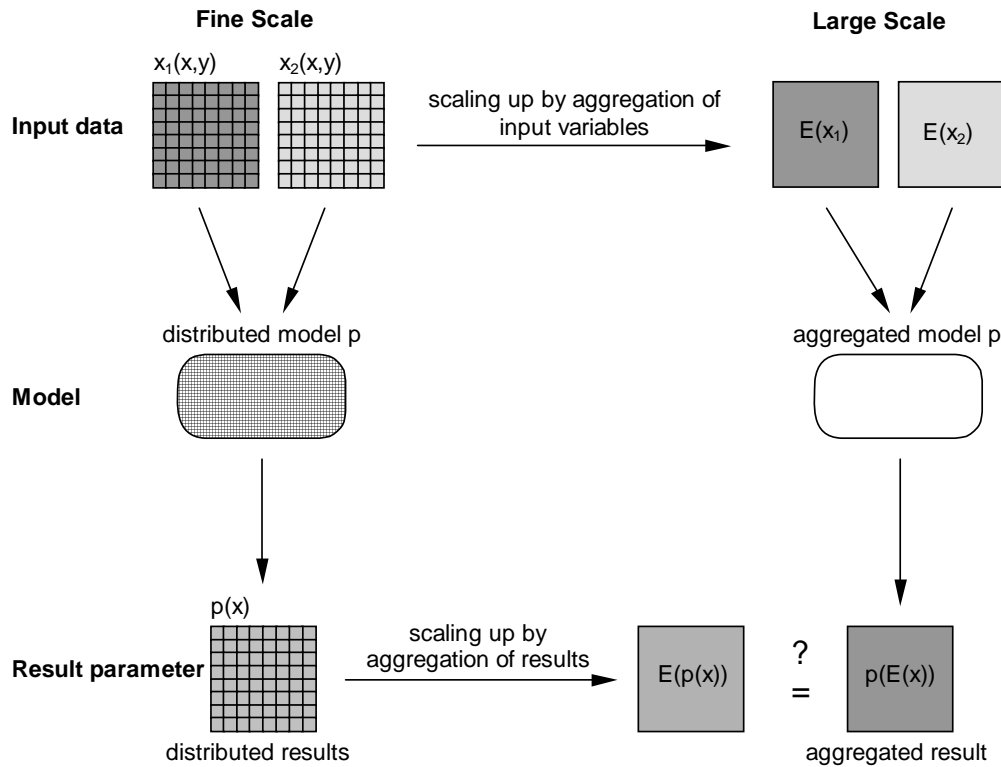


Figure 3.2: Elements to be addressed in scaling environmental and remote sensing models (Pelgrum, 2000, Kellenberger, 2001, modified)

A lot of research has been completed to scale models or assess their abilities to be scaled. For example Bruneau et al. (1995) conducted a sensitivity analysis on the space and time resolutions of TOPMODEL, a catchment water discharge and soil water model. They concluded that the modelling results are constant inside a relevant domain of space and time resolutions and that working outside this domain induces a strong decrease of modelling efficiency. Asner and Wessman (1997) scaled a model for simulating photosynthetically active radiation (PAR) from the leaf level to the canopy level and discovered that landscape characteristics have a strong influence on PAR beyond the effects observed at the leaf level.

Land cover type heterogeneities at the coarse resolution scale are often an important factor for unreliable results in modelling. Taking into account these heterogeneities has been addressed in remote sensing models (Friedl, 1997, Tian et al., 2002, Simic et al., 2004), global atmosphere-biosphere models (DeFries et al. 1997) as well as in modelling of soil-vegetation-atmosphere-transfer (Mauser and Schädlich, 1998). A method for scaling ecosystem productivity from the local to the continental level was presented by Moorcroft et al. (2001). The importance of omitting land cover type heterogeneities in model application is stressed in the method presented in this study.

3.2.3 Measuring and Description of Scale

The recognition of the variation in operational scales of processes, the possible gain and loss of information when moving along a scaling ladder and the problems of scaling environmental and remote sensing models, has led to the development of methods that are capable of measuring or describing scales. Most of such studies were focused on regular grid data sets derived from raster GIS (e.g. digital elevation models), remote sensing imagery or

synthesized imagery (Lam and Quattrochi, 1992, Bian, 1997). The inherent characteristics and abundance of remote sensing data at varying resolution have led to the widespread recognition of remote sensing as a significant contributor to the scale issue (Simmons et al., 1992, Marceau 1999, Lam et al. 2004). Hence, many efforts to measure and describe scale were undertaken by remote sensing scientists.

The analysis of multiscale datasets aims at different aspects of scale. First, methods have been developed to determine appropriate or optimal scales to represent processes, parameters and patterns. Second, the awareness of the existence of appropriate scales lead to the development of finding domains of scales and scale breaks. Finally, methods for scaling and approaches to overcome the MAUP have been presented.

Woodcock and Strahler (1987) developed a measure of local image variance to help finding an appropriate scale retaining information for a forested, an agricultural and a suburban environment. Later, the same authors used variograms as a measure of spatial variation to improve the understanding of the information content in remote sensing imagery (Woodcock et al. 1988a/b). A number of recent studies base on the qualities of variogram analysis and used this approach for evaluating scale (Artan et al., 2000, Oliver, 2001, Treitz, P, 2001, Tian et al. 2002b, Colombo et al. 2004, Zawadzki et al. 2005).

As a mean to assess autocorrelation and self-similarity in data of different scales, fractals have been widely used in geosciences and remote sensing analysis (Quattrochi and Goodchild, 1997, Cao and Lam 1997). Fractals were introduced to geography to overcome the difficulties in spatial analysis using conventional statistics and geometry (Lam and Quattrochi, 1992). They mathematically relate complexity and scale and can be used in the detection of characteristics scales and scale breaks. Computation of the fractal dimension of phenomena can reveal abrupt changes in autocorrelation and help in the identification of the scale where information or patterns vanish in the data (Emerson et al., 1999). They provide a robust tool for both measuring variability at different scales as well as quantification of homogeneity and heterogeneity of land surface and environmental attributes (Lam et al. 1998).

Another more recent method to address scale and scaling has been the application of wavelet transformation (Goodchild and Quattrochi, 1997). A study using the Haar wavelet to derive the length scale of land surface characteristics was presented by Pelgrum (2000). He showed that the wavelet approach provides a valid measure to determine the resolution of remote sensing imagery from three different landscapes.

In search for generalizing rules for scaling and scale characteristics attempts have been made to build frameworks as guidance to scaling. As a multiscale approach to reduce the effects of MAUP, Hay et al. developed an object specific framework to assist in defining landscape thresholds, domains of scale, ecotone boundaries and grain and extend for the application of ecological models (Hay et al. 2001). Another framework presented aims at testing the aggregation and disaggregation properties of remote sensing algorithms (Hu and Islam, 1997).

3.3 Methods of data representation

The issue of scale is ultimately tied to the data model used. In geographic information technology, GIS and environmental modeling two general concepts of data representation dominate: the vector data model and the raster data model (Longley et al. 1999). In the context of this study vector data play a marginal role and are used only in the presented maps. They are omitted in the discussion. Yet, the focus lies on raster data, both in view of the integrated environmental model compound DANUBIA (section 3.4) as well as in the

perspective of remote sensing data (section 3.6). In the following sections concepts of representing data in a rastered modeling environment are discussed.

3.3.1 Raster Data

Raster data structure is a compellingly simple concept. In raster data, cells of a regular pattern represent information. The notion of raster data includes all types of digital imagery but focuses on real world abstraction in the context of this study. In a raster, a surface and its geometry are captured by a cellular decomposition into regular shapes. Although these shapes may be hexagonal or triangular and even irregular (Rigaux et al. 2002), most commonly raster or grid data are associated with an arrangement of square boxes of equal size. These boxes are conceptually organized in a matrix of rows and columns. The geometry of the raster is defined by an origin, the directions of two perpendicular axes along the row and column direction and the spacing of the raster cells (Bernhardsen, 2002).

The origin is most typically located in the upper left corner although some systems to manage raster data have chosen the lower left corner. It provides a relative system for positioning cells in terms of numbers of rows and columns but may represent absolute position in an orthogonal geographic reference system in the case of georeferenced data. In the latter case absolute positions of cells can be derived from the origins absolute position and the cells relative position and raster spacing. The number of rows and columns provide the total area or extend of a raster data set.

A spatial Raster data can be visualized as a grid superimposed on a landscape. Each raster cell represents an area, depending in size on the raster resolution size. It provides a spatially continuous model of a surface where a numerical value is attributed to each cell. These values may be physical quantities such as amount of precipitation or terrain elevation or, in the case of remote sensing raster data, measures of energy of electromagnetic waves in a given wavelength domain. Data may be categorized or classified. In this case a cell value corresponds for example to administrative entities, a land cover class or a soil type. Thirdly, cell values may reference to attribute tables or distances to other cells or objects (Bernhardsen, 2002).

A single cell is assigned one single value and is treated as a homogeneous area. To use rasters to represent multiple thematic topics the concept of single valued rasters is expanded to stacks or multi layered rasters (Nebiker, 1997, Bernhardsen, 2002). Such a stack of multiple layers requires that the grids of all layers be aligned such, that the information of corresponding grid cells correspond to the same spatial entity (see section 4.3). A vertical arrow through a multiple layer stack of gridded data should pierce through different information features of the same point in space (Walford, 2002).

The way of how a cell is attributed a value becomes a question of scale when the attribute does not cover the entire cell. Imprecision may be the consequence. Yet, to build up a raster data layer, the cells need values. Three ways of attributing values have been proposed. The first option is to give the cell the value that lies in the center of the area of the cell. Secondly, the attribute that covers most of the area of the cell is attributed to the cell and thirdly the attributed value is obtained by some way of averaging the multiple attributes of the cells area (Bernhardsen, 2002). The validity of these approaches varies with the type of cell value under consideration and is highly dependent on the size of the cell, i.e. the measurement scale of the used grid.

Raster data are digitally coded depending on the range of values that need to be stored. Common data types range from 8bit integer types per raster cell to 64bit double precision

floating point values. For GIS applications it is highly desirable that different data types may be stored and managed in a processing system (Mauser and Bach, 1993, NCSA, 2003). With given origin along with row and column count, no spatial attributes need to be stored with raster data, which reduces storage requirements. Another advantage of raster data is that they can readily be compressed by run-length encoding or chain codes (Bernhardsen, 2002). A comprehensive study on raster data, managing raster data mosaics and raster pyramids and georeferencing of raster objects in a data base management system has been compiled by Nebiker (1997).

3.3.2 Subscale Gridded Data

Assuming homogeneity of a raster cell is not a valid concept in many cases when representing natural phenomena in a raster data model. The resolution of the raster has paramount influence on the quality at which a raster cells value represents its area. Features smaller than the sampling interval or resolution of a raster grid fail to be adequately captured by a simple raster of single value cells. Concepts have emerged that are able to include information below the grid level of resolution. They break up the single value concept of raster data and expand the information to multiple layers on a cell.

A concept that is designed to preserve the spatial organization of subgrid information and details over multiple levels of resolution is the organization of data in a quadtree model. It is a space driven data structure that uses varying cell size. Large cells are used to represent larger homogeneous areas while finer spatial detail is captured with smaller cells (Ju et al. 2005). Starting from a coarse quadratic cell size, cells are quartered into four smaller cells if heterogeneity is prevalent on the coarse cell. This procedure is repeated down to a suitable level where a square is of homogeneous properties. The structure emerging from this principle resembles a tree subdividing into four leaves at each level (see Figure 3.3) (Rigaux et al. 2002, Csillag, 1997). With large portions of homogeneous areas, substantial reduction in data volume may be achieved while spatial context and detail are retained. Rapid search and data manipulation are further advantages of the quadtree structure as homogeneous areas are treated as one entity rather than many equivalent cells. Yet, establishing the structure requires considerable processing and/or programming time (Bernhardsen, 2002). Regrettably, few available off-the-shelf geographic data manipulation software packages have implemented quadtree data management. Also, complex data may not result in much compaction of data volume.

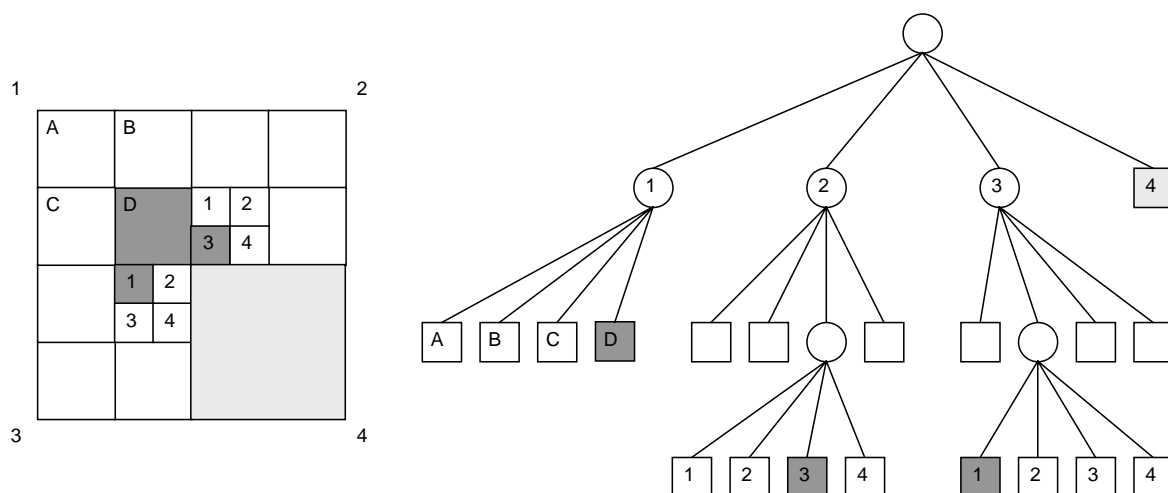


Figure 3.3: The concept of quadtree data representation. An area is repeatedly subdivided into quarters until a subscale feature can be captured (left). The highest and the lowest level in the example are marked with numbers, the moderate level is marked with letters. In a regular raster capable of capturing a feature like the area marked dark, 8x8 raster cells would be stored. In the quadtree (right) only values for the 19 squares need to be stored (Bernhardsen 2002, modified).

A simpler method to preserving information below the grid resolution has been widely used to overcome the MAUPs implications. It is based on the assumption that the heterogeneity of a raster element is made up of multiple areas that can be grouped or categorized into a number of entities with equal characteristics. Each of these entities covers an areal fraction of the raster element. By retaining the areal fraction to the raster cell of each entity along with the properties of the entity, the raster elements are stratified into parts of homogeneous characteristics (see Figure 3.4). The raster cell is conceptualized as a composite of non-modifiable areal units. While the properties of those homogeneous units are preserved, the spatial organization is not. For a raster cell, attributes may be linearly lumped from the area-weighted sum of the subscale homogeneous fractions.

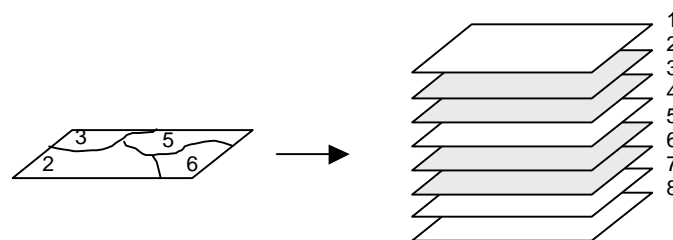


Figure 3.4: Subscale information on a pixel. The properties 2,3,5 and 6 are present on the pixel. Their attributes are stored in the corresponding layers. The other properties are not present on this pixel but may be on others. A prominent example would be the property “land cover type” with the attribute “area fraction”.

The data volume of this data model is substantially reduced in comparison to higher resolution data that captures the subscale entities on homogeneous pixels. Naturally, data

volume is increased as compared to a single data layer, depending on the number of homogeneous entities identified.

While application of the quadtree concept has been scarce, subscale stratification data models have been widely used. A prominent example is the stratification of pixels according to underlying land cover types. Ignoring the exact location of a land cover type within a low-resolution raster cell goes along with resolving the heterogeneity of the cell. The approach has been successfully applied in environmental models (Mauser and Schädlich, 1998, Ludwig et al. 2003b, Simic et al., 2004) and has been the objective in remote sensing applications aimed at the identification of subpixel land cover composition (Strasser et al. 1999, Bateson et al., 2000, Braswell et al. 2003, Lobell and Asner, 2004, Liu and Wu, 2005, Song 2005)

3.3.3 Geocomplexes

Geocomplexes offer a method for scaling both data and process models ingesting the data from detailed high-resolution grids to moderate resolution representations used in regional integrated models like the DANUBIA Decision support system.

A hydrologic process model transferred from the microscale (~100m grid spacing) to the mesoscale (~1000m grid spacing) will change results due to the effects of MAUP on the ingested data. At the coarser resolution much of the hydrologically relevant land surface heterogeneity is lost that is captured by some 100 samples at the micro scale. Means or majorities of high-resolution input may dramatically change the mesoscale modeling results as compared to lumped microscale results (section 3.2.2).

In the framework of the GLOWA Danube project the concept of geocomplexes was developed and validated to provide an effective way to apply detailed process models of evapotranspiration and groundwater recharge in mesoscale catchments on a 1km² grid. Similar to the subscale stratification described in the previous chapter, geocomplexes attempt to reduce the data amount of the microscale while maintaining its heterogeneities. A geocomplex is designed to account for those heterogeneities that are hydrologically relevant. A set of parameters is intelligently bundled to form multiple information entities that represent the area of the mesoscale raster cell. The parameters are aimed at solving the Penman-Monteith equation in soil-vegetation-atmosphere-transfer process simulations.

The parameters hosted by a Geocomplex are comparably stable in time and space such as land cover, soil type and terrain attributes. High-resolution data is a prerequisite to produce the geocomplexes for each raster cell on the mesoscale. In the generation of geocomplexes, a hierarchical aggregation scheme follows rules, which rank spatial parameters according to their priorities in the hydrologic processes.

Land cover has been identified as the predominant factor influencing these processes. In natural and agricultural environments, land cover is often determined by and related to underlying soil type and topography. It is a driving force in boundary layer interactions (Ludwig et al., 2003c). As a consequence each geocomplex represents a land cover type as an areal fraction of a mesoscale raster cell. The dominant soil type, mean elevation and slope as well as dominant aspect are assigned to the geocomplex (Reichert et al., 2004b). In Figure 3.5 a geocomplex is visualized as a barrel of parameters, derived from the fine resolution information of the area of a mesoscale pixel.

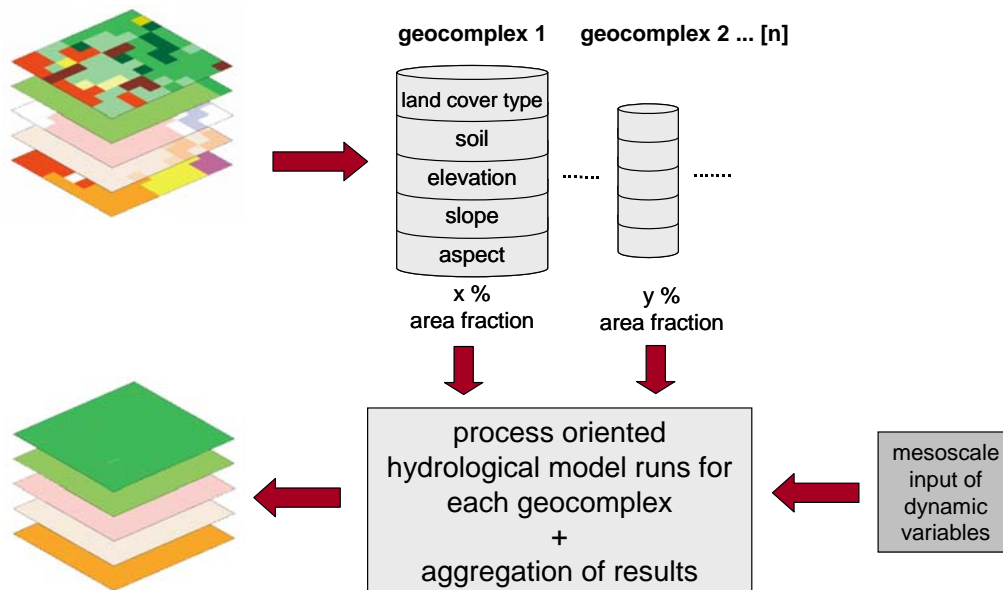


Figure 3.5: The concept of geocomplexes. Derived from high-resolution input, each of n geocomplexes on a mesoscale resolution cell is ingested in a run of a hydrologic model. Mesoscale results are generated by areal weighting of geocomplex based model output.

Hydrologic modeling on the mesoscale can then be performed for each of $n \geq 1$ geocomplexes on the mesoscale pixel. For the homogeneous area fractions the hydrologic processes can be modeled omitting the MAUP by avoiding generalization. Lumping of results from n model runs produces a mesoscale model output (compare Figure 3.5).

The Geocomplex approach has demonstrated its effectiveness in sensitivity analysis and distributed modeling using the GIS-based SVAT modeling environment PROMET. The PROMET model has been applied and validated in a number of earlier studies (Mauser, 1989, Mauser and Schädlich, 1998, Bach et al., 2000, Bach et al. 2003, Taschner, 2003). Using the SVAT scheme with geocomplexes exhibited a dramatic improvement in the modeling of mesoscale hydrologic variables like soil water content, evapotranspiration and suction power (Reichert et al., 2003, Reichert et al. 2004a). It demonstrated the significant contribution of the geocomplex concept to scaling sets of related parameters for hydrologic processes. An example of the reduced deviation from the microscale reference is given in Figure 3.6.

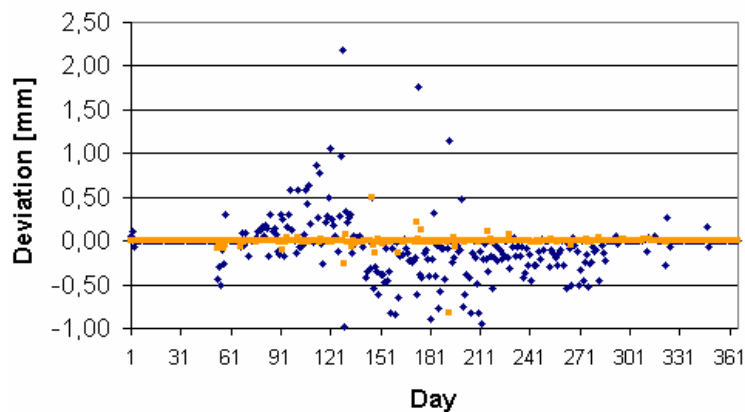


Figure 3.6: Example of the deviation of mesoscale model results from microscale results using geocomplexes (red) and on regular mesoscale data (blue). The plot shows the evapotranspiration of a mixed forest modeled for 1996 (courtesy of D. Reichert)

3.4 Scale in GLOWA-Danube

In the GLOWA-Danube project, scale is addressed from various perspectives. While the observational scale and measurement scale seem readily defined, the interdisciplinary approach and the requirements of individual components of the DANUBIA model reveal different needs for scale and scaling depending on the background of the contributing models.

The extent of the area investigated and modeled in DANUBIA is clearly defined by the delineation of the catchment of the upper Danube (chapter 2). Yet, the observational scale of some models is reduced to only a subset of all DANUBIA proxels. The river routing component, for example focuses on those raster cells only that contain water channels.

For the development of the model, the resolution of the DANUBIA system was set to a 1km grid scale. Every contributing model in the system agrees to provide values at that scale. Fixation of the measurement scale to 1km resolution is a fundamental step for integration in DANUBIA. The 1km proxel is the entity for which all processes described in the compound are forced to provide their parameters. Exchange of data between components takes place on that platform irrespective of the process scales and the scale at which the individual models operate. Some of the processes reflected in the entire system operate on larger scales than the 1km grid, others take place at dimensions smaller than the proxel size. Hence, both upscaling and downscaling of processes and data need to be addressed in GLOWA Danube.

For some, the 1km proxel is a very small item. Particularly, models administered by social science partners involve information collected in census units or other administratively delineated areas that are much larger than 1km squares. In these fields downscaling approaches were addressed to distribute available data from larger administrative entities to the proxel scale by disaggregation (Mauser, 2000, Herrmann, 2002, Schuster et al. 2004). In the natural science section, the atmosphere component of DANUBIA is confronted with the problem of dispersing information to the proxel resolution. Weather observations as well as atmospheric circulation model output are available at coarser scales only. The former required a method for spatial interpolation of point type information as weather stations are scattered and scarce (Mauser, 2002). The latter provides output that is continuous in space but at resolutions coarser than the DANUBIA scale. For the preparation of precipitation data,

downscaling of 45km resolution continental scale model results to the mesoscale was conducted (Schipper, 2005, Fröh et al. 2006).

In contrast, many processes addressed in the DANUBIA system operate at scales below the proxel scale. From their perspective the 1km cell may become a very large unit. For example, in the ground water model component, aquifers are known to have bottlenecks smaller than the DANUBIA resolution. For the modeling of ground water flow, concepts had to emerge that allow the upscaling of this higher resolution information and process to the proxel (Barthel, et al., 2002). Undoubtedly, the pattern of land cover is another such item that operates at finer scale. Areas of homogeneous cover type of the size of a square kilometer are rare in the upper Danube catchment. An analysis of the number of land cover types on pixels of the study area was conducted for a resolution of 240m and is shown in Figure 3.7. It implies more pronounced heterogeneity for the 1km scale. Noticing this heterogeneity of the proxel is of paramount significance for DANUBIA as it simulates many processes where the land cover type is a driving force in the process.

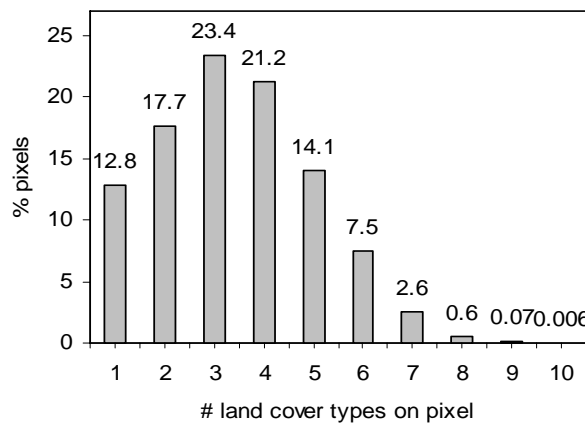


Figure 3.7: Frequencies of the number of land cover types on 240m resolution pixels of the study area cutout of the DANUBIA catchment.

As of the time of this writing, DANUBIA is operated assuming homogeneity for the proxel. However, the framework of the model compound has been laid out to operate on subscale data at an early stage. A concept for land cover collections for a proxel is implemented in the system framework. It aims at the incorporation of subscale concepts such as the stratification of raster cells by land cover type or the ingestion of geocomplexes.

The 1km grid for DANUBIA was agreed upon before the project was even initiated. Especially for the natural scientists involved, using a simple grid was the data model of choice. Interestingly, it were staff members from the GLOWA-Danube computer science project that questioned whether that data model would be a wide enough conception for data storage in a complex modeling environment. In the discussions for the DANUBIA computational framework they suggested that tree structures are an option for keeping data. Although it remained undiscussed, basing a model on a concept like quadtrees would be an exciting undertaking, opening new ways out of the various scaling dilemmas. The programming complexities of such an approach would put new emphasis on the fruitful integrative cooperation between computer scientists and environmental modelers.

3.5 Scales of Leaves and Leaf Area

When focusing on the parameter under study in this thesis some of the aspects of scale can be illustrated. The issue of leaves and leaf area can be inspected at a number of scales itself. When looking at individual stomata of a leaf and its activity, the process of gas exchange at the leaf surface has a very small spatial scale. This activity may change very rapidly within seconds or minutes at a small temporal scale and as a function of the environment.

Backing out and viewing that whole leaf may expose the leaf as a storage device for precipitated water. The process of wetting the leaf, i.e. the rainfall, as well as the drying of the leaf depending on temperature, air humidity and radiation budget takes place at the spatial scale of the leaf size and has a temporal extend of a few minutes to several hours.

Looking at all leaves of a plant again enlarges the observational scale. The cycle of the unfurling of fresh leaves to senescence and litterfall could be observed at this scale and would exhibit a few months to multiple years depending on plant, biome and latitude. Observing an entire forest again would yield a different picture. In the GLOWA-Danube catchment, outside the alpine range, the extent would be from a few hundred meters to several kilometers. Along the northern rim of the Alps extended forests sprawl over several tens of kilometers. The time span it takes for such a forest to grow will be larger accordingly. Half a century may be a good estimate for the temporal scale of the process of growing a forest.

Leaf area may be viewed as a spatial process as well. When moving along a landscape leaf area is changing. Stepping out of the coniferous forest, that little will change its leaf area over the course of the year, a cornfield may be almost barren land with little or no leaf area at all. Here, highest variation in the spatial process of leaf area occurs.

The scale, at which leaf area needs to be captured in the context of the DANUBIA modeling effort, is the defined 1km grid. At this scale individual leaves may not be detected, but the leaf area at the canopy level will. However, leaf area and its spatial and temporal behavior is closely linked to the biome or plant species producing the leaves, i.e. the type of land cover. At the landscape scale, leaf area pattern has to be interpreted as a function of cover type both in terms of distribution and time. Thus, the issue of providing leaf area at the scale aspired is directly linked to the question of land cover type representation on a 1km grid.

More detail on leaf area and the methods to measure and model leaf area index is provided in chapter 5. It also expands on the problems of non-linearity in scaling models as outlined in Section 3.2.2 in regard of modeling of LAI from remote sensing data.

3.6 Scale in Remote Sensing Data

In remote sensing, both observational scale and measurement scale are prominent characteristics. Any particular imaging device is specifically designed to make observations of a defined extent and resolution. The scales range from high-resolution imagery with a sampling size of several centimeters to several kilometers and from local observations to global coverage. In the process of image acquisition in optical remote sensing, the two notions of scale are inextricably interconnected: an image of high resolution covers an area of small extend while lower resolution data cover a larger area. Especially the characteristic of varying resolution and the abundance of remote sensing data have fostered the exertion of scale studies using remote sensing data (Marceau, 1999). Thus, a multitude of research has been conducted in regard of scales and scaling under different aspects (for example Friedl et al.,

1995, Friedl 1997, Hay et al. 1997, Pax-Lenney and Woodcock, 1997, Pelgrum, 2000, Treitz and Howard, 2000, Tian et al. 2002, Garrigues et al. 2002, Ju et al. 2005)

The issue of spatial sampling resolution in remote sensing data is additionally linked to the aspect of temporal resolution. Data of highest resolution are mostly collected from airborne instrumentation and are limited to localized and infrequent campaigns. In contrast, most spaceborne imagers are designed to continuously collect data, yet the frequency of observation diminishes with resolution increase. These conditions are decisive when remote sensing data are to be operationally used. They are also important in the attempt to incorporate remote sensing data into process models like the DANUBIA modeling compound. In this study the focus lies exclusively on spaceborne remote sensing data.

The modifiability of areal units in remote sensing data is prevalent in several ways. First, it should be noted, that two different observations of a remote sensing instrument of the same spot may be dislocated with respect to each other due to altered orbit or orientation of the spacecraft. Thus, two successively collected measurements may be mutually shifted. In this case apparently comparable pixels capture different areas, even after georeferencing. When focusing in on a single pixel it has to be recognized that the observed region on the ground is of round or oval shape while the resulting measurement is abstracted as a square box. When comparing data of different resolution this will result in areas sampled at one resolution that are omitted at another (Figure 3.8). Yet it is common practice to assume identity of the observed areas taken as square raster elements. Thirdly, remote sensing scanners collect data by viewing across their flight track to each side of the nadir direction. Depending on the scan angle and the IFOV of a sensor, the size of the ground area sampled changes. Thus, nominal resolution of a sensor may be substantially deteriorated within a scan line while the pixel size attributed to an image remains constant. An example of this deterioration of resolution within the same scan lines is given in Figure 3.9.

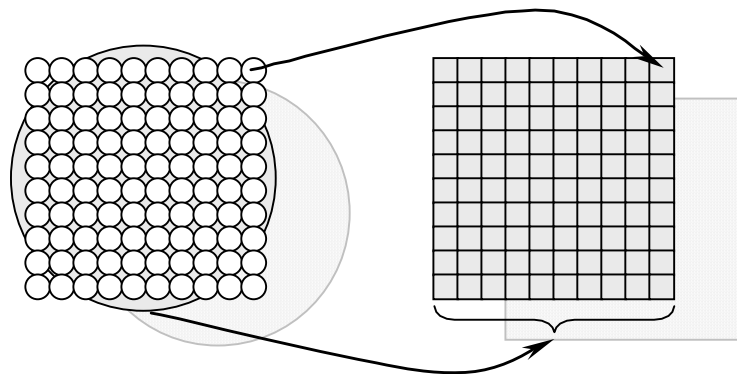


Figure 3.8: Discrepancy between actual measured area of a sensor and the abstraction as pixels. The small circles and squares correspond to a high-resolution sensor; the large circle and square correspond to a low-resolution sensor. The pale shapes in the background illustrate dislocation of a measurement and pixel in data from another orbit for the low-resolution sensor.

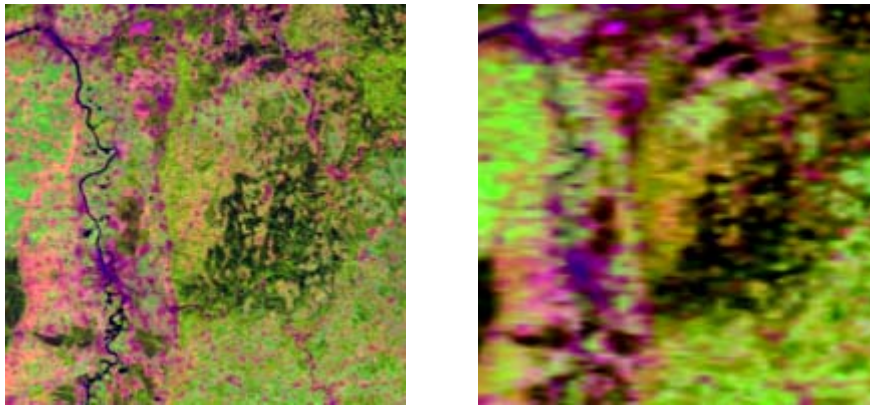


Figure 3.9: Effect of viewing angle on resolution in MODIS imagery; left: close to nadir viewing image; right: off nadir view of the same area at a scan angle of $\sim 40^\circ$

In the context of this study data of two sensors is sought. High-resolution data at 30m ground resolution is used from the Landsat Thematic Mapper TM sensor. Low-resolution data was collected by the Moderate Resolution Imaging Spectrometer MODIS. This instrument collects data for land surface applications at 250m and 500m sampling intervals depending on wavelength. Furthermore, the 1km domain is covered by MODIS. Data are distributed aggregated to that pixel spacing and a host of ready to use products derived at that resolution are available (e.g. Leaf Area Index). The issue of the sensors and imageries detailed characteristics is expanded on in chapter 4.

In order to use these remote sensing data and derived parameters as input for DANUBIA or comparable process models, both spatial as well as temporal resolution have to be reflected. At first glance using high-resolution data of 30m resolution seems enticing. Operation at subscale precision would be at hand for parameter retrieval as well as process modeling. However, temporal availability of these high-resolution data is low and so is spatial coverage. Landsat TM collects data of the same area at repetitive intervals of 16 days. Taking into account frequent cloud cover in mid latitudes, not more than 5-10 cloud free observations per annum can be expected. Additionally, the extent of a mesoscale catchment like the upper Danube requires eight TM images to be fully covered (compare Figure 4.7). Thus, providing regular datasets from this remote sensing device is not feasible. Contrarily, MODIS data will cover the upper Danube basin entirely at least once every day. It is obvious that the attempt to provide frequent parameter retrievals for DANUBIA has to focus on moderate resolution data.

Deriving single data values at the scale level of the 1km proxel would be straightforward. Applying the various MODIS products is the simplest option. However, the scale issues of processes below the proxel scale could not be addressed in this manner. On the other hand MODIS and other environmental optical remote sensing instruments like MERIS do provide samplings at higher levels of resolution. Yet, is the MODIS 500m or 250m resolution appropriate to comply with subscale parameterizations as discussed in Section 3.3? An error would be introduced to subscale parameters even if the higher resolution 250m data were applied. Geocomplexes or stratification of land cover would be derived at precision of at least 1%. Creating subscale information from 250m MODIS resolution however, would provide a precision of only 6.25%. Hence, a substantial possible error would be built into the stratification. It would be desirable to find another way of segmenting moderate scale remote sensing measurements in order to provide more precise subscale stratification.

Mining into the sub-pixel content of remote sensing data is common in remote sensing science. It emerges from the knowledge that moderate resolution sensors will not capture homogeneous surfaces. Heterogeneity prevails in the measurement targets. The analysis of the spectral mixture in mesoscale remote sensing data has been addressed in various studies with many recent advances into the field (Ludwig et al. 2003, Braswell et al. 2003, Lobel and Asner, 2004, Liu and Wu, 2005). The aim of such approaches is to derive the land cover types or surfaces that contribute to the mixed signal received at moderate resolution sensors.

3.7 Scaling by Reflectance Segmentation

In chapter 6 and 7 of this thesis a method is presented that aims at dealing with the difficulties imposed on parameter retrieval by remote sensing models and the incorporation of such parameters in process models. It resolves the MAUP by focusing on homogeneous fractions of mesoscale remote sensing image pixels. With this approach it integrates with the subscale data representation and process modeling described in sections 3.3.2 and 3.3.3.

The method provides estimates of the reflectances of land cover types. A mesoscale reflectance value of a pixel is stacked with the fractions of land covers on that pixel. The fractional land cover information is derived from higher resolution data. In an algorithm ingesting fuzzy a priori expert knowledge, the reflectance value is segmented into the reflectances of the underlying land covers on the pixel. After the process the reflectance of each land cover represented on the pixel is available.

Knowing the reflectance of the land cover types present on a mesoscale cell is especially useful because land cover is used in algorithms such as the retrieval of leaf area index as well as in other algorithms for land surface parameter retrieval. The approach is expected to be helpful whenever the assumption of homogeneous land cover thwarts the application of a remote sensing model.

Figure 3.10 illustrates how the method can be used for scaling in the context of the DANUBIA model. Once the mesoscale reflectance has been processed to individual land cover types reflectances, a land cover dependent model to derive parameters can be applied. These parameters may in turn be lumped together to the mesoscale or be ingested in a process model that is stratified by land cover or using geocomplexes. The method is detailed on in Chapter 6.

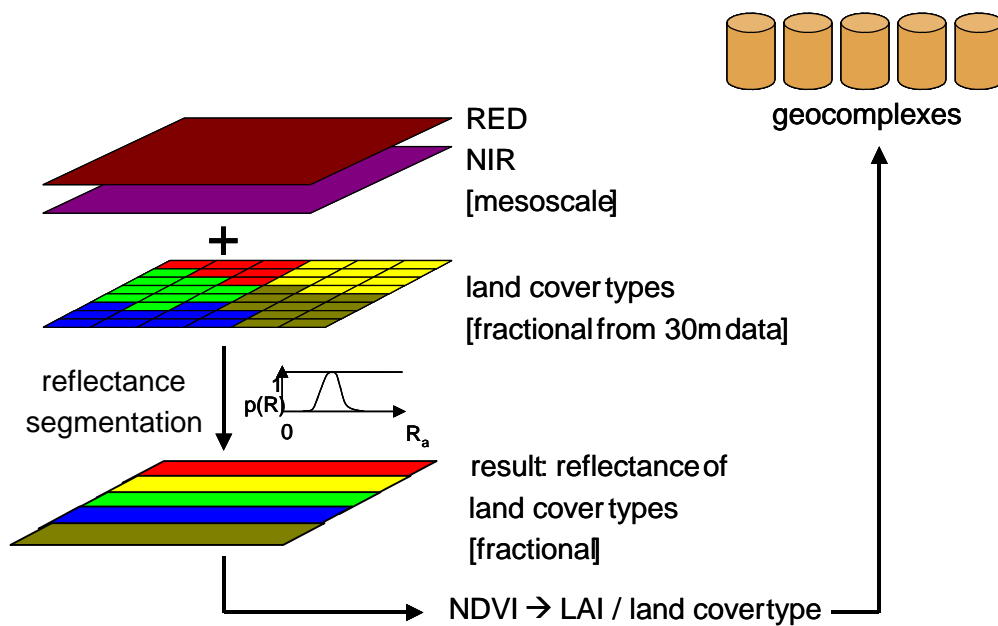


Figure 3.10: Schematic of the scaling of moderate resolution remote sensing data to geocomplexes using reflectance segmentation. LAI algorithms may be applied to fractional reflectances of land cover types. The approach is detailed in Chapter 6.

The charming aspect of the approach is that it is independent of the scale of the measurements. Concerning MODIS, it can be applied to any of the three spatial resolutions provided by the sensor. The fractional subscale output of the algorithm may easily be aggregated to the 1km grid of DANUBIA. Also, translation to other moderate resolution remote sensing instruments is straightforward.

4 Remote Sensing Data and Data Preparation

This chapter provides information on the remote sensing data used in this study. With a focus on the more recent MODIS instrument, the two sensors of which data was sought are presented. Application of remote sensing data requires careful preparation of the data in terms of geometric and radiometric properties. The procedures applied to the data are presented and the results are discussed. The end of this chapter summarizes the datasets used in the study.

4.1 Sensors

The two remote sensing devices, the MODIS instrument and the Landsat Thematic Mapper are designed as whiskbroom scanners. This concept of remotely detecting radiometric surface properties is based on repetitive scanning of stripes of the earth's surface perpendicular to the direction of motion of the spacecraft. Both sensors realize this by a rotating mirror that reflects the sensed radiation into the optical system of the instrument. In the following, the MODIS instrument is expatiated upon in more detail, since it is the newer device than the Landsat Thematic Mapper. Based on habitual language use, Landsat (actually the spacecraft) and Thematic Mapper or TM (the sensor mounted on Landsat) are used synonymously in the following.

4.1.1 MODIS

The Instrument

The MODIS instrument, the Moderate Resolution Imaging Spectroradiometer, continues a series of spaceborne remote sensing devices that have been used for monitoring the earth at moderate spatial resolution for more than the last two decades. Together with four other earth-observing instruments (ASTER, MISR, MOPITT, CERES), the first MODIS was launched aboard the Terra Spacecraft on December 18, 1999. Terra was the first satellite to be launched as part of the Earth Observation System (EOS) program initiated by the U.S. National Aeronautic and Space Administration (NASA). The EOS program is designed to provide observations of the earth to enable a better understanding of the earth's system and the underlying processes. The effort comprises (i) a coordinated series of Earth-observing satellites, (ii) an advanced data system designed to support the production, archival, and dissemination of satellite derived data products, (iii) teams of scientists who are developing the science algorithms to make the data products (Justice et al. 2002). A second MODIS device was successfully launched on the successor to Terra, the Aqua platform, on May 4, 2002. The two almost identical instruments on differently orbiting spacecraft are

complementary in the collection of morning data by MODIS-Terra and afternoon data by MODIS-Aqua. The afternoon/morning contrast was initially reflected in naming the Terra and Aqua missions EOS-AM-1 and EOS-PM-2 respectively. In this constellation, MODIS is a key instrument to the goals of the EOS program providing data for terrestrial, oceanic and atmospheric earth system sciences. Its heritage comes from the experience from a number of previous satellite systems, namely the NOAA Advanced Very High Resolution Radiometer (AVHRR), the Nimbus Coastal Zone Color Scanner (CZCS) and the SeaWiFS sensor, the NOAA High-resolution Infrared Sounder (HIRS), and the Landsat Series Thematic Mapper (TM) (King and Greenstone, 1999, Justice et al. 2002). MODIS was designed as an experimental satellite system in order to address questions related to: atmospheric variables such as cloud properties, radiative fluxes, and aerosol properties; land variables such as land cover and land use change, vegetation dynamics, surface temperature, fire occurrence, volcanic effects, snow cover and ocean variables such as sea surface temperature, and ocean color related to phytoplankton distribution and dynamics and photosynthetic efficiency (Guenther et al. 2002). A novice feature of the MODIS program is the production of a wide array of ready to use global remote sensing products (see below) that have been developed by a large science community in parallel to the planning and design of the instrument itself. Operational processing of these products has been initiated shortly after the launch of the imaging radiometer and validation and improvement of the products has been ongoing since (Justice and Townshend, 2002).

Specifications

Compared to earlier instrumentation, MODIS provides the science community with data of unprecedented ubiquity and quality. It continuously collects data in 36 spectral bands in the visible, near infrared and thermal infrared of the electromagnetic spectrum and provides three different spatial resolutions of 250m, 500m and 1km at nadir, depending on waveband. The large swath of the sensor makes a single MODIS capable of viewing every single point on earth 1-2 times daily, depending on latitude. Thereby the two MODIS track a huge array of the earth's vital signs multiple times every day. The spacecraft the two MODIS are mounted on are flown at an altitude of 705km in a sun-synchronous, near polar, circular orbit. Equator crossing is at 10:30 for MODIS-Terra on a southbound track (descending mode) and at 1:30 for MODIS-Aqua on a northbound track (ascending mode). The repeat cycle of the orbits is 16 days. MODIS relies on a rotating cross-track double-sided scan mirror to reflect radiance into a collecting optical system and onto four focal plane assemblies (FPA). Each FPA is designed for the detection of a section of the electromagnetic spectrum with wavelengths between 0.4 and 0.6 μm collected on the VIS FPA, 0.6–1.0 μm on the NIR FPA, 1.0–5.0 μm on the SWIR/MWIR FPA and 5.0–15.0 μm on the LWIR FPA. The area MODIS views in a single swath (each half revolution of the scan mirror) is 2330km across track and 10km along track at nadir. The 10km along track are sensed by arrays of 10, 20 and 40 detectors for the 1km, 500km and 250m bands respectively. The bands are numbered by spatial resolution rather than wavelength: band 1 and 2 (0.6 μm - 0.9 μm) have a 250m spatial resolution, bands 3 to 7 (0.4 μm - 2.1 μm) 500m and bands 8 to 36 (0.4 μm - 14.4 μm) are the 1km bands. The specifications of the individual bands are listed in Table 4.1.

Table 4.1: MODIS Technical Specifications (NASA, <http://modis.gsfc.nasa.gov>, King et al., 2004)

Orbit:	705 km, 10:30 a.m. descending mode (Terra) or 1:30 p.m. ascending mode (Aqua), sun-synchronous, near-polar, circular
Scan Rate:	20.3 rpm, cross track
Swath Dimensions:	2330 km (cross track) by 10 km (along track at nadir)
Telescope:	17.78 cm diam. off-axis, afocal (collimated), with intermediate field stop
Size:	1.0 x 1.6 x 1.0 m
Weight:	228.7 kg

Power:	162.5 W (single orbit average)
Data Rate:	10.6 Mbps (peak daytime); 6.1 Mbps (orbital average)
Quantization:	12 bits
Spatial Resolution:	250 m (bands 1-2) 500 m (bands 3-7) 1000 m (bands 8-36)
Design Life:	6 years

Primary Use	Band	Bandwidth ¹	Spectral Radiance ²	Required SNR ³
Land/Cloud/Aerosols Boundaries	1	620 - 670	21.8	128
	2	841 - 876	24.7	201
Land/Cloud/Aerosols Properties	3	459 - 479	35.3	243
	4	545 - 565	29.0	228
	5	1230 - 1250	5.4	74
	6	1628 - 1652	7.3	275
	7	2105 - 2155	1.0	110
Ocean Color/ Phytoplankton/ Biogeochemistry	8	405 - 420	44.9	880
	9	438 - 448	41.9	838
	10	483 - 493	32.1	802
	11	526 - 536	27.9	754
	12	546 - 556	21.0	750
	13	662 - 672	9.5	910
	14	673 - 683	8.7	1087
	15	743 - 753	10.2	586
	16	862 - 877	6.2	516
Atmospheric Water Vapor	17	890 - 920	10.0	167
	18	931 - 941	3.6	57
	19	915 - 965	15.0	250
Primary Use	Band	Bandwidth ¹	Spectral Radiance ²	Required NE[delta]T(K) ⁴
Surface/Cloud Temperature	20	3.660 - 3.840	0.45(300K)	0.05
	21	3.929 - 3.989	2.38(335K)	2.00
	22	3.929 - 3.989	0.67(300K)	0.07
	23	4.020 - 4.080	0.79(300K)	0.07
Atmospheric Temperature	24	4.433 - 4.498	0.17(250K)	0.25
	25	4.482 - 4.549	0.59(275K)	0.25
Cirrus Clouds Water Vapor	26	1.360 - 1.390	6.00	150(SNR)
	27	6.535 - 6.895	1.16(240K)	0.25
	28	7.175 - 7.475	2.18(250K)	0.25
Cloud Properties	29	8.400 - 8.700	9.58(300K)	0.05
Ozone	30	9.580 - 9.880	3.69(250K)	0.25
Surface/Cloud Temperature	31	10.780 - 11.280	9.55(300K)	0.05
	32	11.770 - 12.270	8.94(300K)	0.05
Cloud Top Altitude	33	13.185 - 13.485	4.52(260K)	0.25
	34	13.485 - 13.785	3.76(250K)	0.25
	35	13.785 - 14.085	3.11(240K)	0.25
	36	14.085 - 14.385	2.08(220K)	0.35
¹ Bands 1 to 19 are in nm; Bands 20 to 36 are in μm				
² Spectral Radiance values are ($\text{W}/\text{m}^2 \mu\text{m sr}$)				
³ SNR = Signal-to-noise ratio				
⁴ NE(delta)T = Noise-equivalent temperature difference				

The VIS and NIR bands for land remote sensing with MODIS were designed from the experience from the Landsat Thematic Mapper mission, yet they have smaller bandwidths and a new band centered at $1.24\mu\text{m}$ on the NIR plateau was introduced (compare Figure 4.1).

Another unprecedented channel centered at $1.375\mu\text{m}$ (Band 26) was added for the detection of cirrus clouds. For land surface remote sensing purposes in the VIS and NIR, only the first 7 bands are feasible although bands 8 through 19 are also located in the VIS/NIR domain. The latter bands are high gain for ocean color remote sensing and will saturate over land surfaces.

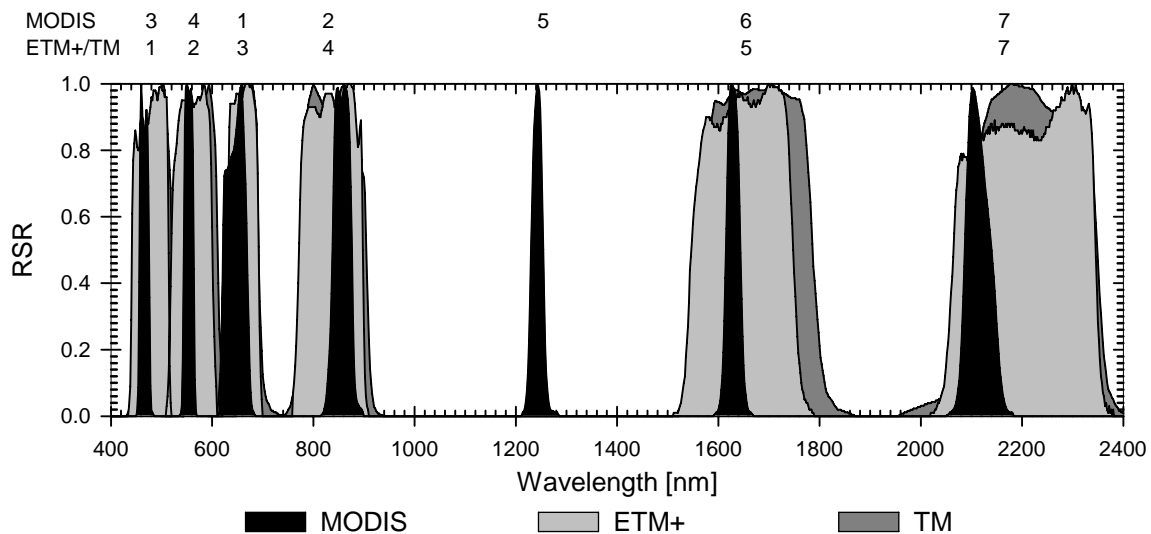


Figure 4.1: Relative spectral response functions of MODIS, ETM+ and TM in the VIS to SWIR region

The 12bit radiometric resolution of data from MODIS overcomes the problem of narrow ranges of DNs (digital numbers), which often resulted in sensor saturation over bright targets such as snow or cloud (Price, 2003). The prelaunch specifications concerning Signal-to-noise-ratios (SNRs) for the reflected solar radiation bands (RSB-Bands 1–19 and 26) and noise-equivalent radiance (NEdLs) for the thermal infrared bands (TEB—Bands 20–25 and 27–36) have been examined to be met by the orbiting instruments (Guenther et al., 2002).

In the design of MODIS, calibration and characterization was given substantial emphasis as these are most critical in the generation of a long-term consistent record of remote sensing data (Justice et al. 2002). As a result MODIS is equipped with a sophisticated calibration unit consisting of four On-Board Calibrators used for radiometric, spectral and spatial calibration: the Blackbody, the Solar Diffusor, the Solar Diffusor Stability Monitor and the Spectroradiometric Calibration Assembly. The Blackbody is the calibration source for the mid- and longwave infrared bands from $3.5\mu\text{m}$ to $14.4\mu\text{m}$, the Solar Diffusor provides a diffuse calibration source for the VIS, NIR and MIR bands from $0.4\mu\text{m}$ to $2.2\mu\text{m}$ and works together with the Solar Diffusor Stability Monitor. The latter tracks changes in the Solar Diffusors reflectance via reference to the sun to ensure that observed instrument changes are not simply changes to the calibration system itself. Finally, the Spectroradiometric Calibration Assembly provides inflight spectral, radiometric and spatial calibration using internal sources, optics, mechanisms, and electronics that enable it to generate and modify input stimuli to MODIS in three modes without interfering with the normal operation of the main sensor. Looking at the moon and into deep space are additional techniques used in the calibration effort for MODIS. A detailed description of the calibration system and its interactions as well as measured system degradation can be found in Guenther et al., 2002. The precise calibration of MODIS can be observed over time in the changes of the calibration factors used in the reflectance calibration of the Level 1B data used in this study.

MODIS data products

One of the outstanding features of the MODIS mission is the production of a whole suite of parameter estimates derived from the measurements made by the sensor. The suite of MODIS data products comprises some 44 standard products with exciting possibilities for different scientific fields to study global change, providing the first state distribution of the main Earth-atmosphere coupled parameters. The products can be classified as calibration products, land, atmosphere, cryosphere and ocean products. Table 4.2 summarizes the products currently available to the user community. These products can be ordered and downloaded at the Distributed Active Archive Center (DAAC) free of charge. A more detailed description of the products used in this work follows in Section 4.6.

Table 4.2: MODIS data products (NASA, <http://modarch.gsfc.nasa.gov/data/dataproduct>, King et al., 2004)

Calibration	MOD 01 - Level-1A Radiance Counts MOD 02 - Level-1B Calibrated Geolocated Radiances MOD 03 - Geolocation Data Set
Atmosphere	MOD 04 - Aerosol Product MOD 05 - Total Precipitable Water (Water Vapor) MOD 06 - Cloud Product MOD 07 - Atmospheric Profiles MOD 08 - Gridded Atmospheric Product MOD 35 - Cloud Mask
Land	MOD 09 - Surface Reflectance MOD 11 - Land Surface Temperature & Emissivity MOD 12 - Land Cover/Land Cover Change MOD 13 - Gridded Vegetation Indices (Max NDVI & Integrated MVI) MOD 14 - Thermal Anomalies, Fires & Biomass Burning MOD 15 - Leaf Area Index & FPAR MOD 16 - Evapotranspiration MOD 17 - Net Photosynthesis and Primary Productivity MOD 43 - Surface Reflectance MOD 44 - Vegetation Cover Conversion
Cryosphere	MOD 10 - Snow Cover MOD 29 - Sea Ice Cover
Ocean	MOD 18 - Normalized Water-leaving Radiance MOD 19 - Pigment Concentration MOD 20 - Chlorophyll Fluorescence MOD 21 - Chlorophyll_a Pigment Concentration MOD 22 - Photosynthetically Available Radiation (PAR) MOD 23 - Suspended-Solids Concentration MOD 24 - Organic Matter Concentration MOD 25 - Coccolith Concentration MOD 26 - Ocean Water Attenuation Coefficient MOD 27 - Ocean Primary Productivity MOD 28 - Sea Surface Temperature MOD 31 - Phycoerythrin Concentration MOD 36 - Total Absorption Coefficient MOD 37 - Ocean Aerosol Properties MOD 39 - Clear Water Epsilon

The data processed from MODIS is categorized in data levels ranging from raw data, the stream received from the observer, to Level 4 where data has been used in models or analysis (Appendix 1). Level 1B data are the data processed to sensor units, that have been geolocated and radiometrically corrected. Higher-level data like the MOD09 Reflectance product (Level 2 Gridded) and the MOD15 LAI/FPAR Product are rastered to a geodetic reference system or map projection and have been produced in interdependent processing chains. For the land

products processing, a description of the data flow can be found in Justice et al. 2002. The production levels and data flow for all products can be found in the EOS Data Products Handbook (Peterson and Greenbelt, 2000, King et al., 2004).

Because of the large swath and number of bands the volume of data produced by MODIS exceeds by far the amount produced by earlier sensors. The 20-year record of AVHRR Level 1B data is approximately equivalent to 7 weeks of MODIS L1B data, an amount of 4 terabytes (Townshend and Justice, 2002). In the processing of these data, hardware and storage requirements are vast and in the early stages the flow of data processing was only capable of processing one days amount of data in one day. At times land product production lagged behind production of L1B data for up to two month while by 2002 it took only 1 to 3 days from acquisition to processed and access ready L1B data. The whole suite of MODIS products was online another 2 to 7 days later (Justice et al. 2002).

The algorithms for the processing were undergoing changes in the first years of MODIS and data products were reprocessed to the maturity of the algorithms (Justice et al. 2002, Townshend and Justice, 2002). The versions of data in this study is 004, the production of 005 was ongoing at the time of this writing. The development stages in MODIS algorithm maturity is distinguished as Beta, Provisional and Validated. Version 001 was designated as Beta, version 003 and 004 contain both Provisional and Validated data (version 002 was never produced) (see http://daac.gsfc.nasa.gov/MODIS/Terra/data_versioning.shtml). The PGE-Version of a dataset denoted in each products metadata contains the exact processing version. The versions are listed in the Product Quality History of MODIS products on the Internet (<http://modis.gsfc.nasa.gov/data/dataprod/index.php>)

4.1.2 Landsat Thematic Mapper

The Landsat satellites have been a long serving series of continuously improved orbiters, the latest carrying the Enhanced Thematic Mapper Plus (ETM+) as the prominent earth observing instrument. The Landsat Project was initiated in 1972 with the launch of Landsat 1 and is the longest running enterprise in imaging of the earth from space. It sent the first unmanned satellite to space that was specifically designed for systematically collecting multispectral data at unprecedented resolution. The instrumentation and orbit of early Landsat 1-3 was changed with Landsat 4 and 5, the inception of the generation of Landsat spacecraft carrying the Thematic Mapper. Landsat 6 was to introduce the Enhanced Thematic Mapper (ETM) but was lost at launch. As of the time of this writing, Landsat 7 was in operation, delivering data from the Enhanced Thematic Mapper Plus (ETM+), the successor of the earlier Thematic Mapper (TM) Instrument. The Thematic Mapper was first mounted on Landsat 4 launched in 1982 (data transmission failure in 1993) and a second TM has been flown on Landsat 5 since 1984. After over 20 years of service, TM 5 although deteriorating, is still delivering data. The single ETM+ that reached orbit on Landsat 7 suffered a permanent failure of the Scan Line Corrector (SLC) on May 31, 2003. The instrument is now collecting data in "SLC-off" mode, which exhibit gaps due to the disturbed scan process (see web page <http://landsat.usgs.gov/dataprod.php> for details). A good overview of the full Landsat Program and a description of the sensors can be found in Lillesand and Kiefer, 2000 and on the USGS Landsat web page (<http://landsat.usgs.gov>).

The TM and ETM+ multispectral scanner instruments share six reflective bands ranging from 0.45 μm to 2.35 μm and one emissive band centered at 11 μm with at nadir ground resolution of 30m and 120m respectively (see Table 4.3 and Figure 4.1). New to ETM+ is a panchromatic band (0.50-0.90 μm) with 15m ground resolution, low and high gain acquisition, the thermal band at 60m ground resolution and an enhanced geometric and radiometric calibration

system. Both instruments are equipped with an oscillating mirror in the Scan Mirror Assembly, which reflects radiation through a telescope onto the Primary Focal Plane (Band 1-4, 8) and the Cold Focal Plane (Band 5-7). On the focal planes 16 detectors (for the 30m bands) are mounted to collect data simultaneously with each scan. The surface swath of the instrument is nominally 480m along track, covering 185km across track. Landsat is in a near polar, sun-synchronous and circular orbit at a 705 km nominal altitude, with an orbit inclination of 98.2 degrees. The repeat cycle of Landsat orbits and ground tracks is 16 days. The orbits of the currently available Landsats 5 and 7 are identical to each other and to the orbit of MODIS on the Terra spacecraft. The time offset between Landsat 5 and 7 orbits is 8 days and Landsat 7 flies 15 minutes ahead of the Terra spacecraft.

Table 4.3: Landsat Thematic Mapper Technical Specifications (NASA, 2006, King and Greenstone, 1999, Lillesand and Kiefer, 2000)

Orbit:	705km, 10:00 a.m. descending mode, 98.8min, sun-synchronous, near-polar circular, inclination 99.2°
Swath Dimensions:	185 km (cross track) by 480 m (along track at nadir)
Data Rate:	85 Mbps (TM); 150 Mbps (ETM+)
Quantization:	8 bits
Spatial Resolution:	15 m (pan, ETM+ only) 30 m (bands 1-5, 7) 60 m (band 6 on ETM+) 120 m (band 6 on TM)
Design Life:	5 years

Band	Thematic Mapper (TM)		Enhanced Thematic Mapper Plus (ETM+)	
	wavelength [μm]	ground resolution [m]	wavelength [μm]	ground resolution [m]
1	0.45 – 0.53	30	0.45 – 0.515	30
2	0.52 – 0.60	30	0.525 – 0.605	30
3	0.63 – 0.69	30	0.63 – 0.690	30
4	0.76 – 0.90	30	0.75 - 0.90	30
5	1.55 – 1.75	30	1.55 - 1.75	30
6	10.40 - 12.50	120	10.40 - 12.50	60
7	2.08 – 2.35	30	2.09 - 2.35	30
PAN	-	-	0.52 - 0.90	15

The product used from Landsat Thematic Mappers is usually the system corrected imagery roughly projected to a WRS-2 based geometry. Systematic errors corrected in this imagery include the panoramic distortion (tangential distortion), earth curvature and rotation, spacecraft ephemeris and scan mirror motion. The data are resampled to 30m ground resolution. Data are distributed in various map projections and geocoded with a residual error of 250m (Eurimage, 2005). The standard data products data lack a correction of the one dimensional relief displacement (see Geometric Correction of data, Section 4.3.2).

Level 1 system corrected (Level 1G) Thematic Mapper imagery is the standard product distributed to the general public. These data are radiometrically and geometrically corrected. The lower level products Level \emptyset Reformatted (Level \emptyset R) and Level 1 Radiometrically Corrected (Level 1R) contain pixels not aligned per scanline. The Systematic Correction (Level 1G) *Gap-filled* is a workaround for the permanent failure of the Scan Line Corrector (SLC) to fill the gaps in the imagery collected by ETM+ in SLC-off mode. Level 1 SLC-off data are distributed containing stripes (gaps) of no data in the images. At USGS, higher data levels Precision Correction (Level 1P) and Terrain Correction (Level 1T) are available to Approved U.S. Government and its Affiliated Users (USGAU) only (<http://edc.usgs.gov/products/satellite/tm.html>, <http://edc.usgs.gov/products/satellite/landsat7.html>). From Eur-

image higher-level data processing services such as mosaicing, pansharpening and orthorectification are available.

Data are distributed in CEOS, FAST, NLAPS, GeoTIFF, NDF or HDF format, depending on the distributor. Data format descriptions are available in the Data Format Control Books (USGS, 1999 and USGS, 2000).

4.2 Data Formats

Storage and distribution of all of NASA's Earth Observing System (EOS) data products relies on the Hierarchical Data Format (HDF). Any MODIS product and, optionally, Landsat data will be delivered in HDF. Due to its complexity, the establishment of this new format has been one of the largest obstacles to MODIS data use. During its onset, available software capable of handling HDF-EOS files has been scarce (Justice, et. al 2002, Townshend and Justice, 2002, Schaaf, C. B., personal communication). For this study the handling of data formatted to HDF-EOS was explored to integrate it with the FAP Areal Data Analysis Software developed and used at the Department of Geography, Chair of Geography and Geographical Remote Sensing (IGGF) at the Ludwig-Maximilians-Universität Munich (Mauser and Bach, 1993). The FAP data format and FAP Image Processing Software was used in all higher processing of the raw data received from the distributor. This chapter summarizes information about the formats, software tools and access to the data.

4.2.1 HDF and HDF-EOS Format

The Hierarchical Data Format (HDF) was developed at the National Center for Supercomputing Applications (NCSA) to address the need for a format suitable for the transfer and manipulation of scientific data across computer platforms and operating systems. The project's mission is to develop, promote, deploy, and support open and free technologies that facilitate scientific data exchange, access, analysis, archiving and discovery (NCSA, 2003). HDF encapsulates a multi-object file structure, which resembles a file system tree within the file. A variety of data types can be stored and grouped in one HDF file: n-dimensional scientific data arrays, a variety of raster images including associated color palettes, tables, text annotations and metadata. HDF has been termed self-describing, as for each data structure in a HDF file there is comprehensive information about the data. But HDF is more than a format to a file. HDF can be viewed as several interactive levels. Only at its lowest level, HDF is simply a physical file format for storing scientific data. At its highest level, HDF is a collection of applications and utilities for working with the data stored in HDF files. Between these levels, HDF provides a software library that has high-level and low-level programming interfaces. See Figure 4.2 for an illustration of the interface levels.

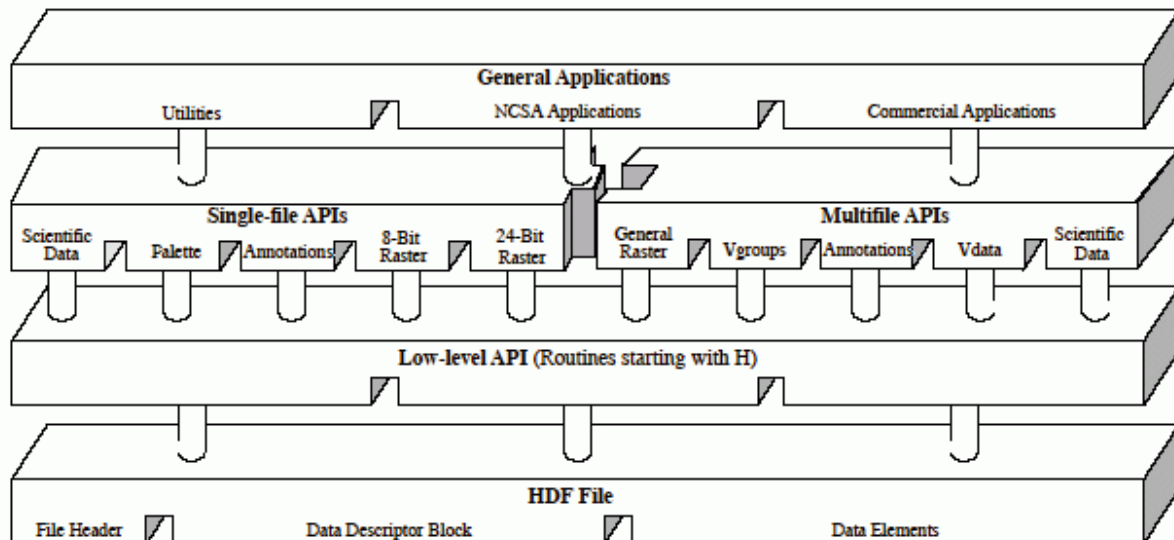


Figure 4.2: Levels of interaction with HDF files (from: NCSA HDF User Guide 2003)

The application programming interface (API) of HDF can be accessed in the programming languages FORTRAN, C and Java. All source code and documentation of the HDF libraries is freely available from the NCSA server at <http://hdf.ncsa.uiuc.edu>.

Many of the data products and data types that result from the EOS missions do not map directly to NCSA/HDF data types. This resulted in an extension of HDF, the HDF-EOS (Hierarchical Data Format-Earth Observing System) software library that was created for the EOSDIS Core System (ECS) by the Raytheon Systems Company (RSC) to fully and optimally support geographical datasets and their requirements regarding temporal or geolocation information. HDF-EOS files support three additional data types, namely grid, swath and point. They allow the file contents to be queried by Earth coordinates and time. These data types can be viewed as a defined structure and organization of data rather than completely new data types. They are constructed using conventions for combining standard HDF data types (Knauss and Klein, 2000). This implies that an HDF-EOS file can be accessed by using the HDF library alone. The application of the HDF-EOS library add-on allows for the subsetting of point, swath, and gridded data sets in terms of time and geolocation (latitude, longitude) additionally to querying image rows and columns like in HDF.

The HDF library comes with a set of command line utilities to extract information from HDF files. One useful tool for dumping data elements is called hdp. It can produce plain binary files from HDF objects. All command line utilities are listed in detail in the HDF User's Guide (NCSA, 2003). A convenient and graphical way to browsing HDF is the free HDFView software. All tools are available from the NCSA HDF web pages.

To convert data from HDF to the FAP format, two tools were developed. HDF2FAP has a simple graphical user interface that will list all scientific data sets (SDS) for selection including tag and reference numbers, dimensions and data type. Selected SDS can be converted to FAP format or flat binary files. For the need of batch processing a command line tool called HDF2PIC was written. It ingests HDF input file and FAP output filename along with a list of SDS names as arguments and produces FAP *.pic files. See Appendix 2 for details on these software.

The current version of HDF is HDF 4. It is compatible with all earlier versions, yet HDF 5 is a completely new product with a new library. Although conceptionally related, HDF 5 is incompatible to HDF 4. Both, HDF 4 and HDF 5 are supported and maintained by the HDF Group at NCSA (NCSA, 2003). Currently as of summer 2006 all EOS data are HDF 4. HDF-EOS for HDF 5 is under development.

4.2.2 FAP Format

The FAP data format was originally developed at the University of Freiburg, Germany and has been extensively used in many studies at the Department of Geography, Chair of Geography and Geographical Remote Sensing (IGGF) at the Ludwig-Maximilians-Universität Munich (LMU). In the conception of the format the idea of a format capable of uniting numerous data types in one file was crucial. This ability of the format results in a very versatile way of data storage and allows the combination of data from a variety of sources in one file. This feature was especially useful and desirable for the data processing in this study, where the integration of multiple source data was required. By discriminating the most significant bit (MSB) of the little endian data types, six different data types can be stored in a FAP file as listed in Table 4.4.

Table 4.4: Data types available for data stored in a FAP image file.

Name of data type	Data type size	Description
Byte-positive Type 1	8-bit	8 bit little endian unsigned integer type
Byte-negative Type 6	8-bit	8 bit little endian signed integer type
Integer*2-positive Type 2	16-bit	16 bit little endian unsigned integer type
Integer*2-negative Type 7	16-bit	16 bit little endian signed integer type
Integer*4	32-bit	32 bit little endian signed integer type
Real*4	32-bit	32 bit little endian floating point type

The FAP file has a file header containing the metadata to the image, including its size in rows and columns, number of bands, data types of bands and a text description of the file. The data itself is stored in a line-interleaved pattern, i. e. one row of the image including all bands is fully written, followed by the next row. Because of the capability of storing different data types, a system was developed to use disc space efficiently. Depending on the size of the image, a record length is determined and a band will use records according to its data size. For example an 8-bit band will use one record, a 32-bit band will use four. The advantage of this way of storing data lies in fast and convenient processing and handling of data from these files (Mauser and Bach, 1993).

The programming for this study was done in the Java programming language. In order to access FAP data files in a Java Program, a library was developed to extract data from this data format. This library makes use of the fast byte oriented java.nio package. It allows flexible access to Pixels of a FAP file or any arbitrary subset of the file. See Appendix 2 for details on this library.

4.3 Geometric Correction

In many applications of remote sensing, the data need to be matched and compared to other sources of data. Whenever spatial data of different origin are to be processed together, there is a need for common ground concerning the geometry of the data: The different layers of information need to be stacked such, that a unique plot in space is attributed the correct

information regardless of the layer. In the context of this study, this matching is necessary in multiple terms. Not only data from different sources are being matched, but also data of different acquisition times are compared. Thus, precise geocoding of all data involved is critical. Usually, some type of orthogonal grid is used to address position in two-dimensional space. Many of such grids or geodetic systems are available and different types may be adequate depending on the area under study. In any case, the curved surface of the earth must be transformed or projected such that it may be represented as a flat plane.

The raw data collected by earth satellite observations are also represented in an orthogonal image raster. Nevertheless, because these data have been projected to the image plane in the process of acquisition, they do not match any geodetic system. They contain systematic and random errors induced by satellite and earth motion, by earth curvature and relief as well as the sensing system itself (Lillesand and Kiefer 2000, Wolfe et al. 2002). The following describes the process of geometrically correcting the remote sensing data of the two sensors involved.

Both, system dependent and system independent errors can be corrected using nonparametric and/or parametric approaches. Nonparametric approaches require a series of ground control points (GCPs) to drive a coordinate transformation for the rectification of the image. Parametric approaches require information concerning the sensing geometry (interior orientation) and the sensor attitude and position (exterior orientation). They describe the circumstances that produced the sensed image. The correction of the Landsat imagery relies on the determination of GCP in the system corrected imagery. MODIS data can be geocoded using the geolocation parameters delivered with the image data

The geodetic system for the GLOWA-Danube model is a Lambert Conformal Conical (LCC) projection based on the Hayford International 1924 ellipsoid. The geodetic datum is DHDN. This is the same projection as it has been specified for the Hydrologischer Atlas Deutschland (HAD) (BMU, 2003). As this projection is somewhat difficult to handle, the processing of the data for this study was done using the Universal Transversal Mercator (UTM) projection based on the WGS84 ellipsoid and geodetic datum. However, reprojection of the data to the GLOWA-Danube geometry is possible.

4.3.1 MODIS

One of the new features of the MODIS instrument is the high quality geolocation information delivered for all MODIS data. This geolocation information is produced by using the spacecraft ephemeris data and the interior coordinate systems of the sensor to derive a viewing vector for each observation. As a result, each 1km sample of the sensor is attributed a pair of latitude and longitude values derived from real time measurements of the exterior orientation of the Terra spacecraft.

On board an inertial gyro and star-tracking sensors are used to determine the attitude. The position is determined by the Tracking Data Relay Satellite System On-board Navigation System (TONS) (Wolfe et al. 2002). During acquisition, the interior orientation of MODIS detectors and mirror results in a complex spatial and temporal relationship for the alignment of the different spectral bands. The various coordinate systems and ephemeris measurements are used to determine longitude and latitude values for all pixels of the 1km bands (Nishihama et al., 1997, Wolfe et al. 2002). The 1km samples need to be interpolated when geolocation for the 500m and 250m bands are required.

Due to the simultaneous sensing of 10km along track in one scan, a phenomenon called the “bow-tie” effect is very pronounced in MODIS imagery. The effect is common in wide-field-

of-view whiskbroom scanner devices. It describes the increase in overlap of consecutive scans with increasing scan angle. In Figure 4.3 a schematic illustration of this effect is given.

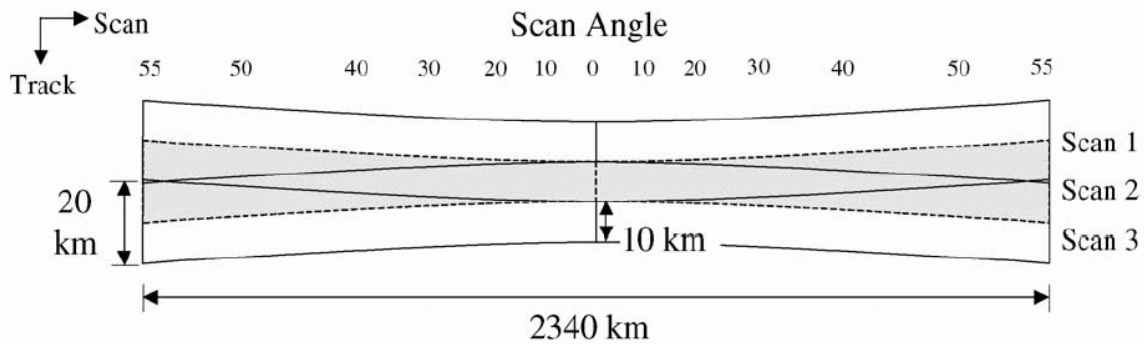


Figure 4.3: Schematic illustration of the ground projection of MODIS scans. The central scan (scan 2, gray) is overlapping with the previous (scan 1) and following scan as the scan angle increases (Wolfe et al. 2002).

Near nadir, across-track scan velocity and along-track spacecraft motion are designed such that one scan abuts on the next, but overlap may be up to 50% at the scans edges. Under large scan angles, an object may be viewed up to three times by three consecutive scans (Wolfe et al. 2002). Figure 4.4 provides an illustration of the effect as it appears in actual swath imagery, showing a coastline section of a MODIS scene.



Figure 4.4: Coastline near Mont St. Michel, France as seen by MODIS under high scan angle (approx. 50°) in three consecutive scans at 250m resolution. A scan has 40 rows in 250m MODIS imagery.

MODIS Level 1 and 2 data will contain this bow-tie effect. They are distributed as data - granules, defined as about 5min of MODIS surface observation. Within this time span, MODIS will cover about 2340km across-track (the swath width) and 2030km along-track. In the geometric rectification of the Level 1B data used in this study the geolocation information distributed with the data was used. These geolocation layers, contained as Scientific Data Sets (SDS) of longitude and latitude in the HDF-EOS files, are produced using the global 1km Platte Carre EOS Digital Elevation Model (DEM) (Nishihama et al., 1997). The DEM is applied in order to compensate for the relief displacement effect (Itten et al., 1992, Itten and

Meyer, 1993, Lillesand and Kiefer, 2000). Without this terrain correction, location errors up to tens of kilometers may result due to the high scan angle of MODIS (Nishihama et al., 1997).

Data from Levels 2G, Level 3 and Level 4 are processed to the Integerized Sinusoidal (ISIN) projection for the MODIS data collections 001 through 003. In collection 004 the Sinusoidal (SIN) Projection was applied (Department of Mathematics and Computer Science South Dakota School of Mines and Technology, 2004). The ISIN projection is unique to the MODIS land products, and analogous to the SIN projection except that the ISIN projection is centered about 0° longitude. Special coefficients are used to flatten the WGS84 ellipsoid. In these projected products the bowtie effect has been removed. The data are distributed in tiles covering an area of 10 by 10 degrees along the equator. The tessellation of the earth is organized in a tile coordinate system, which starts at (0,0) (horizontal tile number, vertical tile number) in the upper left corner and proceeds rightward (horizontal) and downward (vertical). Figure 4.5 depicts the globe in the ISIN/Sinusoidal projection. It shows that not all tiles contain earth data and some will only contain water (see MODLAND developers web page for details)

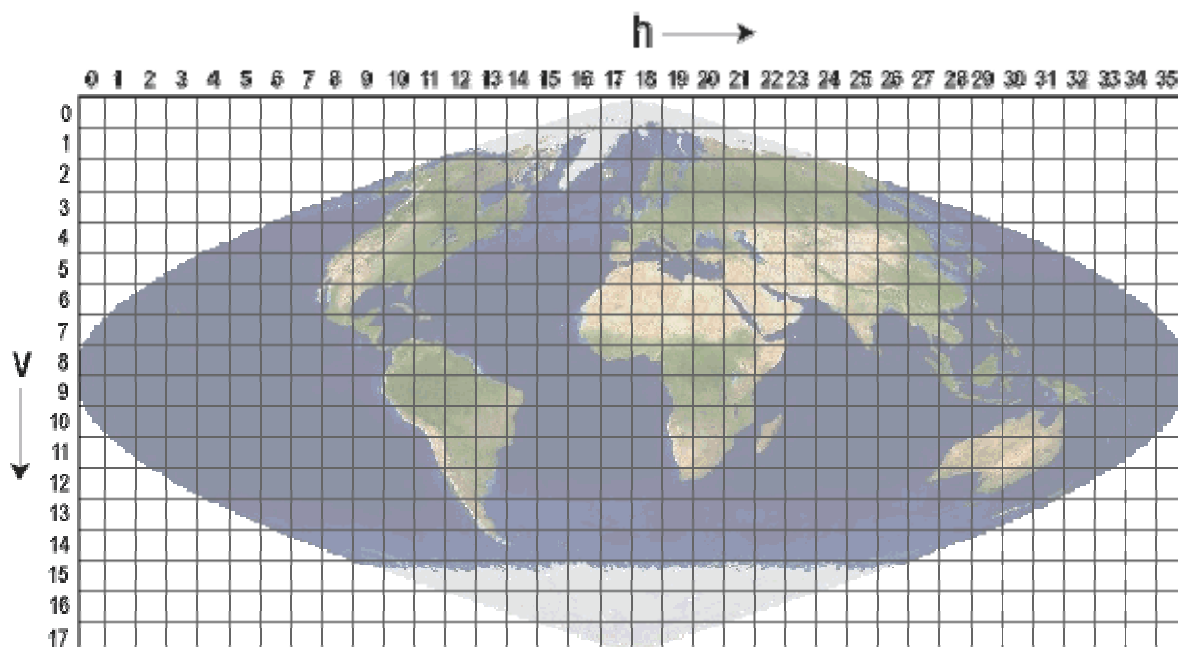


Figure 4.5: Tile coordinate system for MODIS products of Level 2G, Level 3 and Level 4 (Image taken from the National Snow and Ice Data Center (NSIDC) web page, http://nsidc.org/data/docs/daac/mod10_modis_snow/landgrid.html)

The area of the GLOWA catchment upper Danube is located in tile h18 v04. Browsing the DAAC for the GLOWA test sites area will return data on this tile. Data from Level 2G and higher will contain this location in the name of the HDF file. Already projected to a standard projection, these data require reprojection only.

In data granules in swath geometry (Level 1B) the area of the upper Danube catchment is located depending on the path of the satellite and the viewing angle of the system. Thus, location is a function of time of acquisition determined by orbit and overpass and granules are categorized by year, day of year (DOY) and time (UTC). Data granules containing the GLOWA catchment at daytime overpasses are acquired in a time window from about 9:30 UTC to 11:15 UTC. The best geometric conditions for this area are in data with an overpass approximately centered over the catchment. This occurs on days when the acquisition time of

the granule that contains the GLOWA catchment is around 10:20 UTC. On the 7th, 9th and 14th day in the 16-day orbital cycle from such central overpasses at 10:20 UTC, geometric conditions are still considerably better than on all other days, when the ground track does not intersect with the GLOWA catchment and MODIS observes the area under large scan angles. Three cases of overpass patterns of MODIS are shown in Figure 4.6. Data for this study were selected primarily from this subset of preferable geometric conditions for acquisition.

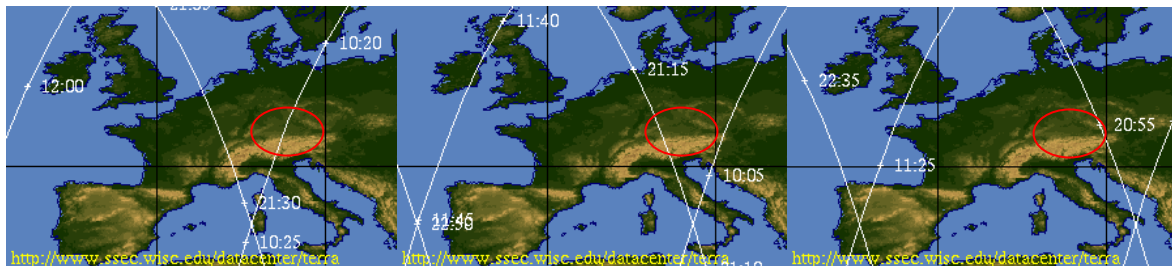


Figure 4.6: Three cases of overpass times and orbit ground tracks for coverage of the upper Danube catchment (red circle) by Terra/MODIS (descending). Best geometric conditions are present when the overpass is intersecting with the catchment around 10:20 UTC (left), moderate conditions for orbits close to the catchment (about 10:05 UTC, center), unfavorable conditions are met around 11:25 UTC with an orbit far to the west of the catchment (right). Note that daytime descending orbits run in a NE to SW direction (Space science and Engineering data center, <http://www.ssec.wisc.edu/datacenter/terra/>, modified)

For the georectification of MODIS HDF-EOS data on Windows platforms three tools were applied in this study: The HDF-EOS to GeoTIFF Tool (HEG-Tool), the MODIS Reprojection Tool (MRT) and the MODIS Reprojection Tool Swath (MRT-Swath). While the first two will handle the gridded MODIS products (Level 2G, Level 3, Level 4), the latter is especially designed for reprojecting data in the swath geometry (Level 1, Level 2). All tools can be used through a graphical user interface or in command line mode. The tools are available free of charge from the [HDF-EOS tools and information center](http://www.ssec.wisc.edu/datacenter/terra/).

The tools were applied to reproject all MODIS data to a UTM frame containing the catchment of the upper Danube. For the Level 1B swath data the MRT-Swath tool was used to remove the bowtie-effect. Gridded data were reprojected to UTM in order to match with all other data. Details on the application of the tools can be found in the corresponding user's manuals. The parameters for the reprojection are given in Table 4.5.

Table 4.5: Parameters used in the reprojection of MODIS data

Projection	Universal Transversal Mercator
Zone	32
Upper left corner (x, y)	434928.76, 5548806.0
Lower right corner (x, y)	871278.76 5180376.0
Ellipsoid	WGS 84
Datum	WGS 84
Interpolation	bilinear

The spatial accuracy specification for MODIS is 150m, with an operational goal of 50m. However, actual operational geolocation accuracy is reported to reach 18 ± 38 m along-track and 4 ± 40 m across track (Rojas et al., 2002, Wolfe et al., 2002).

4.3.2 Landsat

Landsat Thematic Mapper scenes are spatially organized in a preplanned ground track system, the worldwide reference system (WRS). An individual acquisition is localized on the globe in a system of 233 indexed orbits (paths) of the 16-day earth coverage cycle of the satellite and 248 scene centers (rows) along each orbit. To cover the entire extend of the upper Danube basin a total of eight scenes is needed. These scenes are on path 192 to 194 and from row 25 to 28. At the given latitude scenes of adjacent swaths overlap by about 35% (USGS, 1999, USGS, 2000, NASA, 2006). Figure 4.7 provides an overview of the scenes acquired for this study.

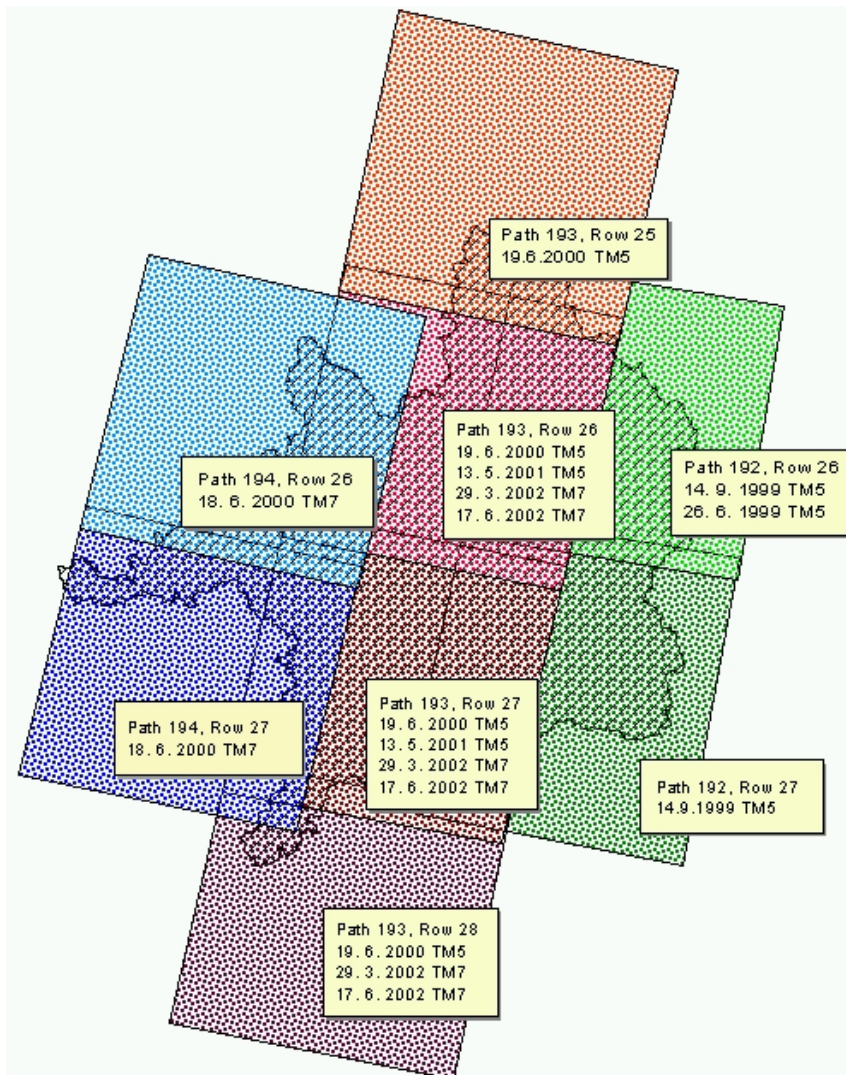


Figure 4.7: Overview of the Landsat TM scenes to cover the GLOWA-Danube catchment.

Landsat scenes were acquired as Level 1G data, which has the systematic errors removed. However, the data are not rotated to northerly orientation and the projection is only a rough approximation of a geodetic system. Data at this processing level need further correction. Nevertheless, this processing level is a prerequisite for the correction of the terrain induced error applied on TM data: In these data, pixels are aligned the way the sensor collected them in each swath, i.e. the samples of a swath form 16 rows of the image. The displacement of pixels induced by rugged terrain will be along the scan line the data is collected in. Thus

correction of this error is only feasible as long as the ordering of samples along the swath (=across-track) is undisturbed and retained along an image row of the unrotated scene. A schematic illustration of the terrain-induced effect in scanner imagery is given in Figure 4.8.

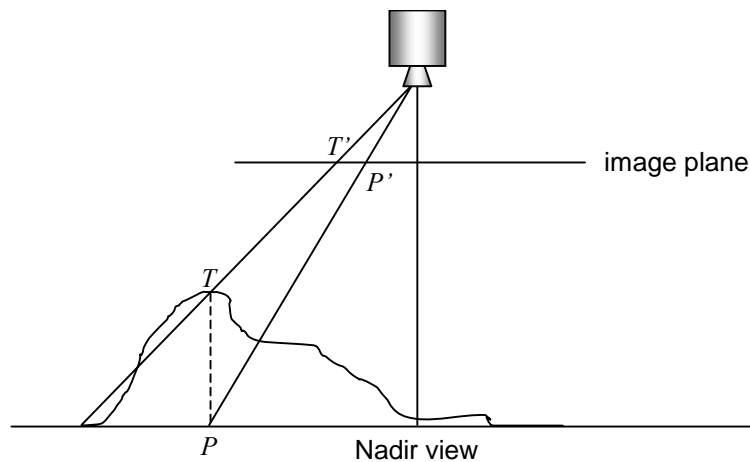


Figure 4.8: Schematic illustration of the terrain induced effect in scanner imagery: Viewing at large angles in scanning direction, a scanner will record a mountaintop T at T' on the image plane. The true location of T is viewed in the direction of P and is mapped to P' on the image plane. The distance $T'P'$ is the terrain induced displacement in scanner imagery.

As stated above, the removal of this error is essential for data of areas with high variation in elevation as it is present in the alpine areas of the Danube catchment. The geocoding of the Landsat imagery was performed by a nonparametric approach with a set of GCPs for each scene used. To remove the relief displacement of pixels, a DTM in UTM32 projection of the area was applied, providing the elevation of each pixel at 30m spatial resolution. The approach for the correction of the data uses terrain corrected GCPs and combines the removal of the terrain error with a polynomial transformation of the scenes to the geometry of the DTM. A detailed description of the algorithm can be found in Itten et al., 1992, Itten and Meyer 1993 and Braun, 1998.

The error in the geometric correction was specified in both, the row and column direction and is well below one Pixel in all cases. Table 4.6 summarizes the error from the polynomial transformation of the images.

Table 4.6: Vertical and horizontal RMS of the geometric correction over all corrected TM images

	RMS vertical [pixels]	RMS vertical [m]	RMS horizontal [pixels]	RMS horizontal [m]
Mean	0.638	19.125	0.676	20.293
STD	0.053	01.586	0.061	1.838
Min	0.537	16.113	0.607	18.216
Max	0.707	21.207	0.831	24.936

In order to countercheck the quality of the geocoding process, a second set of GCP was elaborated from the images rectified to UTM geometry and compared to UTM coordinates taken from digital topographic maps (Bayerisches Landesvermessungsamt, 2003). This check

was performed for about 150 Points, 50 on each of the 3 Landsat paths. The results from this final quality check are presented in Table 4.7.

Table 4.7: Average absolute vertical and horizontal deviation in [m] from the topographic map within each of the three Landsat paths.

	Path 192		Path 193		Path 194	
	northing	easting	northing	easting	northing	easting
Mean	22.90	18.53	19.04	18.63	17.27	22.69
STD	17.04	17.57	13.94	16.12	14.98	19.12

With some exceptions, dislocation of features in the corrected imagery was below one pixel. With this result the quality of the geometric correction of the Landsat imagery can be considered very high. The good spatial agreement was also observed when adjacent images of the same path were merged. Such images overlap by a few scans of the sensor and pixel values are the same when acquired on the same overpass. Checking these pixel values showed that individually corrected scenes resulted in an exact match of pixel values along the overlapping stretch of imagery. This indicates that individually corrected scenes appear in the exact same geometry after the correction sequence.

4.4 Radiometric Correction

Radiometric correction of remotely sensed imagery is a fundamental processing step if radiances captured by measurement devices in outer space are to be translated to surface physical quantities (Teillet, 1986, Lillesand and Kiefer, 2000). The spectral signature of a surface feature observed by a remote sensing device is altered by influences of the atmosphere (Rayleigh- and Mie scattering) and topography and is further dependent on sensor characteristics, path lengths and directions as well as illumination conditions. Although not explicitly compelling for all remote sensing applications, the intercomparison and fusion of data of different dates and sensors in this study makes this step indispensable. The process comprises the quantification and correction of atmospheric influences, variations in scene illumination, viewing geometry and translates spectral radiances to spectral reflectances.

A number of algorithms have been developed to perform this task such as the 5S-Code (Tanré et al., 1990) and the SMAC-Algorithm (Rahman and Dedieu, 1994) both being methods for simple and fast atmospheric correction. A physically based radiometric correction model was presented by Sandmaier (1995), who uses the 6S-Code (Vermote et al. 1994) to model radiative transfer. Proy et al. (1989) modeled and evaluated the influence of the topography on the downward direct and diffuse radiation in remote sensing data. Bach (1995) presented a Procedure to Use LOWTRAN-7 for Reflectance Calibration (PULREF). PULREF uses the results of the physically based radiative transfer model LOWTRAN 7 (Kneizys et al. 1988) to efficiently determine surface reflectances from sensor radiance counts. It can account for topography effects in remote sensing imagery and the adjacency effects as described by Tanré et al. (1987).

For the generation of the MODIS reflectance product, a new atmospheric correction algorithm was developed, again based on the 6S radiative transfer code. It uses novice features of MODIS itself, such as cirrus cloud detection (1.38 μ m channel) and the determination of aerosol optical thickness (3.75 μ m channel) to provide an automated global dataset at scales exceeding 250m (Vermote and Vermeulen, 1999, Vermote et al. 2002). As this procedure is designed to run on an operational, automated basis for global coverage, locally available data on atmospheric state cannot be ingested. Consequently, the Algorithm Theoretical Basis

Document (Vermote and Vermeulen, 1999) states that it is not intended to replace the need for localized atmospheric correction for individualized field studies.

Care has to be taken when differently processed reflectance data are sought. Biases between the different approaches to determining surface reflectance are to be expected. Regrettably, as of the time of this writing there is no intercomparison of the performance of the various approaches mentioned above. Uncertainties in the modeling contribute to the probable variations in differently processed data. To avoid these uncertainties in the radiometric correction of data for this study, instead of using the readily available MODIS reflectance product (MOD09), data of both sensors were procured as Level 1 raw radiance counts data. They were then calibrated using the Procedure to Use LOWTRAN for REFlectance Calibration (PULREF) (Bach, 1995) with the procedure customized for each sensor. Localized input data was applied in the correction. Originally this algorithm had been developed for the radiometric correction of various hyperspectral spectrometer data. It was successfully applied in earlier studies and to different sensor systems (Bach and Mauser, 1994, Stolz, 1998, Braun, 1998, Oppelt, 2002, Bach et al., 2003). The implementation of PULREF proved to be very flexible and was easily adapted to MODIS Level 1B data.

4.4.1 Methodology

The application of the Procedure to Use LOWTRAN for REFlectance Calibration (PULREF) (Bach, 1995) of a satellite image grounds on a simulation of atmospheric transmission assuming four different surface reflectances of 0%, 10%, 30% and 60%. Four runs of the LOWTRAN 7 radiative transfer code (Kneizys et al. 1988) result in top of atmosphere (TOA) radiances that correspond to the four assumed surface reflectances at wavelengths ranging from 0.25 to 28.5 μm . These simulations are customized to the atmospheric conditions at the time of the image acquisition. Their results discriminate fractions of direct and diffuse radiance as well as atmospheric path radiance. The model takes into account:

- solar irradiance
- molecular absorption of irradiance
- aerosol absorption of irradiance
- single and multiple scattering by molecules
- single and multiple scattering by aerosols
- emitted thermal radiance

When radiative transfer is simulated, an atmospheric model is ingested to specify regional and seasonal atmospheric properties. For the determination of the phase function an aerosol model is used and layers of varying aerosol types are assumed. In the calculation of solar irradiance a lat/lon position, time and elevation is needed. Optionally, measurements of atmospheric profiles as well as horizontal visibility can be incorporated into the model (Bach, 1995).

In order to use the model output from the LOWTRAN simulations for atmospheric correction of satellite imagery, the characteristics of the sensor are required. The information inquired by the model is (i) the sensor response in the individual wavebands of the imager and (ii) parameters for the calibration of the gray values of the image to physical unit. The sensor response specifies the sensitivity of the sensor and is ingested by PULREF as sensor response functions for each band of the sensor at a resolution of 2nm. The calibration is a linear transformation of digital dimensionless values to the corresponding physical quantity of irradiance ($\text{W}/\text{m}^2 \mu\text{m sr}$) measured at the sensor. Band specific gain and offset parameters are usually available from the literature (TM) or distributed with the data (ETM+, MODIS).

For the application of the atmospheric correction to data in mountainous terrain PULREF will call LOWTRAN to be run for 6 different ground elevations. Each run at 0km, 0.5km, 1km, 2km, 3km and 5km asl will ingest a unique value for the horizontal visibility in order to account for the vertical change of atmospheric properties and path lengths. At each elevation total irradiance, direct and diffuse components and path radiance are modeled for the four assumed targets of 0%, 10%, 30%, 60% albedo. Then the sensor response is used in a convolution with the LOWTRAN output. The result is the radiance that the specified sensor would receive in each waveband had it observed targets at 6 different elevations. The radiance components are given at each of these pivots.

By linear interpolation, these pivots allow for the calculation of the radiance components of a signal received at the sensor from arbitrary elevations. DTM elevation data is used for each pixel to interpolate radiances at that elevation. To compensate for varying terrain illumination, radiance over an inclined surface is modeled by a four component weighting function, taking into account terrain slope, the local solar incidence angle and terrain radiance (Bach et al. 2003) The four pivots for radiance at 0%, 10%, 30% and 60% reflection over an inclined surface are finally used to make a distinction between the irradiance received by the sensor and the actually reflected radiance of the target. The inversion determines by interpolation the reflectance of a pixel from the radiance actually measured at the sensor. Bach showed that the interpolation error from the four pivots is below 0.5% at albedos below 70% (Bach, 1995).

4.4.2 MODIS

Atmospheric correction of MODIS data was performed for 250m data (QKM = quarter kilometer) and the 500m data (HKM = half kilometer) of the same acquisition time and date. Equal parameters were applied in the processing of the datasets. Both datasets were processed because the two bands of the QKM data (RED, NIR) are, although aggregated, contained amongst the 7 bands of the HKM data. The two bands of the QKM data alone hardly admit an evaluation of the reflectance spectra after the atmospheric correction. With the seven bands of the HKM data, reflectance spectra provide a better impression of the output from the PULREF algorithm and allow the comparison to TM data and the MODIS Reflectance Product MOD09.

The bands of the HKM data were processed sorted by wavelength rather than band number. This results in the sequence 3-4-1-2-5-6-7 of the MODIS bands after processing. Each MODIS L1B calibrated radiances data granule is distributed with calibration factors included in the HDF file. These calibration factors were used in the calibration of the grayvalues to radiance units prior to the atmospheric correction. During the time series of 2003 used in this study a slight change in the calibration factors of the sensor could be observed. While the bands in the visible part of the spectrum (band 3, 4, 1) exhibit a rise in gain factors, the bands in the near and middle infrared section of the electromagnetic spectrum (band 2, 5, 6, 7) have a trend of decreasing gain values.

In order to parameterize PULREF, a set of input information is required. The following table (Table 4.8) lists the parameterizations that were applied to all MODIS imagery alike.

Table 4.8: Parameters set for all images in the processing of MODIS imagery for atmospheric correction

Atmospheric Model	mid-latitude, summer
Specification of Radiosonde Profile	no
Aerosol Model	rural, horizontal visibility 23km
Seasonal Aerosol Type	spring/summer

The available 30m DTM was aggregated to 250m and 500m for the QKM and HKM data respectively. For each image the DTM was used to calculate the local incidence angle of the sun. This angle was approximated for each pixel by using a central lon/lat position (E 11.0°, N 48.0°) for all pixels and the unique acquisition time of the image in order to derive the position of the sun.

The horizontal visibility is a crucial value in the parameterization of the reflectance calibration. To determine valid parameters for the six elevation layers distinguished by PULREF, horizontal visibilities from synoptic weather observations by the *Deutscher Wetterdienst* (DWD, German Weather Service) were used. The data from synoptic stations have the advantage that a value in meter units is given, while DWD climate stations only provide a scheme of 10 classes of horizontal visibility. The data was collected at the airports at Augsburg-Mühlhausen (463m asl), Erdinger Moos (444m asl) and Altenstadt (756m asl). Observations at these stations at 9:00 am, 10:00 am, and 11:00 am were interpolated to the time of the satellite acquisition. These interpolated values were then used to determine corresponding horizontal visibilities at the required six elevations. This was achieved by application of a formula by Elterman (1964), which provides a functional dependence of horizontal visibility to elevation. The same function has been used earlier by Sandmaier (1995) and Bach et al. (2003)

4.4.3 Landsat

Atmospheric Correction and preparation of Landsat TM data was performed very much analogous to the preparation of MODIS data. Unlike the application of PULREF to MODIS data, the procedure had previously been applied to Landsat TM data, thus, existing spectral response functions for both, TM and ETM+ could be used. Calibration values for Landsat data were taken from the literature (TM) and the values delivered with the data (ETM+). For the parameterization of the atmosphere the same general settings applied to Landsat data as those listed in Table 4.8 for the MODIS correction. Because of the only partial coverage of the GLOWA catchment by each of the Landsat scenes, the specification of horizontal visibilities was done by selecting adequate weather stations individually for each scene. Data were taken from stations located within the scene. This included data from climate stations in some cases. For the dates on which data from Landsat coincides with MODIS data, equal parameters were applied to the datasets of both sensors.

Parts of the DTM used in the correction were available at a horizontal resolution of 75m only. Interpolation of this section of the DTM to the 30m resolution required in the atmospheric correction of Landsat data resulted in artifacts in the data. These artifacts will be visible in derivatives of the data such as the dataset of the local incidence angle of the sun. Visualized, it resembles a waffle-like structure and will be contained in the reflectance data if applied in the atmospheric correction. To avoid this, interpolation to 30m was not performed on the DTM but on the derived data, i.e. the calculation of the local incidence angle was performed on the 75m DTM data and the resulting data was interpolated. This prevents the artifact from appearing in the desired reflectance data at 30m resolution. The effect is illustrated in Figure 4.9. The image shows a portion where the 75m resolution DTM of Tyrol abuts the 30m DTM of Bavaria.



Figure 4.9: Artifacts in the data derived from the DTM. The images show a visualization of the cosine of the local solar incidence in an area where the 75m DTM of Tyrol (southeast section) abuts the 30m resolution DTM of Bavaria (northwest section). In the left image, the calculation was performed on interpolated data at 30m. In the right image the calculation was performed on the 75m data and the local solar incidence angle was interpolated and merged with the 30m data.

4.4.4 Validation of the Reflectance Calibration

The validation of atmospheric correction of the MODIS and TM data for this work has to rely on a qualitative approach. The mesoscale resolution of the data makes it unfeasible to collect ground truth information in the form of in situ measurements of reflectances. Nevertheless the context of this study allows a relative validation of the results of the reflectance calibration by comparing reflectances obtained from TM and MODIS on the same date. These coincident datasets should exhibit equivalent properties when compared to each other, which is also a prerequisite for the reliable development of the process of reflectance segmentation presented in chapter 6. Additionally, the results were compared to the MODIS Reflectance Product MOD09.

Absolute values of reflection properties of land surfaces will always be erroneous to some 5 to 10 percent. This error will be function of a number of influences on the data, such as the truth in the parameterization of the atmosphere, the heterogeneity of the atmosphere across the area of the satellite observation, the quality of ancillary data such as the DTM and the quality of the input data itself. However, data that was collected on the same day with a time lag of only 40 minutes and processed with the same ancillary information should yield a high level of correlation if atmospheric correction was successful. Thus, this validation focuses on the intercomparison of reflectances derived from data of two different sensors.

The high performance of the atmospheric correction procedure itself has been proven in various other studies, including the investigation of the quality of the illumination compensation (Braun, 1998, Bach et al., 2003) and its validation by means of contemporal collection of ground truth (Oppelt, 2002). This matured state of PULREF allows the application of the procedure to a full dataset of MODIS imagery where the validity relies on

the expertise in the data processing, but validation of individual scenes processed is not feasible.

Six datasets will be compared in this validation as listed in Table 4.9. The focus lies on elaborating the observations of MODIS and TM with highest similarities. They are greatly influenced by (i) time of acquisition and (ii) observation geometry. First, observations on DOY 171 are compared. On that day an observation made by Landsat TM is preceded and followed by observations by MODIS by about an hour each. However, the MODIS observations on this day regrettably both have the lowest geometrical quality possible: They were acquired under high scan angles from orbits far to the east and west of the study area, with ground tracks of the satellite cutting through western Russia and Greece around 9:45 and through Wales and Brittany around 11:25 (compare Figure 4.6). One day earlier (DOY 170) a MODIS observation with very good geometrical properties is available where the area is observed almost nadir looking. This image is also addressed in this validation, assuming that changes to reflectance properties of the surface are minimal during some 24 hours. The period under address had no precipitation and cloud free skies over most of Europe. Finally, the Surface Reflectance product MOD09 was sought for both days to compare the product to the MODIS reflectances obtained by calibration using PULREF.

Table 4.9: Datasets compared in the validation of the atmospheric correction

Dataset	Date of Acquisition	Time of Acquisition	Spatial Resolution	Short Name
Landsat TM5 PULREF corrected	19.06.2000 DOY 171	10:40	30m agg. to 500m	TM (TMsimMOD_171)
MOD02 HKM PULREF corrected	18.06.2000 DOY 170	10:40	500m	MOD02PUL_170
MOD02 HKM PULREF corrected	19.06.2000 DOY 171	09:45	500m	MOD02PUL_171east
MOD02 HKM PULREF corrected	19.06.2000 DOY 171	11:25	500m	MOD02PUL_171west
MOD09 Reflectance	18.06.2000 DOY 170	unspecified	500m	MOD09_170
MOD09 Reflectance	19.06.2000 DOY 171	unspecified	500m	MOD09_171

The Landsat TM data was aggregated to 500m resolution to match with the coarser MODIS datasets. In order to compare TM reflectances to MODIS reflectances a linear transformation was applied to the TM data. This transformation developed by Liang et al. (2002) is based on simple linear regression and uses the 6 TM bands reflectances to derive the 7 MODIS bands reflectances. The formulae for the transformation are given in Table 4.10. The transformation allows for a direct comparison of the reflectances without the differences in wavelength and spectral response between the TM bands and the MODIS bands. The resulting synthetic data is referred to as TMsimMOD_171.

Table 4.10: Formulae for predicting MODIS reflectances (R_i) from Landsat TM reflectances (r_i) (Liang et al., 2002)

$$R_1 = 0.0798r_2 + 0.9209r_3$$

$$R_2 = 0.1711r_1 - 0.2007r_2 + 1.0107r_4 + 0.0427r_5$$

$$R_3 = 1.0848r_1 - 0.1115r_2 + 0.0186r_3 + 0.0102r_4 - 0.0138r_5$$

$$R_4 = 1.1592r_2 - 0.1783r_3 + 0.0191r_4$$

$$R_5 = 0.5191r_1 - 0.7254r_2 + 0.7126r_4 + 0.5719r_5$$

$$R_6 = -0.0246r_4 + 1.1889r_5 - 0.1846r_7$$

$$R_7 = -0.1061r_1 + 0.1145r_2 - 0.0554r_4 + 0.0944r_5 + 0.9582r_7$$

In Figure 4.10, spectra of three surface types from the six datasets are plotted. The plots display average reflectances of 3x3 boxes of corresponding pixels in the different images. By averaging 9 pixels, differences resulting from remaining co registration errors as well as local deviations on single pixels are mitigated. Nevertheless the plots display a general trend in the relation of the reflectances of the six images and will be found for most individual pixels alike.

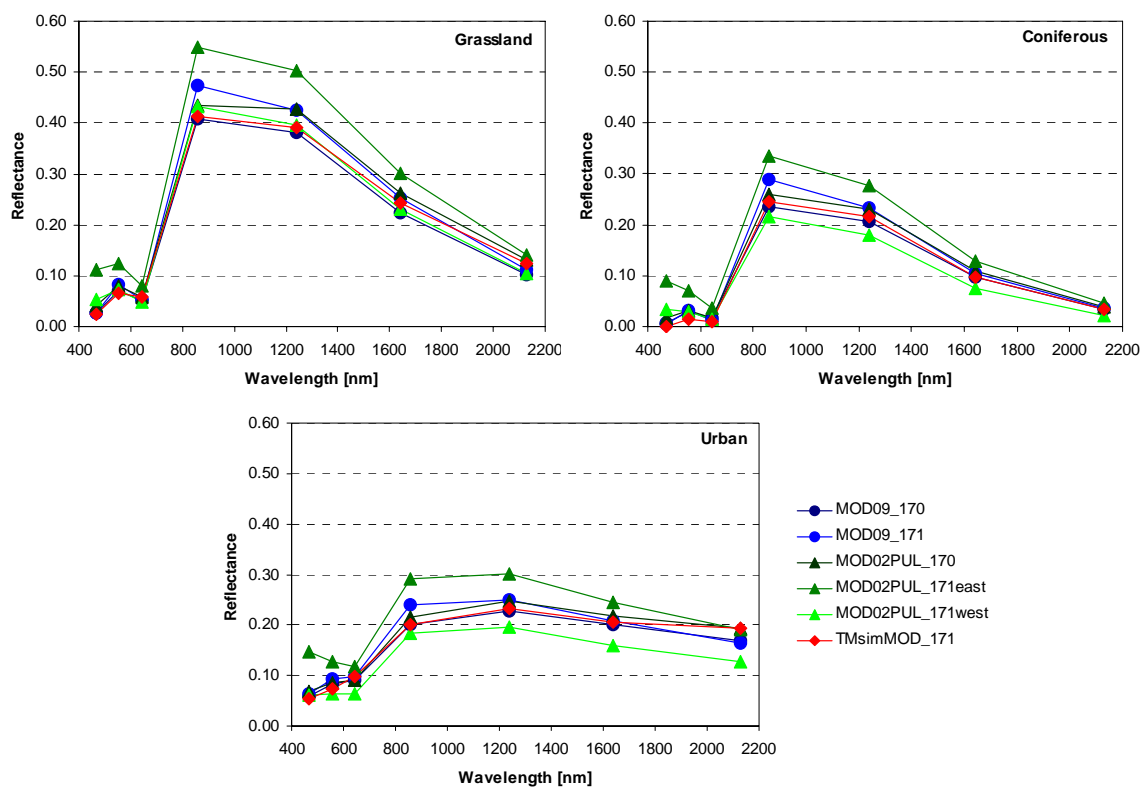


Figure 4.10: Spectra of surfaces in the six images compared in the validation of the reflectance calibration. The spectra are averaged from 3x3 boxes of homogeneous land cover.

First the images corrected with PULREF shall be discussed. Plots for MODIS are in green, plots for TM are in red. Most evident in the plots is the extreme overestimation of reflectances from the early image at 9:45 from DOY 171 (MOD02PUL_171east). Not only are the reflectances in the NIR and MIR bands higher than the rest of the images but also an unreasonable deviation in the VIS bands can be observed. On the other hand the later image from that day, MOD02PUL_171west, exhibits a lower spectral curve for the coniferous forest plot and the urban plot. In the grassland plot this image agrees well with the general trend of the other spectra. The curve of the MODIS spectra simulated from the TM image (TMsimMOD_171) has reflectance values between the two MODIS scenes from that same day. Comparing TMsimMOD_171 to the MODIS scene from one day earlier

(MOD02PUL_170) shows very good agreement in all bands and for all surfaces. In the figure the markers of TMsimMOD_171 mostly hide the markers of MOD02PUL_170.

Comparing the PULREF corrected scenes to the MOD09 imagery (plots in blue) shows poor agreement of the DOY 171 product (MOD09_171), which exhibits substantially higher reflectances in the NIR bands and higher values in the VIS bands. Nevertheless, this images spectra are more similar to the TMsimMOD_171 image than the PULREF corrected images of DOY 171. The DOY 171 product also deviates from the DOY 170 product (MOD09_170). The spectra from the earlier date DOY 170 show best agreement with the MODIS simulation from TM from the later date and also agree very well with the reflectances obtained from PULREF on DOY 170.

For a further comparison of the images, pixel values of individual bands of the scenes were plotted against each other and mean differences as well as the standard deviation of the difference were computed. A linear correlation indicates how close the image pairs are related. Comparing the images of DOY 171 it can be concluded that the MOD09 product is the most similar to the TM image. The coefficient of determination of the correlation for the 7 spectral bands is highest between those two images and the mean difference is lowest for most bands. The values calculated for the pairs MOD02PUL_171west-TMsimMOD_171, MOD02PUL_171east-TMsimMOD_171 and MOD09_171-TMsimMOD_171 are listed in Table 4.11. Generally correlation between those images is low and coefficients of determination range between 0.4 and 0.7 and standard deviation of differences may exceed 6%.

Table 4.11: Coefficient of determination, mean difference and standard deviation of mean difference for the seven bands comparing MODIS simulated from TM to MODIS reflectances of PULREF corrected imagery and MOD09 product on DOY 171

TMsim MOD_171 compared to	MOD09_171			MOD02PUL_171west			MOD02PUL_171east		
	Band	R ²	mean diff	std diff	R ²	mean diff	std diff	R ²	mean diff
3	0.7067	-0.0012	0.0168	0.7093	0.0231	0.0171	0.6752	0.0921	0.0191
4	0.6933	0.0102	0.0201	0.6698	0.0002	0.0211	0.6383	0.0535	0.0228
1	0.7140	-0.0067	0.0235	0.7216	-0.0139	0.0266	0.6953	0.0223	0.0249
2	0.6526	0.0477	0.0514	0.6268	-0.0238	0.0526	0.5299	0.0992	0.0644
5	0.6402	0.0226	0.0450	0.5785	-0.0365	0.0499	0.4403	0.0750	0.0616
6	0.5822	0.0041	0.0381	0.4856	-0.0325	0.0417	0.4370	0.0408	0.0472
7	0.5883	-0.0124	0.0321	0.5472	-0.0304	0.0353	0.5222	0.0076	0.0354

The same comparison was performed for the simulated MODIS bands and the imagery of DOY 170. Although the comparison here is for images that were collected with a time lag of about 24 hours, it shall be noted that the acquisition geometry of these image pairs are closer than the imagery acquired on the same date on DOY 171. Table 4.12 summarizes the comparison of the image pairs MOD02PUL_170-TMsimMOD_171 and MOD09_170-TMsimMOD_171. For these pairs coefficients of determination are above 0.7 and standard deviation of differences is well below 5% in all cases.

Table 4.12: Coefficient of determination, mean difference and standard deviation of mean difference for the seven bands comparing MODIS simulated from TM on DOY 171 to MODIS reflectances of PULREF corrected imagery and MOD09 product on DOY 170

TMsim MOD_171 compared to	MOD09_170			MOD02PUL_170			
	Band	R ²	mean diff	std diff	R ²	mean diff	std diff
	3	0.7806	-0.0003	0.0153	0.8324	0.0144	0.0133
	4	0.7941	0.0036	0.0169	0.8063	0.0094	0.0156
	1	0.8072	-0.0081	0.0194	0.8256	-0.0036	0.0182
	2	0.7799	-0.0083	0.0385	0.7188	0.0184	0.0436
	5	0.7463	-0.0119	0.0377	0.6454	0.0175	0.0453
	6	0.7213	-0.0111	0.0306	0.6337	0.0089	0.0353
	7	0.7457	-0.0156	0.0256	0.6631	-0.0011	0.0289

The results of the reflectance calibration indicate that the highest similarities between the Thematic Mapper image and the MODIS images is evident for the two MODIS scenes from a day earlier than the Thematic Mapper image. This may be astounding at first glance but can be explained by the geometric properties during acquisition. MODIS imagery of DOY 171 was collected under high scanning angles. This fact substantially deteriorates the quality of the image frame under observation for both images from that day that were corrected using PULREF. In the production of the MOD09 reflectance product both images from that date may be processed (Vermote and Vermeulen, 1999) but the overall quality cannot be meliorated. Nevertheless, the MOD09 product exhibits closer agreement with the “good” images than the individual correction of MOD02 by application of PULREF. The extreme scanning angle looking westward at 9:45 on DOY 171 and eastward at 11:25 implies strong bidirectional effects in the scanning process. Looking at the surface from about the direction of the sun at 9:25 results in very bright targets caused by a high proportion of directly reflected radiance and little visible shadow. This is reflected in the overestimation of reflectances for that image. On the other hand, at 11:25, the scanner is looking in the opposite direction, viewing a larger portion of shadow on the surface observed. A higher sun zenith angle closer to midday may be responsible for the better quality of the 11:25 image on DOY 171. The design of the PULREF algorithm does not account for these extremes in viewing geometry, which implies longer paths through the atmosphere. Also, bidirectional reflectance distribution is not parameterized. The MOD09 algorithm, designed for MODIS, does take into account the shape of the bidirectional reflectance distribution function (BRDF) and will parameterize path lengths through the atmosphere (Vermote and Vermeulen, 1999). This explains the better calibration of MOD09 for the imagery for high viewing angles.

When viewing conditions are better, i.e. the target objects are close to the nadir viewing direction, PULREF performs very well. The results of the atmospheric correction show that PULREF correctly calibrates the data from both, TM/ETM+ and MODIS. When comparing PULREF results with the reflectance product MOD09 the derived reflectances are highly correlated. This can be observed for all three images under comparable viewing conditions: TMsimMOD_171, MOD02PUL_170 and MOD09_170. Figure 4.11 shows the correlation between the PULREF corrected image MOD02PUL_170 and the MOD09 reflectance product, illustrating the profound similarities in the results from the two approaches to reflectance calibration.

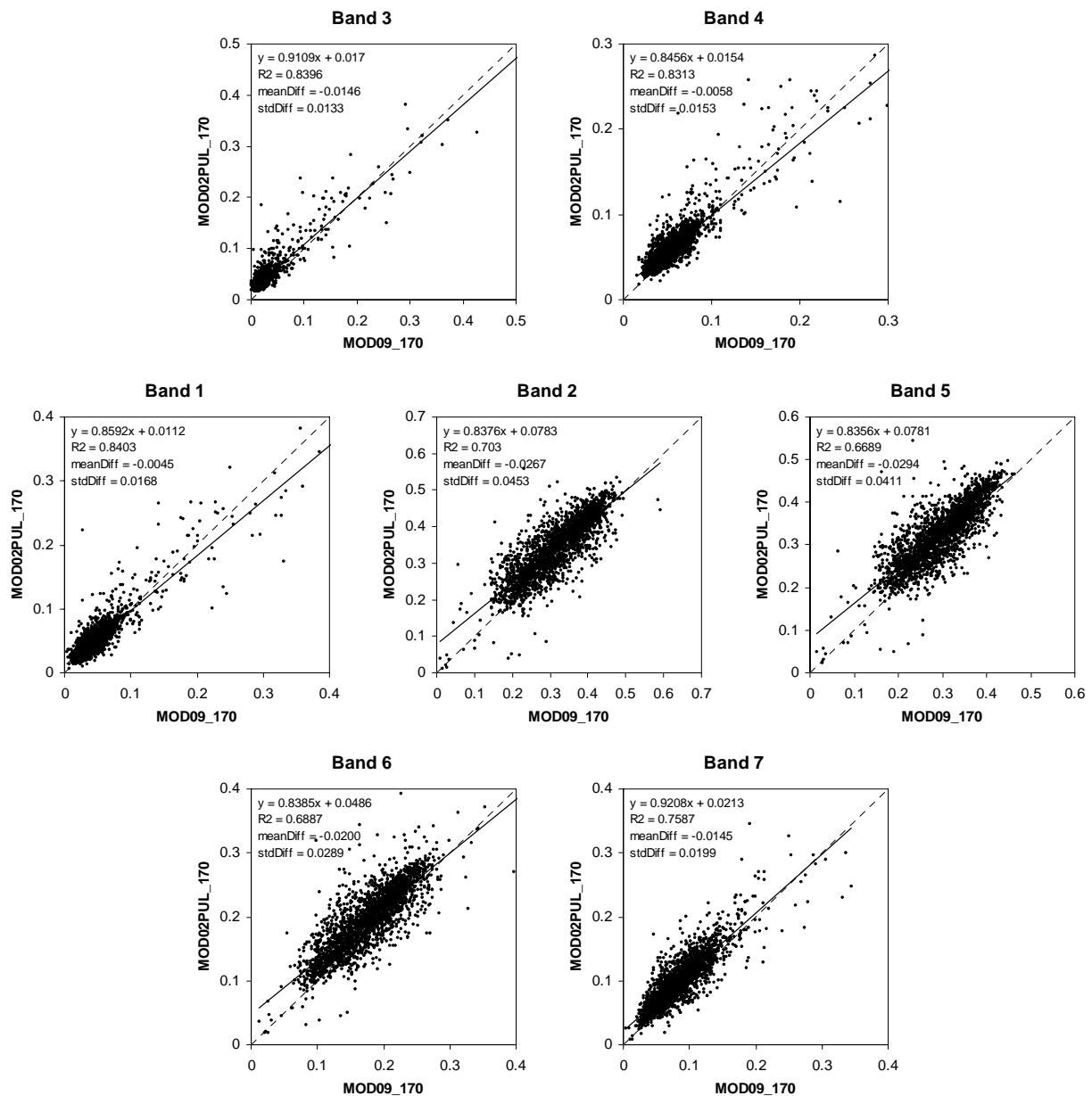


Figure 4.11: Correlations of MODIS reflectances for band 1-7 from PULREF corrected imagery versus the reflectances from the MOD09 reflectance product on DOY 170 year 2000

It may be concluded that viewing geometry has a substantial impact on image quality when data from wide swath remote sensing instrumentation like MODIS is sought. Imagery with a time lag may, as it is the case for the data used in this study, be closer related than coincident imagery exhibiting geometric discrepancies. This observation should be kept in mind whenever time series of wide swath instrumentation are applicable. Consecutive imagery acquired under varying geometric conditions may disturb the consistency of a time series profoundly. For the MODIS instruments, advantage may be taken from the AM and PM instruments and the sequences of appropriate viewing conditions, which can be elaborated from the orbit locations of MODIS within the 16-day orbital cycle. These can be found on the Internet for both the Terra and Aqua spacecraft (<http://www.ssec.wisc.edu/datacenter/terra/>).

4.5 Land Cover Classification derived from Landsat data

In the course of the GLOWA-Danube project, a vast effort was made to produce a high resolution, up to date land cover classification. Landsat imagery from the 8 scenes outlined in Figure 4.7 were processed in a fuzzy logic based classification scheme that ingests remote sensing data together with other GIS data (Stolz, 1998, Stolz, et al. 1999). Classifiers combining remote sensing data with ancillary geographic knowledge are very effective in the separation of land use classes in heterogeneous environments (Binaghi, 1997, Stuckens et al. 2000, Bach, et al. 2003, Sun et al., 2003). The extent of the area and the variety of geographic zones in the area required a new approach to land use classification. This approach includes a separate identification of settlement and urban areas using a multisensor data fusion method as well as a stratification of the data based on physiogeographically similar units. The applied Environmental Possibility Classifier (ENPOC) ingests a large set of ancillary GIS data along with a geographical knowledge base. It contains a highly diversified set of fuzzy descriptions to the desired final classes. The merits of the approach are the separability of a large number of land cover classes and a reasonably high classification accuracy (88%) in the classification of a highly heterogeneous area (Stolz et al., 2005).

The classification delivered a land use map indicating 27 classes (Stolz et al., 2005). For the application in this study these 27 classes were condensed to 13 classes including a class for unclassified pixels. This reduction was achieved by summarizing specialized differentiations to one class. For example, alpine pastures and meadows, lowland pastures and meadows and moorland were aggregated to a single grassland class. Other aggregations include the summarizing of different types of winter crops and other springtime active crops, mountain forest and lowland forests or different types of rocky surfaces. Some classes of the original classification with very low areal percentages, such as hops or potatoes were added to the maize class. In the context of this study this was justified by high spectral similarity of those classes. The section of the study area of the land cover map is shown in Figure 4.12. The 12 classes are listed in the legend to the figure.

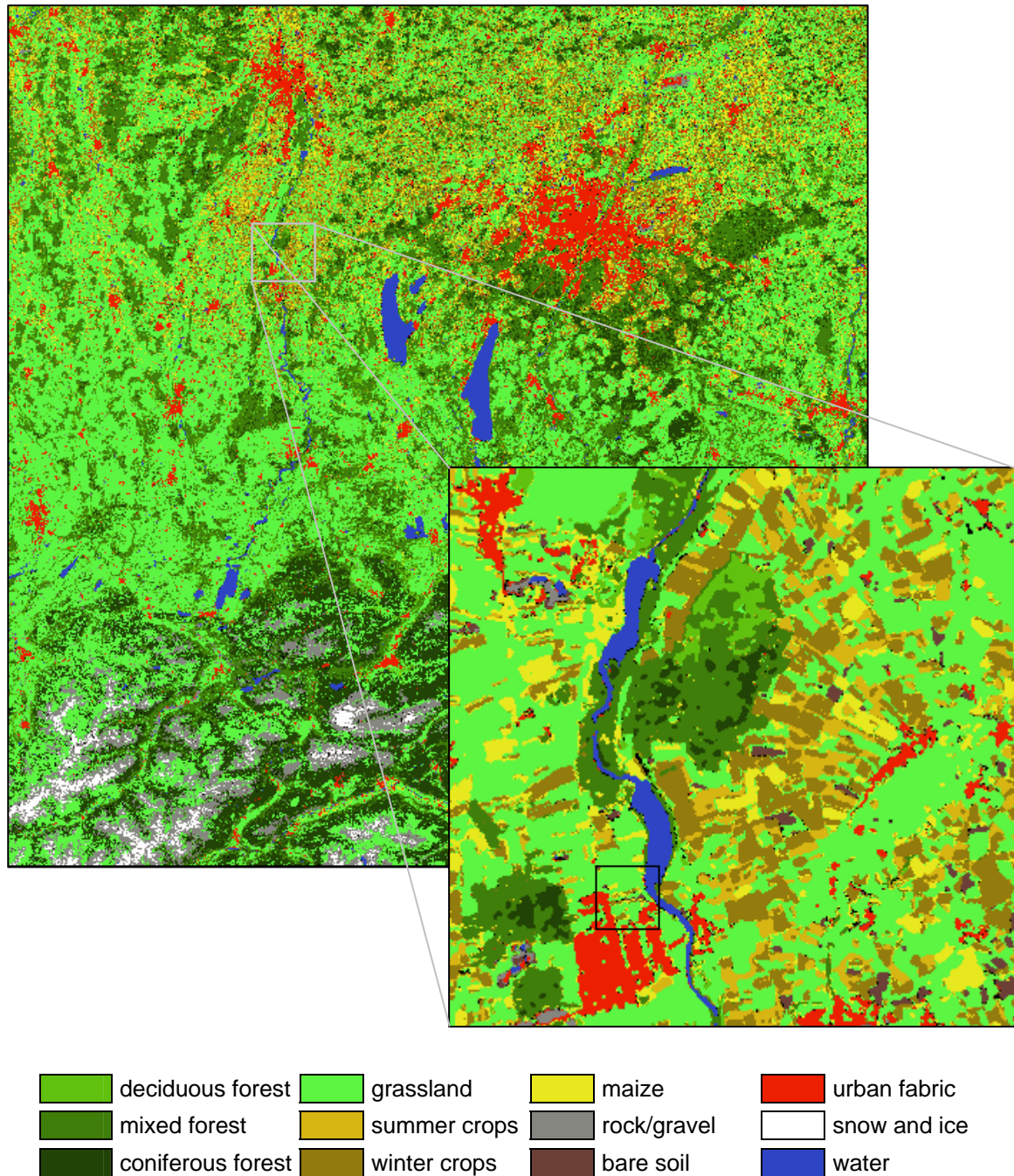


Figure 4.12: Classification of land covers for the study area and detail. Unclassified pixels are shown in black. The little black square in the detail indicates an area of 1km by 1km

The enhanced frame in Figure 4.12 shows the detail of the classification dataset, as it appears when all pixels are displayed. In this accuracy it reveals objects such as a watercourse with barrage water management facilities, the changes in tree types in a nearby forest, the spatial alignment of agriculture fields or the layout of settlements and their structures. The frame does contain errors such as the missing values (pixels in black), which accumulate along the river shore and appear singled throughout the image. At some narrow stretches the river is disrupted by forest or even settlement pixels. Although single settlement pixels derived from RS data often do indeed indicate built up structures of only one or two buildings, some pixels

along the river may fail to be attributable to the water energy management effort in the area. The small black frame on the detail frame indicates an area of 1km² to provide an idea of what section of this detail may be understood as aggregated to one single information in data gridded by 1km. It illustrates the change in land cover within a 1km pixel.

A drawback of the land cover classification is not visible in this dataset and remained undetected at first. It derives from the separate classification of physiologically differing units and will appear as a horizontal divide. For some classes frequency changes along this line, disclosing discrepancies in the results of a northern physiological unit and a southern. This issue was unknown until further processing of the dataset was undertaken. It is discussed more detailed in Chapter 8.

4.6 Datasets

A large amount of datasets were sought and acquired in this study. Many were dismissed in the course of this research, largely because newer collection versions of the data became available. The following sections provide a brief description of the datasets that were used and summarize the purpose and application of those datasets.

MODIS products filenames follow conventions to provide necessary information on each file. For data in swath geometry and in gridded SIN projection the conventions are summarized in Table 4.13.

Table 4.13: File naming conventions for MODIS products of production Level 1 and 2 (swath geometry) and production Level 2G, 3 and 4 (SIN projected grids)

Swath geometry example:

MODIS/Terra: MOD02HKM.AYYYYDDD.HHMM.VVV.YYYYDDDHMMSS.hdf

MODIS/Aqua: MYD02HKM.AYYYYDDD.HHMM.VVV.YYYYDDDHMMSS.hdf

SIN projected grids example:

MODIS/Terra: MOD15A2.AYYYYDDD.hHHvVV.VVV.YYYYDDDHMMSS.hdf

MODIS/Aqua: MYD15A2.AYYYYDDD.hHHvVV.VVV.YYYYDDDHMMSS.hdf

Definitions:

MOD02HKM = Earth Science Data Type Name

A = Acquisition Date

YYYYDDD = Data Year and Julian Date

HHMM = Data Hour and Minute Start Time

hHHvVV = horizontal and vertical tile index of SIN grid

VVV = Collection Version

YYYYDDDHMMSS = Processing Date and Time

hdf = Suffix denoting HDF file

4.6.1 MODIS Calibrated, Geolocated Radiances (MOD02)

The Level 1B data set contains calibrated and geolocated at-aperture radiances for 36 bands. It is generated from the raw dataset of MODIS Level 1A sensor counts (MOD01). The radiances are in W/(m² μm sr). The datasets provide additional information about the data, including quality flags, error estimates, and calibration data. Also, Geolocation latitude and longitude at 1km resolution are contained with the data. During daytime, visible, SWIR, and NIR measurements are made, while radiances for TIR are measured continuously.

Three different datasets are available, varying in spatial resolution. Band 1 and 2 at 250m resolution (MOD02QKM), Bands 1 through 7 at 500m (MOD02HKM) and all 36 Bands at

1km (MOD021KM). The 250m Bands will be contained aggregated to appear at 500m in the HKM product and 250m and 500m bands will be contained aggregated to appear at 1000m resolution in the 1km dataset. The size of MOD02 files is between 270 and 350 megabyte. Each granule contains 203 scans of the MODIS instrument. At 1km/500m/250m resolution, this is equivalent to 1354/2708/5416 measurements along scan (image columns) and 2030/4060/8120 measurements along track (image rows). Global coverage is provided for this product and 288 files are produced daily for the MOD021KM and 144 for MOD02QKM and MOD02HKM (Troller et al., 2003, Parkinson and Greenstone, 2000). The data are available at the Distributed Active Archive Center (DAAC) free of charge.

The data sought for this study are from collection version 004. At the time of this writing v005 was being produced. The times from which data was acquired are from year 2000 and 2003. For 2000, the data used dates from DOY 170 and 171 (June 18 and 19). For 2003 a time series of 19 cloud free scenes was elaborated, with most of them collected from orbits above or close to the upper Danube catchment. The MODIS Atmosphere Quicklook Archive (<http://modis-atmos.gsfc.nasa.gov/IMAGES/index.html>) was helpful in browsing MODIS imagery for cloud state and overpass geometry. All dates of the scenes used are listed in Table 4.14.

Table 4.14: Table of dates of year 2003 MODIS imagery time series.

DOY	Date	DOY	Date	DOY	Date	DOY	Date
91	04/01/2003	139	05/19/2003	215	08/03/2003	258	09/15/2003
98	04/08/2003	153	06/02/2003	219	08/07/2003	262	09/19/2003
105	04/15/2003	173	06/22/2003	225	08/13/2003	265	09/22/2003
107	04/17/2003	196	07/15/2003	235	08/23/2003	290	10/17/2003
125	05/05/2003	201	07/20/2003	247	09/04/2003		

The time series covers the vegetation period from April to mid October with approximate intervals of observations of 2 weeks. The average time between observations is 11 days. The images selected represent only the best observations available during that period.

The MOD02 data represent the most important dataset in this study. These data were used in (i) the first evaluation of the algorithm for reflectance segmentation and (ii) in the production of a time series of subscale leaf area index estimates over the vegetation period 2003.

4.6.2 MODIS Geolocation Data Set (MOD03)

The Level 1B MODIS Geolocation product contains geodetic coordinates, ground elevation, and solar and satellite zenith, and azimuth angle for each MODIS 1-km sample. These data are affiliate to the Level 1B calibrated radiances and the Level 2 data sets to enable further processing. The geolocation fields are derived from spacecraft attitude and orbit during acquisition, instrument telemetry, and a digital elevation model.

Although geolocation at the same resolution is contained in all MOD02 data, these datasets were needed in the processing of the MOD02 swath data. The MODIS Swath Reprojection Tool (MRT Swath) requires the MOD03 file associated with a MOD02 file to perform projection (Parkinson and Greenstone, 2000, Nishihama et al., 1997, Land Processes DAAC, 2006) Sensor and solar zenith and azimuth angles were retrieved from the data to gain insight into these properties for the simulation of reflectances as described in Section 6.2.2.

4.6.3 MODIS Surface Reflectance: Atmospheric Correction Algorithm Product (MOD09)

The MODIS Surface-Reflectance Product (MOD09) is calculated from the MODIS Level 1B land bands 1 through 7, centered at 648nm, 858nm, 470nm, 555nm, 1240nm, 1640nm, and 2130nm. The product is an estimate of the surface spectral reflectance for each of the seven bands as it would have been measured at ground level if there were no atmospheric scattering or absorption.

In the algorithm the effects of atmospheric gases, aerosols, and thin cirrus clouds are corrected. It is applied to all non-cloudy MOD35 (see 4.6.6) Level 1B pixels that pass the Level 1B quality control. To detect cirrus cloud, the correction uses band 26, water vapor is derived from MOD05 (Total Precipitable Water / Water Vapor), aerosol from MOD04 (Aerosol Product), and ozone from MOD07 (Atmospheric Profiles). If these products are unavailable, best available climate data are used. Finally, the correction uses MOD43 (BRDF) without topography, from the previous 16-day time period for the atmosphere-BRDF coupling term (Vermote and Vermeulen, 1999).

The surface reflectance product serves as input for the generation of a number of land products such as the vegetation indices product (MOD13), BRDF (MOD43), thermal anomaly (MOD14), snow and ice cover (MOD10), and Fraction of Photosynthetically Active Radiation/Leaf Area Index (FPAR/LAI; MOD15). It is applicable in fields such as global and regional climate modeling or surface energy balance modeling. MOD09 can be seen as the most essential of a series of products as it forms the root of the processing chain.

Surface Reflectance is produced for the global land surface. It is a Level 2G gridded product, produced as tiles in the Sinusoidal Projection (SIN). The MOD09GQK at 250m resolution provides band 1 and 2 reflectances, the MOD09GHK delivers bands 1-7 reflectances at 500m. File size varies and may be up to over 400MB (Parkinson and Greenstone, 2000).

For this study MOD09 data were applied in the validation of the localized atmospheric correction performed with PULREF on the Landsat dataset and on the MOD02 calibrated radiances. The results of the validation presented in section 4.4 showed that the root mean square deviation of the differing procedures was 1.5-4.5% depending on waveband.

4.6.4 MODIS Land Cover Type (MOD12)

The Level 3 MODIS Land Cover Type Product contains land cover type and land cover change parameters, which are produced at 1-km resolution. The product identifies 5 different land cover classifications, the most prominent being the 17 categories of land cover following the International Geosphere-Biosphere Programme (IGBP) global vegetation classification scheme (LC Type 1). The other dataset layers include the University of Maryland modification of the IGBP scheme (LC Type 2), the MODIS LAI/FPAR MOD15 scheme (LC Type 3), the MODIS Net Primary Production scheme (LC Type 4), and the Plant Functional Types (LC Type 5). The classification is based on a supervised decision tree classification method that draws from a number of information domains including directional surface reflectance, texture, land-water masks, vegetation index, snow cover, land surface temperature and elevation (Strahler et al., 1999).

The Land Cover Type 3, the MODIS LAI/FPAR scheme was relevant in the context of this study. It was used to analyze the MOD15 LAI Product to determine the land cover type of LAI pixels. The classes of that scheme are listed in Table 4.15

Table 4.15: Land Cover Type 3 from MOD12 Land Cover Types. This is the classification scheme used in the production of the MOD15 LAI/FPAR dataset (Strahler et al., 1999, HDF-EOS metadata)

Class	LAI/FPAR Type	Class	LAI/FPAR Type
0	water	5	broadleaf forest
1	grasses/cereal crops	6	needleleaf forest
2	shrubs	7	unvegetated
3	broadleaf crops	8	urban
4	savannah	254	unclassified

Although the descriptions of the dataset claim a new land cover classification every 96 days (Parkinson and Greenstone, 2000, MODIS Products related website), the availability of MOD12 Land Cover Types for the area of the upper Danube catchment is very limited on the DAAC database. Datasets for 2002 and 2003 were added in March 2006. Until then, only two MOD12Q1 datasets were available from Julian day 289 in 2000 (Collection Version 003) and from Julian day 1 in 2001 (Collection Version 004). In the production of the Collection Version 004 MOD15 product, the MODIS Leaf Area Index (LAI) and the Fraction of Photosynthetically Active Radiation (FPAR), the year 2000 Collection Version 003 product was used (Yang, W., Myneni, R. personal communication).

Generally, these data are available for the global extent of land area as Level 3 gridded data in the Sinusoidal Grid projection (SIN).

4.6.5 MODIS Leaf Area Index Product (MOD15)

The MOD15 product combines Leaf Area Index (LAI) and Fraction of Photosynthetically Active Radiation absorbed by vegetation (FPAR) in one file. The 1-km resolution Level 4 product is provided on an 8-day basis. LAI represents an important structural property of a plant canopy, namely the one-sided leaf area per unit ground area (see chapter 5). FPAR is defined as the proportion of available radiation in the photosynthetically active wavelengths (400 to 700 nm) that is absorbed by a canopy. The LAI product contains LAI values between 0 and 8 on the global gridded database. The FPAR product will be an FPAR value between 0.0 and 1.0 assigned to each 1-km cell (Parkinson and Greenstone, 2000). All valid pixels of an 8-day period from the MOD09 Surface Reflectance product of both MODIS instruments are ingested. Composition is based on the selection of the maximum FPAR in the compositing period. The same day chosen for the computation of the FPAR measure also contributes the pixels LAI value (Knyazikhin et al., 1999).

Besides MOD09 Surface Reflectance the Land Cover Type product (MOD12), and ancillary information on surface characteristics such as land cover type and background is vital in the LAI/FPAR algorithms. The LAI/FPAR algorithm uses a three-dimensional formulation of the radiative transfer to compute spectral and angular biome-specific signatures of vegetation canopies. If the main algorithm fails, a back-up algorithm is triggered to estimate LAI and FPAR using regressions to the Normalized Difference Vegetation Index (NDVI). The procedure for global LAI products is further detailed in section 5.4.2.

In this study MODIS LAI was sought to evaluate its performance in the area of the GLOWA catchment of the upper Danube and to compare it to the results from the subscale LAI research conducted here. The difficulties arising from the scale of 1km of the product are discussed. The datasets of the Level 4 gridded product that were acquired comprise all MOD15A2 and MYD15A2 files of the h18v04 tile that were produced until the end of 2004. All LAI data are from collection version 004.

4.6.6 MODIS Cloud Mask (MOD35)

The MODIS Cloud Mask product provides daily, global Level 2 information on cloud cover at 1km and 250m spatial resolutions. The algorithm is based on a series of visible and infrared threshold and consistency tests to determine confidence that an unobstructed view of the Earth's surface is possible. Also, an indication of shadows in the scene is provided. The 250m cloud-mask is provided as a 16-bit cloud non-cloud indicator for each 1km pixel.

The Product information is stored as bit flags not readily accessible by common HDF-EOS software. Bitflags need to be extracted. This can be achieved using the `unpack_sds_bits` tool available from the MODIS Land Data Operational Product Evaluation (LDOPE) software tools website.

MOD35 Cloud Mask was acquired and unpacked for all MOD09 scenes. It is used to mask out cloudy pixel in the MOD09 Surface Reflectance datasets.

4.6.7 Landsat Data

Landsat Thematic Mapper and Enhanced Thematic Mapper data were acquired as Level 1G data. They contain the at-aperture spectral radiances of 6 bands centered at 480nm, 570nm, 660nm, 830nm, 1670nm and 2210nm. The imagery is system corrected including the alignment of scans. Radiances are provided as $W/(m^2 \mu m sr)$. The thermal band contained in the dataset was not used.

Multitemporal scenes were used in the land cover classification for the upper Danube catchment that were sensed from three Landsat paths 192, 193 and 194. In the development of the reflectance segmentation algorithm for this study a frame from the imagery from the central path 193 covering row 26 and 27 was used. It was collected on June 19, 2000 by the Thematic Mapper on Landsat 5 (see chapter 2).

Together with the MODIS MOD02 radiance counts data this is the most important dataset in this study. The high-resolution data was used for deriving surface specific reflectance characteristics and in the validation of coarse scale results. Finally the high-resolution land cover was produced using the Landsat data.

5 Plant Leaves, Leaf Area and Leaf Area Index - LAI

This chapter gives an introduction to the quantity which has the focus in the research presented in this thesis and the underlying biophysical and biochemical processes. A thorough review of the various aspects and considerations concerning the concept of the highly alternating physiological variable “Leaf Area Index” is given. This review includes a definition of the leaf area index for this work, a discussion of measurement techniques as well as available measurements. The physiological and physical significance of leaves in a landscape is stressed and a summary of the role of LAI in physically based environmental modeling is presented. A section on the derivation of LAI from remote sensing data discusses methods and introduces algorithms used in the derivation of LAI values for this research. Finally, a view is cast on the validity, availability and feasibility of existing LAI datasets for incorporation into the decision support system DANUBIA.

5.1 Defining Leaf Area Index

As a theoretical concept, the Leaf Area Index (LAI) is the total area of all leaves over a unit of ground area and can be described as:

$$LAI = \frac{\text{leaf area}}{\text{ground area}} \quad (5.1)$$

where both *leaf area* and *ground area* are commonly taken as [m²]. This results in LAI having no explicit dimension while the dimension [m²/m²] is often used to emphasize the physical context of the index. This simple definition, however, leaves space for a number of variations and influences that may or may not be reflected in an actual given value of LAI. The following discusses possible biases whenever a value of LAI is considered.

First, LAI has been understood in two different ways: as the one-sided leaf area or the double (all-) sided leaf area. While the first is quite straightforward at glance it implies another conceptual variability when considering the different approaches of seeing one side as (i) the actual spread out area of leaves on a plane or (ii) the projection of live leaves on a plant. From the latter perspective the three-dimensional organization of leaves in a canopy becomes reflected in an LAI value, as most leaves would have an inclined position. This also means that the orientation of the axis along which projection is done will alter the resulting LAI

value. Finally, the non-leaf structure of the canopy – trunks, stems, branches, blossoms – will be most difficult to exclude as contributors to a projection of naturally organized leaves. Conceptualizing LAI as the double sided or total outside area will result in doubling of LAI when considering flat leaves in a simple model and will result in more than doubling LAI when considering needle-shaped and succulent leaves.

This leads to the second contextual influence on a LAI value, the question of what is being addressed by that value. What is actually meant when saying “LAI” may be the LAI of a single plant as well as a whole canopy, it may comprise but a single species as for example a specific crop while excluding potential undergrowth, weeds or the like. In natural ecosystems, most likely a variety of species in often more than one vegetation story will be intertwined in providing the area of leaves over an area of ground. This results in the necessity that a value of LAI should be attributable to (i) either plant or canopy and (ii) a single species or biome as a 3-dimensional space between the ground surface and the top of the canopy (TOC). Which of the mentioned LAI is actually used is often determined by the type of the study encountered. A study of a single plant may require that plants LAI while a global model may call for distributed LAI fields expanding across vegetation zones.

Often, the application of LAI is closely coupled with the functionality of leaves in landscape metabolism, including for instance fluxes of water and matter, generation of biomass or interception of radiation. This functionality is greatly determined by the lifecycle of leaves. From the growth of new leaves through senescence to fallen litter leaves change their physiological and physical properties. These changes may also be due to various types of stresses. This has often been accounted for by defining leaf area index as green or brown leaf area index. In many cases, however, depending on methodology of acquisition of LAI this differentiation is not made and LAI will be simply the area of all leaves on plants, regardless of their physical or phenological state.

Viewing the leaves of a canopy or plant as important parts involved in the phenological processes brings the factor of time into the discussion of variables influencing a LAI value. Therefore, another mandatory attribute to LAI values is the point in time it refers to. This point in time may be an absolute value depending on the age of the plant or canopy, thus describing for example the age and therefore size of a tree or a tree canopy. Nevertheless, in most cases it is more suitable to use the relative time of the year or phenological stage to account for the annual development of LAI. This could apply for trees as well as for annual and perennial plants, natural or agricultural the like.

Finally the location in space for which a given LAI value was determined is of great significance to its interpretation. The sensitivity of plants to environmental factors such as the radiation regime, nutrient availability or climatological impacts is directly reflected in the development of a canopy. Thus, environmental factors changing across space will have an impact on LAI. For instance, the same species of trees may exhibit different features and phenological development depending on the elevation at which it grows. The attribute “point in space” is especially desirable when LAI is considered in areas of great natural gradients.

Taking into account the different aspects that impact on any LAI value, a definition of LAI would require to mark these aspects in the definition:

$$LAI = \frac{\psi(def, P, T, S)}{ground\ area} \quad (5.2)$$

Where ψ is the functional leaf area depending on its definition *def* as one-sided, double-sided, brown or green leaf area, the species or biome of plants P , the point in time T and the point in space S .

This definition makes a precise differentiation of what exactly is addressed by an arbitrary LAI value. Nevertheless, LAI remains a continuum in the landscape. To any plot, area or region, a value of LAI can be ascribed, no matter what land cover, canopy, biome or species is present. This means that LAI will range from the highest possible values down to 0 where no vegetation is present.

The thorough consideration of the attributed influences on LAI make it necessary to take caution when making comparisons between LAI determinations, for they may not necessarily use the same methodology in acquisition and/or even the same definition of LAI. Regrettably many reports of LAI in the literature do not provide details of the definition assumed (Scurlock et al. 2001b).

The definition of LAI for the work presented here is based on the simple definition in its sense that for any section of land surface an area of leaves will be present. LAI is understood as the single-sided inclined projected LAI. Nevertheless the second definition plays a vital role in the effort of retrieving LAI from remote sensing data, which “sees” all surface of the earth and is available through time.

5.2 Leaf Area as an agent in the Environment

The area or amount of leaves present in a stretch of land surface or landscape is of paramount significance for a number of biological and physical processes and interactions taking place on the interface between the solid earth and the atmosphere. As stressed in the definition above, temporal and spatial variation in leaf area is one of the key factors that influences many of these processes and interactions. Nevertheless, on a global scale, leaf area will not vary significantly given abundance of nutrients and water, for instance between temperate deciduous forest and tropical evergreen forest (Winkler, 1980).

For most plants, leaves are the driving force of plant metabolism, responsible for photosynthetic carbon assimilation. This involves gas exchange at the leaves surface as well as fluxes of energy and matter and momentum between the surface and the planetary boundary layer. Thereby, leaves control the water and nutrient uptake of the plant from the underlying soil, leaves respire to turn over carbon dioxide and oxygen with the atmosphere and leaves absorb fractions of incoming radiation for photosynthesis (Peterson and Running, 1989, Knyazikhin, Martonchik, Myneni et al., 1998). This causes leaves to be the “power plant” of vegetation for the production of biomass. In this role, the biochemistry of canopy leaves has a significant impact on the radiation regime within the canopy itself and the albedo of the land surface in total, the carbon budget and water balance. Thus, leaf area influences not only the chemical composition of the atmosphere, but also the local and global climate as well as the water cycle.

The state of leaf area as a biophysiological quantity will attenuate air fluxes, and act as storage for precipitation water by interception. By shading the underlying ground, leaf area reduces evaporation from the surface, which again is critical in the hydrologic cycle. Finally, leaves themselves are a nutrient for all kinds of other living creatures and leaf area is highly correlated to biomass and crop yield.

Leaf area, expressed by leaf area index, has been established as the most common and most useful comparative measure of foliage quantity (Peterson and Running, 1989, Thomas and

Winner, 2000, Scurlock et al., 2001b). It is widely used in ecological models describing the energy and mass balance and transfer at the soil-vegetation-atmosphere interface (SVAT-Models). The estimation of LAI provides an indicator of growth potential and biomass production and has been used in stand management, yield prediction and precision farming (Demircan and Mauser 1996).

Depending on canopy closure, leaf area is the central agent in light interception and reflection of vegetated surfaces, making it a main link between remote sensing data and ecosystem functioning. In ecological and biochemical modeling, LAI can be used to include parameters such as leaf life span, litterfall rate, leaf carbon to nitrogen ration, and canopy nitrogen content (Lymburner et al., 2000).

5.3 Optical Properties of Vegetation

5.3.1 Leaf Optical Properties

Many studies have focused on the exploration of optical properties of absorption, reflection and transmittance of radiation on individual plant leaves (e.g. Woolley 1971, Gausman 1974, Gausman 1977, Wessman 1988, Verdebout et al. 1994, Govaerts 1996, Jacquemoud and Ustin 2001) and how these optical properties can be interpreted in terms of physical and chemical properties of the leaf (Curran 1989, Baret and Fourty, 1997, Fourty et al. 1996). For the context of this study, only a brief overview over the optical properties and characteristics of plant leaves shall be given.

Generally, the reaction of a plant leaf to incident radiation is a function of leaf structure, water content and concentration of biochemicals within the leaf. Reflection at the leaf surface results from a combination of specular and diffuse reflection at the leaves outer skin and in the cell walls of the spongy mesophyll within the leaf, respectively. Leaf morphology, cell size and amount of intercellular space (i.e. air-cell interfaces) are critical in the reflectance characteristics of plant leaves.

The amount of electromagnetic radiation absorbed by a leaf is due to two processes, electronic transitions and vibrations of polyatomic molecules. The first is vital in the foliar pigments chlorophyll a and b, carotenoids and brown pigments. The latter takes place in leaf compounds like water, cellulose, lignin, starch, pectins, waxes, tannins and nitrogens. A portion of radiation is able to transmit the leaf, exiting the leaf as diffuse radiation (Kneubühler, 2002).

In the following discussion, three regions of the reflective part of electromagnetic spectrum are addressed separately. Figure 5.1 presents a typical reflectance spectrum of live green vegetation that is divided up into 3 sections: The visible range (VIS), the near infrared range (NIR) and the middle infrared range (MIR).

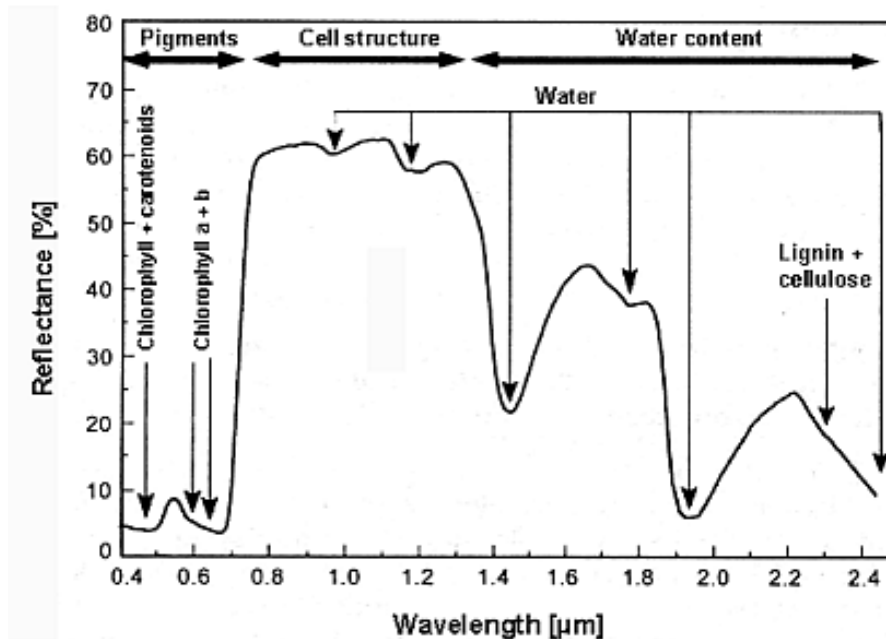


Figure 5.1: Parameters determining the reflectance properties of plant leaves (taken from Oppelt, 2002)

The visible range (400-700nm)

Foliar pigments dominate the strong absorption of radiation by plant leaves in the visible range of the solar spectrum with absorption maxima between 300-500nm. Mainly chlorophyll a and b sign responsible for the low reflectance and transmittance of in vivo vegetation in these wavelengths. Carotenoids with an approximately ten times lower concentration than chlorophylls exhibit overlapping absorption features, but these normally are masked by more pronounced features of chlorophyll a and b. Nevertheless, the carotenoids contribution will become visible during senescence, when chlorophylls degrade faster than carotenoids. At wavelength beyond about 670nm, absorption of chlorophylls rapidly decreases, causing a strong increase of reflectance in the region between 670-780nm known as the “red edge” of vegetation reflectance.

The near infrared range (700-1300nm)

In the NIR range beyond the red edge, green vegetation exhibits high reflectance and transmittance while absorption is low. This characteristic is connected to internal leaf structure, the size and distribution of cells and the cell-air interfaces within the mesophyll (Gates et al., 1965). Small water absorption features are present around 975nm and 1175nm, caused by agitation of water molecules and varying as a function of cellular arrangement and water content of the leaf. The interaction of high chlorophyll absorption in the visible range and high reflectance in the NIR range is a primary feature for the distinction of type as well as the state of vegetation (Gates et al. 1965, Horler et al. 1985, Oppelt 2002).

The middle infrared range (1300-2500nm)

In this range of the electromagnetic spectrum, water content is the critical parameter determining the spectral behavior of plant leaves. Other foliar biochemical components do affect the reflectance properties, but the main water absorption bands around 1450nm,

1940nm, and 2500nm form the shape of live leaf reflectance spectra of this wavelength region. In a dehydrating leaf, the reflectance and transmittance in the MIR region will increase and the spectral characteristics of foliar constituents like cellulose, lignin and starch appear. This makes this wavelength region sensitive to standing litter in vegetation canopies (Asner, 1998).

5.3.2 Canopy Optical Properties

Obviously, leaf optical properties established under laboratory conditions cannot readily be extrapolated to the spectral characteristics of a natural vegetation canopy. Compared to observing the radiation exiting a canopy, the mere measurement and description of single leaves omits the contributing elements such as stems or bark, branches, flowers, standing litter, understory vegetation, underlying soil or litter, but most importantly leaf orientation and spatial organization as well as shaded areas within the canopy or on the ground (Goel, 1989, Ross, 1981, van Leeuwen and Huete, 1996, Asner, 1998, Blackburn, 1998, Hurcom et al. 1996, Huete et al. 1985, Huete, 1988). Although leaves represent the main surface of plant canopies (Jacquemoud and Ustin, 2001) these other factors will contribute to any integrative measurement of canopy spectral properties from above the canopy. Additionally, incident radiation angles and view angles of instrumentation have an effect on the exiting radiation field observed over vegetation canopies. However, according to Jacquemoud and Ustin, 2001 the understanding of leaf and canopy bidirectional properties and their Bidirectional Reflectance Distribution Function (BRDF) is still in its infancy.

Directing the focus from leaf optical properties to the canopy level is a substantial step in scaling. In this step, not only observational scale is changed but also the process observed. The operational scale of canopy reflective behavior has to be distinguished from the leaf level scale. Quantification and analysis of the contributors to canopy reflectance is very demanding, yet clearly, it is a fundamental step in scaling from leaf to canopy, to regional and continental scales.

A combination of field measurements and radiative transfer modeling has been used by Asner, 1998 to establish a finer knowledge of causes of variability of canopy reflectance. Based on Kuusk, 1991, he proposes the following equation to fully describe the reflectance of a vegetation canopy. It accounts for structural parameters (leaf area index (LAI), nonphotosynthetic vegetation area index (NPVAI), leaf angle distribution (LAD), nonphotosynthetic vegetation angle distribution (NPVAD)), leaf and NPV hemispherical reflectance (ρ) and transmittance (τ), soil reflectance, sun and sensor geometry (θ_{sun} , φ_{sun} , θ_{view} , φ_{view}) and a hot spot parameter for leaf and NPV (H_{leaf} , H_{npv}):

$$R(\lambda) = f(\text{GEOMETRY, STRUCTURE, TISSUES}, \rho_{\text{soil}}(\lambda)) \quad (5.3)$$

where

$$\text{GEOMETRY} = (\theta_{\text{sun}}, \varphi_{\text{sun}}, \theta_{\text{view}}),$$

$$\text{STRUCTURE} = (\text{LAI}, \text{NPVAI}, \text{LAD}, \text{NPVAD}), \varphi_{\text{view}}, H_{\text{leaf}}, H_{\text{npv}},$$

$$\text{TISSUES} = (\rho_{\text{leaf}}(\lambda), \tau_{\text{leaf}}(\lambda), \rho_{\text{npv}}(\lambda), \tau_{\text{npv}}(\lambda)).$$

Several studies have shown, that the structural parameter LAI in combination with LAD is the main control on the reflectance of a canopy, dominating over actual leaf optical properties (Asner, 1998, Jacquemoud and Ustin, 2001, Kneubühler, 2002). This is true for high LAI canopies but cannot hold when the variability of LAI through phenological stages is considered. Seedlings of a cornfield, for example contribute to a neglectable part to the reflectance of the previously ploughed field, which therefore will predominantly exhibit soil spectral properties with a neglectable contribution of plant or leaf area reflectance. As the crop matures (or a deciduous forest grows fresh leaves in spring), the expanding leaf area establishes the complex radiation regime of a canopy which results from refraction, transmittance, absorption and reflectance of incoming radiation within the canopy.

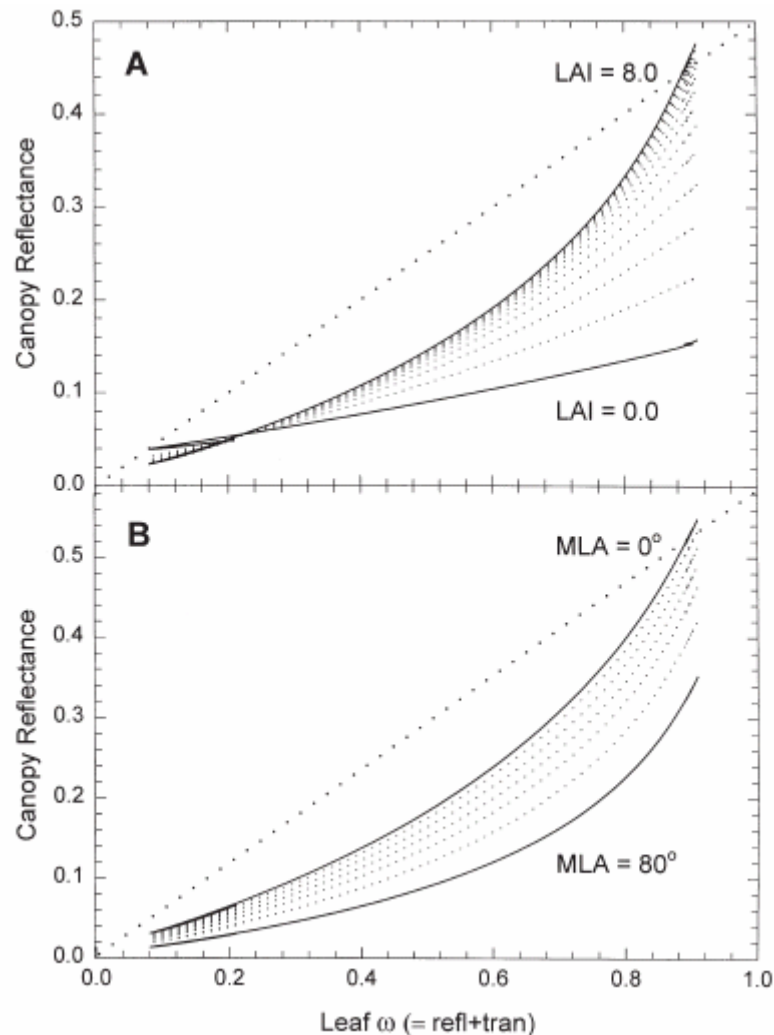


Figure 5.2: Relationship between leaf single scattering albedo (ω =reflectance+transmittance) and canopy reflectance with A) changing LAI and B) changing mean leaf angle of an ellipsoidal distribution. The best translation of leaf optical properties to the canopy level occurred when $\omega > 0.9$ which corresponds to NIR reflectance (taken from Asner, 1998)

Single leaf optical properties translation to canopy optical properties largely depends on the structure of the foliage, i. e. LAI and LAD. As Figure 5.2 A illustrates, high values of LAI translate the most leaf level information to the canopy while with low LAI other factors dominate canopy reflectance. Figure B shows how in a canopy with mainly horizontally

oriented leaves, leaf-level optical information is more directly resolved at canopy scales (Asner, 1998).

When addressing canopy optical properties from a remote sensing perspective it can be stated that (i) strong relationships can be established between LAI and canopy reflectance, especially in the NIR region (ii) viewing geometry is critical in these relationships and (iii) fractional vegetation cover (background influence) plays an important role in canopy reflectance. Thus, extraction of LAI from reflectance information appears to be a much simpler task than the extraction of other canopy biophysical or biochemical attributes, but at the same time this is heavily dependent on foliage amount.

The influence of structural and biochemical factors on canopy reflectance is wavelength dependent. When focusing on the three wavelength regions discriminated above for the address of leaf optical properties, different reaction to changes in leaf area can be observed for canopy optical properties. In the visible wavelength region, variation of LAI has only a small effect on canopy exitant radiation. Highest sensitivity within a narrow dynamic range is reported with LAI between 0.5-1.0 and must be attributed to canopy closure. An almost exponential decrease is observed, reaching saturation at around LAI 2-3 (Goel, 1989). Standing litter in the canopy will have a strong effect on VIS reflectance (Asner, 1998).

The near infrared wavelength region generally exhibits the highest sensitivity to LAI, with an again almost exponential positive relationship of reflectance with LAI. Due to the high transmissivity of the scatterers (leaves) in this spectral domain, photons penetrate deep into the canopy and strongest multiple scattering occurs. Thus, near infrared canopy reflectance is sensitive to changes in LAI in the vertical of the entire canopy (Demircan, 1995). Sensitivity decreases with increasing LAI and saturation is reached at LAI between 6 and 8 (Peterson and Running, 1989). With high LAI, leaf optical properties and leaf biochemistry are very directly expressed at canopy scale and as photons interact with multiple layers of the canopy, higher water content of capacious leaf area is reflected in more pronounced water absorption features (Asner, 1998, Goel, 1989). The effect of standing litter and woody stem material in the NIR is reported to be low but dependent on total leaf area.

The middle infrared region is only moderately sensitive to LAI. Here, the strong influence of water absorption in green foliage dominates the reflectance characteristics. Hence, standing litter with low water content causes higher variations than in the VIS and NIR but sensitivity to woody stem material is low (Asner, 1998)

Leaf angle distribution (LAD) is an important factor in canopy reflectance. High angles will allow more photons to travel uncollided into the canopy, giving space for other than leaf material to contribute to the reflectance signal. Generally, a canopy with mostly horizontally inclined leaves will exhibit less variability in reflectance than a canopy of erectophile plants. Any measurement of live canopy reflectance may additionally be affected by the presence of stochastic elements such as wind and dew (Goel, 1989) and clumping and gaps in the canopy drive spatial variance of above canopy reflectance. Along with LAD, the bidirectional behavior of vegetation canopies has been observed to be driven mainly by the first layer of scatterers at the top of the canopy (Myneni et al., 1989). Finally, the structural factors such as foliar density and orientation of a canopy strongly depend on the ecosystem or biome under consideration.

Most of the knowledge in this field has been derived from studies with hyperspectral remote sensing instrumentation and high-resolution models. An issue rarely addressed in this context is the actual placement of materials in the canopy (van Leeuwen and Huete, 1996, Asner, 1998) The information derived from broadband remote sensing from space as applied in this study will not provide the detail both in spectral and spatial resolution.

5.4 Measuring Leaf Area and Leaf Area Index

Measuring leaf area or leaf area index can be achieved in several ways. The approaches may be divided in ground based measurements and estimates from remote sensing. Some general concepts of measuring leaf area are provided in this section for both approaches. A fundamental difference between the two, however, is their scale. Ground based estimates are rudimentary in regard of observational as well as measurement scale when compared to remote sensing estimates. When derived from spaceborne sensor devices, spatial continuity and extent is undisputed and favorable in regard of environmental research needs.

5.4.1 Ground based estimates

A number of methodologies have been introduced for the ground-based estimation of LAI. Scurlock et al. (2001b) summarize the following approaches for determining LAI:

- (i) destructive harvesting and direct determination of one-sided leaf area, using squared grid paper, weighing of paper replicates, or an optically based automatic area measurement system;
- (ii) collection and weighing of total leaf litterfall, converted to leaf area by determining specific leaf area (leaf area/leaf mass) for sub-samples;
- (iii) allometry (based on simple physical dimensions, such as stem diameter at breast height), using species-specific or stand specific relationships based on detailed destructive measurement of a subsample of leaves, branches, or whole individuals;
- (iv) indirect contact methods, such as plumb lines and inclined point quadrats;
- (v) indirect noncontact methods, such as the Decagon Ceptometer (Decagon Devices, Inc., Pullman, Washington), the LICOR LAI-2000 (Li-Cor, Inc., Lincoln, Nebraska), and analysis of hemispheric photographs.

Any methodology applied will be closely coupled to the way the resulting LAI is defined. While methods (i) and (ii) will commonly result in one-sided LAI, method (iv) and (v) will give horizontally projected and inclined projected LAI values, respectively. Allometric determination of LAI may provide single or double-sided LAI depending on the calibration of allometric equations. The individual methods may be calibrated to obtain measurements of individual plants or canopies.

Usually, the choice of methodology is a matter of applicability and cost involved. Direct measurements tend to require great effort and manpower. Especially destructive methods will often conflict with economic interests of owners of cultivated land and allometric methods are difficult to apply on crops and pastures. The most convenient method to obtain ground measurements of LAI for this study was to apply the LICOR LAI-2000 instrument for measuring different types of crops and forests. The measuring campaign undertaken and the obtained LAI estimates are described in section 5.6.1. Generally, measurements taken in the field will have an error attributed to the obtained LAI values. This error has been reported to amount to an order of 10% (Asner, 1998).

5.4.2 Remote Sensing based estimates

Measurements of LAI in the field yield estimates at very localized scale and for rather discrete plots. The cost and effort involved constrain the extent to which LAI can be assessed by the addressed methods. The close relationship of leaf area and spectral properties of a surface have early led to the advent of attempts to use remote sensing for the retrieval of LAI estimates. The spatial continuity of remote sensing data provide the only feasible way for obtaining continuous fields of LAI values (Verstraete et al. 1996)

Three approaches can be identified for deriving LAI from remote sensing imagery. First, there is a strong correlation between transforms of reflectances called vegetation indices (VI) and vegetation leaf area (Myneni et al. 1995). From empirical studies, relationships have been derived for a variety of vegetation cover types and for different vegetation indices (e.g. Spanner, 1990, Demircan, 1995, Gregoire and Raffy, 1997). These relationships have been used for the successful retrieval and investigation of LAI (Baret and Guyot, 1991, Carlson and Ripley, 1997, Chen and Cihlar, 1996, Turner et al., 1999, Bach et al., 2003, Schneider, 2003). Among other vegetation indices, application of the normalized difference vegetation index (NDVI) has been a very prominent approach to correlating vegetation index to LAI. NDVI can easily be calculated from the RED and NIR bands of many remote sensing sensors:

$$NDVI = \frac{\rho_{NIR} - \rho_{RED}}{\rho_{NIR} + \rho_{RED}} \quad (5.4)$$

The performance of NDVI in correlating it to LAI has shown to provide better estimates than the application of simple ratio VI. Non-linear relationships provide more accurate models than linear regressions (Gross, 1989). Other indices have been developed and used such as the soil adjusted vegetation index (SAVI) (Huete 1988), the transformed soil adjusted vegetation index (TSAVI) (Baret et al. 1989, Baret and Guyot, 1990), the weighted difference vegetation index (WDVI) (Clevers, 1989, Kneubühler 2002) or the modified normalized difference vegetation index (MNDVI) (Liu and Huete 1995, van Leeuwen and Huete 1996). These VIs were designed to account for the background and atmospheric influences contaminating simpler indices. Removing atmospheric bias from NDVI has been achieved by using atmospherically corrected input to obtain absolute reflectance NDVI (arNDVI) (Bach 1995, Demircan 1995, Spanner et al. 1990, Carlson and Ripley 1997, Schneider 2003). Along with arNDVI, the more recently developed enhanced vegetation index (EVI) is operationally available from the MODIS Vegetation Indices Product MOD13 (Huete et al. 1999). A comparative study of NDVI and EVI was conducted by Huete et al. (2002).

Empirical regressions between LAI and NDVI tend to represent local particularities of vegetation and have been developed from numerous field experiments for various vegetation covers. Some collected NDVI-LAI equations for different cover types can be found in Schneider (2003) or Wang et al. (2004). A set of such equations was used in this study and is presented in section 6.2.4.

In order to establish a physical basis for deriving LAI from remote sensing, the theoretical background of the large body of empirical relations of vegetation indices and biophysical parameters such as LAI has been formulated. The relations can be used to decode the information of reflectance spectra of vegetation. Myneni et al. (1995) showed that VIs can be generalized to show a derivative of spectral reflectances, which is a function of leaves and soil background. This derivative is an indicator of abundance and activity of the absorbers in the

canopy. The theory was used to derive cover type specific NDVI-LAI relations in a subsequent study (Myneni et al. 1997). For the application of the theory, global land cover was classified into six structural cover types, or biomes. For each biome, 3D radiative transfer is modeled to simulate scattering and absorption in the canopy and the results are used to derive NDVI-LAI relationships for each biome (Myneni et al. 1997).

A third alternative for LAI retrieval from remote sensing data is the inversion of radiative transfer models (Knyazikhin, Martonchik, Myneni et al. 1998). However, the remotely sensed spectral signatures will not suffice to solve the inversion problem. For example, different three-dimensional canopy structure essentially influences the exitant radiation while LAI may remain unchanged. In order to simplify the problem, a vegetation cover classification is used that is parameterized by variables relevant in photon transport theory (Myneni et al. 1997). This classification distinguishes biome types that may be represented by individual tree architecture (leaf orientation, stem-trunk-branch area fractions, leaf size, crown size) and canopy topography, soil and/or understory background. Further characteristics of the biomes are patterns of spectral reflectance and transmittance of vegetation elements and the distribution of leaves in the canopy. The six biomes are grasses/cereal crops, shrubs, broadleaf crops, savannas, broadleaf forest and needleleaf forest (Myneni et al. 1997, Knyazikhin, Martonchik, Myneni et al. 1998)

These attributes are used to parameterize the radiative transfer model. Solutions of the three-dimensional radiative transfer equation are used to model bi-directional reflectance factors (BRF) of each biome for varying sun-view geometry and canopy/soil patterns. Thereby, the biome is characterized by the basic components of the energy conservation law, canopy transmittance, reflectance and absorptance. The results are stored in a look up table (Knyazikhin, Martonchik, Myneni et al. 1998). The retrieval algorithm interacts with this lookup table only and compares observed and modeled BRFs for a suite of canopy structures and soil realizations. All possible results not exceeding uncertainties are used in averaging to obtain final LAI (Knyazikhin, Martonchik, Myneni et al. 1998, Knyazikhin, Martonchik, Diner et al. 1998). The approach of producing a lookup table is used with the advantage of keeping the LAI retrieval algorithm independent from the radiative transfer code applied for the physical modeling of reflectances.

The last approach described is implemented in the operational production of the MOD15 LAI Product. In the processing the NDVI-LAI relations derived from the spectral derivative (Myneni et al. 1997) are used as a backup algorithm. Data from the MOD12 Land cover product and the MOD09 Reflectance Product are ingested in the processing (Knyazikhin, Glassy et al. 1999). The product and the algorithm have been prototyped (Tian, Zhang et al. 2000, Zhang et al. 2000) and validated (Tian et al. 2002a/b, Privette et al. 2002, Cohen et al. 2003, Wang et al. 2004) as well as investigated as a scale invariant approach to LAI retrieval (Tian, et al. 2002).

All approaches have an important feature in common: reliable retrieval of LAI from remote sensing is directly coupled to a land cover classification. The variation in model descriptions to derive estimates of LAI is tied to the cover type producing the leaf area. Thus, the cover type as a representative of canopy structure is most decisive in LAI retrieval from remote sensing data.

5.5 Leaf Area in Environmental Modeling

The modeling of environmental phenomena involves the leaf area in various ways as indicated by the interaction of leaves with their environment (see section 5.2). The importance

of the incorporation of leaf area state variable into environmental models is based on its prominent influence on the interaction of leaves with solar radiation and their responsibility for carbon absorption and exchange with the atmosphere. Two general directions may be distinguished in which leaf area is prevalent in models: as an active quantity influencing the described process being modeled or as a target quantity of the model.

As an active quantity in a model LAI is vital in canopy radiative transfer models, in hydrologic models at the soil-vegetation-atmosphere interface (SVAT-Models) and in modeling biomass productivity models or crop models. A radiative transfer model for vegetated canopy uses leaf area as the driving dynamic variable to describe radiative processes of transmission, absorption and reflection in the canopy. In hydrologic models the leaf area determines the surface for evaporation, transpiration and interception. When modeling plant productivity a positive feedback on leaf area exists so that leaf area will be both a parameter going into the model as well as an output variable changed by the modeling process. Thus, plant productivity models may provide leaf area estimates as the model progresses over time.

Except for the direct and destructive methods for ground measurement of leaf area, some model is always involved to derive LAI as a target quantity. Allometric equations model LAI from stem diameter and optical measuring devices such as the Licor LAI-2000 compute leaf area from detected canopy gap fraction (see Section 5.6.1). As in remote sensing, this non-contact method requires a model to describe the correlation between the measured quantity and leaf area. The most sophisticated way of inferring leaf area from a related measure is by the inversion the radiative transfer process. One such method has been addressed in the previous section as the procedure implemented for the operational production of the MOD15 LAI Product from MODIS imagery.

Each category of models involving LAI knows many implementations of which some prominent examples are used here. A model used extensively in the remote sensing community to determine reflectance spectra of reflectance and transmittance of single leaves is the PROSPECT model (Jacquemoud and Baret, 1990). It samples spectra at a spectral range from 400 to 2400nm at 1nm intervals from chlorophyll concentration, water content, dry matter and structural parameters. The plate model takes the leaf as several absorbing plates with rough surfaces giving rise to scattering of light. Since 1990 it has experienced widespread use and additional improvements in the representation of leaf biochemistry (Jacquemoud and Ustin, 2001).

The PROSPECT model has repeatedly been coupled to the SAIL model (Verhoef, 1984) to describe the scattering of arbitrarily inclined leaves. SAIL is a four stream turbid medium radiative transfer model that estimates spectral bidirectional reflectance from a canopy. The model appeals due to its simplicity of a two-layer abstraction of the canopy and limited number of input variables and compromises between computational cost and realism of the simulation. LAI and LAD along with a hot-spot parameter go into the model as canopy structural input. Together with leaf and soil reflectance properties, sun position and viewing geometry, the radiation regime is determined. In coupling the two models, leaf hemispherical reflectance and transmittance may be taken from PROSPECT to be ingested by SAIL. Such a combination of the two models has been approached in various studies to predict BRDF of canopies (Weiss and Baret, 1999) and to produce look up tables (LUT) for inverse parameter retrieval (Combal et al., 2001, Atzberger, 2004, Fang and Liang, 2005). Recently, the models have been used to simulate hyperspectral images to prototype future remote sensing sensors (Verhoef and Bach, 2003).

A further step of sophistication in modeling with LAI involved is the integration of a radiative transfer model with a land surface process model as proposed by Bach, Verhoef et al. (2000).

The Process-oriented Modular Environment and Vegetation model PROMET-V (Mauser and Schädlich, 1998, Schneider, 2003) is run to calculate plant growth, water, and nitrogen fluxes using meteorological and environmental data. PROMET-V generates LAI, fraction of brown leaves and surface soil moisture to be ingested by GeoSAIL, an extended version of the SAIL model (Bach, Verhoef et al. 2000). By minimizing the difference between actual remote sensing data and the reflectances modeled by GeoSAIL, biophysical parameters retrieved from Thematic Mapper imagery could be improved.

In an advanced combination of the PROMET-V surface process model and GeoSAIL, the canopy reflectance model is used in forward mode to simulate satellite data and in an inverse mode to retrieve bio-geophysical parameters from different remote sensing sensors (Bach et al., 2001). The two models are coupled by two feedback-loops that enable the derivation of LAI, fraction of brown leaves and surface soil moisture from optical satellite imagery and allow the adjustment of the land surface model to improve simulation of biomass, canopy height and yield (Bach and Mauser, 2003).

In the GLOWA-Danube model compound DANUBIA, LAI is a decisive quantity in a number of contributing models. Leaf area is produced by the Biological component as plant growth progresses. The Biological model ingests input of meteorological, soil and management parameters and computes LAI, leaf biomass, transpiration, fraction of brown leaves, leaf transmissivity and leaf temperatures. The model abstracts the canopy into canopy layers, each having its own value for LAI. These layers are provided to other components as canopy layer stacks containing the canopy layers distinguished in the model (Lenz et al., 2006). The receiving components are the one modeling the radiation regime in the canopy called RadiationBalance, and the Surface component. In the former all layers LAI is accumulated to a total LAI, which is then used to compute shaded area, absorbed radiation and attenuation of wind speed (Niemeyer, 2002a). In the surface model, LAI is the quantity involved in a term to compute interception. The amount of precipitation reaching the soil is reduced by the present leaf area (Niemeyer, 2002b).

In this study models involving LAI are used in three ways. To produce LAI estimates from remote sensing data regression models of LAI with NDVI are applied. A host of land cover type specific LAI-NDIV relations is used to model LAI from the satellite imagery introduced in chapter 4. The functions listed in section 6.2.4 are used in retrieving LAI from both, regular VIS/NIR satellite imagery and from segmented VIS/NIR reflectances from the unmixing process presented in this work. The advantages of advanced process modeling, namely control of input and temporal continuity, are sought in both ways described: producing LAI estimates and driving the model with LAI. To support a database of temporal change of LAI, results from the land surface model PROMET-V were used. They provide annual progression of LAI for a number of cover types (see section 5.6.2). A version of GeoSAIL was run to estimate valid ranges of reflectance values from ranges of LAI (see section 6.2.2).

5.6 LAI Data

Examination of the temporal dynamics of LAI is a key issue in this work. Prior knowledge on the development of cover type specific LAI was sought by elaboration of a database of multitemporal LAI estimates. It provides an impression of different cover types temporal behavior and substantiates the theory for the algorithm developed in chapter 6. This section presents the various sources of LAI data.

5.6.1 LAI Measurements using Li-Cor LAI-2000

Measurement campaigns to assess LAI of sites located in the study area were conducted during the vegetation periods of 2002, 2003 and 2004. Different types of crops and forest were addressed in the measurements of weekly to two-weekly intervals. The instrument used for the measurements was the Licor LAI-2000 plant canopy analyzer (Li-Cor, Inc., 1992).

Measuring with the LAI-2000 Instrument

The LAI-2000 plant canopy analyzer consists of a LAI-2070 control unit that collects and computes the measured data and the LAI-2050 sensor head. The instrument's sensor incorporates a fisheye optic with a 148° field of view that projects its almost hemispheric image onto five silicon detectors arranged in concentric rings. A filter restricts the sensed radiation to wavelengths below 490nm to minimize the amount of transmitted and reflected radiation (Li-Cor, Inc., 1992).

A single measurement consists of at least two readings directed skyward, one above and one below the canopy. The canopy volume captured by the instrument resembles an inverted cone or a segment of it if the lens is covered with a viewcap to exclude part of the field of view. Each sensor ring's samplings are taken as equivalent to the canopy's gap fraction. From the ratio of the received radiation of the two measurements foliage amount (LAI) and mean foliage tilt angle (MTA) are computed. Four assumptions for the calculations to be correct must be met, (i) only sky radiation reaches the sensor (ii) foliage is randomly positioned in the canopy (iii) foliage elements are small and (iv) foliage inclination is not important but the leaves are facing in azimuthally randomly oriented directions (Welles and Norman, 1991).

In practice, these assumptions require some aspects to be considered when taking measurements. To ensure only sky radiance entering the sensor, measurements were taken preferably under overcast weather conditions. Rejecting direct irradiance can also be achieved by shading the sensor and the canopy with a large cardboard. This, however works for low canopies only, not simply because tall canopy may not be reached to shade it, but also because the radius sensed by LAI-2000 is approximated by three times the canopy height (Li-Cor, Inc, 1992, Welles and Norman, 1991). Evening hours until 15 minutes after sunset have been found to be a good time for measurements due to radiation conditions (Holzhauser, 2002). At this time, shading of larger areas is also simplified by high solar zenith angles. Measurements were always directed away from the sun.

Random distribution is given for row crops and forest (Li-Cor, Inc, 1992) and is ensured by selecting plots for measurements well within the agricultural fields. Forest sites were selected to exhibit homogeneous cover and understory vegetation. In order to keep foliar elements small, the sensor is kept at least four times the leaf width apart from the nearest leaf over it. Assumption four is met by making multiple measurements below the canopy. For each plot four below canopy measurements were made, each moved slightly as compared to the previous. This ensures a wide range of measuring directions keeping the random orientation assumption in effect. A scheme of placing multiple below canopy measurements in a row diagonal to the planting direction is suggested for row crops (Li-Cor, Inc, 1992). In the campaign, 180° viewcaps were used to exclude the operator and the direction of the sun from the view. This leaves the view wide enough for a large portion of the canopy to be sampled so that many leaf orientations are included.

Two Li-Cor LAI-2000 devices were available for the measurements. They were used in one sensor mode for all crop types, using single instruments to take above canopy and below canopy readings. For sampling forest two sensor mode was used. In this mode one sensor is mounted on a tripod positioned on open field to sample the sky radiation every few seconds.

These measurements deliver the above canopy estimates. The other sensor is taken to the forest to take below canopy readings. The samplings from the two sensors can be synchronized using the PC software distributed with the instrument.

Sites

During the three years of measurements, different crops and forest sites were sampled. All are located in the center of the study area, about 20km to the southwest of Munich. Some sites changed from year to year. The sites and cover types for each year are listed in Table 5.1.

Table 5.1: Sites of leaf area index measurement campaign 2002-2004.

Year	Maize	Wheat	Triticale	Rape	Broadleaf Forest	Needleleaf Forest
2002	DLR St.Gilgen Wastian	DLR Mitterwies Stuerzer	-	-	Meiling 1 Meiling 2 Neuhochstadt	Oberbrunn 1 Oberbrunn 2
2003	Argelsried Tiefenbrunn	Stuerzer	Stuerzer	Stuerzer	Muehltalerleiten Weiherbuchet	Bocksfeld Reissmuehlweg
2004	Argelsried	Stuerzer	-	-	-	-

The measurements were attempted to be made every two weeks. However, weather and lighting conditions may seriously disturb the measurement plan. While measuring crops could be performed quite regularly and apace applying both instruments, forest measurements took longer effort. While lighting conditions could be compensated by shading crop canopy with cardboards, forest measurements have to rely on uniform overcast conditions but no rain. These conditions were very difficult to nab.

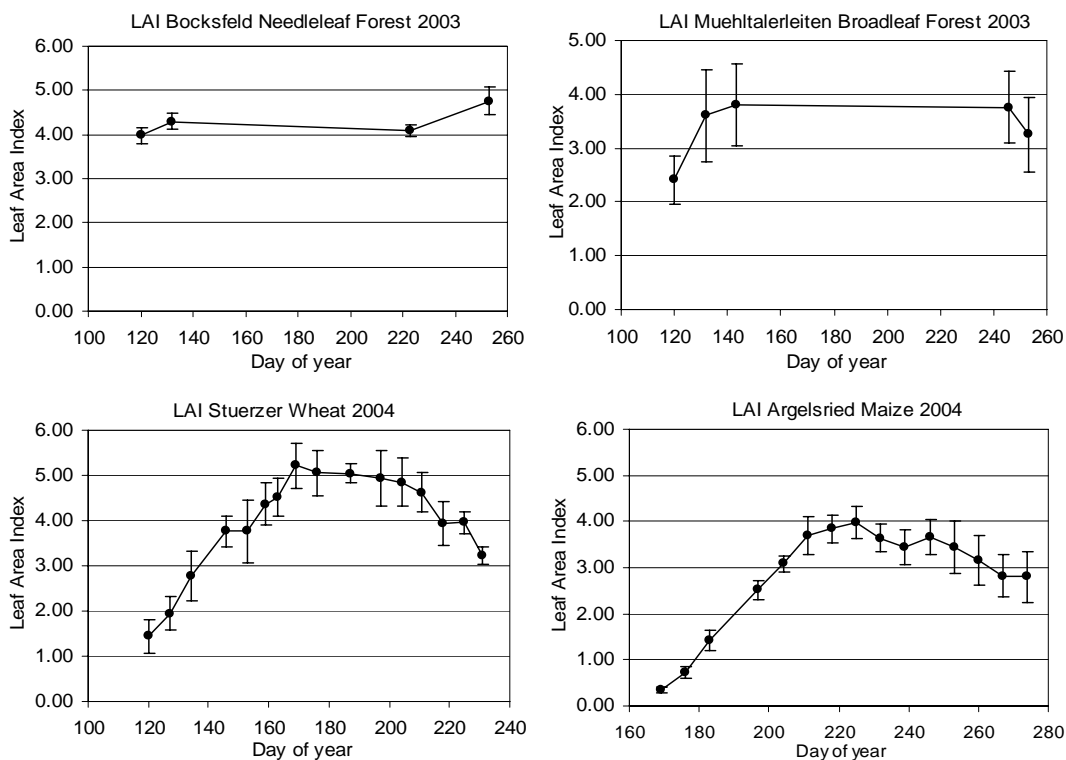


Figure 5.3: Temporal development of four sites sampled in the LAI field measurement campaign.

Examples of the measurements are given in Figure 5.3 for four selected sites. With the reduction of fields sampled, the 2004 campaign concentrated on only two fields with a higher

sampling interval. Measurements of the forest sites were scarce but could capture the onset of leaves in spring. All measured values are provided in Appendix 3.

5.6.2 Modeled LAI

A dataset of LAI development was extracted from a model run of PROMET-V (Schneider, 2003) for the hydrological year 2000. As Figure 5.4 illustrates, the advantage of these progressions of LAI over the year lies in the continuity of the information for individual land cover types. Each step in the model provides a dataset of LAI. The data were modeled for an area in the alpine foreland southwest of Munich. The area covers about 4000km² around the two large lakes in southern Bavaria, Ammersee and Starnberger See. It lies fully within the GLOWA Danube catchment and the study area. The plots shown below include the standard deviation of LAI values over the area with the mean values. Courses of maximum and minimum LAI are also provided. The plots were created from 10-day intervals selected from daily data.

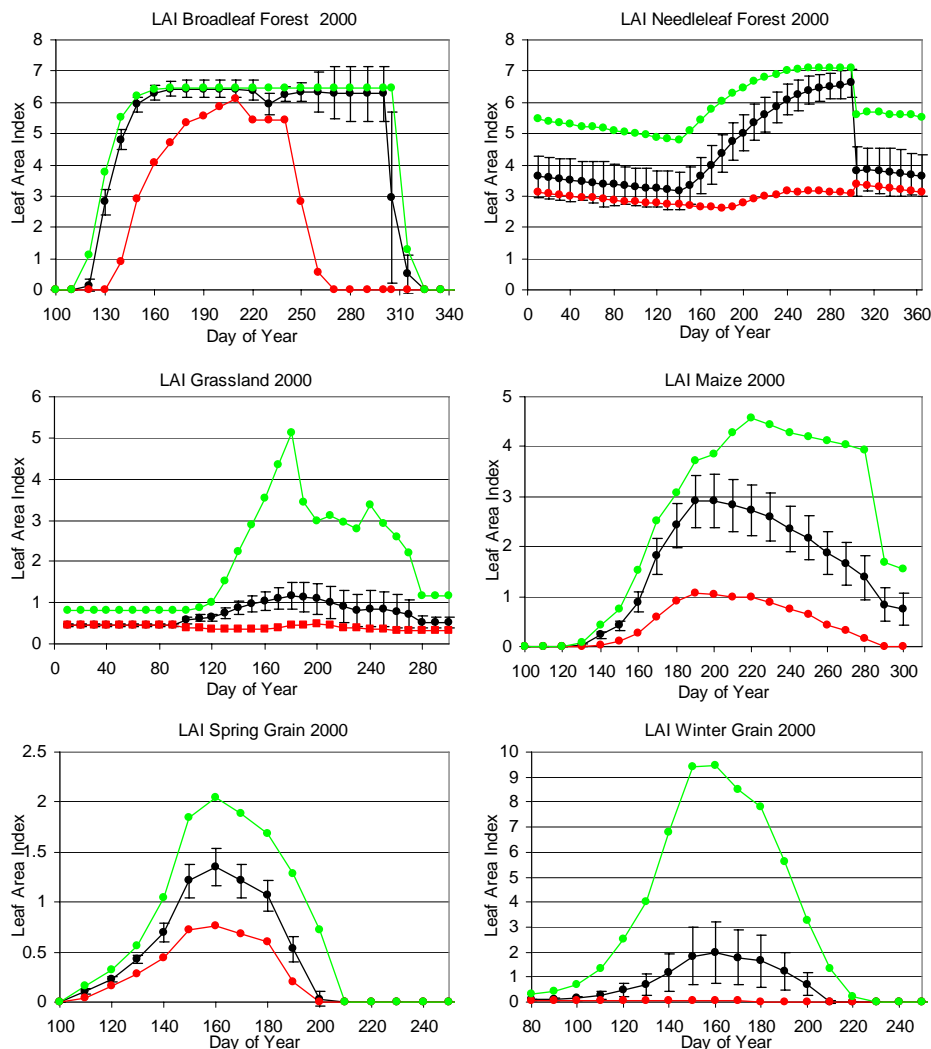


Figure 5.4: Seasonal development of LAI as modeled by PROMET-V for six cover types. Mean values of model results including standard deviation are in black, maximum values in green and minimum values in red.

5.6.3 LAI from the Literature

A review of available LAI data in the literature was undertaken to assess this possible source of data. Scurlock et al. (2001b) have compiled a comprehensive collection of LAI field data sets from 1932-2000 (Scurlock et al. 2001a). This database contains about 1000 estimates of LAI from 400 unique field sites. The database provides quite unique insight into the development of LAI measurement effort. However, most of these data are one-time measurements of leaf area. Although, with most data the year of the measurement is provided, 80% of the data do not give any information on the date of measurement and many mention merely the month or season when the measurement was conducted. Sites including lat/lon position and biomes are given with the data. Species are listed where available and about half of the datasets provide the methodology of measurement including the definition of LAI. Thus, the layout of the database meets the requirements of the more detailed definition given above (Equation (5.2)), but with large gaps in the data many individual records will not provide the full information desirable. From the dataset, LAI data of only four grassland sites could be exploited, each with 3 measurements at different times of the year (Appendix 4).

An exhaustive acquisition of LAI of maize, various types of grain and soja providing seasonal development of LAI was conducted by Demircan, 1995 (see Figure 5.5). Destructive harvesting and measurement of leaf area was performed from 1990 through 1993. While the estimates from the database described above stem from sites around the world, this dataset was elaborated in the southwest of Germany. Although not located directly within the GLOWA-Danube basin, the estimates are from an area with quite comparable environmental conditions.

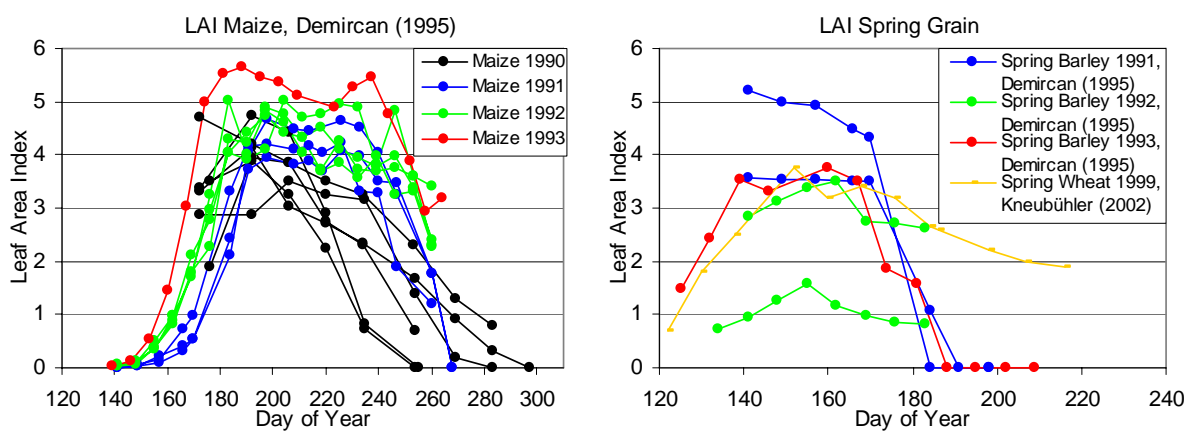


Figure 5.5: Field estimates of LAI from the literature (Demircan, 1995, Kneubühler, 2002)

Another source of LAI data for agricultural crops was the work by Kneubühler (2002). He provides data of spring wheat and winter barley from two fields located in the north of Switzerland. In the assessment the Li-Cor LAI-2000 was used to measure LAI. Extracts from the data from the two previous mentioned sources are given in Figure 5.5. All data are shown in Appendix 3 and 4.

For forest sites, seasonal development of LAI could not be derived from the literature. This is probably due to the difficulties in measuring forest LAI as was experienced in the measurement campaign for this study.

5.6.4 LAI derived from Remote Sensing Data

Operational production of leaf area index has emerged with the MODIS 1km MOD15 LAI Product. Since MOD15 LAI values are derived based on a biome classification, cover type specific LAI may be extracted from the product (see section 4.6.5). The temporal development of LAI for four cover types is shown in Figure 5.6. Data were taken from five years of MOD15 LAI Product from the collection version 004.

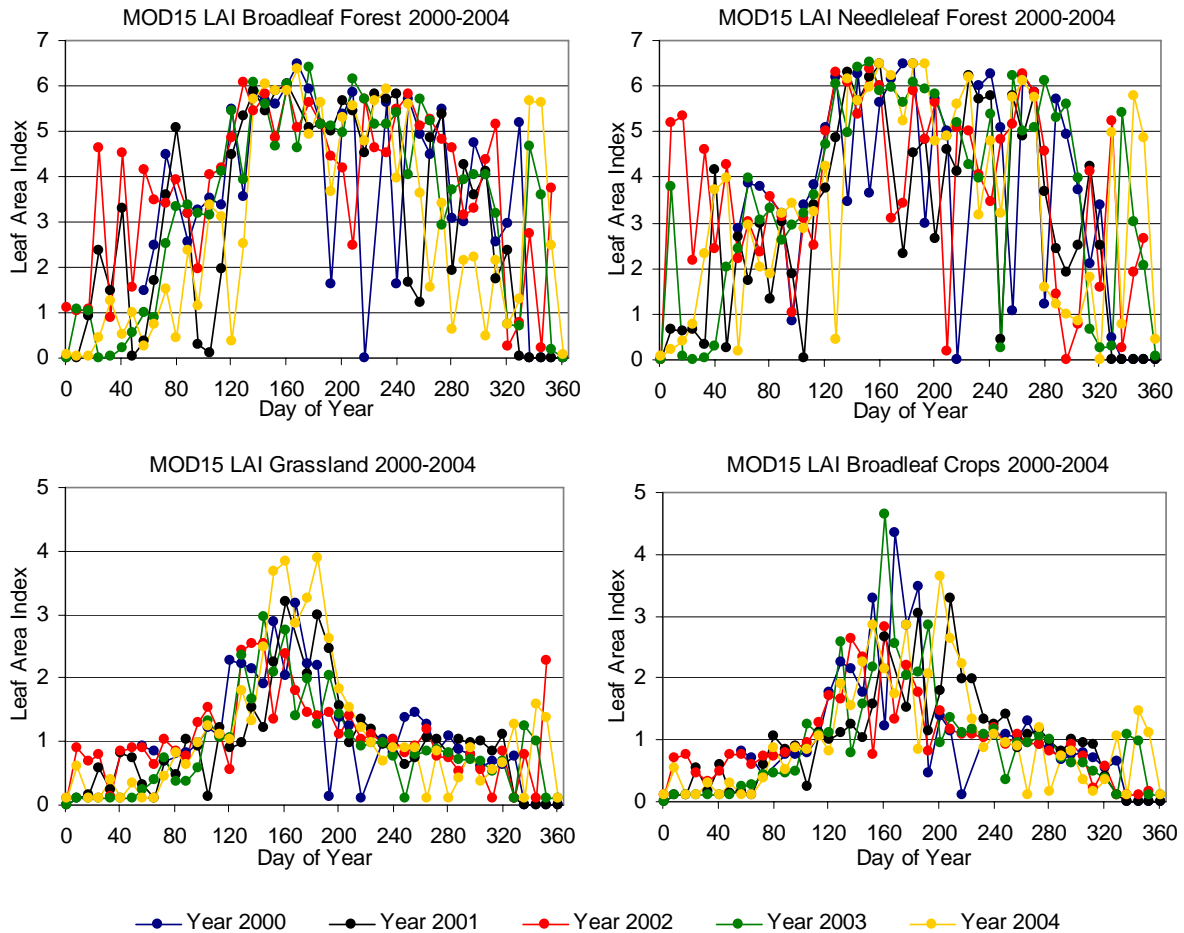


Figure 5.6: Seasonal development of LAI derived from the MOD15 LAI Product 2000-2004 for four cover types/biomes. Plots are based on averages from 3x3 boxes of homogeneous land cover.

The same MOD12 Land Cover product that went into the production of the LAI fields was used to identify cover types within the area of the GLOWA-Danube catchment. The data are taken from homogeneous areas of the specified cover type. The plots represent average values of the 9 pixels of homogeneous 3x3 boxes. For each year between 37 and 45 datasets were available. If LAI was not produced on a pixel the value was omitted in the averaging.

5.7 Discussion of available LAI data

5.7.1 Applicability of data

The most continuous data in the LAI data presented above stem from the results of an environmental model. Daily data may be provided for all land cover types present in the model. But the values computed in the model need to be counterchecked. In the context of distributed environmental modeling, LAI measurements are desirable to update the model state variable. This can be performed if the measurements are up to date and availability is given for the area modeled. Distributed data can not be achieved with point measurements on the ground. The effort is simply not manageable. The only feasible way to obtain data for an area as large as the GLOWA-Danube catchment is through the derivation of LAI from remote sensing data.

The MODIS MOD15 LAI product is readily available as a global dataset and would cover the area of the GLOWA-Danube basin on a regular temporal basis. Also, the resolution of the dataset of 1km matches the resolution of the current implementation of the decision support system DANUBIA. However, the land cover classification used in the production of MOD15 is quite different from the land cover applied in DANUBIA. For example, the MOD12 Land Cover Type 3, the biome classification used to derive MOD15 LAI, contains a class “savanna” which also appears in the area of the GLOWA-Danube catchment. This seems irritating at first glance, as savanna is a land cover not readily expected in central Europe. This class becomes more reasonable when realizing that the biome type of MOD12 Land Cover Type 3 is attributable to a structural type of vegetation cover rather than a biological composition. Understanding “savanna” as a grassed cover with dispersed trees explains how this cover type can appear in the upper Danube basin. Still, translating this conception of land covers to the cover types present in the DANUBIA model compound is a difficult task.

When inspecting the temporal development of LAI from MOD15 in the previous section the pronounced zigzag of the plot strikes. LAI from one 8-day interval may drop to the next by several units of LAI and then rise to the previous level on the following date of a LAI estimate. This is not the development the LAI of land covers is expected to exhibit. The measurements provided in the previous section as well as pure common sense indicate that these courses of LAI as derived from the MODIS product are not reasonable. This is the case although averages of areas larger than a single pixel were examined. The fact that a single pixel of the MOD15 LAI product may exhibit significant bias compared to higher resolution remote sensing estimates and ground truth has been reported earlier (Tian et al. 2002, Wang et al. 2005). The application of error prone single pixel values of MOD15 in a land surface model would be an equivocal undertaking.

Finally, the DANUBIA model is laid out to operate on subscale fractional entities, based on land cover types. The 1km MOD15 product cannot provide information on a subscale basis. A concept of dividing up a 1km LAI value to subscale fractions as proposed for reflectances will not hold as is shown in the next section.

5.7.2 The paradox in scaling LAI from remote sensing

It has been stated earlier that any surface may be attributed a value of LAI. Thus at any resolution a dataset may provide a spatially continuous field of LAI values. A paradox arises when comparison of LAI values of different scales is sought and if those values were derived from remote sensing data in either fashion mentioned above. The problem lies in the land cover dependence of LAI retrieval. If any surface has a LAI value, areal units may be lumped

to provide a LAI value on a coarser scale. However, if this aggregated value is to be compared to a LAI value derived at the coarse scale, this coarse scale value is attributed to a certain land cover type that specified the retrieval algorithm. In many cases, homogeneity of the coarse pixel is not given. The LAI value lumped from (assumably) homogeneous finer scale units is the true LAI value attributable to the lumped area. But then, the coarse scale derivation of LAI is the LAI that is attributable to the area were it of the land cover type used in the derivation of the LAI. Consequently, a comparison of such LAI from different scales is not feasible.

The same problem occurs if a coarse scale LAI value were to be disaggregated to a finer scale. Again, the coarse scale value of LAI would be linked to the land cover type that was used in the retrieval. If the finer scale segmentation of the coarse scale areal unit is not homogeneous, a value derived from an algorithm specific to one land cover type would be attributed to another. This again, does not withstand to logic. Subsequently, it becomes a serious dilemma when a model ingests LAI and land cover and links the two in process description.

As a consequence, no scaling of LAI is admissible if land cover type was involved in the retrieval of the LAI value. What needs to be scaled is the algorithm for the retrieval and as reliable remote sensing models rely on land cover, the land cover as a fundamental element in the algorithms needs to be scaled.

6 A Method for Reflectance Segmentation

Bringing together the statements from the previous chapters leads to the conception of a method to reasonably divide a single remote sensing measurement into its contributing segments. From the previously said, some conclusions can be drawn. The first is related to scale and is based on the cognition that properties and processes of the environment operate on specific scales (chapter 3). In order to measure or mimic these properties and processes, adequacy of the scale at which they are captured is required. Regional landscape models are tuned to scales at which they are capable of appropriately representing the processes and parameters they describe. In this context, the size of patches is most often tied to the type of surface cover type or land use. Consequently, parameter provision for process models needs to be oriented at the scale of the model and most likely coincides with the land cover types' spatial representation. For land surface process models it has been shown, that subscale fractional land cover may be applied to substantially improve model results at moderate scale resolution (~1000m).

The second conclusion is connected to the role of remote sensing and its capabilities of being used in conjunction with process models. Remote sensing, on the one hand is the only feasible measurement technique to provide distributed data over large areas at operational temporal and spatial sampling intervals. On the other hand, today's available remote sensing devices fail to meet the observation scale requirements of regional landscape models (Mauser et al. 1999). In optical remote sensing, spatial resolution is inversely proportional to temporal resolution. Thus, high spatial resolution data is not available at reasonable temporal intervals while data available at high frequencies come in lower spatial resolution. Also, the areal extent covered by high resolution imagery is lower than the area sensed with low-resolution sensors (section 3.6 and chapter 4). Consequently, one needs to compromise between high spatial and high temporal resolution. Using the frequently available low-resolution conflicts with the scale requirements stated above. High-resolution imagery is not available at sufficient temporal intervals. Ways need to be established to overcome this dichotomy. This could be achieved by installing more high-resolution imagers that fill the temporal gaps between acquisitions or by a way of spatial data enhancement of coarse resolution data. The latter is what is sought with the method presented here.

Thirdly, the parameter models to derive physical quantities such as leaf area index from remote sensing data take into account the land cover type in the retrieval algorithms (section 5.4.2). Land cover type is a parameter that is (i) comparably stable in time and (ii) is available at spatial resolution exceeding the pixel spacing of coarse resolution imagers. Due to its temporal stability it may be derived from temporally sparse high-resolution imagery. To obtain fractional land cover at the pixel resolution of coarse resolution satellite data, means of spectral unmixing of coarse spatial resolution data may also be applied. The method presented here relies on such fractional information only. Also, for Europe the publicly available Corine

Land Cover 2000 is produced at 100m spatial resolution which is finer than the wide swath moderate resolution remote sensing data. Consequently, the input postulates are met to potentially derive surface parameters tied to land cover at scales finer than the frequently available satellite data.

It may be argued that a surface parameter at a coarse scale may be downscaled to higher resolution. However, due to two facts it is not feasible to first derive such a parameter at a coarse scale with the intention to then downscale the parameter to a finer scale. One is the land cover often involved in the derivation of land surface parameters. Scaling that parameter contains the risk of transferring values obtained for a certain land cover type to a land cover it was not derived for (see Section 5.7.2). The other lies in non-linearity that may be involved in the parameter models applied in the retrieval. Both are true for the derivation of LAI from remote sensing data. Thus, if segmentation of a measure on a pixel is sought, the segmentation needs to be performed prior to the application of a non-linear model and prior to the incorporation of additional unsegmented information such as a land cover type. This means that the segmentation may only be applied to the “raw” data that serves as input to a parameter retrieval model. The raw data are the reflectances on a pixel in a single band. The method for segmentation presented below seeks to determine how fractions of the pixel area contribute to the integrated reflectance value available for a coarse pixel.

6.1 Conception of the Algorithm

The basic idea behind the algorithm presented here can be described by a short story. Imagine taking your dog for a longer walk every week or so. You would stroll along the pastures beside the creek, take a left up through the beech forest and then follow the trail along the wheat and cornfields. The forest would be bald, the soils bare along the winter and you know, some week in spring you will come back through the wood and the leaves will be out and shading the undergrowth. When you notice the first thick leaves of maize sprouts, the wheat on the next field will look much like the pastures down by the creek, yet smoother and all lined up. Later in the summer you find the wheat matured and one day the field harvested and ploughed. The maize then is a thicket of tall sturdy plants inside dim and damp under multiple layers of large leaves. About the time when the beech will lose their leaves you expect the maize field to disappear... a long story could be told here. But: You'd be surprised to find new maize sprouts in November. And something would seem wrong if the maize stood 3 meters tall in mid May.

In other words: When we go out there to look at landscape phenomena we have an idea of what to expect. In a scientific sense: When we take measurements, we have a range of values in mind that appear reasonable. We have expectations and these expectations change over time and they change with the subject we're looking at. Expectations are valuable when they allow us for example to judge errors in data or measurements. And they provide us with a fuzzy knowledge about the current state of a current subject.

The subject here is the land surface and the properties of its land covers. About these land covers and their properties, fuzzy knowledge can be found. For example for the land cover type “cornfield” a reasonable semantic approach to some fuzzy knowledge would be a simple statement like: On May 18, maize fields in the GLOWA-Danube catchment are no taller than 45cm but at least 15cm. This would give a fuzzy parameterization of the height of a maize field in May. A realistic range is set and its limits are provided. This kind of knowledge is not only valuable in ecological modeling, where it is important that parameters are within realistic

expected ranges (Asner, 1998) but can itself be ingested in numerical modeling based on the fuzzy set theory established by Zadeh (1965).

In the study pursued here, very similar fuzzy statements are applied. When translating the idea of prior expectations to the field of remote sensing, plant height is not a feasible parameter. What a remote sensing device measures is radiation that can be translated to surface reflectance properties. Reflectance properties change simultaneously with the changes in natural phenomena, i.e. plant height, leaf development and senescence. Thus, reflectance properties of a land cover type will be within a certain range at a certain time. They can, just like plant height, be described as within realistic expected ranges. These realistic expected ranges are used in the algorithm for the segmentation of moderate resolution remote sensing imagery.

A pixel of a moderate resolution image scene is very likely to integrate over a number of land covers. A reflectance value of that pixel will represent the reflectance properties of a heterogeneous surface, combining the reflectance properties of all underlying surface types. For the moderate resolution pixel, the underlying surface types are available at very good resolution. Precise area fractions of land covers on a pixel can be computed. Thus we know, what surface types contribute on what area to the reflectance of a coarse pixel. Considering the above said, additional but vague knowledge exists about how much a land cover type contributes to the reflectance of the pixel. Yet, it is not known in which way all those contributing land covers make up the reflected radiation measured at the imaging sensor. Figure 6.1 illustrates the components involved in this question.

If a true constellation is found of how much each of the land covers contributes to the moderate scale reflectance, the reflectance of the individual land covers will be available. The method for reflectance segmentation presented here was developed to find such a constellation. It aims at computing a solution for the reflectance of each land cover type. This is accomplished by combining fuzzy descriptions of expected reflectances of contributing land cover types with the fractional area of these land cover types. The algorithm is constrained by the moderate resolution measurement. An optimization procedure is established to find the most probable reflectances of land cover types that sum to the measured coarse pixels value.

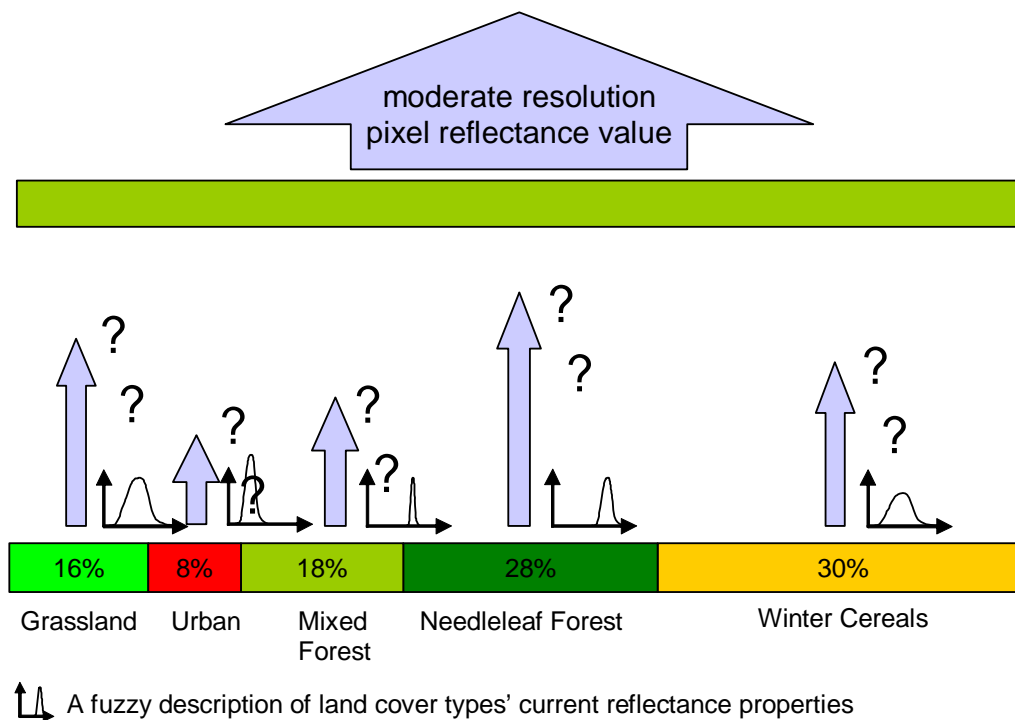


Figure 6.1: Schematic view of a set of land covers contributing to the reflectance value of a moderate resolution spectral measurement. For the algorithm, fractions of land covers are known and a fuzzy description of each land cover types current reflectance properties is provided. The blue upward pointing arrows indicate the unknown reflectance of the land cover types.

The illustration of Figure 6.1 refers to a single moderate resolution sample in a single band. The resulting reflectance values associated with the land cover types refer to the bandwidth of that band. The procedure can be transformed to any remote sensing bandwidth, given that the provided ranges for fuzzy reflectance description apply to that bandwidth. All spectral bands can be subject to the segmentation of the reflectance in that band. As a prerequisite, knowledge about land covers expected reflectances in the bandwidth is in demand. Segmentation of multispectral moderate resolution imagery should result in land cover specific spectra on a subscale basis.

All of the calculations described in the following were performed for the RED and NIR wavelength regions.

6.2 Methods

In this section the algorithm and the data essentials for the segmentation of moderate scale reflectances are introduced. First, details on the mathematics of the algorithm are presented. Then, the input data are described and how this data may be generated. Finally, the LAI retrieval algorithm is provided.

The first dataset is the digital land cover map that needs to be processed to area fractions of a coarse scale pixel. Next, the core of the algorithm relies on the fuzzy parameterization of reflectance properties of the land cover types under address. Land cover types were analyzed

using the high resolution Landsat imagery. From this analysis, a fuzzy description of land covers reflectance properties was derived.

A schematic idea of the inputs and outputs of the algorithm is given in Figure 6.2. The figure also suggests that the amount of data that goes into the computation as well as the output is a function of the detail of the land cover used.

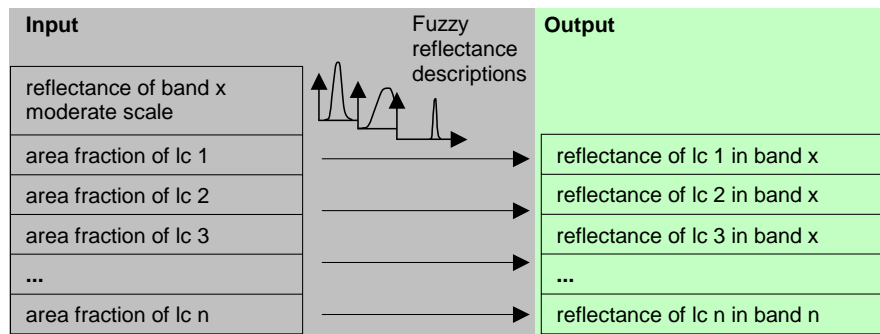


Figure 6.2: Inputs and outputs of the algorithm for reflectance segmentation

The more land cover types are addressed in the land cover data set the more layers of data need to be processed. Thereby the complexity of the algorithm itself varies with the structure of the land cover, i.e. the number of land cover types that are present on each moderate scale pixel. Computational cost depends on how many land cover types are ingested in the assessment of reflectances for each of the land cover types. Land cover types not present on a pixel consequently will have zero reflectance in the result.

6.2.1 Optimization of land cover specific reflectances on pixels of multiple land cover

The core of the algorithm for the computation of land cover specific reflectances from a moderate resolution pixel lies in the concept of fuzzy description of land cover reflectance. It is based on the notion, that for a point in time a certain degree of reflection can be expected from categorized natural surfaces. A way to mathematically describe such an imprecise notion has been established by the concept of fuzzy sets (Zadeh, 1965, Zimmermann, 1987, Zimmermann, 1991). Contrary to Boolean algebra where membership to a set is either true or false, fuzzy set theory provides a mathematical logical approach to membership to a set that is gradual in nature. A fuzzy set A is given by a membership function defined over a domain X .

$$m_A: X \rightarrow [0,1] \quad (6.1)$$

The value of the function $m_A(x_i)$ where $x_i \in X$ is the degree of membership to the set A . In order to describe a fuzzy set or imprecise knowledge a membership function is needed. The translation of linguistic approaches to fuzzy knowledge as stated above has been termed the semantic import model (Burrough, 1989). Membership functions can exhibit various shapes and can be expressed as a function term, a table or a graph of m_A . Their shape and properties are as numerous as the fields of application and so are the ways to derive membership functions (Hootsmans, 1996, Civanlar and Trussel, 1986). They may be monotonically

increasing or decreasing or both, linear or curved, even waveforms are imaginable, depending on application.

In the application for reflectance segmentation the purpose of the membership functions is to provide an idea of how probable a certain degree of reflectance is for a certain land cover. Each land cover has its membership function assigning a grade of membership to a reflectance domain. The reflectance domain and the membership function are specific for a point in time. A high grade of membership indicates that the degree of reflectance of the land cover has a high probability to be true at a certain time of the year. The membership functions describe how likely it is that a land cover is in a certain state of reflectivity.

Two natural surfaces of the same type or class will be very unlikely to exhibit the same properties. Both pasture fields we look at may be green (or have a high reflectance in the green portion of the electromagnetic spectrum), but still one may be “greener” than the other. Thus, the perception of a green field is disturbed by a certain fuzziness in the notion. The application of membership functions takes into consideration that environmental phenomena are fuzzy in nature.

The optimization applied for the segmentation of reflectances requires that the membership functions providing the fuzzy knowledge are at least two times differentiable. A function was developed that fulfills this requirement and that prove adequate to describe the reflectance domains of all land covers under address in the RED and NIR spectral domains. The function has the form

$$\psi(x)_i = a \cdot e^{\left(-\frac{(x - \mu)^2}{\sigma^2 \cdot (1 + b \cdot x + c \cdot x^2)} \right)} \quad (6.2)$$

and was derived from the Gaussian peak distribution form

$$f(x)_i = a \cdot e^{\left(-\frac{(x - \mu)^2}{2\sigma^2} \right)} \quad (6.3)$$

In Equation (6.2) the parameter a , b and c add the capability of the function to exhibit a right or left skewness of the curve in addition to uniform distribution. The parameter μ determines the maximum of the curve, σ will control the left and right convergence to zero.

In Figure 6.3 three functions of type (6.2) are shown. They describe the probability of reflectance in the NIR region for different cover types. Note the skewness of the urban type function as well as the different shapes for the land covers achieved by changing the parameterization (a , b , c , μ , σ).

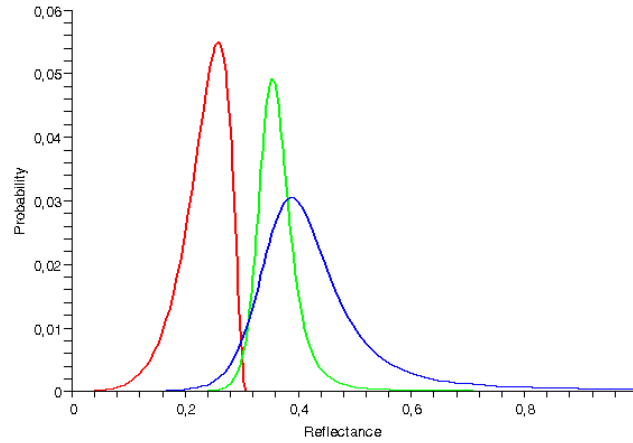


Figure 6.3: Multiple differentiable functions Ψ_i for fuzzy description of the probability of the degree of reflectance in the NIR region for three surface types on June 18: Urban (red), Maize (green) and grassland (blue)

Assuming a coarse resolution pixel whose area is made up by n land cover types, there need to be n functions Ψ_i available. They provide probability densities of the reflectance value attributable to each land cover type at a certain time.

All reflectances R_i of all n land covers need to be weighted by their fractional area a_i of the pixel to sum up to the total reflectance R_{total} of the pixel:

$$R_{total} = R_1 \cdot a_1 + R_2 \cdot a_2 + R_3 \cdot a_3 + \dots + R_n \cdot a_n \quad (6.4)$$

Here, R_{total} is the reflectance given by a coarse scale pixel. Although in physical terms not precisely correct, this linear totaling of areal partitions of a pixel is common practice in remote sensing applications dealing with subscale parameterizations. Equation (6.4) can be rewritten as

$$R_n = \frac{1}{a_n} \cdot (R_{total} - R_1 \cdot a_1 - R_2 \cdot a_2 - R_3 \cdot a_3 - \dots - R_{n-1} \cdot a_{n-1}) \quad (6.5)$$

In this form Equation (6.5) delivers the constraint in the multicriteria decision making process. Any solution to the reflectances of contributing land covers have to comply to the requirement of (6.4) in order to meet this simplification of the energy conservation law.

Given n land covers, the combined probabilities Ψ_i of reflectances R_i of those land covers can be written as

$$\Psi_{total} = \Psi_1(R_1) \cdot \Psi_2(R_2) \cdot \Psi_3(R_3) \cdot \dots \cdot \Psi_n(R_n) \quad (6.6)$$

ψ_{total} is a measure for the likeliness that the whole host of land covers on a coarse scale pixel together reflects a certain amount of radiation in the given wavelength. This likeliness changes with the reflectances of individual land covers R_1, R_2, \dots, R_n and is valid at a given point in time.

In order to assure that the host of land covers together does reflect the given amount of radiation measured by a moderate resolution imager, equation (6.6) is constrained using equation (6.5) and is written as

$$\psi_{total} = \psi_1(R_1) \cdot \psi_2(R_2) \cdot \dots \cdot \psi_{n-1}(R_{n-1}) \cdot \psi_n(R_n(R_1, R_2, \dots, R_{n-1})) \quad (6.7)$$

In this form, ψ_{total} is a measure for the likeliness that the whole host of land covers on a coarse pixel together reflects the amount of radiation measured as R_{total} . Many solutions are possible for this constrained equation, yet the probability for the solution changes. The solution with the highest probability can be found by maximization of (6.7).

An efficient way to the maximization of ψ_{total} is the Newton-Raphson Algorithm (Bronstein et al. 2001, Quinn, 2001). It will iteratively walk to the next peak of the function. The algorithm is used in many fields such as Chemical Engineering, Physics and Economic Sciences for the solution of optimization problems. One iteration from \bar{x}_0 to \bar{x}_1 is given by

$$\bar{x}_1 = \bar{x}_0 + \nabla \psi_{total}(\bar{x}_0) \cdot (\mathbf{H} \psi_{total}(\bar{x}_0))^{-1} \quad (6.8)$$

with $\nabla \psi_{total}$ being the vector of the first partial derivatives of ψ_{total} :

$$\nabla \psi_{total}(x_1, x_2, \dots, x_n) = \begin{pmatrix} \frac{\partial \psi_{total}}{\partial x_1} \\ \frac{\partial \psi_{total}}{\partial x_2} \\ \vdots \\ \frac{\partial \psi_{total}}{\partial x_n} \end{pmatrix} \quad (6.9)$$

and $(\mathbf{H} \psi_{total}(\bar{x}_0))^{-1}$ is the inverse of the Hessian matrix at \bar{x}_0 . The Hessian is defined as the matrix of second order partial derivatives:

$$H \psi_{total} (x_1, x_2, \dots, x_n) = \begin{pmatrix} \frac{\partial^2 \psi_{total}}{\partial x_1^2} & \frac{\partial^2 \psi_{total}}{\partial x_1 \partial x_2} & \dots & \frac{\partial^2 \psi_{total}}{\partial x_1 \partial x_n} \\ \frac{\partial^2 \psi_{total}}{\partial x_2 \partial x_1} & \frac{\partial^2 \psi_{total}}{\partial x_2^2} & & \frac{\partial^2 \psi_{total}}{\partial x_2 \partial x_n} \\ \vdots & & \ddots & \vdots \\ \frac{\partial^2 \psi_{total}}{\partial x_n \partial x_1} & \frac{\partial^2 \psi_{total}}{\partial x_n \partial x_2} & \dots & \frac{\partial^2 \psi_{total}}{\partial x_n^2} \end{pmatrix} \quad (6.10)$$

The matrix is symmetrical because the second partials are continuous. This reduces the cost of solving the matrix. With a quadratic convergence rate the algorithm is very quick to find a solution and computational effort is kept low.

The algorithm has to be triggered at some point in the n -dimensional space. A position close to the expected solution can be established by selecting the maxima of the reflectance distributions functions of type (6.2) from land cover 1 to land cover $n-1$ and determining a reflectance for land cover n using equation (6.5). If this reflectance of land cover n is not within the interval $[0,1]$ computation is aborted and the land covers are resorted. Changing the order of land covers changes the starting position. This procedure eventually finds a good position to trigger the algorithm.

A solution for the reflectances of land covers 1 through $n-1$ is found when the square root of the Euclidean norm of the gradient of ψ_{total} is smaller than a predefined threshold ε . The reflectance for the n -th land cover will be computed using equation (6.5). Any solution needs to be tested for plausibility. In the n -dimensional space many mathematically correct solutions are possible but a solution may be false in the context of the physical quantity of reflectance. Reflectance values are accepted if all reflectances are within the interval $[0,1]$. If this requirement is not met, the algorithm is triggered again after resorting of land covers. Resorting sets the algorithm off at a different position leading it to a different extremum.

Triggered in a wrong direction the iteration may never find a solution. To avoid the algorithm to get caught in an endless loop, the number of iterations is limited to 25. With this limit exceeded, again the algorithm is stopped and retriggered after resorting the land covers. The number of 25 iterations is large enough to always find a solution in the well-defined interval $[0,1]$. In most cases a solution is found after less than 10 iterations with a threshold of $\varepsilon = 1.0E-09$.

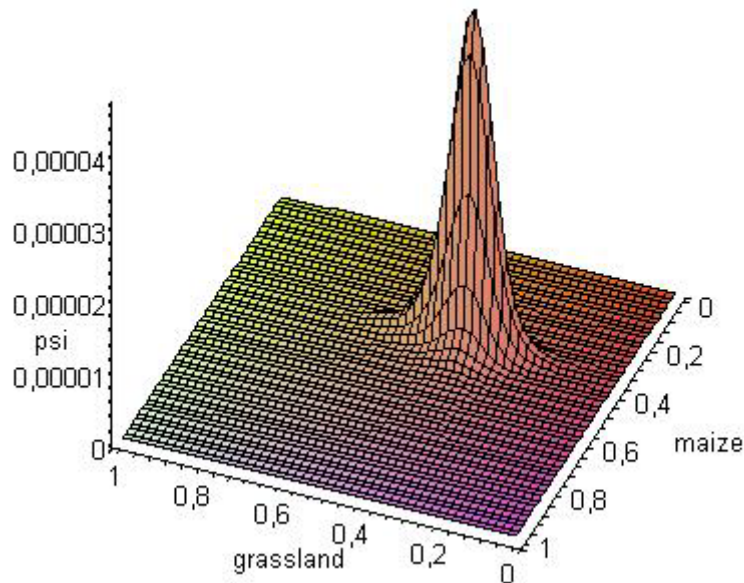


Figure 6.4: A graphical representation of the function Ψ_{total} (ψ). The optimization using the Newton-Raphson iteration will find the position of the peak of the surface. In the example shown a pixel with the land covers grassland, maize and urban fabric was simulated. The urban fabric land cover type is contained in the constraint of Ψ_{total} .

In Figure 6.4 a 3D graphical representation of the function that is optimized to find the solution of the algorithm is shown. With three land cover types on a pixel, the surface representing Ψ_{total} can be plotted and visualized. As the function Ψ_{total} is constrained by Equation (6.5), only two of the three underlying land cover types appear in the graph. The third is contained in the constraint. The surface represents the probabilities of different solutions to the various combinations of reflectance contributions of the 3 land cover types on the coarse pixel that sum to the measured reflectance. The algorithm will “crawl” along this surface until it reaches the peak of the surface and identifies the reflectances with the highest probability. This kind of graphic illustration is not possible if more than 3 land cover types are involved in the calculation.

6.2.2 Fuzzy Representation of Reflectance Properties of Land Cover Types

A fundamental principle of remote sensing lies in the physical fact that materials exhibit explicit spectral reflectance properties. When similar surfaces are grouped into classes as in land surface classification, spectral properties of the members of each class will show spectral similarities. The distribution of the within class variation of these spectral properties is expected to be a single peak distribution close to a Gaussian distribution (Lillesand and Kiefer, 2000). More peaks usually indicate class contamination or heterogeneity. Thus, spectral reflectances of homogeneous land cover type classes may be approximated as single peak probability density functions such as the Gaussian distribution given in Equation (6.3) and the more flexible peak distribution of Equation (6.2).

In order to conceptualize the reflectance properties of land covers in a fuzzy manner, the land covers were analyzed regarding their statistical properties. This was done by superimposing the land cover classification on the reflective bands of the Landsat image from June 19th,

2000. For the NIR and RED bands, histograms of the land cover types were computed to gain insight into the ranges of reflectances that are characteristic for each land cover on that day. The histograms were normalized to the maximum value in the class. In a preliminary analysis, the reflectance domains of all 30 classes were analyzed. This analysis was used to cluster the 30 land cover classes and reduce the number of classes to 12. The ENPOC classifier used in the production of the 30 class land cover classification is capable of distinguishing land cover types that exhibit quite similar spectral properties. For the segmentation of reflectances these similar classes were grouped together again based on structural and spectral properties. For needleleaf forest and grassland, examples of this bundling of classes are given in Figure 6.5. The ranges of the histograms of the classes of each plot are very close so that the classes can be bundled into one class.

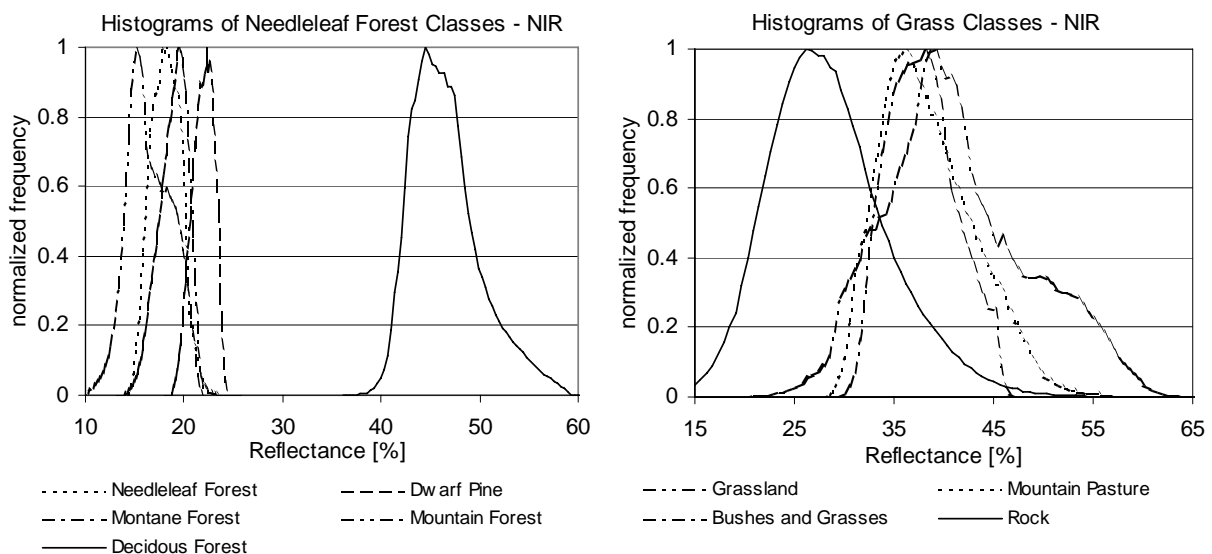


Figure 6.5: Histograms of NIR Reflectances of similar cover types. For comparison a differing land cover (deciduous forest, rock) is provided in each plot. The similar classes were combined to a class “needleleaf forest” and “grassland”.

For the 12 remaining classes new histograms were computed and the functions of Equation (6.2) and (6.3) were fitted to the frequencies. This was done for both VIS and NIR reflectances. As a result, for each land cover type functions were derived that provide the probability of the cover type to reflect radiation to a certain degree. Each function covers the domain of reflectance that is characteristic for that cover type at the date of the Landsat scene, June 19th, 2000 and is a fuzzy description of that reflectance. The results from these fits are shown in Figure 6.6 for RED reflectances and Figure 6.7 for NIR reflectances.

While the modified Gaussian function (6.2) was more difficult to fit to the histograms than the standard Gaussian function (6.3), the former displayed slightly better R^2 values in the regression than the latter. However, most fits to the histograms of both reflective bands of the Landsat scene showed very high coefficients of determination indicating the good quality of representation of the histograms by the peak distribution functions. All coefficients of determination for both functions are listed in Table 6.1. The function parameters are provided in Appendix 5.

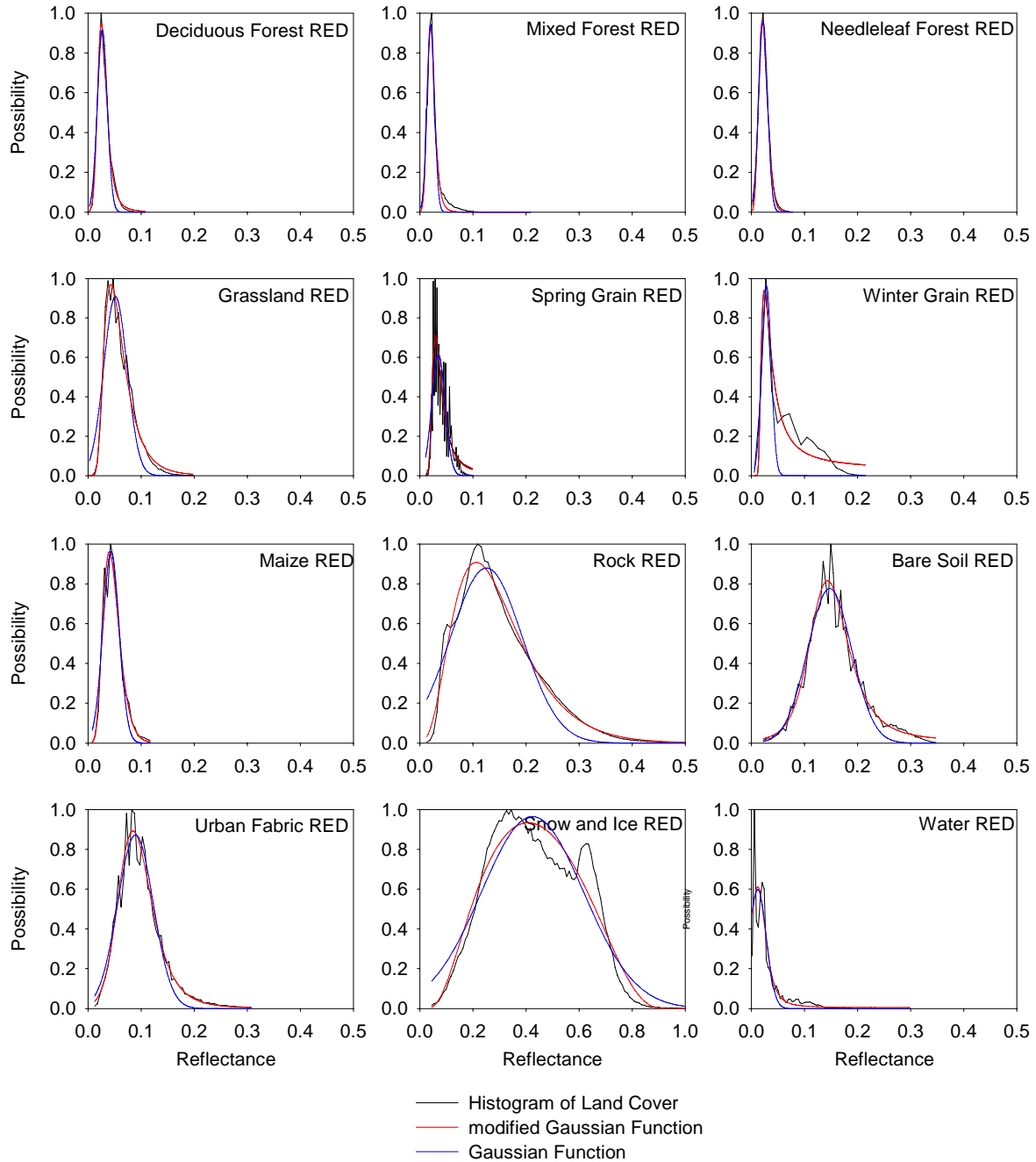


Figure 6.6: Histograms of the RED reflective Landsat band and fitted modified Gaussian function and Gaussian function for the 12 land cover types.

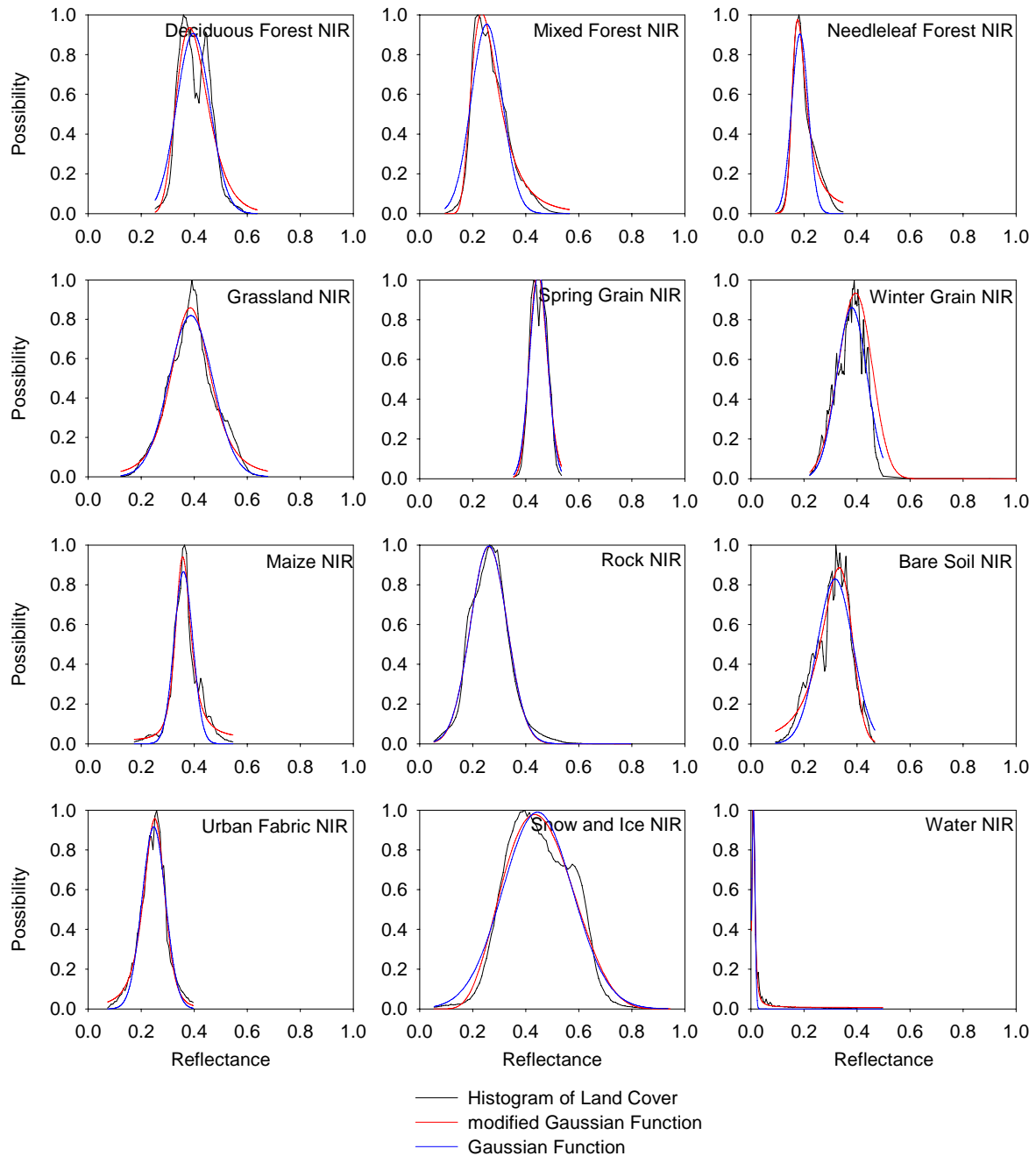


Figure 6.7: Histograms of the NIR reflective Landsat band and fitted modified Gaussian function and Gaussian function for the 12 land cover types.

Table 6.1: Coefficients of determination of the regression of land cover types histograms with the peak distribution functions.

Land Cover Type	modified Gaussian (5 parameter)		Gaussian (3 parameter)	
	RED	NIR	RED	NIR
Deciduous Forest	0.993	0.895	0.965	0.877
Mixed Forest	0.983	0.986	0.974	0.927
Needleleaf Forest	0.997	0.988	0.985	0.891
Grassland	0.983	0.973	0.903	0.964
Spring Grain	0.714	0.948	0.621	0.945
Winter Grain	0.902	0.787	0.575	0.913
Maize	0.971	0.967	0.948	0.925
Rock	0.986	0.990	0.943	0.990
Soil	0.966	0.939	0.945	0.885
Urban Fabric	0.970	0.984	0.955	0.970
Snow	0.940	0.970	0.892	0.952
Water	0.835	0.993	0.828	0.964
Mean	0.937	0.952	0.878	0.934

The land cover reflectance possibilities are represented almost equally well with either function type. Since their objective is to provide an imprecise approximation of ranges of valid reflectance of the land cover types, both are well suited to provide fuzzy reflectance properties. Because the algorithm needs to compute function values and first and second order derivatives of the functions, computational cost is reduced with simplicity of the applied fuzzy reflectance description. This makes the simple Gaussian function the preferable candidate for the execution of the algorithm.

The functions given above are best estimates of fuzzy reflectance properties for the 12 land cover types for the date they were derived for (June 19th, 2000). They are most suitable for the application in the prototyping of the algorithm with synthetic data (see section 7.1) and also for the application to the MODIS imagery best related to that date. However, for different dates these functions are not applicable as the reflectance properties change dynamically with time. The peak position as well as the width of the curves are subject to change during the vegetation period. For the application of the method to a time series of MODIS images availability of these functions is fundamental.

These functions, however fuzzy in nature, are not readily available. While they could be derived for a date where high-resolution reflectance data are available, this approach to obtain fuzzy land cover reflectance descriptions is not feasible for most other times. In order to derive functions to fuzzily describe the reflectance properties of land cover types for arbitrary dates, simulations of reflectances of the cover types under address were performed using a version of the GeoSAIL model (Verhoef and Bach, 2003, Bach and Mauser, 2003). This model was used to simulate bottom of atmosphere (BOA) reflectances, as they would be obtained from arbitrary remote sensing sensors measurements. The simulations are based on a set of surface properties that determine the reflectance characteristics. The model was run to obtain estimates of mean minimum and maximum reflectances of the land cover types as a function of changing LAI. These reflectances were taken as pivots to generate Gaussian functions for the reflectance segmentation of mesoscale remote sensing data.

The inputs required for the simulations are cover type, soil type and soil moisture, percent surface cover, chlorophyll content, phenology, along with green and brown LAI. Also, the sun and viewing geometry, time of day and the sensor response functions are taken into account in the simulation.

Simulations were run for 365 days of the year with the only surface parameter changed in the simulations being the LAI values. Except for the sun geometry, all other parameters were set to fixed values. Simulations were run three times for each land cover type namely for the minimum, maximum and mean LAI. The temporal progressions of minimum, maximum and mean LAI for the vegetation period were approximated from the available measurements of LAI. As the overall conception of the required functions is fuzzy, a mean trajectory and upper and lower hulls were created in an imprecise interactive manner. They will capture the host of LAI development curves as described by all the available data collected in section 5.6. An example of the development of LAI is given in Figure 6.8. The development of all vegetation land cover types are listed in Appendix 4.

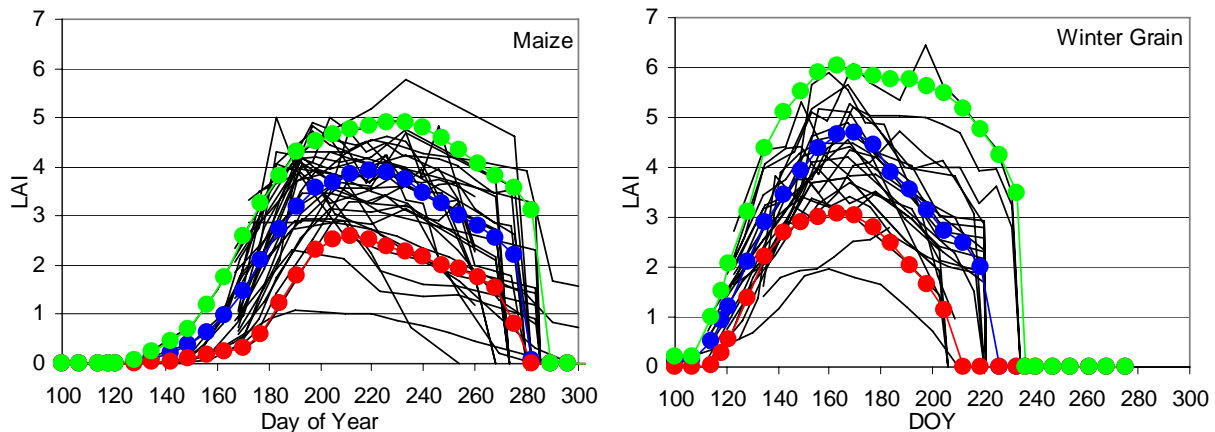


Figure 6.8: Approximations of mean (blue), maximum (green) and minimum (red) leaf area index derived from hosts of available measurements of LAI (black) for maize and winter grain.

To generate a Gaussian function (Equation (6.3)) that provides a fuzzy description of reflectance properties for a day of the year in a band, the mean reflectance in the band was taken as the μ parameter in the function. The σ parameter was approximated by quartering the difference of the minimum and maximum reflectance. This procedure results in functions that include the minimum and maximum reflectance as very low possibilities in the fuzzy description. The scaling parameter a was set to 1 as the algorithm is insensitive to the amplitude of the functions.

Functions derived in this manner are shown in Figure 6.9. The trajectories for mean, minimum and maximum from Figure 6.8 went into the generation of the functions. Days of year 139, 153 and 201 are plotted. They indicate how reflectance continuously increases during that period for maize, but is already in a decreasing phase for the cereal crops on the last day of the time series.

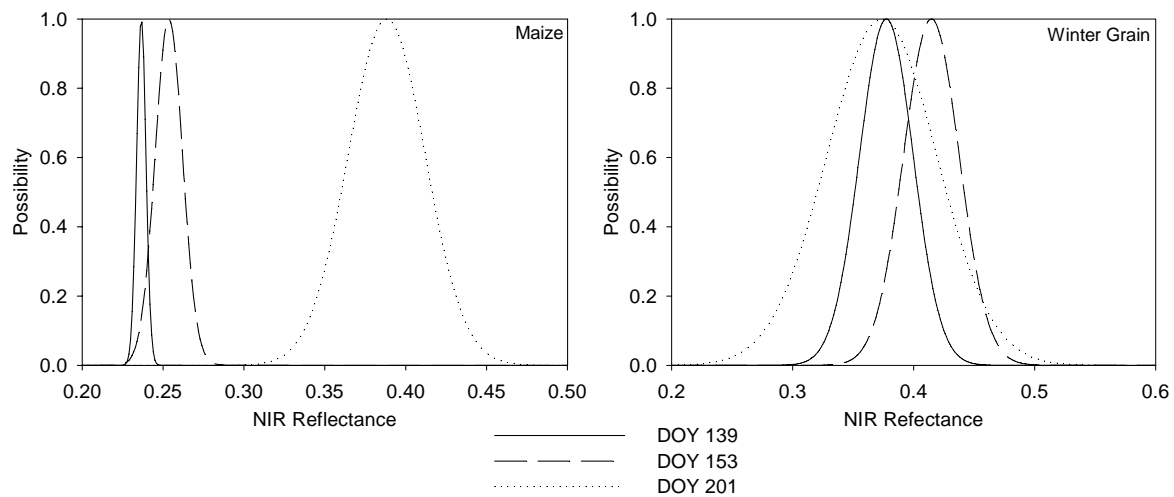


Figure 6.9: Reflectance probability functions generated from GeoSAIL model results. Possible reflectance values change with the temporal development of the vegetated surfaces.

The unvegetated land cover types, namely rock, bare soil, urban fabric, snow/ice and water bodies are assumed to retain constant fuzzy reflectance properties over time within the ranges elaborated from the image analysis described above. The functions derived for these surfaces from the high resolution Landsat image were used in all runs of the reflectance segmentation algorithm.

6.2.3 Subscale Land Cover

The algorithm for reflectance segmentation requires the land cover map to be stratified into percentages of each land cover types proportion on the mesoscale pixel. With the land cover types mapped from the Landsat Thematic Mapper imagery, land cover types were available at 30m spatial resolution. However, to derive the percentages of land cover types on coarser scale pixels, the spatial resolution of the coarse pixel has to be divisible without remainder by the resolution of the high-resolution land cover. This is not the case for either of the MODIS bands. To overcome this problem, the 30m resolution land cover was resampled to 10m resolution in a fashion that each 30m pixel would be represented by 3x3 10m pixels. From this 10m resolution grid, percentages for all pixel sizes that are multiples of 10 can easily be computed.

The land cover classification contains pixels that are unclassified. A fuzzy description of unclassified pixels is not possible. Thus, unclassified fractions on the coarse pixel need to be eradicated. This was achieved by distributing any unclassified fraction on a pixel to the other classes present on that pixel according to their fractional area on the pixel. This procedure produces pixels that are fully covered by a combination of a subset of the 12 possible land cover types.

6.2.4 LAI Algorithm

Approaches to deriving LAI from remote sensing data were discussed above in section 5.4.2. To produce LAI estimates from reflectances, the simple approach of NDVI-LAI relation was

used. In the aforesaid, a key factor for the derivation of leaf area was identified to be the structure of the canopy. Structure is closely interconnected with type of land cover. To account for this important influence on LAI, a host of absolute reflectance NDVI-LAI relations was applied, depending on land cover type. These relations were carefully selected from the literature. Each relation has been used in earlier studies and has proven to deliver reasonable estimates in environments as the upper Danube catchment. Some have been derived and developed in parts of the catchment itself. The relations are listed in Table 6.2.

Table 6.2: Land cover type specific functions to derive LAI from arNDVI

Land cover type	Function	Authors
deciduous forest	$LAI = (1.63 \cdot NDVI)^{**4.7}$	Bach et al., 2003
mixed forest	$LAI = (NDVI \cdot 1.75)^{**5.4}$	Bach et al., 2003
needleleaf forest	$LAI = (NDVI \cdot 1.859)^{**6.061}$	Bach et al., 2003
grassland	$LAI = (NDVI \cdot 1.6)^{**3.0}$	Ludwig et al., 1998
spring grain	$LAI = 4.07 \cdot NDVI^{**2.3}$	Schneider, 2003
winter grain	$LAI = 4.07 \cdot NDVI^{**2.3}$	Schneider, 2003
maize	$LAI = 6.1 \cdot NDVI^{**1.97} - 0.28$	Demircan, 1995

In the processing, arNDVI was computed from the RED and NIR bands. In the cases of the assumption of homogeneous land cover on pixels, the land cover classification was used in selecting the appropriate function for LAI. In the case of subscale fractional reflectances, the layer of the dataset indicated the land cover type and determined the function to be applied.

7 Application of the Algorithm

This Chapter is concerned with the practical use of the algorithm for reflectance segmentation. Before the algorithm is applied to real moderate resolution MODIS data it is investigated and tested for plausibility and used on synthetic data derived from the Landsat Thematic Mapper dataset. Thus, all in section 7.1 applies to the conditions on the date of acquisition of the TM images from June 19th, 2000 (DOY 171). The application to an artificially constructed coarse resolution dataset allows for a verification of the performance of the algorithm as compared to its source or high resolution “truth”. The reflectances of land cover types obtained as results from the segmentation of the coarse synthetic data can be evaluated against averaged values computed from the high-resolution data. With this approach datasets from different scales are generated that are directly comparable because the fine resolution data were used to produce the synthetic coarse data. Additionally, the results from reflectance segmentation are compared to data directly derived at the coarse scale. This will show the difference between the reflectance segmentation approach and the alternative assumption of homogeneous pixels.

The method for reflectance segmentation was designed and developed to support the use of data of current mesoscale optical imagers like the MODIS and MERIS instrument in conjunction with numerical environmental models. After the profound exploration of the behavior and capabilities of the algorithm in the first subsection of this chapter, sections 7.2 and 7.3 expose the method to its application to actual moderate scale data from MODIS. The aspects brought into focus are connected to spatial and temporal effects of the application of the methodology.

In chapters 3 and 4 scale and resolution effects of MODIS data were expounded, showing that data collected under varying viewing conditions may exhibit substantial differences in resolution and radiometric quality. This issue is addressed in the investigation of reflectance segmentation applied to the MODIS data presented above that stem from two consecutive days of acquisition. The investigation takes advantage of the coincident Thematic Mapper data.

Fruitful application of an algorithm to derive surface parameters for the ingestion in environmental models requires that the resulting quantities are consistent over time. While moderate bias between consecutive acquisitions of data may be inevitable in measurements and parameter retrieval, general plausible trends should not be violated. This issue is addressed in the application of reflectance segmentation to a time series of MODIS data from the growing season of the year 2003.

7.1 Prototyping of the Algorithm

7.1.1 Simulation of possible Results

In a first step to verify the plausibility of the approach, all possible values that could result from the computations were evaluated. This was done by generating matrices to produce the full range of potential values of NDVI and LAI that may result from the reflectance segmentation. Because each band is segmented separately, extreme values of high and low reflectance may result for a land cover type from the segmentation. This begs the question if computation of LAI from these extremes will still produce reasonable estimates.

To produce a matrix of possible results for a land cover type, ranges of RED and NIR reflectances were derived from the functions of Figure 6.6 and Figure 6.7 respectively. The ranges were taken by selecting the interval of the function where the possibility $\psi > 0.2$. It is within this range that the algorithm most likely will produce the reflectance result. Lower and higher reflectances are very unlikely to result from the optimization that seeks the highest possible general possibilities for all land cover types involved on a pixel. From these ranges, NDVI was computed resulting in a range of NDVI values. Different combinations of RED and NIR reflectance may yield the same NDVI. This is illustrated for possible NDVI for maize in Figure 7.1. The 3D plot of the NDVI shows the surface produced for all possible combinations of RED and NIR reflectance. Only a small area of the whole surface contains the NDVI that may potentially be produced from values from within valid RED and NIR ranges that stem from land cover type specific histograms.

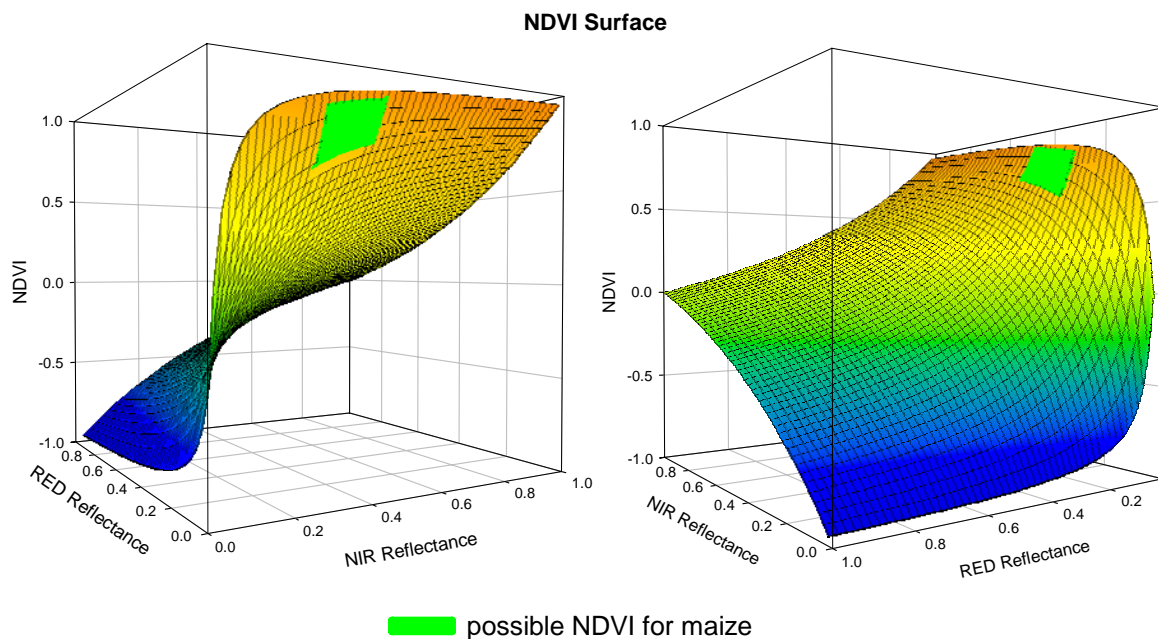


Figure 7.1: The surface formed by possible NDVI values viewed from two angles (the graph to the right is rotated 90° to the right as compared to the graph on the left). The solid green part of the surface is the NDVI that may result from valid ranges of RED and NIR reflectances of maize on June 19th. A horizontal plane intersecting the surface would cut along equal values of NDVI obtained from different combinations of RED and NIR reflectances.

The tetragons formed by the clipping of RED and NIR reflectances according to land cover specific properties contain the NDVI for the application of the land cover specific LAI algorithms. Analysis results of the obtained LAI are presented in Table 7.1.

Table 7.1: Statistics of LAI values obtained when possible NDVI are applied in land cover specific LAI algorithms of Table 6.2.

Land Cover Type	Deciduous Forest	Mixed Forest	Needleleaf Forest	Grassland	Spring Grain	Winter Grain	Maize
NDVI							
RED range	0.001-0.079	0.008-0.034	0.004-0.040	0.014-0.900	0.020-0.060	0.022-0.060	0.030-0.080
NIR range	0.22-0.60	0.15-0.35	0.12-0.25	0.25-0.52	0.39-0.51	0.28-0.48	0.30-0.45
NDVI min	0.47	0.63	0.50	0.47	0.73	0.65	0.58
NDVI max	0.99	0.95	0.97	0.95	0.92	0.91	0.88
LAI							
LAI mean	4.45	6.87	6.61	1.89	5.41	4.77	3.71
LAI min	0.29	1.70	0.64	0.43	3.52	2.35	2.36
LAI max	9.78	8.00	8.00	3.48	7.31	7.01	4.97
stddev	2.52	1.63	2.10	0.73	0.95	1.06	0.60

The values indicate a general applicability of results from the segmentation of reflectances to be used for the computation of LAI. No extreme values occur that are not within reasonable expected intervals of LAI. Only the LAI algorithms for forest classes of mixed and needleleaf forest lead to very high values in the saturation domain of the NDVI. This however is conditional upon the exponential nature of the LAI algorithm and possibly very low RED reflectances of needleleaf canopies. With the very steep slope of the functions for RED reflectances towards the lower margin, very low RED reflectances are rather unlikely to occur. This leads to an overestimation of very high values in this simulation. In order to avoid this extreme overestimation of LAI, the algorithms of needleleaf forest and mixed forest were restricted to producing no values greater than LAI = 12.5. The validity of the ranges is supported by the fact that even without this restriction, the most frequent values are around LAI = 7 and LAI = 5.5 for mixed and needleleaf forest, respectively.

7.1.2 Application to a synthetic data pyramid

A first application of the method for reflectance segmentation was conducted using a synthetic dataset generated from high resolution 30m Thematic Mapper reflectance data and the land cover classification produced from this data. The generated dataset is a data pyramid ranging from the 30m TM resolution to 3 aggregated resolutions at 240m, 480m, 960m. These aggregation levels were chosen in order to obtain a data pyramid of resolutions comparable to available MODIS resolutions on the one hand and, at the coarsest level, resemble the 1km resolution of the DANUBIA model on the other. The original 30m resolution data also serves as the reference or “truth” dataset.

Within this data pyramid the two components of the Modifiable Areal Unit Problem (MAUP) are addressed. In the raster data the zoning scheme is predefined for each aggregation level and hierarchical across aggregation levels. Thus, the effect of varying zonation does not occur. The scale effect on coarser pixel resolution is mitigated by the approach of holding subscale fractional land cover information for each aggregation level. Topical characteristics are maintained across scales to reduce the effect on model results at different aggregations.

For each of the three coarse resolutions, the following datasets were computed:

- aggregated reflectances of the RED and NIR bands (Landsat channels 3 and 4)
- fractions of 12 land cover types on the coarse pixels (from 13 classes of 30m land cover classification, removing unclassified areas, see section 6.2.3)
- majority land cover type derived from the largest fraction in the fractional land cover types
- segmentation of reflectances of the RED and NIR bands using the aggregated reflectances, the fractional land cover dataset and the reflectance possibility functions.
- true average reflectances of each land cover type on the coarse pixels area for RED and NIR bands. These were derived by averaging the 30m resolution pixels reflectances within the coarse pixels area that belong to the same land cover type. Subsequently, this dataset is referred to as the “truth dataset” or simply “truth”
- LAI for each vegetation land cover type on a pixel, computed from the segmentation of reflectances and the true average reflectances as a reference
- LAI for the homogeneous coarse resolution pixels using the aggregated reflectances and the majority land cover type
- Aggregation of the land cover specific fractional LAI to the fractional land cover specific LAI at the coarser levels (i.e. land cover specific fractional LAI aggregated from 240m to 480m/960m and 480m to 960m)
- Total LAI on a pixel computed as the area weighted sum of all fractional LAI of all land cover types on the pixel

The average reflectance dataset was produced by averaging the reflectances of a 30m resolution band over 8x8, 16x16 and 32x32 boxes for the 240m, 480m and 960m respectively. Fractional land cover is derived from the high-resolution land cover classification applying the same box sizes and computing fractional area of the land cover types present. The output from this operation is a 12 layer stack, each layer representing a land cover type. Finding the layer with the maximum fraction on a pixel provided the majority land cover type for that pixel, i.e. the aggregated land cover at each coarse level.

The high-resolution 30m reflectances were used in combination with the high-resolution 30m land cover classification to produce a reference dataset. This “truth dataset” contains the average reflectance of all high-resolution pixels of the same land cover type on the area of a coarse pixel. The true reflectance Rt of a land cover type i on a coarse pixel is given by:

$$Rt_i = \frac{1}{n_i} \sum_{p=1}^{n_i} R_{ip} \quad (7.1)$$

where n_i is the number of pixels of land cover i on the area of the coarse pixel and R_{ip} is the reflectance of a single high-resolution pixel of land cover i . Figure 7.2 illustrates how this dataset compares to the subscale fractional data.

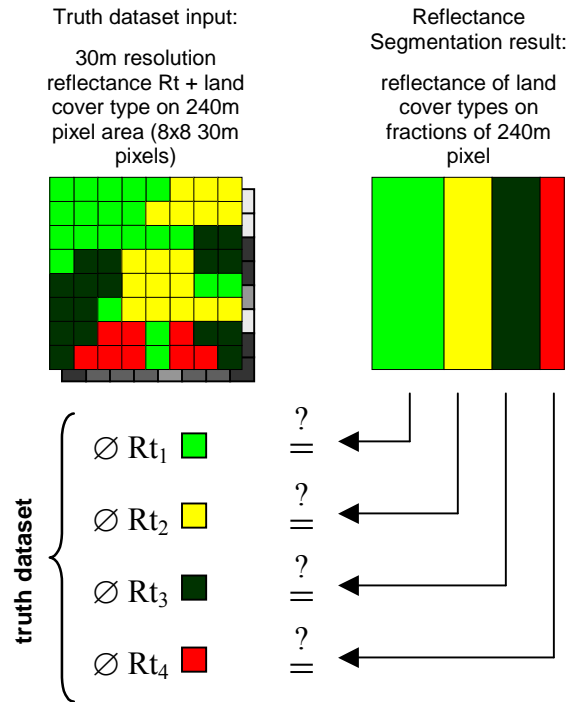


Figure 7.2: Illustration of the truth dataset for a single reflective band. It allows the comparison of information contained in high-resolution 30m data (left) and results from reflectance segmentation (right).

Land cover specific RED and NIR reflectances R_t were used to compute land cover specific NDVI and subsequently LAI by applying land cover specific NDVI-LAI relations (listed in Table 6.2).

Aggregation of land cover specific fractional LAI to a coarser scale fractional LAI (LAI_{frac}) was conducted by computing the area weighted sum of all pixels p containing fractional LAI values of land cover type i at the the fine scale ($\sum_{p=1}^{n_i} lai_i \cdot a_i$) and relating these to their total

area $\sum_{p=1}^{n_i} a_i$ on the coarser pixel:

$$LAI_{frac} = \frac{\sum_{p=1}^{n_i} lai_i \cdot a_i}{\sum_{p=1}^{n_i} a_i} \tag{7.2}$$

where n_i is the number of pixels p containing land cover type i . Equation (7.2) provides the way of scaling a quantity provided as a fractional value to a larger scale.

The total single value LAI on a coarse pixel is given by the area weighted sum of the LAI of all land cover types present on the pixel.

7.1.3 Results of reflectance segmentation at 240m

To assess the quality of the results from the reflectance segmentation for both RED and NIR reflectances, they are compared to the “truth” reflectance dataset obtained from averaging the reflectances of high-resolution pixels of the same land cover type. The results presented in this section are based on the 240m resolution data. Figure 7.3 shows the histograms obtained from the two datasets for each of the 12 land cover types and for the RED and NIR bands. As a general trend for all land cover types it can be observed that the peaks of the distributions in the reflectance segmentation (dotted line) agree well with the location of the peaks in the truth dataset in most cases (solid line). This however does not apply to the magnitude. The distributions of the reflectances from the reflectance segmentation are grouped very much closer around the maximum occurrence. Also the shapes of the distributions change from a convex normal distribution form to a concave characteristic. In some cases the location of the most frequent reflectances in the results from the reflectance segmentation is shifted compared to the highest frequencies in the truth dataset. This applies for example to the RED reflectance of rock and for the RED and NIR reflectances of snow and ice. When comparing the location of these shifted peaks with the Gaussian probability functions used in the algorithm (see Figure 6.6 and Figure 6.7) a very similar shift of the peaks of the functions in relation to the histograms can be observed. This indicates the strong influence of the position of the peak of the probability functions along the abscissa for the resulting reflectances.

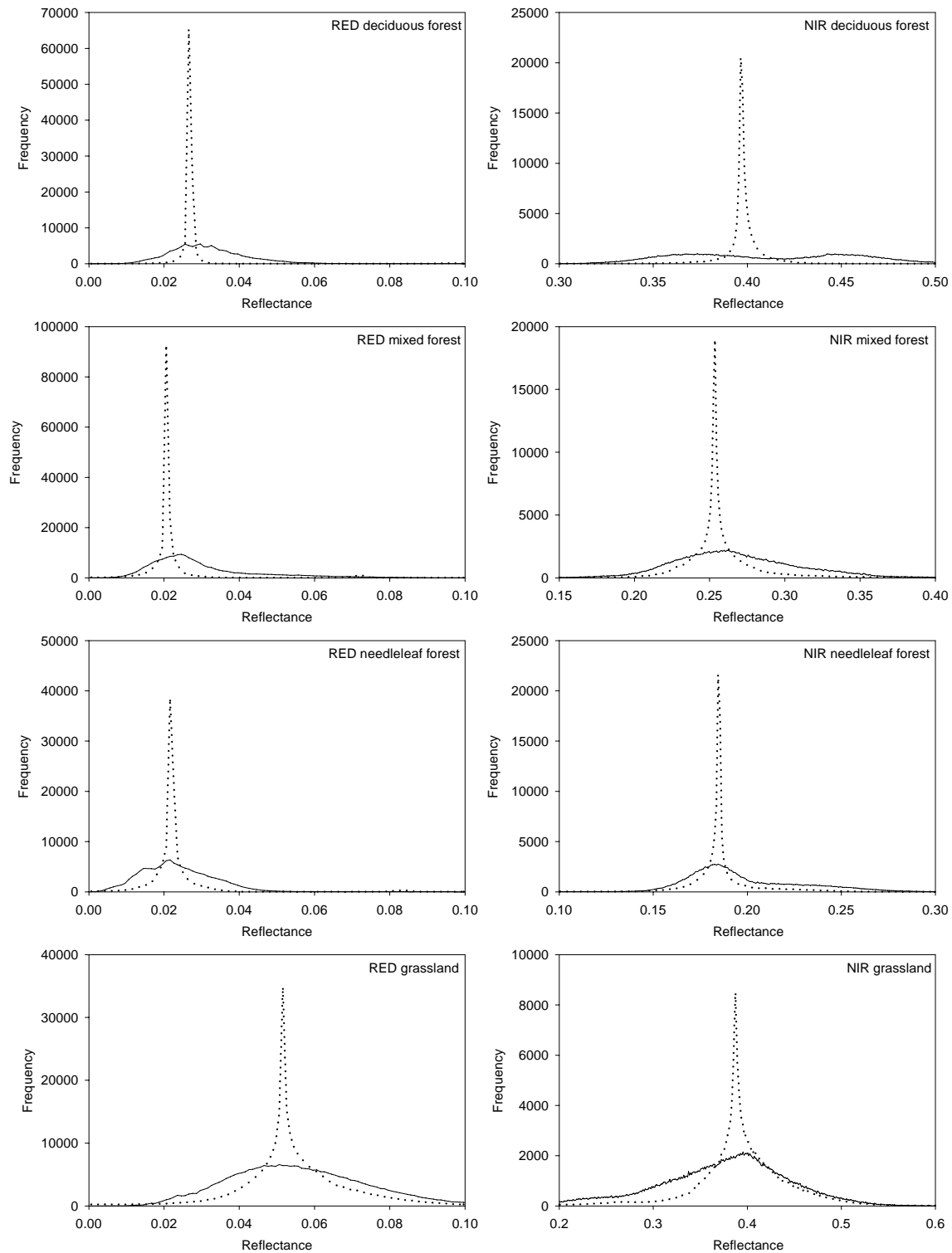


Figure 7.3: Histograms of the RED and NIR reflectances of each of the 12 land cover types. Histograms are for the full test site at 240m resolution. Results from the reflectance segmentation are shown as dotted lines, the histograms from the truth dataset are the solid lines

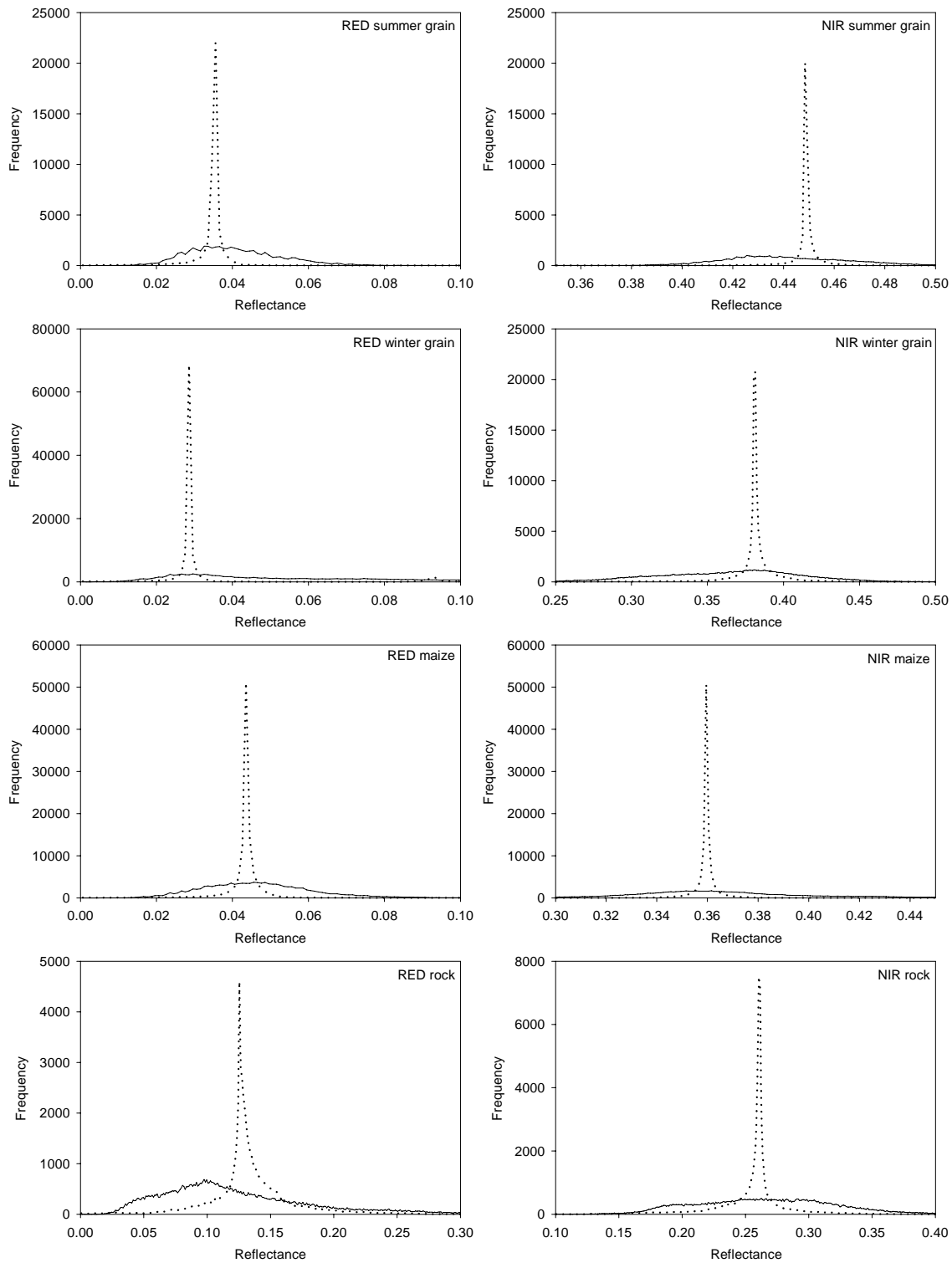


Figure 7.3 (continued)

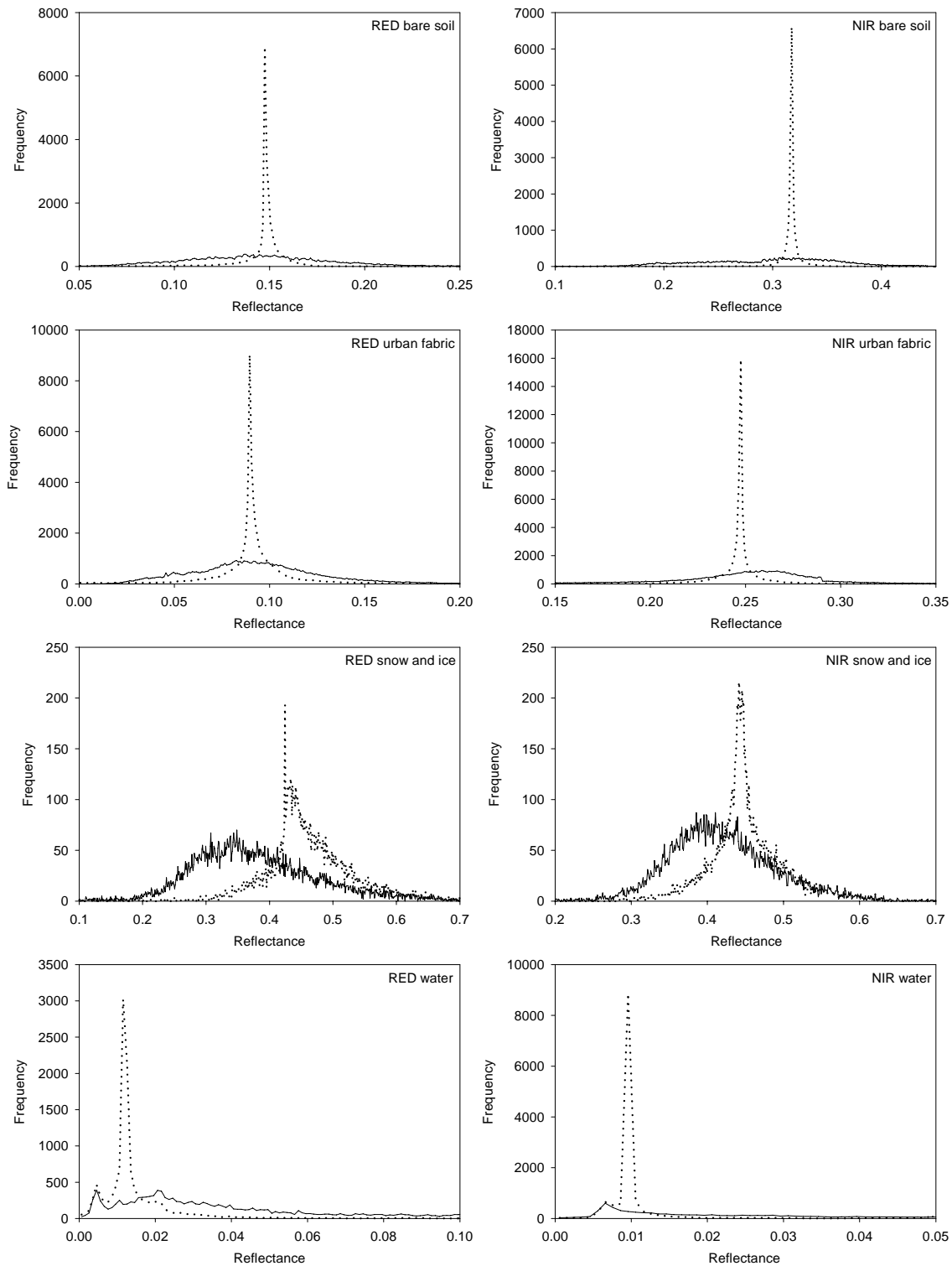


Figure 7.3 (continued)

Some of the histograms from the reflectance segmentation agree quite well with the histograms of the truth dataset, namely those that belong to the classes mixed forest, needleleaf forest and grassland. When comparing these with the portion of these land cover types in the full image frame processed (see Figure 7.4), a connection between the frequency of the land cover type and the quality of the result of the reflectance segmentation can be deduced.

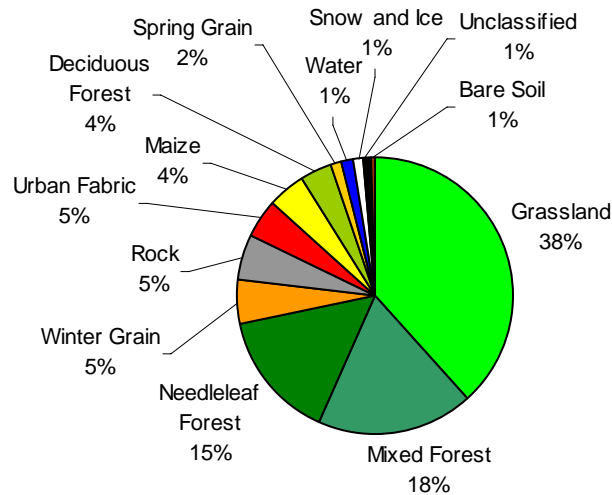


Figure 7.4: Area fractions of the 12 land cover types for the frame of the entire study area derived from the 30m land cover classification.

The histograms do not provide the information how well the absolute reflectance values obtained from the reflectance segmentation meet the true reflectances of the individual land cover types. This information is provided by relating the reflectance values of each land cover type from the 240m reflectance segmentation and the truth dataset on a pixel-by-pixel basis. The scatter plots are shown for RED and NIR reflectances in Figure 7.5 and Figure 7.6 respectively. The plots indicate but a low connection between the truth dataset and the result from the reflectance segmentation. Also, the extreme outliers do not allow the computation of coefficients of correlation. The scatter plots show a strong grouping of the results from the reflectance segmentation around a mean value indicated by a horizontal orientation of a large portion of the samples. However, in some plots a strong second “axis” along the 1:1 line can be observed. This again is the case with the land cover types taking up the larger area fractions of the test area. All of these classes also exhibit a grouped set of extreme outliers, most pronounced in the grassland class.

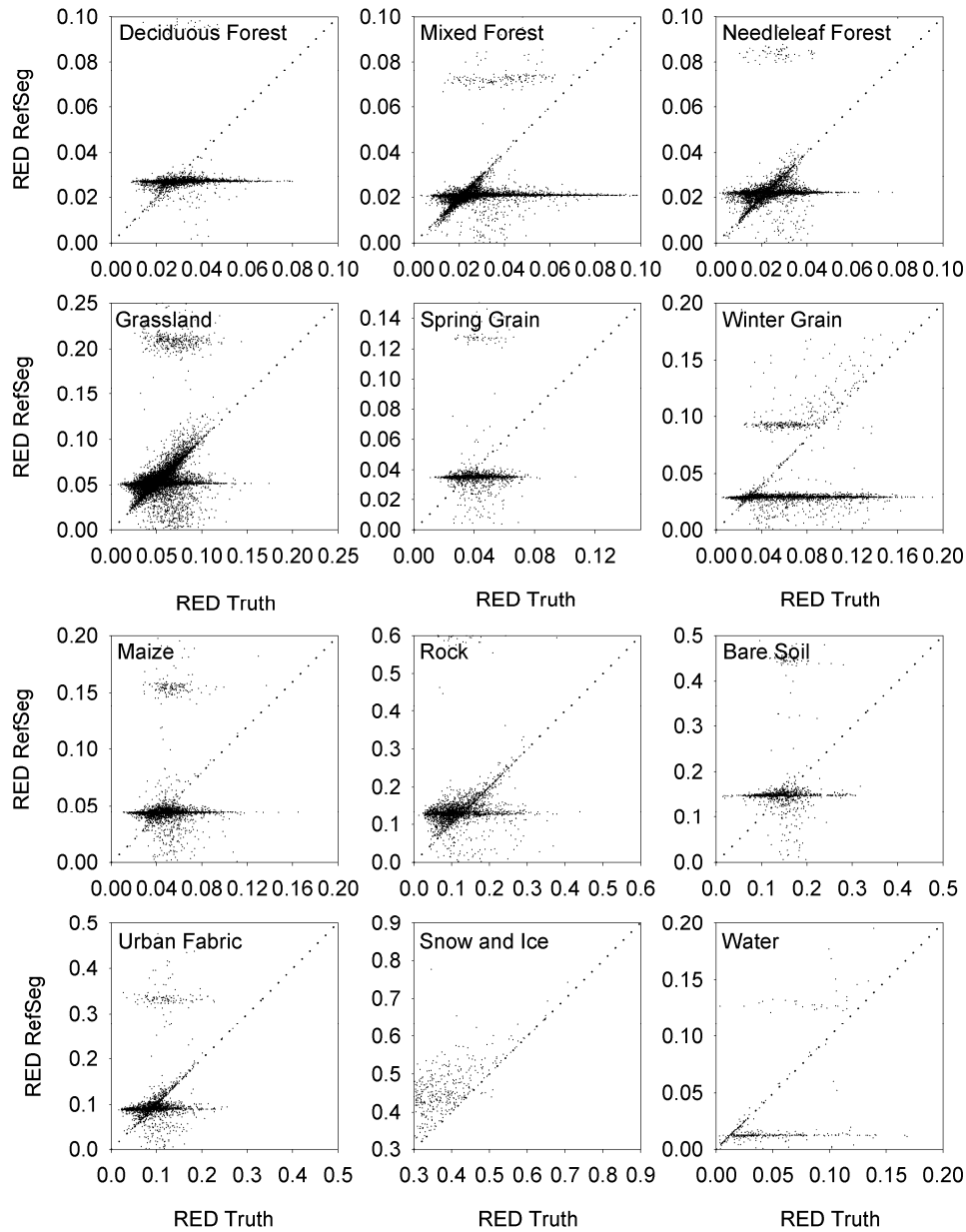


Figure 7.5: Scatter plots on a pixel by pixel basis of the 12 land cover types comparing the RED reflectances obtained from the reflectance segmentation (RED RefSeg) to the true RED reflectances obtained from the high resolution Landsat TM image (RED Truth). Data are from the full test area at 240m resolution. The diagonal dotted line is the 1:1 line.

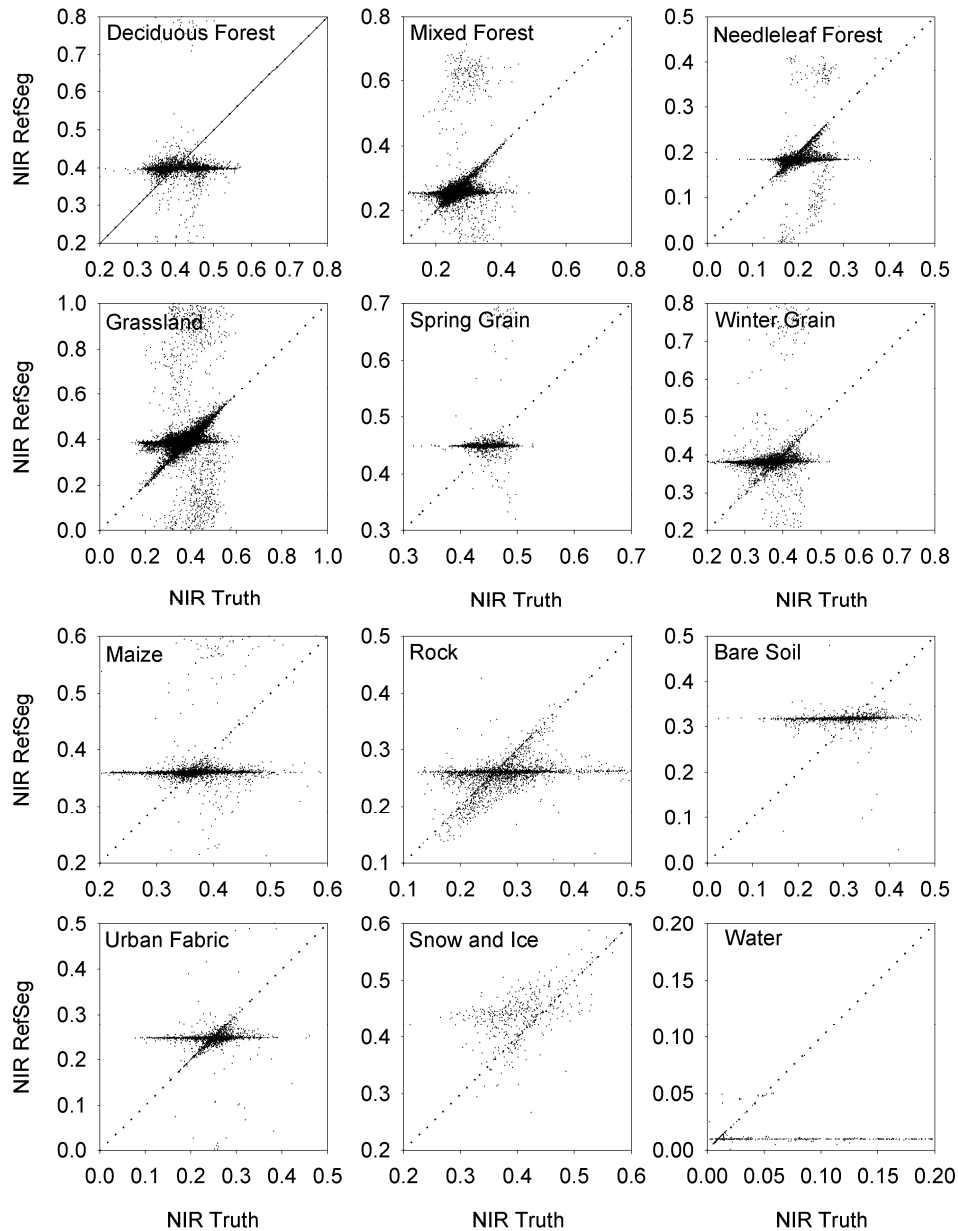


Figure 7.6: Scatter plots on a pixel by pixel basis of the 12 land cover types comparing the NIR reflectances obtained from the reflectance segmentation (NIR RefSeg) to the true NIR reflectances obtained from the high resolution Landsat TM image (NIR Truth). Data are from the full test area at 240m resolution. The diagonal dotted line is the 1:1 line.

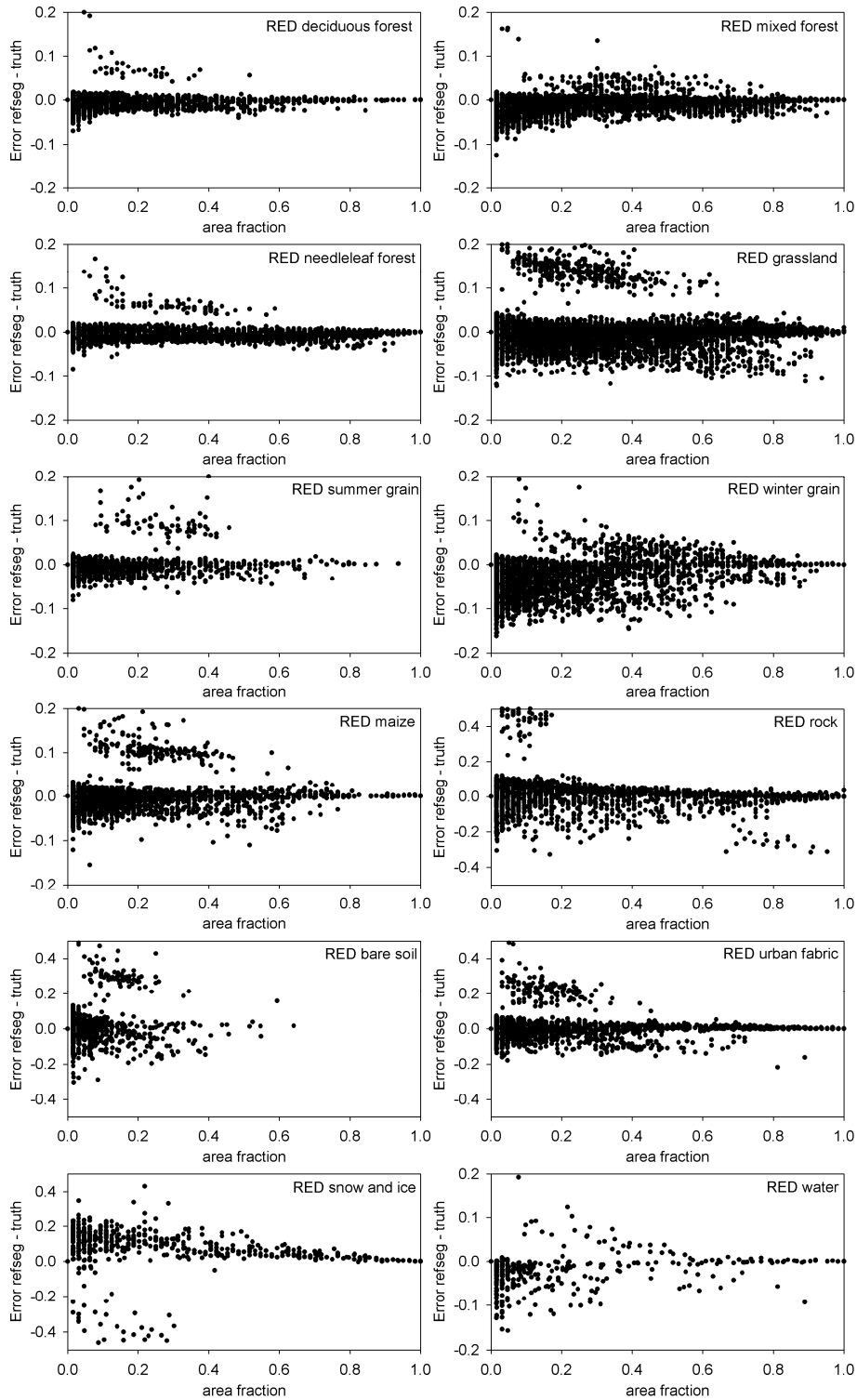


Figure 7.7: Absolute error between land cover types 240m RED reflectances in the truth dataset and the reflectance segmentation result depending on the area fraction of the land cover type.

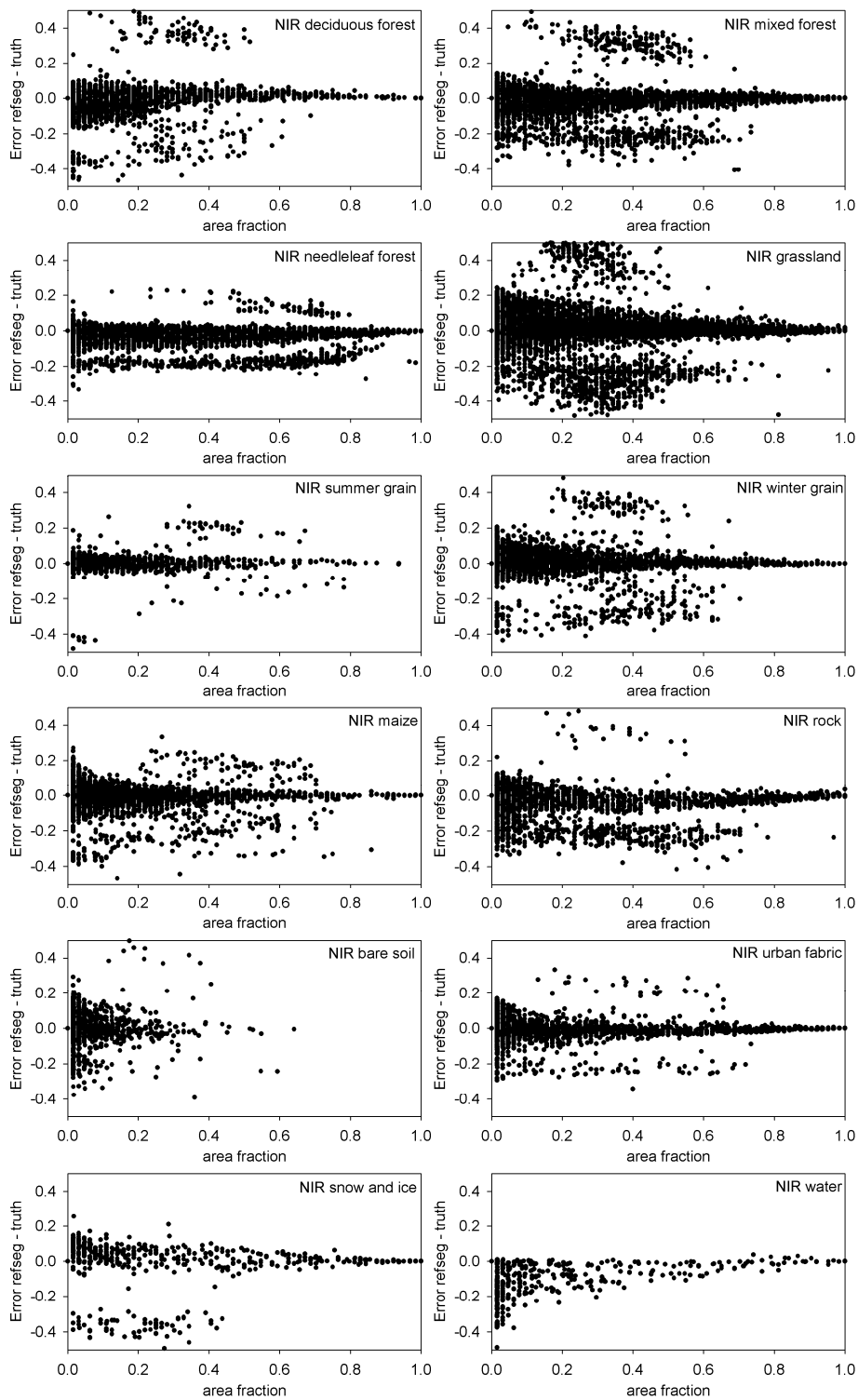


Figure 7.8: Absolute error between land cover types 240m NIR reflectances in the truth dataset and the reflectance segmentation result depending on the area fraction of the land cover type.

On a homogeneous pixel, the algorithm will not change the reflectance for the single land cover type. Thus, no error will result for these cases. The above said suggests a dependency between the error introduced by the reflectance segmentation algorithm and the area fraction of the land cover type. This dependency is investigated in Figure 7.7 and Figure 7.8 for the RED and NIR bands respectively. The plots show a mitigation of error with the increase of area fraction on a pixel for all land cover types. The smaller the land cover types fraction on a pixel the larger the error observed. In the reflectance segmentation of the RED band underestimation of the true reflectance is dominant (Figure 7.7). In the reflectance segmentation of the NIR band both under- and overestimation of the true reflectance occur (Figure 7.8).

Another characteristic of the reflectance segmentation algorithm can be observed in Figure 7.7 and Figure 7.8: There seems to be a gap between smaller error and larger error. Lesser “moderate” error in between occurs. This phenomenon is most pronounced in the NIR reflectance error of the needleleaf class (Figure 7.8) but can be observed in the error of numerous other land cover types.

The vertical striping in the plots of Figure 7.7 and Figure 7.8 is due to the fact that land cover fractions in the datasets examined are multiples of 1/64. This is a result from the aggregation of the 8x8 boxes of 30m pixels to the 240m pixels.

The results from the reflectance segmentation can be summarized in three points:

- the reflectance segmentation greatly reduces the variance of the true reflectances, putting an emphasis on the mean values of a land cover type. A smoothing of the images occurs (see also the visual interpretation in section 7.1.5).
- this results in poor reproduction of the true reflectances in the results from the reflectance segmentation of all land cover types.
- errors in the reflectance segmentation are greater where the fractional area of a land cover type is small. Error is zero whenever a pixel is homogeneously covered by a single cover type.

A random factor that can not be specified more precisely drives the results of the reflectance segmentation. Extreme deviations of reflectances from the mean are only met by chance in the results of the reflectance segmentation. However, the information content on a single pixel is greatly enhanced as compared to generally assumed homogeneity of pixels. This allows for a further investigation and comparison of the results of the reflectance segmentation to the single pixel value alternative when LAI algorithms are applied to the data.

7.1.4 Results of LAI retrievals based on reflectance segments at 240m

The layers of RED and NIR reflectances of the individual land cover types were used to compute NDVI and subsequently LAI for the vegetation cover types. This was performed for both, the truth dataset and the results from the reflectance segmentation. Using the true average land cover type specific reflectances to compute land cover type specific LAI is one way of generating a LAI reference dataset. Another way is the computation of LAI from the original 30m resolution data and subsequent averaging of this high resolution LAI for each land cover type on a coarse pixel. However, the two ways of deriving a truth dataset for LAI are on a par with each other as illustrated in Figure 7.9. The regression line is close to identical with the 1:1 line and $r^2 = 0.9964$. The LAI dataset derived from the averaged high-resolution reflectances was preferred in the comparison with the results from the reflectance segmentation because with this method, the procedure of parameter retrieval is equivalent to the method applicable to the data obtained from reflectance segmentation. The high correlation of the two options of a truth dataset is a strong indicator for the plausibility of the

approach of the derivation of a land surface parameter like LAI based on homogeneous land cover type units.

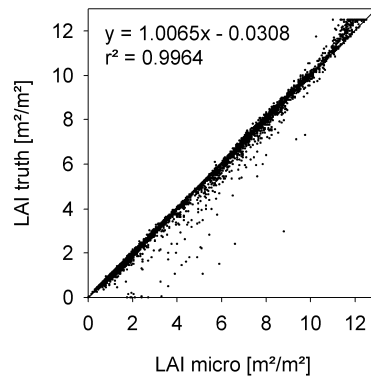


Figure 7.9: Correlation of the two options of generating a reference dataset for land cover type specific LAI at 240m. LAI micro is the 30m resolution LAI averaged per land cover type. LAI truth is derived from average reflectances of land cover types.

The following of this section focuses on four areas of the 240m dataset to directly compare the LAI values obtained from true land cover types reflectances, the segmented reflectances and the mesoscale LAI for the homogeneity assumption. Two small areas, Hochstadt and Gut Huell, are typical rural landscapes. Their land cover types are shown in Figure 7.10. A grid superimposed on the land cover classification cutouts suggests the areas of the corresponding 240m pixels. Each grid cell represents a pixel whose single reflectance value goes into the reflectance segmentation. While the Hochstadt area has rather rapidly changing cover types and smaller homogeneous areas, the Gut Huell area exhibits larger patches of homogeneous cover type resulting in a larger number of homogeneous 240m pixels. Both areas are used in a pixel-by-pixel analysis of LAI derived from reflectance segmentation. Their size is 1920x1920m.

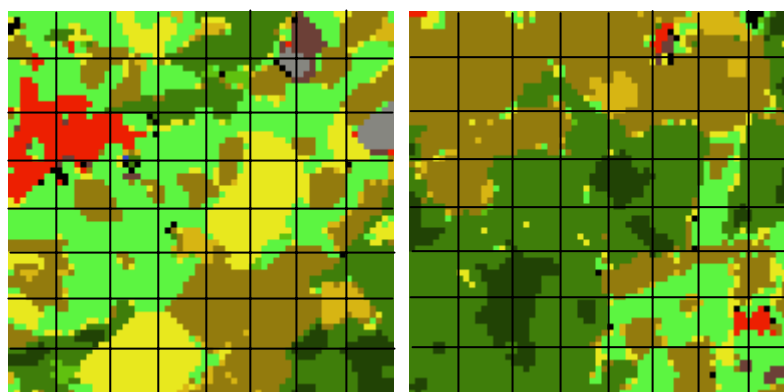


Figure 7.10: Test areas Hochstadt (left) and Gut Huell (right) used in the investigation of LAI values obtained from reflectance segmentation. The images show the land cover types at 30m resolution with a 240m grid superimposed.

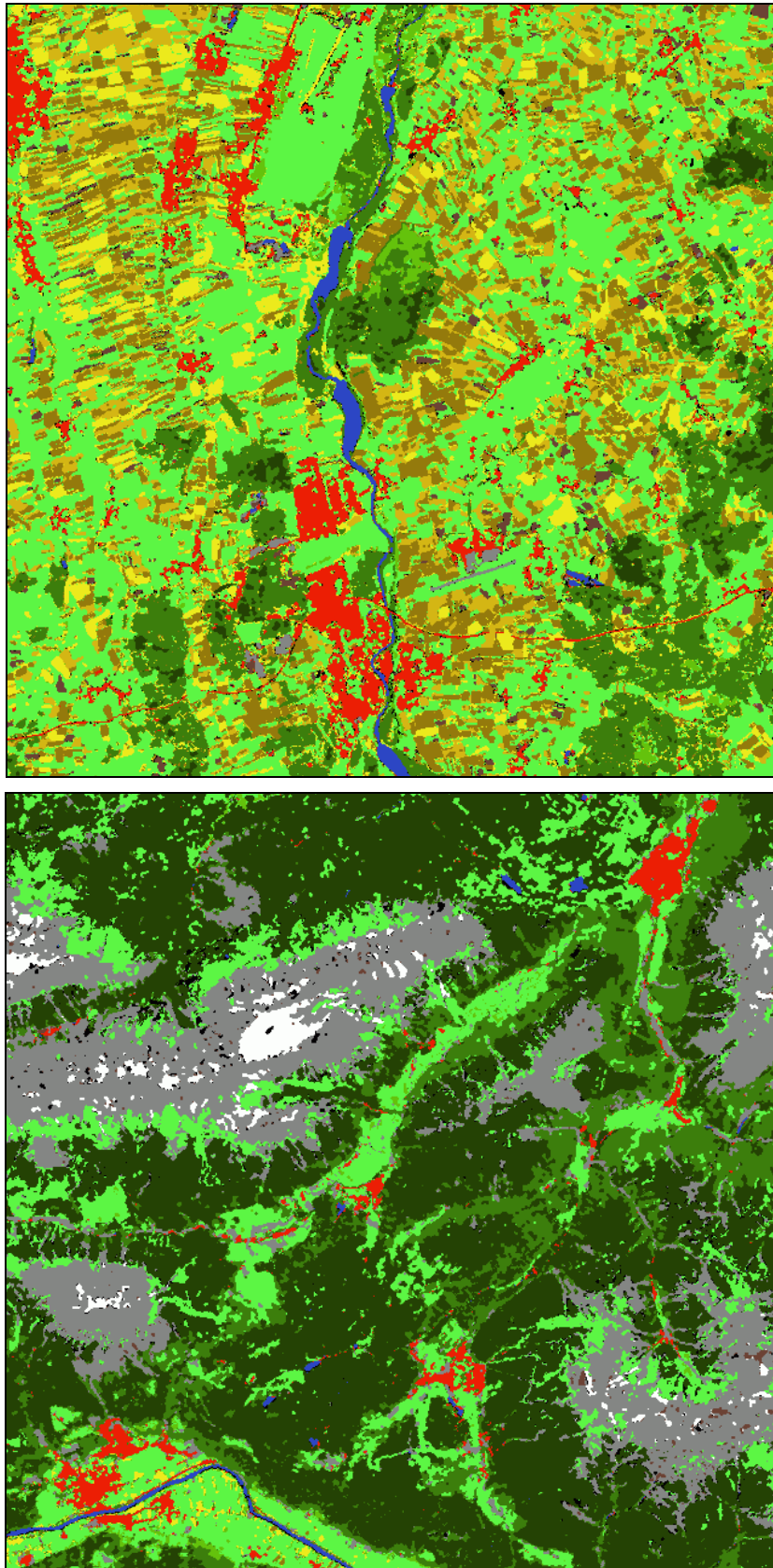


Figure 7.11: Test areas Landsberg (above) and Wetterstein (below) used in the investigation of LAI values obtained from reflectance segmentation. Size: 640x640 pixel at 30m resolution; 19.2x19.2 km. Legend see Figure 7.10.

Two larger areas shown in Figure 7.11 were chosen to obtain a statistically significant amount of data. The first, named Landsberg is structurally very much similar to the smaller areas of Hochstadt and Gut Huell. It characterizes the northern part of the study area and is made up of the different types of agricultural crops, grassland, forests and urban areas. The second, named Wetterstein is located in the southern part of the test area and resembles a typical alpine landscape. It is made up of large mixed and needleleaf forests, rock and snow surfaces and grassland as well as some settlements and agricultural fields on the valley floors. The size of the larger areas is 19.2x19.2 km. UTM Coordinates of all four areas are listed in Table 7.2.

Table 7.2: Corner Coordinates (UL, UR, LR, LL) of the test areas used in the analysis of LAI results from reflectance segmentation.

Area name	UL UTM32 (easting/northing)	UR UTM32 (easting/northing)	LR UTM32 (easting/northing)	LL UTM32 (easting/northing)
Hochstadt	668808.76 5325726.00	670728.76 5325726.00	670728.76 5323806.00	668808.76 5323806.00
Gut Huell	671688.76 5329566.00	673608.76 5329566.00	673608.76 5327646.00	671688.76 5327646.00
Landsberg	629928.76 5340606.00	649128.76 5340606.00	649128.76 5321406.00	629928.76 5321406.00
Wetterstein	654408.76 5258526.00	673608.76 5258526.00	673608.76 5239326.00	654408.76 5239326.00

Analysis of single segmented Pixels

Table 7.3 presents a selection of the results of LAI computation on single moderate resolution pixels from the Hochstadt and Gut Huell areas. From either area six pixels were chosen showing two examples of each, good, moderate and poor results. Additionally two homogeneous pixels from the Gut Huell area were added. The latter only demonstrate the 100% agreement of reflectance segmentation results with the majority on homogeneous pixels.

The first two pixels in the Hochstadt part of the table (197/320 and 193/317) are examples of good results of reflectance segmentation. In the first pixel two almost equally sized fractions (mixed forest, winter grain) make up more than 70% of the pixel area. All fractional land cover types show little error in the RED and NIR reflectances as well as in the LAI estimates. Consequently, the LAI sum on the pixel of reflectance segmentation shows much better agreement with the truth than the LAI derived from majority land cover and moderate scale reflectance. In the second pixel the mixed forest class dominates the area of the pixel. The segment of this class is modeled quite well while the classes with minor fractions exhibit much larger error. When validated against the majority alternative however, the total LAI on the pixel is still closer to truth when computed by reflectance segmentation than by majority assumption.

Two pixels with moderate error follow in the table (200/317 and 199/319). Again, the distribution of areas is dominated by one class in the first case and well spread to four classes in the second. Both pixels show a very large relative error in one of the minor fractions and large relative error in most other fractions. This leads to a relative error on the moderate pixel LAI of approximately 20%. In the first case this result may be still be close to the truth but is outperformed by the majority LAI. In the second the 20% error amounts to less than half the absolute error of LAI from the majority data leading to a still better estimate of LAI from the reflectance segmentation. Land cover type specific fractional LAI is substantially error prone on these pixels.

However, in the last case the majority land cover type rock predicts zero LAI for the pixel. This is the case although about 40% of the pixel are covered by vegetation. Thus, the relatively better result of the homogeneity model does remain questionable.

In the Gut Huell section of the table, pixels with fewer cover types present on the pixel are shown. Again the first two pixels listed (178/327 and 183/326) show good fractional results whose sum is a better estimate than the majority LAI. In the first pixel, largest error occurs on the grassland fraction of the pixel. This fraction however is only 3% of the pixel area. Neglecting the second largest fraction on the pixel, mixed forest, leads to substantial error in the LAI derived from the majority dataset. The result from reflectance segmentation is closer to truth even though its error (relative error of RED/NIR reflectances) is up to 37%. In the second pixel the influence of neglecting a land cover type on the pixel is less pronounced, mainly because of the higher similarity of LAI amount of the two forest classes. But also, for both classes' fractions, error is low in the reflectances as well as in LAI.

On the pixels with moderate result (182/332 and 183/332), large error in the reflectance segmentation of the RED band results in error exceeding 50% on the LAI of the land cover types. The lumped value on the mesoscale pixel may still be acceptable when compared to the truth dataset, but the homogeneity model yields better estimates in both cases. In both pixels the largest fraction holds the majority of the pixel area, which may support a good estimate from the majority dataset. The absolute error of 0.3 and 0.15 units of LAI from reflectance segmentation remains quite close to the truth values. In the two cases, aggregation to the mesoscale mitigates error to a moderate degree. Land cover type specific values, however, are examples of failure of the prediction of LAI.

The next two cases are examples of poor results in the Gut Huell area (184/332 and 179/328). In both cases, the larger area fraction cover types exhibit the largest error. Here, the error results from both, the reflectance segmentation of the RED band and the NIR band. Absolute error is tremendous in the fractional LAI estimates as well as in the moderate scale lumped value. These larger errors occur on pixel samples with a larger host of land cover types, while most cases of fewer land cover types exhibit better estimates. In both cases the majority model yields LAI closer to the truth reference values.

The last two pixels are cases of homogeneous cover type on the pixel. In both cases results from reflectance segmentation are equivalent to the majority model results. The small deviation of RED and NIR reflectances in the second example (180/327) are due to rounding errors in the reflectance segmentation computation and the precision of data storage.

Comparison with the truth dataset

Regression analysis was conducted for all four test areas. For each site, the fractional land cover type specific LAI values (*LAI refseg*) were validated against the truth dataset (*LAI truth*). Land cover types with zero area fraction were omitted in the statistic. On the lumped 240m level, the area weighted sum of reflectance segmentation derived LAI (*LAI sum refseg*) and the result of the majority LAI model (*LAI majority*) were compared with the sum of the fractional LAI from the truth dataset (*LAI sum truth*). Pixels with zero LAI were omitted in this comparison.

The result from the regression analysis of all fractional LAI for all land cover types are shown in Figure 7.12. The coefficient of determination of the Hochstadt, Gut Huell and the Landsberg areas of 0.76, 0.83 and 0.74 respectively, suggest a fairly good explanation of the true LAI. In the Wetterstein area the coefficient is only 0.54 showing poorer agreement with the truth dataset. The plots in Figure 7.12, however uncover a similar striping or layering in the data as it was observed in the analysis of the reflectances. This is best observed in the

plots of Landsberg and Wetterstein with a much larger number of samples (~250 in the small test areas, ~20.000 in the larger areas). The striping is a result from the strong concentration of reflectances around a mean value that is reflected in the LAI retrievals. Each layer of dense grouping of samples corresponds to a land cover type. The quite frequent values close to the mean of RED and NIR reflectances that go into the land cover specific LAI algorithms produce this effect. It can be interpreted as the low variance that results from reflectance segmentation and that is transported to LAI by the algorithms. It needs to be stated that for this kind of distribution regression analysis is an inadequate tool so that the coefficients of correlation are questionable for the Landsberg and Wetterstein areas.

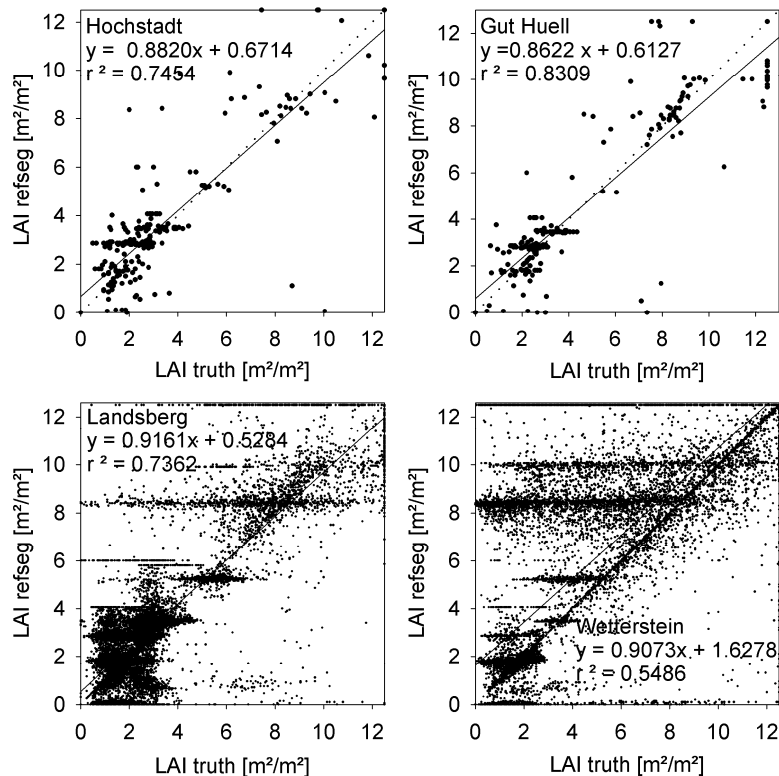


Figure 7.12: Results from regression analysis of all fractional LAI values for all land cover types in the four test areas. LAI from reflectance segmentation (LAI refseg) is plotted against LAI from the truth dataset (LAI truth). Spatial resolution is 240m.

The striping is no longer prevalent when LAI is aggregated to the 240m scale. The lumping of all land cover types LAI on a 240m pixel allows to compare the results to the alternative of deriving LAI on homogeneous pixels. In Figure 7.13 the plots from this analysis are shown. The regressions of all areas except the Wetterstein area show that the lumped LAI from reflectance segmentation correlates to the truth dataset to about the same degree as the LAI from the majority data ($r^2 \approx 0.9$). This is cut back in the Wetterstein area with a regression of only 0.71. A frequent overestimation of LAI is observed for this area. In conjunction with the poor regression of that area in the comparison of the land cover type specific LAI these results suggest a much lower performance of the algorithm in the mountainous environment. Reasons for this shall be addressed later in the discussion of the results.

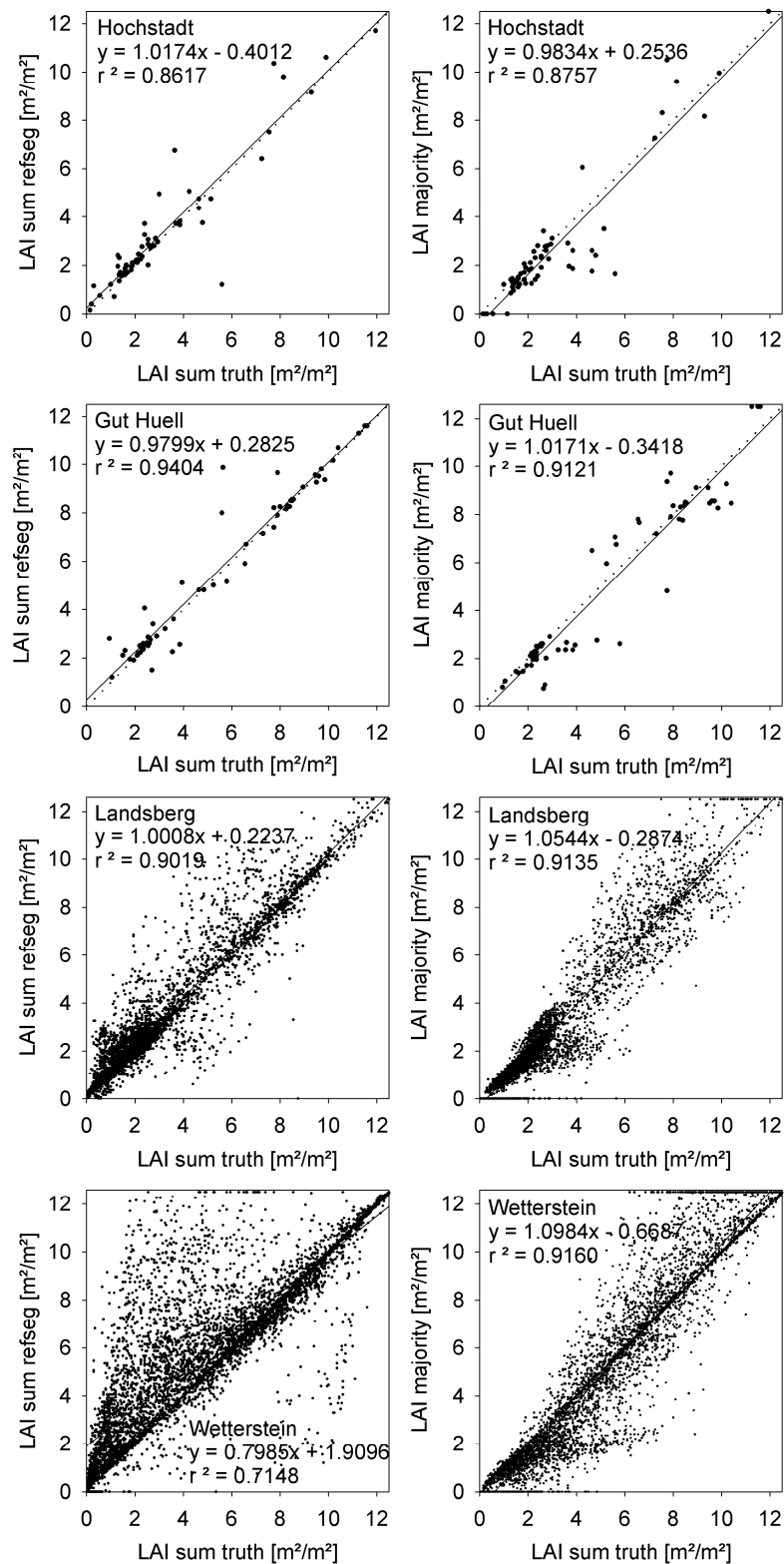


Figure 7.13: Regressions of the lumped values of LAI on 240m pixels. The left column compares the area-weighted sums of different land cover types LAI from reflectance segmentation (LAI sum refseg) to the area-weighted sums of LAI from the truth dataset (LAI sum truth). The right column compares the LAI obtained from the homogeneity method (LAI majority) to the truth dataset.

Statistics of the test areas

Statistics of the relative and absolute error of the results of the reflectance segmentation were assessed for the fractional land cover type specific LAI and the aggregation to the homogeneous 240m scale. The error was computed against the truth dataset and the aggregation of these data. The result from the majority dataset was again used as a comparative measure on the 240m scale. This comparison may provide an estimate of the inherent quality of the results from the reflectance segmentation algorithm when considering a representative value of LAI for the (in most cases) heterogeneous area of a 240m pixel. All statistics were derived excluding land cover types with no fractions on a pixel (i.e. zero values) and 240m pixels exhibiting zero LAI.

As can already be concluded from the aforesaid, extreme maximum values occur in the data. These unacceptably high maxima adulterate the mean and the standard deviation, drawing an inappropriate picture of the results. This can best be observed in the maximum relative error of the two larger test sites Landsberg and Wetterstein with errors of several thousand percent (see Table 7.4). In order to correct this false impression, the 95th percentile of each error data set was taken and mean maxima and standard deviation was computed for this percentile. This removal of the 5% of maximal error excludes the values that are positively inappropriate.

In the fractional LAI results, the three areas of Hochstadt, Gut Huell and Landsberg show absolute error around 0.6 units of LAI in the 95th percentile and still below one in the mean of the full dataset. The value of the error at the 95th percentile ranges around three units of LAI. This maximum error is a large deviation, but greatly reduced as compared to the statistics of the full dataset. Standard deviations smaller than one unit of LAI suggest a reasonable amount of error in the data. Relative error however may still be large and depends greatly on the land cover type because each cover type has a different appearance concerning the possible maximal leaf area. In the three agriculturally dominated sites mean relative error remains between 20% and 30%.

The results in the mountainous Wetterstein area exhibit errors that amount to approximately double the values as compared to the other sites.

Table 7.4: Statistics of the relative and absolute error in the land cover type specific fractional LAI from reflectance segmentation for the four test areas. Error was assessed against the truth dataset.

	relative error LAI refseg [%]				absolute error LAI refseg [m ² /m ²]			
	Hochstadt	Gut Huell	Landsberg	Wetterstein	Hochstadt	Gut Huell	Landsberg	Wetterstein
mean	37.7	27.5	44.4	124.5	0.86	0.91	0.80	1.78
median	13.5	3.0	14.6	10.5	0.43	2.78	0.45	0.35
max	470.0	338.5	16700.0	24900.0	10.00	7.35	12.50	12.50
min	0.0	0.0	0.0	0.0	0.00	0.00	0.00	0.00
stdev	62.3	46.1	175.3	514.9	1.32	1.28	1.09	2.75
95th percentile								
value	148.8	94.3	171.4	534.5	2.79	3.30	2.65	7.85
mean	26.8	19.4	27.2	54.8	0.63	0.69	0.61	1.36
max	147.8	93.0	171.0	534.4	2.75	3.25	2.60	7.80
min	0.0	0.0	0.0	0.0	0.00	0.00	0.00	0.00
stddev	33.6	22.5	34.5	100.6	0.67	0.78	0.65	2.09

The aggregation of LAI from the land cover type fractions to the homogeneous 240m level greatly reduces the error in the data. Even without removing very large error by focusing on the 95th percentile, the mean absolute error is 0.53, 0.40 and 0.39 in the Hochstadt, the Gut Huell and the Landsberg area, respectively. Again, the mountainous Wetterstein area exhibits poorer results. These mean absolute errors are all lower than the error introduced in the homogeneity assumption alternative. While standard deviations are close to equivalent in the absolute errors observed in lumped results from reflectance segmentation and the majority LAI, maxima from the reflectance segmentation exceed the extremes in the majority data. Looking at the 95th percentile of the data, the mean absolute error of the lumped reflectance segmentation results remains lower than the majority LAI's error. It is well below 0.3 units of LAI, even in the larger dataset of the Landsberg area. Remarkably, the maximal absolute error is also lower in the results from the reflectance segmentation data, when the top 5% of the largest error is removed. However, in the small test areas, standard deviations are reduced, reflecting the reduced dynamics in the results from reflectance segmentation. In the larger Landsberg areas data, standard deviation retains a level commensurate to the majority LAI error. However, from the aforementioned it remains questionable if the dispersion in the reflectance segmentation results has comparable bias as the truth data.

In the small agricultural test areas, mean relative error in the data is very low in the 95th percentile for the smaller test areas and always lower than the error in the majority LAI. A mean 22% error in the full dataset of the more representative Landsberg area is almost halved to 13% when removing the largest 5% in the error. The maximum relative error, however, is lower than in the majority LAI only in the results of the Gut Huell area.

The results of the Wetterstein area are much less convincing, even when focusing on the data lumped to the 240m scale. While the mean absolute error is below one unit of LAI, maximum error of 5.4 m²/m² is almost twice the maximum error observed when deriving LAI on homogeneous pixels after the removal of the most extreme error. Then, the relative error in this area still amounts to 50% and can be over 300% in the most extreme cases. Although the LAI derived by the majority method on 240m pixels is the most error prone of all four areas, the estimates from aggregating the reflectance segmentation results are of still lower quality.

Table 7.5: Statistics of the relative and absolute error in the summed LAI from reflectance segmentation on 240m pixels and the LAI from the majority data for the four test areas. Error was assessed against the sums of LAI from the truth dataset.

relative error LAI [%]								
	Hochstadt		Gut Huell		Landsberg		Wetterstein	
	refseg	major	refseg	major	refseg	major	refseg	major
mean	25.8	26.5	12.7	22.7	21.7	19.3	73.91	29.01
median	8.3	17.2	2.2	11.0	5.9	10.7	12.9	15.1
max	283.3	100.0	194.7	253.3	983.3	128.6	1842.9	113.3
min	0.0	0.0	0.0	0.0	0.0	0.0	0.0	0.0
stdev	50.5	27.9	28.2	42.8	50.5	25.1	143.0	33.4
95 th percentile								
value	84.8	100.0	44.3	74.5	93.2	100.0	350.0	100.0
mean	3.5	4.3	1.9	3.6	12.9	13.7	49.0	18.3
max	84.6	70.5	43.8	63.8	93.1	85.2	346.2	99.1
min	0.0	0.0	0.0	0.0	0.0	0.0	0.0	0.0
stddev	11.6	11.4	6.7	10.0	18.5	13.9	76.3	20.3

absolute error LAI [m ² /m ²]								
	Hochstadt		Gut Huell		Landsberg		Wetterstein	
	refseg	major	refseg	major	refseg	major	refseg	major
mean	0.53	0.69	0.40	0.71	0.39	0.44	1.22	0.80
median	0.20	0.30	0.10	0.38	0.15	0.20	0.50	0.45
max	4.40	3.95	4.20	3.20	8.75	5.65	10.30	6.50
stddev	0.89	0.88	0.71	0.76	0.68	0.62	1.75	0.97
95 th percentile								
value	2.37	2.63	1.74	1.94	1.80	1.82	5.45	2.90
mean	0.08	0.12	0.07	0.16	0.26	0.33	0.92	0.64
max	1.95	2.40	1.65	1.90	1.75	1.80	5.40	2.85
stddev	0.24	0.35	0.22	0.41	0.35	0.39	1.19	0.68

The removal of the top 5% of the largest error raises the question of how much of the area is affected by these large errors. The mean size of area fractions charged with highest error is always smaller than the mean of all area fraction's sizes. Thus, the error extremes tend to occur on rather small area fractions. This is observed in all four test areas. Total area of the removed highest error depends on whether the assessment of this measure is performed for relative or absolute error. Generally, areas are smaller when the area of the highest *relative* error is sought. The area of the largest errors ranges from 1.5-5% of the test sites.

Further investigation of the results was conducted concerning the statistics of individual land cover types. Here, the areal fraction of the individual land cover type burdened with the 5% of the largest errors may exceed 40% of the total area of a land cover type in the test site. This observation was made for the small test areas Gut Huell and Hochstadt. The land cover types affected are those with the smallest portions in the test area so that it is always less than 1% of the total test area exhibiting these extreme errors. In the larger test sites Landsberg and Wetterstein, the areal extend of these extreme errors is smaller. The area fraction of a land cover type that shows the 5% largest error is usually below 5% in the larger test sites but is larger than 10% in the case of some cover types. These latter cases occur for the land cover types which are the most weakly represented in the test area. Again, for each land cover type, the portion of the error-burdened area is rarely more than 1% of the total area of the test site. This once more supports the notion that larger error occurs on smaller areas. The land cover type specific statistics do not yield any more significant information. Error can not explicitly be attributed to any specific land cover type in the survey of the four test areas.

7.1.5 Visual Interpretation of results at 240m

The visual display of the results from the reflectance segmentation and the subsequent computation of LAI from the land cover specific reflectances reveals the spatial component of the methodology. The images shown here comprise the full study area as delineated in chapter 2. This section displays and describes a selection of the 12 land cover types under address. Images of all land cover types are provided in the galleries in Appendix 7.

The figures show the relation between the reflectances/LAI if derived from the homogeneous majority data at 240m and the fractional data on that scale on the one hand. The difference between the reflectance segmentation and the truth dataset are illustrated on the other. Images

of the datasets are shown in the order majority-reflectance segmentation-truth from top to bottom.

Figure 7.14 shows the results from the reflectance segmentation of the NIR band of the land cover types needleleaf forest, winter grain and urban fabric. In the following, aspects of the results of these three land cover types are discussed.

In the needleleaf forest imagery, a belt of higher reflectances is observed along the northern fringe of the Alps and some patches of higher reflectance are dispersed in the northern and western part. Comparing the result from the reflectance segmentation to the truth image reveals that reflectance segmentation will capture these general large-scale changes in reflectivity. However, when focusing in on the needleleaf forests on the valley slopes in the southern mountainous area and also in the larger patches around the Munich area it can be observed that some of the dynamics in the reflectances is lost in the land cover types reflectances derived by reflectance segmentation. In comparison to the reflectance of needleleaf forest in the majority image a small change in the total number of pixels containing needleleaf forest is prevalent. This does not signify a change in area of needleleaf forest as the portion of the cover type is close to 15% of the total area in both datasets. In the extended needleleaf forest areas in the mountainous part to the south as well as in the dispersed pixels of needleleaf forest in the northern two thirds of the image the dispersion of the forest type is increased. Especially the needleleaf forest pixels in the mountains, though, exhibit more pronounced changes in gray values in the majority image's forest pixels.

In the reflectances of the winter grain land cover type the change in dissemination of the areas is most conspicuous. While the entire northern half of the images of fractional data contain this class, much lesser pixels are assigned to that class in the majority dataset. In this case, a change from 4.8% to 5.4% of the total area is observed when moving from the fractions derived from 30m data to the 240m scale. Again, in the fractional data the reduction of dynamics from the truth dataset to the reflectance segmentation data is obvious. Although in some parts of the area, such as southeast of Munich, in the very northwest of the frame and between the two urban centers of Augsburg and Munich, increased reflectivity of the winter grain land cover type is captured, the overall impression of the reflectance segmentation image is a reduced contrast in grayvalues. To the south, cultivation of winter grain is impeded by higher precipitation and elevation. It diminishes approximately south of the latitude of the large lakes, the Ammersee and Starnberger See. Only along some of the larger valleys such as the Inn valley, winter grain was classified. It is very noticeable that lower reflectance of the crop in this southern part is not captured by reflectance segmentation.

The imagery of the urban fabric land cover type is an impressive example of spatial detail that is retained in the fractional data representation. While the urban fabric areas in the majority data comprise the larger towns only and, by chance of the aggregation, some smaller villages, the fractional data reveals the general density of settlement in the area. This is quite well observed in the southern part of the frame, where settlement along the valley floors in the mountains is omitted in the majority data but retained in the fractional data. Another detail contained in the fractional data is the linear structures of transportation infrastructure. Larger roads that are detected in the 30m TM data are conserved in the images of the truth data and the reflectance segmentation. An interesting features lies in the change of reflectance in the large urban centers. Obviously, higher reflectances occur at the outskirts of the cities. As this can be observed in all three images, it may be attributable to increased contamination of the class with vegetated patches as distance from the city center increases. This contamination transports to the fractional land cover by the generation from the 30m land cover classification and is increased in the majority land cover at 240m resolution.

NIR reflectance of LCT3: Needleleaf Forest

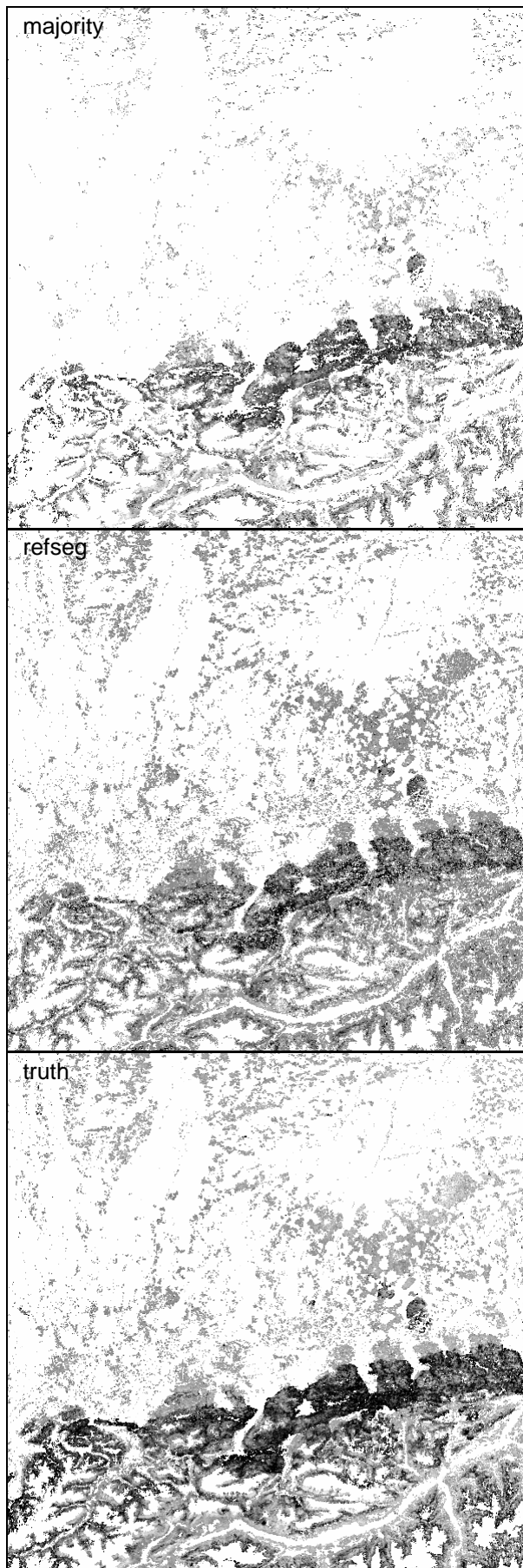
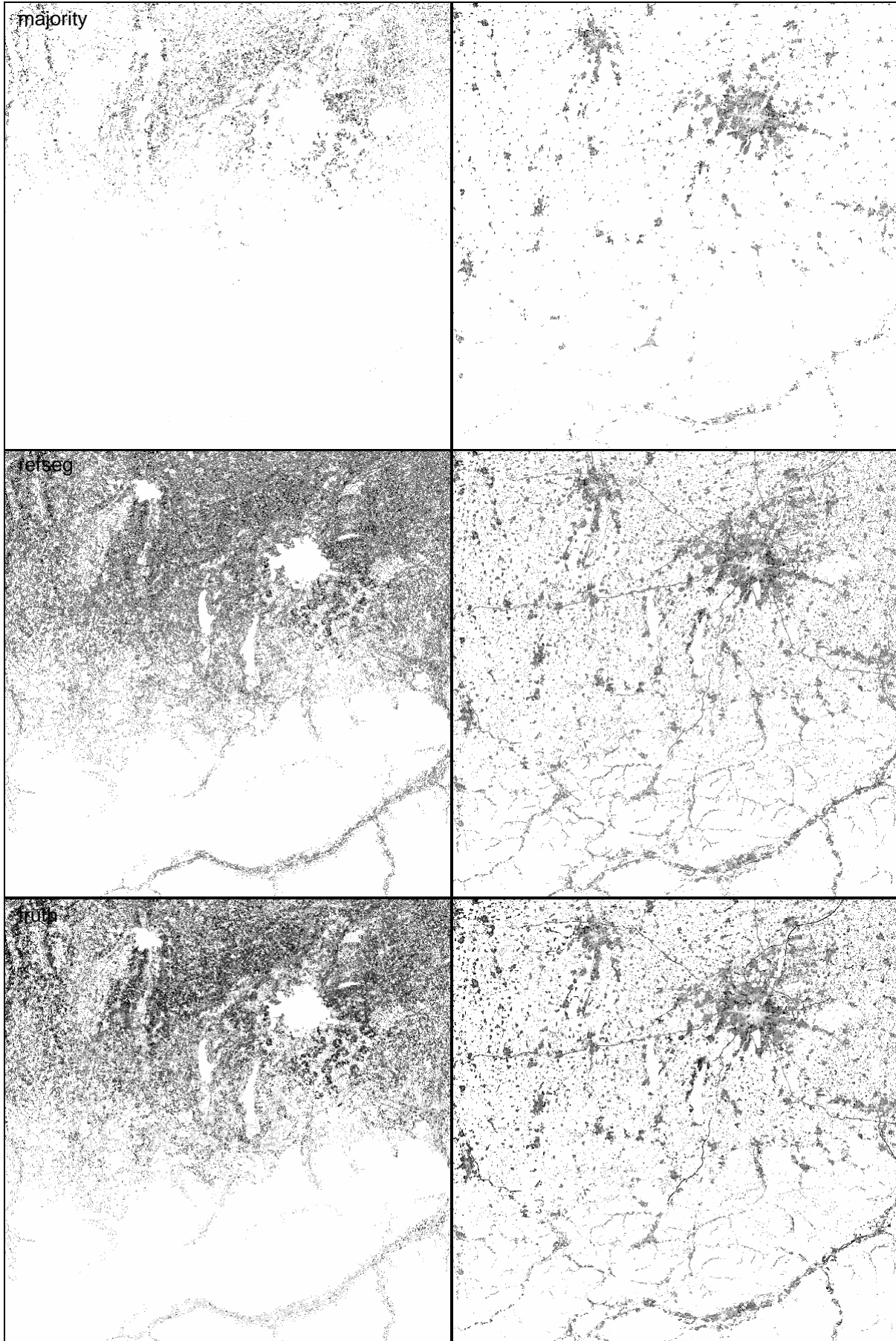
0  max

Figure 7.14: Reflectances of the NIR band of the land cover types needleleaf forest (this page), winter grain (next page left) and urban fabric (next page right). Top to bottom: majority dataset, reflectance segmentation result, truth dataset.

NIR reflectance of LCT6: Winter Grain (left) and LCT10: Urban Fabric (right)



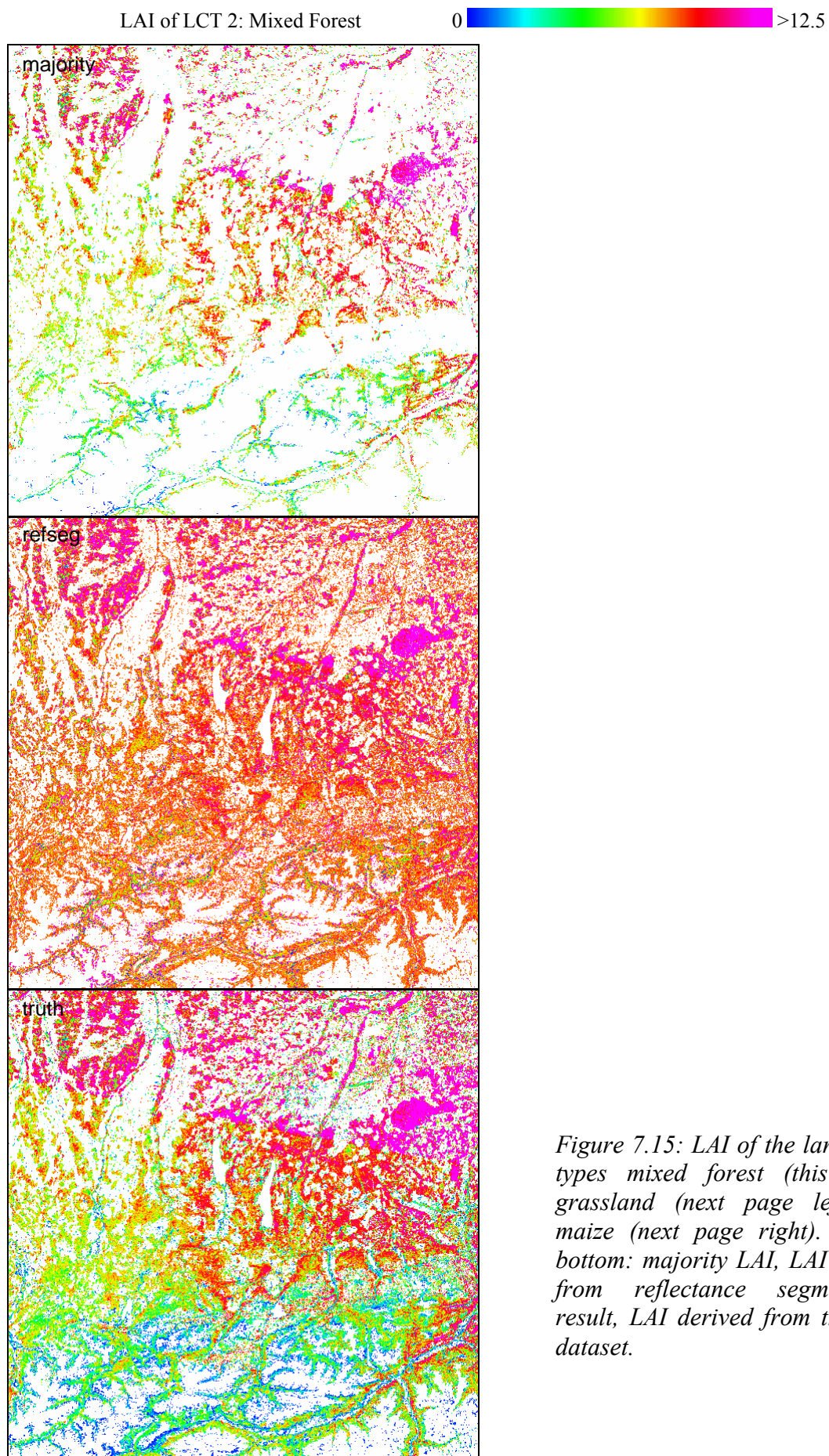
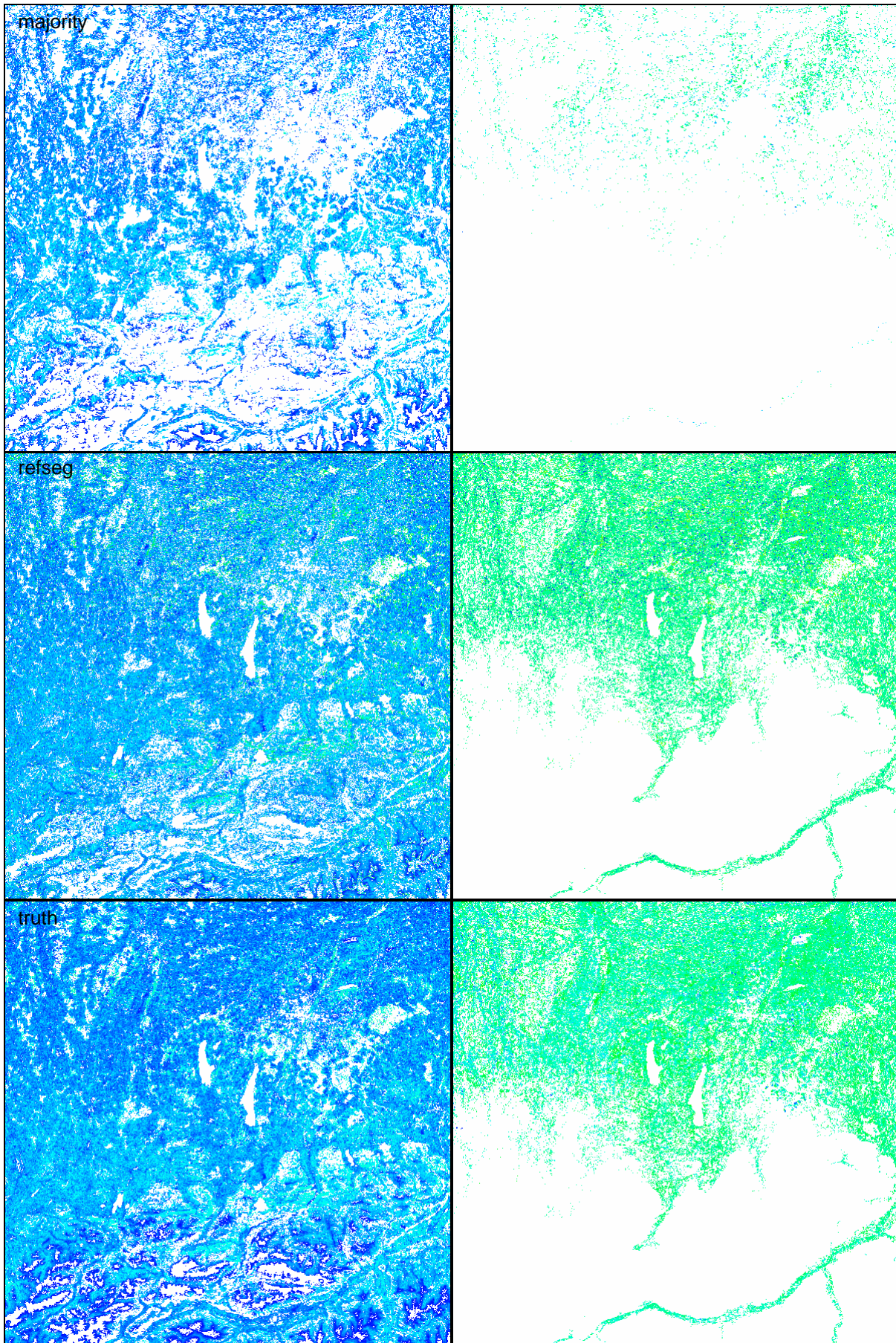


Figure 7.15: LAI of the land cover types mixed forest (this page), grassland (next page left) and maize (next page right). Top to bottom: majority LAI, LAI derived from reflectance segmentation result, LAI derived from the truth dataset.

LAI of LCT 4: Grassland

LAI of LCT 7: Maize



In Figure 7.15 the results of the LAI retrieval from the reflectance datasets are presented. The land cover types shown are mixed forest, grassland and maize. As can be expected from the previous results, the LAI derived from the reflectance segmentation suffers losses in dynamics when compared to the LAI computed from the truth dataset. On the other hand, spatial coverage and detail is equivalent to the truth dataset and more explicit than the dispersion in the majority data. For this presentation of LAI, other land cover types were chosen than for the presentation of the reflectance results with the advantage of showing the spatial distribution of another three cover types. As with the reflectance dataset, all images of the LAI are provided in Appendix 7.

In the data of the mixed forest land cover type a dramatic change in the number of pixels containing that cover type is prevalent. The class is attributed to many more pixels in the fractional data, even though the portion of mixed forest in the image frame is 1.5% larger in the majority data. Most obvious in the LAI of this land cover type is the failure of the reflectance segmentation to detect the pronounced decrease in LAI in the southern half of the image frame. In the truth data's image, a continuous attenuation of LAI can be observed especially from the valley floors to the higher elevation forest stands (blue colors in the truth data set image). In the LAI derived from the majority dataset this decrease can also be detected. These higher elevation areas do not exhibit lower LAI values in the LAI derived from reflectance segmentation. However, in the larger continuous forested areas some of the dynamics in LAI observable in the truth image will also be reflected in the reflectance segmentation image. Also, a general trend over the entire image frame of higher LAI in the north and northeast to lower LAI in the southwest is well contained in the LAI from reflectance segmentation.

The grassland class is the class with the largest proportion of the total area. Also, that land cover type experiences the largest modification of all 12 types in absolute change in area fraction from 38.5% in the 30m and fractional data to 43.1% in the majority land cover. Nevertheless, as in all fractional data, the number of pixels containing the class is larger in the fractional data. The spatial pattern of higher and lower LAI of grassland in the truth data is characterized by some darker shaded patches of higher LAI in the surroundings of the Munich area, along the northern fringe of the mountains and a triangle of higher LAI in the central western part of the image frame. Analogously to the mixed forest, LAI of grassland is lower in the elevated areas of the alpine part of the study area. This pattern is much weaker in the result from the reflectance segmentation but remains observable. Especially, the areas of higher LAI along the northern part of the Alps as well as the darker shadings around Munich and in the west are documented. However, the decrease of LAI with elevation is not reconstructed by reflectance segmentation. Also a spotty, grainy appearance of the image, especially in the northernmost and southernmost thirds coats the spatial structures when compared to the truth image. This is attributable to the previously mentioned random component in the results from the reflectance segmentation. In the southeastern corner of the grassland image of the reflectance segmentation results it is noticeable that lower LAI in the areas of higher elevation is detected while this is barely the case in the rest of the mountainous parts. This feature can be explained by numerous homogeneous grassland pixels in this area where segmented reflectances are equivalent to the majority or truth dataset and consequently so is LAI.

Most striking in the imagery of the maize land cover type is the extreme difference of dispersion of maize in the majority type and the fractional data of the truth dataset as well as the reflectance segmentation results. In this case it is a fact, that the generation of majority land cover reduces the 4.3% area of maize fields of the high resolution and fractional data to 2.6%. In the scattered pixels of the majority type a pattern is hardly observed. However, the truth dataset does show spatial variability in the LAI of the maize plants. In comparison, the

LAI of maize from the segmented reflectances rarely contains any of that spatial variability. Merely some of the spots of extremely high LAI are mirrored in the LAI from reflectance segmentation. In the case of maize, a benefit of the methodology may lie in the improved spatial representation of the land cover type only.

7.1.6 Effects of varying scale

As a final examination of the prototyping of the methodology with the synthetic data pyramid, the results from the computations at lower resolutions of 480m and 960m are analyzed. This analysis focuses on the results of LAI only. As in the previous statistical results, two different aspects are addressed: the fractional data and the data lumped to homogeneous pixel information. Analysis for this section is based on the test area Landsberg only.

In view of three different scales, the 240m, 480m and 960m resolution, another comparison may be conducted: the aggregation of land cover specific fractional LAI of the finer scale may be compared to the coarser scale results. In the aggregation of the finer resolution, the results specific to each fractional land cover type are merged to produce fractional information on the coarser scale. The aggregation was described earlier in this chapter in Equation (7.2).

The method for the segmentation of reflectances based on fuzzy a priori knowledge of reflectances can be applied to any scale as long as the land cover types resolution is sufficiently higher than the reflectance to be segmented. In any case, a land cover type will be assigned reflectance values in each band undergoing the algorithm. Changing the scale will change but the absolute area of each cover type and the area to which the single reflectance value that is segmented refers to. However, the larger the area represented by the single reflectance value the more variability within a cover types reflectance characteristics and subsequently retrieved parameters will be hidden by the values attributed to the cover type. This section casts a brief view on accuracy and consistency of results from varying scales.

When comparing the statistics of the error of LAI in fractional results from different resolutions a decrease in absolute and relative error can be observed with decrease in resolution. The LAI derived from the truth dataset at each scale is met better, the coarser the resolution selected. On the other hand, in all cases the aggregation of fractional results to coarser fractional results yields still lower mean errors when compared to the truth dataset at the aggregation scale. The results from this analysis are given in Table 7.6.

Table 7.6: Statistics of relative and absolute error of fractional LAI derived at different scales and aggregations of fractional LAI in the Landsberg test area.

	relative error in LAI on land cover specific fractions						absolute error in LAI on land cover specific fractions					
	240m	480m	240m agg. to 480m	960m	480m agg. to 960m	240m agg. to 960m	240m	480m	240m agg. to 480m	960m	480m agg. to 960m	240m agg. to 960m
mean	44.4	38.2	32.4	28.1	23.3	19.5	0.80	0.77	0.65	0.73	0.64	0.55
max	16700.0	16700.0	16700.0	1013.3	993.3	1000.0	12.50	12.40	11.50	12.50	9.95	8.85
min	0.0	0.0	0.0	0.0	0.0	0.0	0.00	0.00	0.00	0.00	0.00	0.00
stddev	175.3	200.4	202.9	53.0	47.4	47.1	1.09	1.12	0.99	1.14	1.03	0.97

When fractional LAI values are summed to a single value of LAI on a pixel, error is also reduced with higher aggregation levels. Mean absolute error is always smaller than the error produced by application of the majority method. Also the maximal error in the single value LAI derived from reflectance segmentation is reduced to a level close to the maximal error in the majority method in the lower resolution pixels. A very convincing result is achieved, when results from reflectance segmentation at the 240m scale are lumped to a single value of LAI at the 960m level. Results of the error in the LAI sums on different scales are shown in Table 7.7.

Table 7.7: Statistics of relative and absolute error of lumped single value LAI on different scales and the error of the majority method for LAI retrieval.

	relative error							absolute error						
	240m		480m		960m			240m		480m		960m		
	refseg sum	majority	refseg sum	majority	refseg sum	majority	refseg 240m agg. sum	refseg sum	majority	refseg sum	majority	refseg sum	majority	refseg 240m agg. sum
mean	21.7	19.3	19.4	21.6	16.8	23.8	11.9	0.39	0.44	0.42	0.52	0.44	0.60	0.25
max	983.3	128.6	400.0	100.0	210.5	100.0	93.8	8.75	5.65	4.85	5.20	3.90	3.55	1.85
min	0.0	0.0	0.0	0.0	0.0	0.0	0.0	0.00	0.00	0.00	0.00	0.00	0.00	0.00
stddev	50.5	25.1	32.9	23.5	23.5	22.7	12.9	0.68	0.62	0.66	0.64	0.67	0.65	0.25

7.2 Application to coincident data of high and low resolution

The data from the MODIS instrument prepared and compared in the validation of the atmospheric correction in chapter 4 are brought to bear in this section. Reflectance segmentation was applied to two of the MODIS images taken in the year 2000, namely the image from doy 170 and the image from doy 171 acquired at 11:25 UTC, both radiometrically prepared by application of PULREF. The latter scene is one of two images collected on the same day and contains the data that was imaged from an orbit west of the study area (above named MOD02PUL_171west). It exhibited much better agreement with the rest of the datasets in the validation of section 4.4.4 than the second image from that date that was produced from an orbit to the east of the catchment of the river Danube.

As stated above, the validation of the reflectance calibration was conducted using the 500m (HKM) MODIS dataset. This dataset contains aggregated reflectances from the 250m (QKM) dataset in MODIS bands 1 and 2. The application of reflectance segmentation was performed on the analogously prepared MOD02QKM data that contain the RED and NIR bands at 250m spatial resolution. These are the bands that are required for the retrieval algorithm for LAI.

The images collected with a time lag of about 24 hours are assumed to be radiometrically close to equivalent. It was argued above that, besides some radiometric disagreement of the two images, the most substantial difference of the two images is their spatial characteristics. Although both images used are labeled with the 250m spatial resolution, Figure 7.16 reveals their quite different appearance. It is the effect of viewing angle in the data. The image from doy 171 collected under a large viewing angle appears blurred and out of focus when

compared to the image from one day earlier. Substantial detail is lost in delineation of features as well as in contrast.

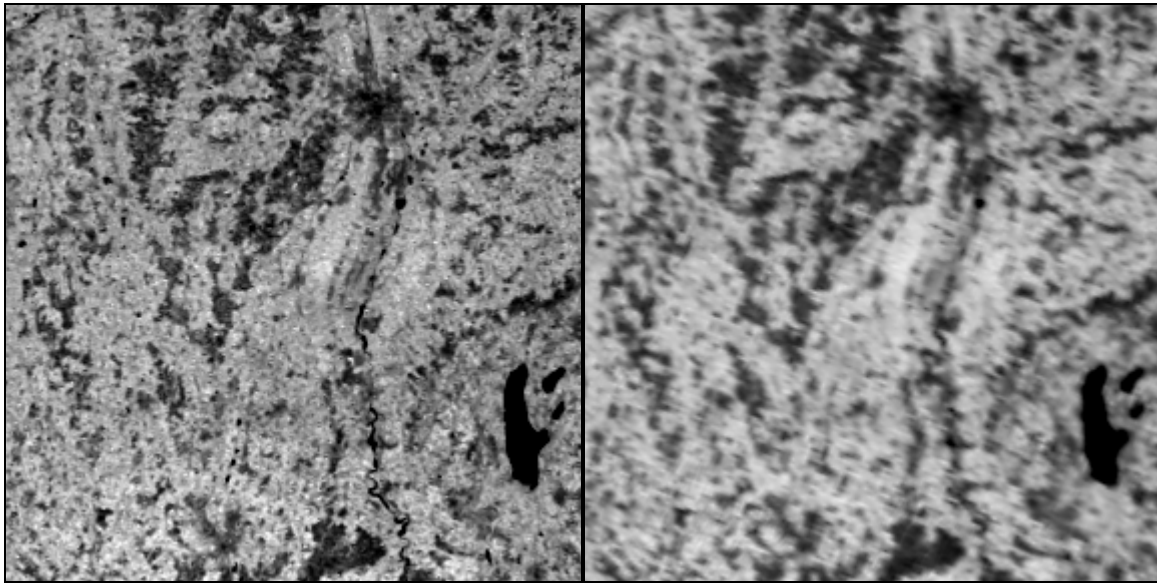


Figure 7.16: MODIS imagery from day 170 (left) and day 171 (right) of year 2000 acquired under different viewing angles. The images shown are NIR band cutouts of the northwestern quarter from the study area. Images are displayed without a reduction factor.

A reference dataset was produced for the MODIS imagery. This reference dataset representing the “true” reflectances could be derived because of the availability of coincident Thematic Mapper imagery collected 45min before the MODIS data on day 171. First, the aforementioned formulae of Table 4.10 (Liang et al., 2002) were applied to produce a synthetic 30m spatial resolution image with MODIS-like bandwidths reflectances. These reflectances were used to compute another “truth” dataset, similar to the truth data used in the prototyping of the algorithm. High-resolution pixels reflectances of the same land cover type were averaged over the area of 250m pixels resulting in the land cover type specific reflectance for the coarse pixel.

The complete frame of the study area was processed for both images. The fractional land cover was computed for the 250m MODIS resolution as described in the previous chapter. The same functions to approximate expected reflectances that were used in the prototyping of day 171 were applied to both datasets. The notion of fuzziness in the functions justifies their application to (i) MODIS data of slightly different radiometric properties than the synthetic data derived from TM data and (ii) two consecutive days of imagery.

The following analysis focuses on the Landsberg test area delineated in the previous chapter. It is representative for the northern part of the study area and significantly large to supply statistically valid amounts of data (6,400 pixels, ~27,000 area fractions). Due to the different resolution, the area is not exactly the same as in the prototyping. It is slightly shifted and altered in size.

Note that in the comparison of these datasets additional scaling effects in remote sensing data are present. Pixels of the three acquisitions will most likely match spatially only to a limited degree. Although, geometric correction was applied carefully, resampling to the defined spatial grid provides no guaranty of exact stapling of the data. Different orbits in the collection of the data result in a modified alignment of the picture elements. Moreover, distinct IFOVs of the two sensors will alter the actual areas sensed by the instruments

(compare Figure 3.8 in section 3.6). Error is introduced by this modification of areal units. It is subject to the modifiable areal unit problem (MAUP) in remote sensing data and the characteristics of satellite imagery of different resolutions (see chapter 3). These features are contained in the differences observed between MODIS data of different acquisitions as well as in any comparison with the Thematic Mapper data. An identification of this error is most challenging and will not be addressed in the context of this study. However, in regard of the errors produced by the processing of the data in reflectance segmentation, acquisition and sensor discrepancies can be neglected.

7.2.1 Reflectances

In a first step, reflectances were analyzed. In order to understand the differences in the results from the segmentation of commensurate 250m MODIS data, a view must be cast on the differences of the image frame under investigation before the algorithm is applied. Figure 7.17 shows the relations of MODIS bands 1 and 2 of the two acquisitions. Coefficients of determination in the regression of the two images are almost equivalent in both bands, however lower variance and lower values are contained in the RED band of the blurry image of day 171. The reason for this effect is to be found in the stronger atmospheric influence in the visible band in an acquisition under high scan angles. Potentially lower values in RED reflectance will provoke higher NDVI and consequently higher LAI.

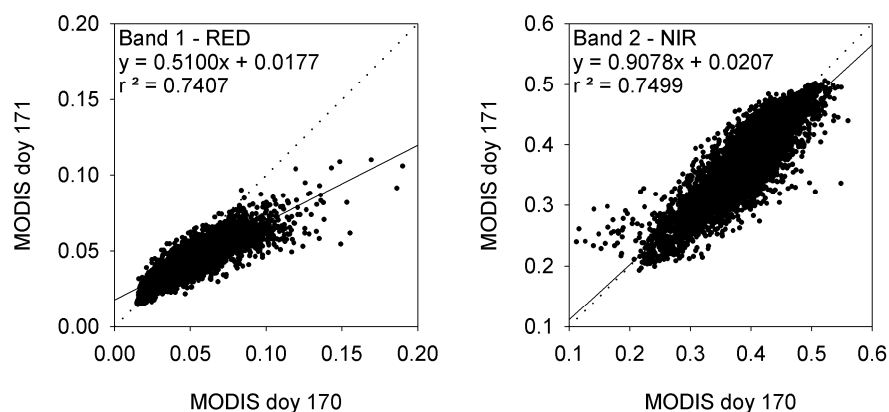


Figure 7.17: Reflectance of the RED and NIR MODIS bands of day 170 and day 171 in the Landsberg test area.

The quality of the land cover types reflectances after the reflectance segmentation are similar to the results observed in the prototyping of the algorithm. Due to the distribution of the data no computation of regressions is allowed. A random scatter in the results is observed in all possible combinations of comparison, i.e. the relation of each image to the truth dataset as well as between the two images themselves. In the latter case, after the reflectance segmentation no regression may compare to the interrelation of the two original images of Figure 7.17. As an example of the poor agreement, the NIR band plots of land cover type specific reflectances from the reflectance segmentation of the images from the two dates are shown in Figure 7.18.

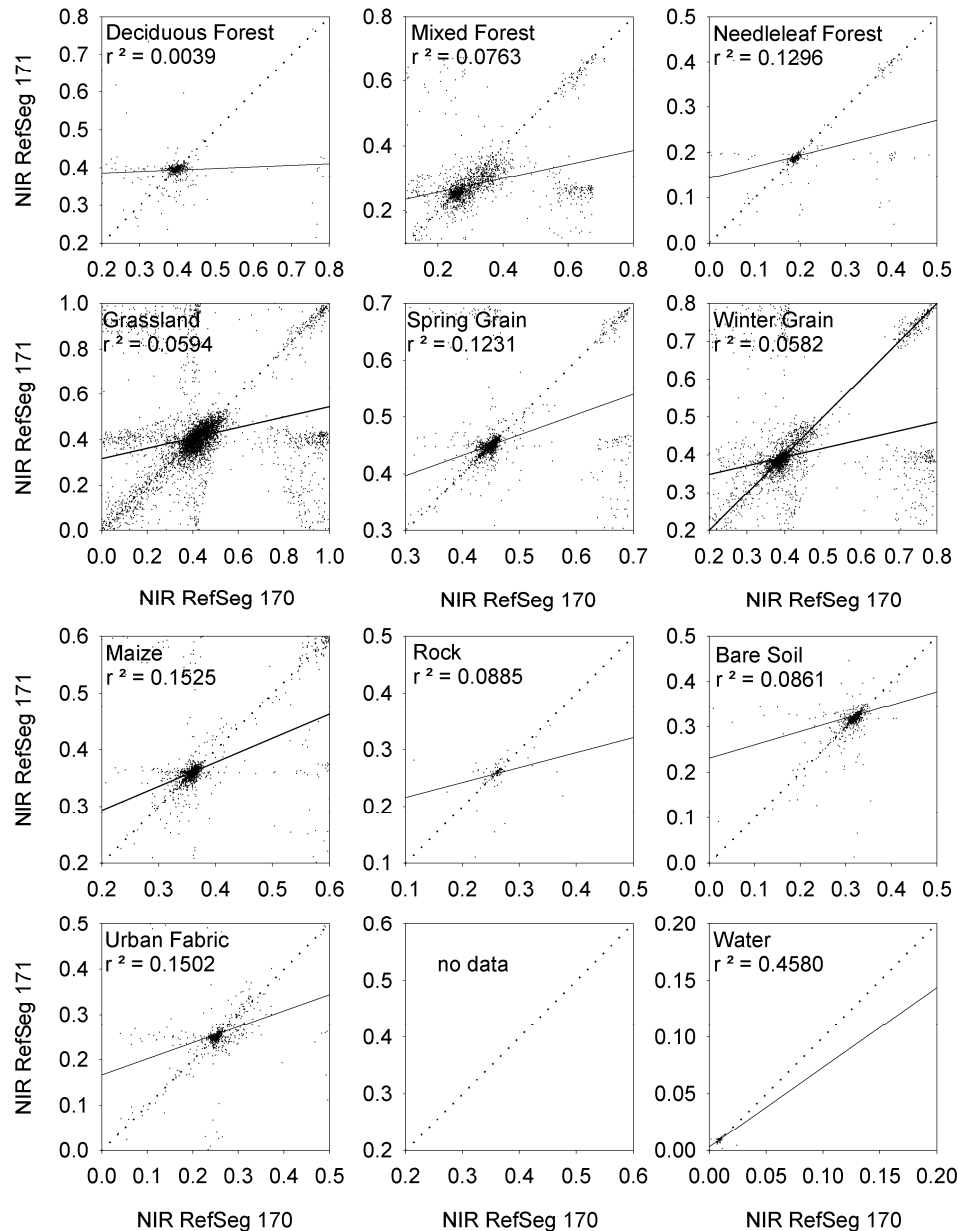


Figure 7.18: Distribution of results from the segmentation of NIR reflectances of the two MODIS images from doy 170 and doy 171, 2000 in the Landsberg test area. The regression lines and coefficients of correlation are equivocal.

While the reflectances of the unsegmented data of doy 170 and doy 171 exhibit but a slight deviation, the reflectances from the reflectance segmentation reveal equivocal agreement. The clear correlation of the original data is not preserved in the segmentation process. Arbitrary scattering dominates the comparison of land cover type's reflectances. Contingently, the gradient smaller than 1 in all regressions may be interpreted as resulting from the same trend in the original data.

7.2.2 Leaf Area Index

Generation of LAI from the reflectances was performed for the two images. As in the prototyping of the algorithm, fractional LAI results are (i) compared to the land cover type

specific LAI derived from the truth dataset and (ii) results are lumped to the 250m scale and compared to the results from the majority type data.

Results from the regression analysis of the pixel fractions LAI in the Landsberg area are shown in Figure 7.19. They reveal the same stratification of the LAI from reflectance segmentation that was observed in the prototyping of the algorithm. The horizontal alignments of fractional LAI values in the plots are grouped around the LAI obtained from the most frequent results of reflectance segmentation of the RED and NIR bands. Results of the two dates of MODIS data are very much alike with an only slightly lower explanation of the true variance in the LAI derived from the reflectance segmentation of the poorer image of day 171. In the case of zero LAI on fractions of the land cover types, these may not be taken out of the statistics as they do represent either a non vegetation land cover type or no leaves. If only the fractions of vegetation land cover types are used in the regression, r^2 is only slightly reduced from 0.70 to 0.67 on day 170 and from 0.67 to 0.63 on day 171. Again, however, regressions are equivocal considering the distribution of the samples.

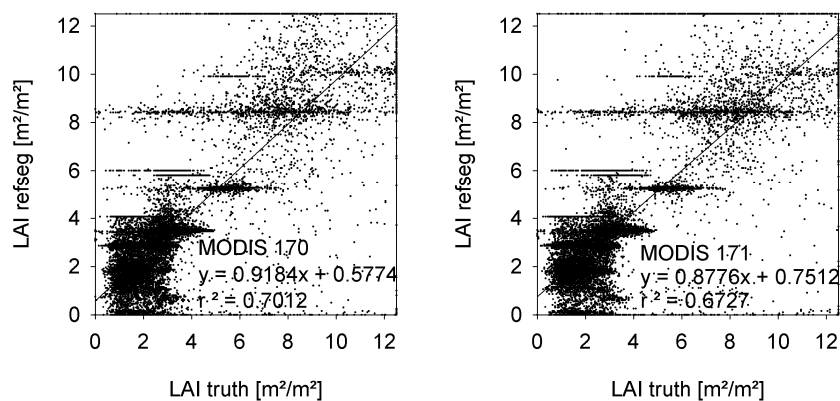


Figure 7.19: Results from the regression analysis of land cover type specific fractional LAI versus the truth dataset of the Landsberg test area of the two MODIS scenes of day 170 and day 171, 2000.

The distribution indicates that large errors are contained in the data. In the application to MODIS data, these are quite on a level with the mean error observed for the Landsat test area in the prototyping. Differences in the magnitudes of relative and absolute error in the two MODIS images are marginal. As in the prototyping of the algorithm, mean and maximum error is reduced to reasonable amounts in the 95th percentile. Table 7.8 summarizes the statistics of fractional LAI for the two days MODIS images.

Table 7.8: Statistics of the error of LAI derived from reflectance segments for the MODIS imagery of day 170 and day 171, 2000 compared to the truth dataset.

	MODIS doy 170		MODIS doy 171	
	relErr LAI refseg [%]	absErr LAI refseg [m ² /m ²]	relErr LAI refseg [%]	absErr LAI refseg [m ² /m ²]
mean	46.5	0.91	49.7	0.94
max	16700.0	12.50	16900.0	12.50
min	0.0	0.00	0.0	0.00
stddev	211.7	1.23	225.9	1.29
95th percentile				
value	171.4	3.00	187.4	3.10
mean	30.1	0.70	31.9	0.71
max	171.2	2.95	187.4	3.05
min	0.0	0.00	0.0	0.00
std	35.3	0.71	38.7	0.73

A comparison of the refseg results for LAI of the two MODIS scenes (Figure 7.20) reveals once more that the algorithm produces a random scatter in the results. LAI from the two days is rarely aligned along the 1:1 line. The gradient of the regression line suggests a slightly lower LAI from the blurry image of day 171. Although r^2 is 0.73 the results do not appear to be interchangeable and the number of outliers is large.

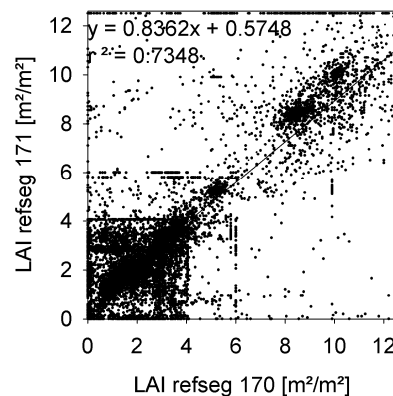


Figure 7.20: Regression of the fractional land cover type specific LAI deduced from the reflectance segmentation of MODIS images of day 170 and 171

When fractional LAI results are lumped to the 250m pixel, parity persists between the two datasets. While in the prototyping, fractional LAI lumped to the coarse pixel was somewhat closer to the truth dataset, this is less emphasized in the results from the MODIS data of day 170. On day 171 the LAI derived from the majority dataset is closer to the truth data.

Comparison of the lumped LAI and the majority LAI versus the truth dataset are shown in Figure 7.21 for both days of MODIS data.

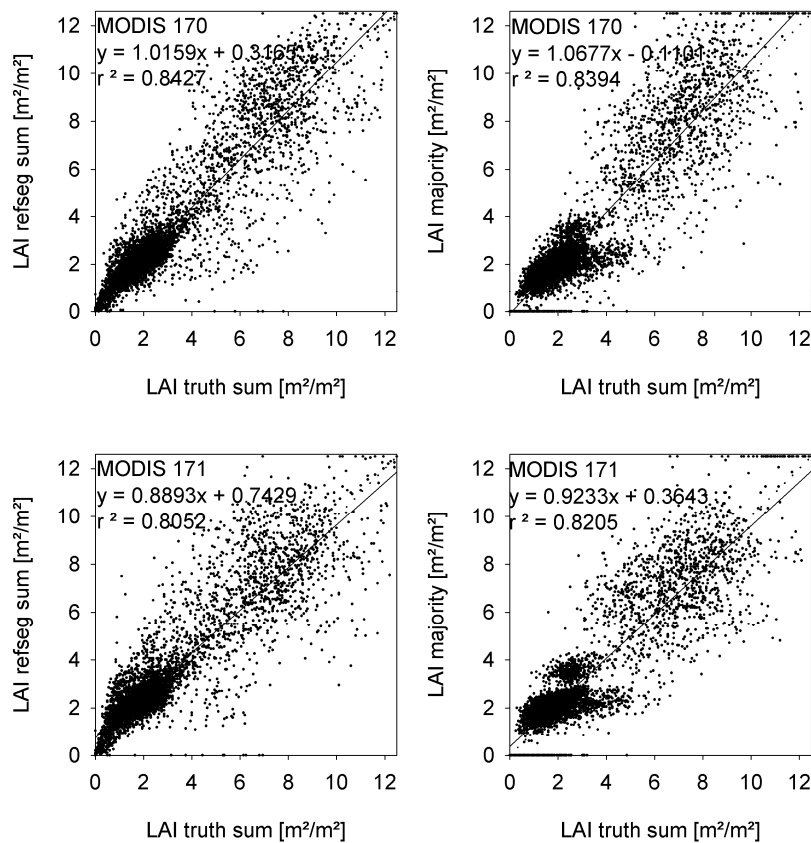


Figure 7.21: Results from the regression analysis of the lumped LAI derived from reflectance segmentation and the majority LAI produced from MODIS data of day 170 (upper row) and day 171 (lower row) versus the lumped LAI from the truth dataset.

The LAI for the 250m pixel derived by reflectance segmentation from MODIS data of day 170 exhibits the best regression with the truth dataset. Table 7.9 reveals that this dataset also contains the lowest mean absolute error. Mean relative error is slightly lower in the majority type LAI. The 95th percentile is not shown in Table 7.9 as the relation of the error estimates does not change in this case of LAI on 250m pixels.

Table 7.9: Statistics of the error of LAI at 250m in the Landsberg test area. Data were lumped from the fractional LAI and derived from majority data and compared to lumped LAI of the truth dataset.

	MODIS day 170				MODIS day 171			
	relErr LAI 250m [%]		absErr LAI 250m [m ² /m ²]		relErr LAI 250m [%]		absErr LAI 250m [m ² /m ²]	
	refseg	major	refseg	major	refseg	major	refseg	major
mean	31.5	29.7	0.70	0.71	39.9	35.1	0.76	0.72
max	600.0	233.3	7.80	7.30	583.3	566.7	7.15	6.40
min	0.0	0.0	0.00	0.00	0.0	0.0	0.00	0.00
stddev	40.0	29.6	0.85	0.86	52.1	37.9	0.86	0.76

7.3 Application to a time series of the 2003 growing season

MODIS data of the growing season 2003 were processed in the attempt to elaborate the capabilities of the reflectance segmentation algorithm to produce a reliable time series of leaf area index. The dataset were introduced earlier as MOD02 raw radiance counts in Section 4.6.1. All 19 scenes available were processed using the PULREF algorithm to produce reflectance datasets. Figure 7.22 marks the temporal distribution of the images. For each day, reflectance probabilities were determined from the GeoSAIL model results and formulated as Gaussian functions as described in section 6.2.2. Parameters of all functions are listed in Appendix 5. Consistency of the functions with reflectances of the MODIS bands is provided for the computations by parameterization of the GeoSAIL model with the MODIS bandwidths. The 250m fractional land cover derived for the processing of MODIS data described in the previous section was ingested in the algorithm for the computation of land cover type specific reflectances for the time series.

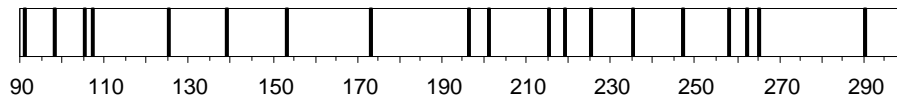


Figure 7.22: Time scale indicating the dates of acquisition (day) of the 19 MODIS scenes of the time series of 2003

LAI algorithms were applied to the land cover types reflectances to derive land cover type specific LAI. Each dates fractional LAI values were summed to produce a single 250m scale LAI value. Also, for comparison the majority types LAI was computed.

The findings from the previous section suggest that consistency of results may not be given when applying the proposed method for reflectance segmentation. The differences between the two consecutive scenes were too large. Thus, results from the application of the algorithm to a time series are devastating. No continuous development of LAI could be derived from the reflectance segments of the time series. Examples of LAI progressions on four pixels taken from the test areas Landsberg and Hochstadt are shown in Figure 7.23.

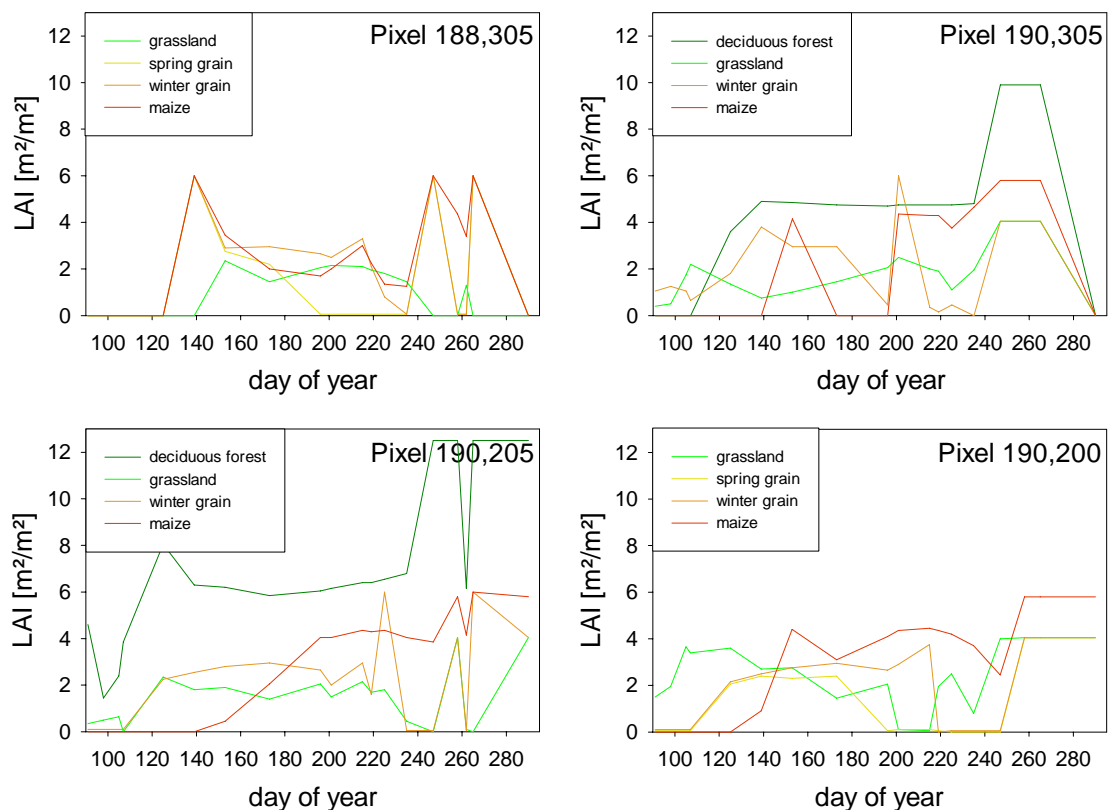


Figure 7.23: Temporal development of LAI on four pixels derived from the time series of reflectance segments of the 19 MODIS scenes.

None of the examples exhibits a convincing rise and fall of leaf area during the growing season. On all pixels each land covers trajectory shows abrupt changes in LAI. Especially the high values of LAI of the grain land cover types after mid August (~doy 225) or the extremely high LAI estimates for maize at the start of the growing period document deficiencies of the approach to obtain land cover type specific LAI time series. Pixel 190,200 may be judged as the single example of fairly decent LAI development when ignoring the rise in LAI at the end of the vegetation period.

The aggregation of land cover types LAI to a single LAI value on the 250m pixels are shown in Figure 7.24 (left). Aggregating the fractional LAI smoothes the curves of LAI development to a limited degree only. Peaks that are impossible to be explained by natural phenomena remain in the data.

The pixel labeled with the Maize majority (86%) suggests that maize plants LAI peaks in May with subsequent decline until mid August. Three more peaks to be reached in late summer and early fall appear unreasonable. This is even more the case when taking into account the remaining 10% of grain and 4% grassland land cover types on that pixel.

The plot of the pixel with a majority cover of winter grain (60%) appears to adequately describe a rise and maybe too early decline of LAI until a date of harvesting around doy 200. Extremely dry conditions of the summer of 2003 may explain an early decline of LAI. However, the immediately following peak and a plateau of high LAI in September are unlikely to be caused by the remaining land cover types on the pixel made up of 23% maize, 14% grassland and 4% deciduous forest.

The pixel with the mixed forest classes majority (58%) may almost be accepted with a quite continuous LAI around reasonable $4\text{m}^2/\text{m}^2$. The trajectory however starts out with a value around $3\text{m}^2/\text{m}^2$ followed by a decline and peaks at the end of the vegetation period after day 240. The gap induced by a very low LAI around day 260 is another unrealistic feature in this LAI development. This is hard to explain, even when noticing that 14% of the pixel are grassland, 23% belong to the maize class while 21% are covered by urban fabric.

The behavior of grassland LAI seems acceptable except the high rise in September (after day 240). However, only 40% of the pixel actually are covered by grassland, while the rest is made up of crops and 16% of urban fabric. These remaining cover types may not explain a rise in LAI in late summer.

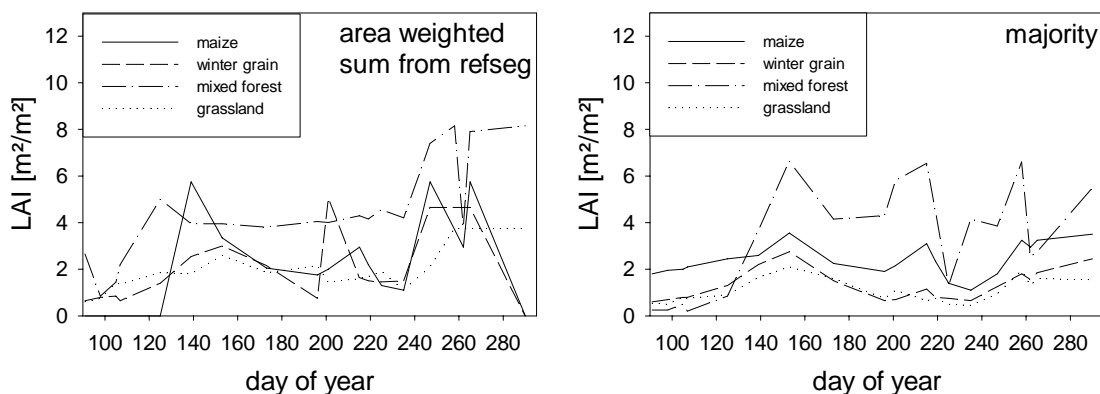


Figure 7.24: Seasonal development of LAI at the 250m scale. LAI from the area weighted sum of fractional land cover type specific LAI (left) and LAI derived based on the majority land cover type (right). Pixel coordinates: Maize (188,305), winter grain (190,305), mixed forest (190,205), grassland (190,200).

The depiction of Figure 7.24 (right) compares these results to the LAI development obtained from majority type estimates. The courses of the plots for the majority type LAI are more convincing than the fractional and lumped results from the segmented reflectances. However, discrepancies are contained in these results as well. LAI of maize starts out far too high in April at $2\text{m}^2/\text{m}^2$, and just as all other cover types, rises at the end of the growing season. Lowering of LAI of maize during the summer with a new rise in August is unlikely but may be induced by the dry conditions of 2003. Winter grain and grassland show plausible courses until day 240 after which a rise in LAI occurs. The remaining LAI in the winter grain class after harvesting around day 200 must be attributed to the actual impurity of the pixel. The mixed forests LAI development exhibits a similar dip as the maize class. In the case of forest however this is unlikely to be attributable to the hot summer. The extreme rise and fall in the last third of the growing season suggests that other reasons are responsible for these unreasonable courses of the plots.

A general feature of all above observations are values of unreasonably high LAI at the end of the growing season. These are most likely to be ascribed to errors in the atmospheric correction of the data or other artifacts contained in the imagery.

8 Discussion

The method for the segmentation of moderate scale reflectances from optical remote sensing imagery was developed in consideration of three boundary conditions. First, the development and operation of numerical environmental models on moderate and large scales imperatively needs to take into account the operational scales of the processes they describe (Blöschl, 1996, Stewart et al. 1996, Van Gardingen et al. 1997). These models require distributed spatial input data that can best be provided by remote sensing measurements (Schultz and Engman, 2000, Lakshmi et al. 2001). Secondly however, there is the physical limitation of today's spaceborne operational optical remote sensing devices that prohibits temporally frequent and at the same time spatially high resolution imagery. In order to reproduce the environmental processes that are addressed in models like the DANUBIA compound of the GLOWA-Danube project, for many of these processes sufficient temporal resolution is a vital concern. Yet, if remote sensing data is to be used, this implies low spatial resolution for these data. Low spatial resolution data again causes individual measurements (pixels) to integrate over more than one process or entity that an environmental model needs to distinguish. Then thirdly, knowledge may be brought forward about the surface features the coarser satellite image pixel integrates over. This knowledge includes information about temporally static features contained in the imagery and fuzzy knowledge about what will be sensed by a recurring imager at different times of observation. Virtually static features like land cover type may be derived at high resolution from infrequent high resolution remote sensing observations. Fuzzy knowledge like expectable reflectance characteristics may be formalized and used by adequate mathematical methods.

Bringing together these findings resulted in the development of the method presented above. One key static feature in environmental models has been identified to be the information on land cover types. The quest for an improvement of land cover type information led to the idea of stratification of pixel information in order to represent subscale land cover types. The conception of Geocomplexes described above, which is based on subscale fractional land cover, has proven to substantially advance the possibilities for process description (Reichert et al. 2004a). In order to enable parameter retrieval from remote sensing data with the same kind of data representation, such subscale fractional land cover is used in the method for reflectance segmentation.

From the remote sensing perspective, the prime process under observation is the reflectance characteristics of the surface sensed. It is the base process for the deduction of other interconnected physical properties. This prime process, in turn, is substantially dependent on land cover type. Consequently, the deduction of land cover type from remote sensing data is a common operational application of satellite imagery.

In remote sensing natural surfaces, land cover type is one decisive driving variable for reflectance. Another is time. Many land cover types considerably change their reflectance

characteristics over time and these changes are mainly due to phenology. Phenological development is well documented yet these changes are gradual in nature and depend on influences, like location, weather conditions or agricultural practice. Thus, no hard facts may be provided about the state of the reflectance characteristics of a cover type at any given time. Nevertheless, a reasonable guess, an imprecise estimate may be given. If a land cover type is provided as a hard fact at a point in time, a fuzzy prediction of its reflectance is possible.

If high resolution information on surface reflectances were available in which homogeneous surfaces of individual land cover types are identified, no fuzzy prediction of reflectance would be of any interest. The reality of today's remote sensing, however, provides us with coarse resolution surface reflectances. In these available data, the sensed reflectances are a mixture of signals from a set of different land cover types. In this case, the segmentation of the reflectance of the coarse pixel by making use of the hard fact of subscale land cover type and the fuzzy estimate of expected land cover type specific signals, becomes a well-founded option.

The feasibility of this option was explored in the previous sections. The method developed was tested on an artificially produced data pyramid and applied to real coarse scale MODIS imagery. It was shown that the method is capable of computing a result for specific reflectances for 12 land cover types at different resolutions. The computation of land cover types reflectances is independent of pixel resolution, but the fractional land cover information is required at the resolution under address. Fuzzy information about the probabilities of reflectances for each cover type needs to be furnished in the form of a two times differentiable function. The method only acts on pixels with multiple land cover types and does not alter the reflectance of homogeneous pixels. The segmentation algorithm runs on individual spectral bands and may be set up for each band of multispectral data.

The presented method delivers reflectances attributable to land cover types of subscale pixel fractions. This output bears the potential to be used with arbitrary remote sensing models that require reflectances as input. With this, parameters like vegetation indices, FPAR, net photosynthesis or primary productivity could be deduced on a subscale basis. In this study it was the objective to derive LAI based on the simple NDVI-LAI model. For this it was necessary to apply the algorithm for reflectance segmentation to RED and NIR band reflectances of the test data. The results were evaluated against a dataset that was produced from the highest available spatial resolution data and that served as a reference.

The results obtained from the above investigations are equivocal. On the one hand, analysis of the single date synthetic data pyramid appear promising in the prototyping experiment. On the other hand, the testing of the algorithm on MODIS data clearly revealed that consistency of results is scant when used on real data. In the application to two very similar MODIS scenes the current implementation of the algorithm was not able to produce results that would approximate the good correlation of the input data. In the attempt to derive seasonal development of leaf area for land cover fractions from a time series of MODIS data, extreme outliers produce an unrealistic discontinuous image of the progression of leaf area. The same problem, however, was also identified in the operational MODIS LAI product, which in the current implementation will produce extreme artifacts in an LAI progression, even on the full pixel scale (Wang et al. 2005).

The reflectances of a land cover type obtained from reflectance segmentation contain little of the variance that is contained in the comparable "truth" dataset. Most reflectances obtained are very close to the mean true reflectance, which is greatly determined by the peak of the reflectance probability functions used in the computation. The scattering around that peak that does occur in the results is error-prone. A lower or higher reflectance value for a land cover type does not coincide with a similar deviation in the truth dataset. The histograms

investigated in Section 7.1.3 agree well with the truth data only if large areas of the land cover type lie on homogeneous pixels because on these the truth dataset is exactly reproduced. Error of 20% reflectance and above is common in the reflectance segments. These large errors tend to concentrate on the smaller area fractions. It may be argued that this observation reduces the overall error produced by the method. However, even if only a part of a pixel is burdened with 20% error in reflectance it is questionable that a quantity derived from that error loaded reflectance will be useful considering that most models ingesting reflectances will add further artifacts.

The method has shown to produce reflectances that, if they deviate from the mean, are mainly chosen on a random basis. In order to meet the constraint that all land cover types reflectances on the pixel sum to the measured value, the algorithm often tends to shift one of the reflectances away from the mean until the constraint is met. This explains the observation that the error of the resulting reflectances of many land cover types is either low or very high. This is reflected in the striped distribution of the error plots in the analysis of the relation of error to the area fractions (Figure 7.7 and Figure 7.8). In the implemented form of the optimization algorithm, in many cases the error is not kept small by splitting it to different land cover types on the pixel, but exaggerated on one of the land cover types. Although, some reflectances are very well reproduced, this deteriorates the validity of the method.

Despite these discouraging results, the segmented reflectances were applied to produce land cover type specific LAI. This experiment is justified because having subscale reflectance information available for the land cover types on a pixel corresponds to the driving force of the LAI process. This is expected to improve LAI estimates. Also, in the computation of NDVI the results of two runs of reflectance segmentation for the RED and NIR bands are combined. If the error is related to area fractions, the relation of the two bands may be preserved in the segmented reflectances. The function of NDVI may be less affected. The application of LAI algorithms may benefit from this fact. Nevertheless, the occurrence of simultaneous error in the RED and NIR band are equally coincidental as the error in a single run. An improvement to this could lie in finding a way of linking the reflectance segmentation of RED and NIR bands in order to avoid extreme outliers.

With the randomness in mind, the results of the LAI derivation from the data of the synthetic data pyramid appear quite surprising. They suggest that, (i) even though individual pixel fractions reflectance is radically error prone, reasonable agreement with the reference data set with coefficients of determination between 0.5 and 0.8 are possible for land cover type specific LAI derived for the pixel fractions and that (ii) the correlation of the aggregation of this fractional LAI yields better results than the alternative of deriving LAI from coarse scale majority type land cover and coarse scale reflectances. The fact that an assumed majority land cover type on a pixel is in most cases contaminated by other types, produces larger absolute mean error in LAI than the application of the same LAI algorithms to vastly error-burdened reflectances of the fractions of multiple pure land cover types on the pixel. This was observed in three out of four test areas. It is a strong indication for the importance of taking into account the process scale in the retrieval of land surface parameters from remote sensing data.

The display of the reflectances and there from derived LAI reveals the great differences between the spatial representation of either quantity in the two opposing concepts of data storage, that is, the single pixel values that correspond to a land cover majority type and the values that correspond to a subscale areal fraction. Although overall percentages of the land cover types remain almost constant in both data representations, distributions are substantially different. The concept of storing subscale land cover information on a pixel reveals much more detail in distribution although the localization within the pixel is elided. This detail is lost in storing single majority types values. The measurement scale and pixel size in both cases remains the same, however data amount is expanded in the case of storage of each land

cover types value by a factor equal to the number of land cover type. The information about the corresponding area fractions of land cover types is but a single static dataset.

The majority of the data amount required for this data model is filled with zeros, an obvious dissipation of storage capacities. This is due to the fact that in most cases 2-5 land cover types out of 12 are present on a pixel. Only for these, actual information is stored. The remaining positions hold fill values to hold up the structure of the data grid. In this context the conception of quadtrees comes to mind again, where higher scale information is only stored where necessary. The definition of quadtrees however, does not conceptualize subscale fractional information. Exploring possibilities of combining quadtree data structure with subscale fractional information appears to be a challenging task.

The application of reflectance segmentation brings the benefit of enhanced spatial detail and the supposed higher reliability of the remote sensing model by working it on pure land cover. On the other hand artifacts are produced in the data and variance is greatly reduced. Judgement is difficult in pondering upon what we get and what we lose along the way, for the two effects of the approach – spatial advantage and loss in variance and reliability – may not be readily compared. A way to address the loss in variance could be a more diversified application of fuzzy reflectance description. This can best be exemplified with the results in the mountainous Wetterstein test area. Results were the poorest in this test site, which is attributable to the generalization of land cover types of the area. Forests as well as grasslands are subject to quite different environmental conditions in the mountainous part of the study area. However, mountain forest types and mountain pastures were united with structurally similar types of the lowland test sites. Application of the same fuzzy reflectance description to these land cover types in both environments lead to the larger error in the Wetterstein area. This can well be observed in the altered reflectances and lower LAI in the high regions in the south of the study area. A more sophisticated approach may take into account these differences. It could be achieved for example by introducing additional information such as elevation in the algorithm and using it in selecting appropriate fuzzy reflectance descriptions.

A final investigation of the effect of scale on the method showed that the error produced by the method declines with increasing pixel resolution of the ingested data. This seems astonishing at first. It is, however, explicable when considering that the method produces reflectances for a land cover type that concentrate around a mean value. The larger the area of a pixel and the larger the fraction of a land cover on that pixel the lesser the effect of varying reflectance within the land cover types area. Thus, results improve with coarsening of the spatial resolution of the data. This agrees with the findings of the effect of aggregation of different scales (Bian, 1996, Bian and Butler, 1999)

As promising as some of the results of the prototyping are, the disappointing is the outcome of actual application of the method. The attempt to positively validate the results on coincident data of high and low resolution failed with the presented implementation of the method. While the two MODIS scenes in this investigation show almost equal relation to the truth dataset, the intercomparison of the results of the two acquisitions reveals some shortcomings of the approach. If the method was already sound, results of highly correlated images should yield comparable results. This could not be confirmed. The investigation using two images of different characteristics also indicates that the image itself has too little an effect on the computation of the current algorithm after all. The strongest components in the method remain the functions for the fuzzy description of expected reflectances and a randomness in the assignment of more extreme values of reflectance to the land cover types. In this context, it needs to be considered that the functions used in this application were derived from the statistics of imagery of the same date. Consequently, in this case, the means of the land cover types are quite precisely met. This is unlikely to be achieved when the functions are produced by approximation from model results.

Thus, the application of the method to the MODIS time series did not deliver satisfying results either. Neither the seasonal development of individual land cover types on fractions of pixels could be deduced in a convincing manner, nor would the aggregation to pixel-wide LAI mitigate the errors in the temporal development. Note that in the latter, the paradox of scaling LAI comes to effect. Lumping different land cover types LAI to a pixels area is valid. Yet, the claim that this lumped LAI describes the seasonal development of a land cover type is not. It is contained in the above illustrations of seasonal development of LAI at the 250m scale. The LAI generated from majority type land cover and 250m reflectances does also not show a convincing course. This may be attributed to errors induced by the atmospheric correction and other artifacts in the data and a more thoroughgoing preparation of the data of the time series may improve the result. In regard of the substantially larger error produced by the segmentation of reflectances, however, this attempt of improvement of data preparation was not pursued. Also a comparison with the data of the MOD09 reflectance product may be an interesting task, but was not conducted in the context of this work.

An unresolved issue remains with the final feasibility of the approach of using the simple regression models for deriving LAI from VIS/NIR remote sensing data. In the study, they were used in consistent relative comparison and their specification by land cover was a key factor in the presented approach. This was sufficient for the experiments conducted with the reflectance segmentation results. Absolute validation, however, was not sought. Such validation is greatly hindered by lack of adequate methods for achieving LAI data in the field that could be compared to the computed fractional LAI. Thus, absolute quantities derived in the computations may deviate from real observations depending on the regression model. Exploration of these models at the land cover types level would be needed for an advancement of the regression model approach for LAI retrieval.

Some additional interesting observations were made in the context of this study. One is connected to the generation of the dataset used as the “truth” reference. The production of LAI on homogeneous land cover type fractions produced almost equivalent results as the averaging of high resolution pixels LAI of the same land cover type. This supports the hypothesis that concentrating on land cover homogeneity on pixel fractions can serve as an excellent surrogate for actual higher resolution data grids. The approach may be interpreted as a scaling function for land cover related processes.

Another observation resulted from the modeling of reflectances using the GeoSAIL model (Verhoef and Bach, 2003). Internally the model makes plants grow, ripen and decay over the season with LAI being an internal variable. The models output provided diurnal reflectances that result from the states of the plant modeled. A plot of the models LAI against the NDVI deduced from the diurnal reflectances revealed that, according to the model, the NDVI-LAI relation is different for the greening period as opposed to the senescing period. An investigation of this output of the model may be fruitful for an improvement of the hosts of available vegetation indexes relation to leaf area.

Finally, the way the land cover used in this study disclosed a way of detecting inconsistencies in such data that are a compound from different sources. In the case of the land cover used, the classification of the study area was (i) derived from two Thematic Mapper scenes that were independently prepared and (ii) was composed from two parts that were the result of two separate runs of the ENPOC classifier. Atmospheric correction was performed prior to the stitching of the images and the separate classifications were parameterized differently due to regional variations of the areas. The borders of both of the stitching of the data are not detectable in the classification (see Figure 4.12). However, the computation of fractional land cover revealed that frequencies of some of the land cover classes change along these lines where the different datasets were put together. While the differences that stem from the different TM scenes are rarely recognizable as a diagonal line, the horizontal break in

frequencies is dramatic for some cover types. This effect can best be observed in the deciduous forest, spring grain and rock classes and is due to the need of different fuzzy characterization of the classes in the runs of the ENPOC classifier. Images that illustrate the described inconsistencies for these classes are contained in the galleries of Appendix 7. For the purpose of this study, however, they were disregarded. The lines where these frequencies change are most definitely errors in the data but they will not affect the pixelwise computations performed.

9 Conclusion

The success of the method presented in this study is ambiguous. Some of the results in the investigations presented indicate a potential of the method to provide estimates of land cover type specific reflectances that are useful for the retrieval of leaf area index. This applies although the individual bands reflectances used for the computation of NDVI are not correlated to corresponding reflectances deduced from high-resolution data. In the case of a single date dataset good correlation of the retrieved parameter with the reference data set is achieved. The result seems even more reliable when the subscale assignment of LAI is given up and the mesoscale information is regained by lumping the results of the subscale homogeneous units. In the sense of a mesoscale LAI this is a success for the method. Apparently, the method gains ground by avoiding the false assumption of homogeneity.

The intended benefit of subscale parameter retrieval, however, is much less granted. The choice for the LAI values obtained appears to be either “close to the mean” or “burdened with large error”. The former is a result of the optimization that seeks highest probabilities that are achieved by their definition via the reflectance probability functions. The latter is subject to rather undetermined arbitrary behavior of the algorithm. It was mentioned in the discussion that the assessment of usefulness would need to balance between the advantage of the improved spatial representation of LAI and the obviously introduced error. However, this ambiguity would justify the experiment of actually using the information in hydrologic or other environmental modeling.

The ingestion into a hydrologic model may be successful in the case of the application to short term events for flood modeling. The observation that larger error occurs on smaller area fractions could lead to a mitigation of the negative effect of the artifacts in the segmented parameter. The long term runs of the DANUBIA model for periods of one or several years, however, would require time series information in order to capture the effect of LAI on the water balance. The experiment of deriving LAI time series from the MODIS data of 2003 indicated that these time series are inadequate. The method for reflectance segmentation as presented does not operate effectively in this case. Continuity of leaf area as exhibited by natural plants is not achieved with neither the subscale LAI nor the aggregation to the moderate scale. At this point it shall be noted that time series from the MOD15 product are similarly ambiguous (Figure 5.6)

The results from the derivation of LAI on the basis of NDVI from the segmentation of reflectances by the presented method disprove the above claim that arbitrary remote sensing models may be applied on the results. Although retrieval of LAI by the simple algorithms applied works to a certain extend, the retrieval of subscale reflectances is not robust. Even if the fractional LAI would withstand the test in an environmental model, it is questionable that the same applies to another algorithm that may require different bands reflectances to be segmented.

One of the advantages of remote sensing data is the timeliness of information. Radical changes on the surface like the cutting of grasslands fire or flooding can be detected and provided to a model. These kinds of changes will not at all appear in segmented reflectances. It shall be noted though, that flooding or fire may not interpreted as actual development of the land cover, but rather are changes to the land cover. It corrodes the assumption of static land cover.

Nevertheless it is worthwhile to ponder upon possibilities to improve the method. Two approaches were already addressed in the context of the above discussion. One was concerned with the lack of control over the relation of the bands undergoing the process of reflectance segmentation. This relation may be fully disturbed by the separate segmentation of the RED and NIR bands used for the subsequent LAI algorithms. Establishing a way of connecting the segmentation of individual bands may yield an improvement of the method. Another thought was directed at the idea of more precisely controlling the functions used in the segmentation. If the a priori knowledge put into the algorithm becomes less fuzzy so that the degrees of freedom are reduced the result should become more accurate. This approach, however, begs the question of how much remote sensing remains in the result.

More promising appears the conception of installing a feedback loop between the estimation of fractional reflectances and an environmental model, similar to the four-dimensional data assimilation approach proposed by Bach and Mauser (2003). If an environmental model provided the required input variables around the time of the acquisition of the scene undergoing segmentation, actual reflectances ranges could be derived by feeding an inverse radiative transfer model. This resembles the procedure conducted in the derivation of the reflectance probability functions for the time series experiment. Yet still, the question remains of how much of the information of the remote sensing image drives the result.

It can be concluded that the aspired derivation of subscale LAI from remote sensing as a temporally changing quantity remains a challenging task. The same holds for LAI on the moderate scale as indicated by the time series derived on the basis of majority land cover as well as from the MOD15 LAI product. In the wake of the latter findings, however, the attempt of decomposing moderate scale reflectances to fractional information remains an exciting experiment.

10 References

- Ackerman, S., Strabala, K., Menzel, P., Frey, R., Moeller, C., Gumley, L., Baum, B., Wetzel Seemann, S. and Zhang, H. (2002): Discriminating Clear-Sky from Cloud with MODIS, Algorithm Theoretical Basis Document (MOD35), Version 4.0, MODIS Cloud Mask Team, (available online at: http://modis.gsfc.nasa.gov/data/atbd/atbd_mod06.pdf)
- Artan, G. A., Neale, C. M. U., Tarboton, D. G. (2000) : Characteristic length scale of input data in distributed models: implications for modeling grid size, *J. Hydrol.*, Vol. 227, Iss. 1-4, pp. 128-139
- Asner, G.P. (1998): Biophysical and Biochemical Sources of Variability in Canopy Reflectance, *Remote Sensing of Environment*, Vol. 64, Iss. 3, pp.234–253
- Asner, G.P. and Wessman, C.A. (1997): Scaling PAR absorption from the leaf to landscape level in spatially heterogenous ecosystems, *Ecological Modelling*, Vol. 103, pp. 81-97
- Asrar, G. (Ed.) (1989): *Theory and Application of Optical Remote Sensing*, New York
- Asrar, G. Myneni, R. B. and Edward, T. K. (1989): Estimation of Plant-Canopy Attributes from Spectral Reflectance Measurements, in: Asrar, G. (Ed.): *Theory and Applications of Optical Remote Sensing*, New York
- Atkinson, P. M. (1997): Scale and spatial dependence, in: Van Gardingen, P. R., Foody G. M. and Curran P. J. (Eds.): *Scaling-up from cell to landscape*. pp 386, Cambridge
- Atzberger, C. (2004): Object-based retrieval of biophysical canopy variables using artificial neural nets and radiative transfer models, *Remote Sens. Environ.*, Vol 93., pp. 53-67
- Bach, H, and Mauser, W. (2003): Methods and Examples for Remote Sensing Data Assimilation in Land Surface Process Modeling, *IEEE Trans. Geosc. Remote Sens.*, Vol. 41, No. 7, pp. 1629-1637
- Bach, H. (1995): Die Bestimmung hydrologischer und landwirtschaftlicher Oberflächenparameter aus hyperspektralen Fernerkundungsdaten. *Münchener Geographische Abhandlungen*, Band B 21
- Bach, H., Braun, M., Lampart, G. and Mauser, W. (2003): Use of remote sensing for hydrological parameterization of Alpine catchments, *Hydrology and Earth System Sciences*, Vol. 7, Iss. 6, pp. 862-876
- Bach, H., Braun, M., Lampart, G. and Ranzi, R. (2000): Estimates of surface parameters via remote sensing for the Toce watershed, in: Bacchi, B. and Ranzi, R. (Eds.):

- RAPHAEL – runoff and atmospheric processes for flood hazard forecasting and control. Final report, University of Brescia, Brescia
- Bach, H., Schneider, K., Verhoef, W., Stolz, R., Mauser, W., van Leeuwen, H., Schouten, L., and Borgeaud, M (2001): Retrieval of geo- and biophysical information from remote sensing through advanced combination of a land surface process model with inversion techniques in the optical and microwave spectral range, Proc. of the 8th Int. Symp. “Physical measurements and signature in remote sensing”, Aussois, CNES, pp.639-647
- Bach, H., Verhoef, W. and Schneider, K. (2000): Coupling remote sensing observation models and a growth model for improved retrieval of (geo)biophysical information from optical remote sensing data, Remote Sensing for agriculture, Ecosystems and Hydrology, SPIE Vol. 4171, pp. 1-11
- Bach, H. and Mauser, W. (1994): Atmospheric Correction of Hyperspectral Data in Terms of the Determination of Plant Parameters - Proceedings of EUROPTO Series “Recent Advances in Remote Sensing and Hyperspectral Remote Sensing”, 27-29 September, Rome
- Baret, F. and Fourty, T. (1991): Estimation of leaf water content and specific leaf weight from reflectance and transmittance measurements, Agronomie, Vol. 17, Iss. 9-10, pp. 455-464
- Baret, F. and Guyot, G. (1991): Potential and Limits of Vegetation Indices for LAI and APAR Assessment, Remote Sens. Environ., Vol. 35, pp. 161-173
- Baret, F., Guyot, G. and Major, D. (1989): TSAVI: a Vegetation Index Which Minimizes Soil Brightness Effects on LAI and APAR Estimation, in: Proc. IGARRS '89, pp. 1355-1358
- Barthel, R., Braun, J., Rojanschi, V., Wolf, J., Schmid, C and Nickel, D. (2002): Global Change and Sustainable Groundwater Management in the Upper Danube Catchment – Groundwater Flow Modelling within the Framework of the GLOWA-Danube project, in: 5th International Conference on Hydroscience and -Engineering (ICHE-2002), 18.-21. September, Warsaw
- Bateson, C.A., Asner, G.P., Wessman, C.A. (2000): Endmember Bundles: A new Approach to Incorporating Endmember Variability into Spectral Mixture Analysis, IEEE Transactions on Geosciences and Remote Sensing, Vol. 38, No. 2, pp. 1083-1094
- Bayerisches Landesvermessungsamt (2003): Bayern (Süd). Amtliche topographische Karte TOP50, Landesamt für Vermessung und Geoinformation, München
- BLfW – Bayerisches Landesamt für Wasserwirtschaft (Eds.) (1999): Deutsches Gewässerkundliches Jahrbuch – Donaugebiet 1995, Munich
- Bernhardsen, T. (2002): Geographic Information Systems – An Introduction, New York
- Bian, L. (1996): Multiscale Nature of Spatial Data in Scaling Up Environmental Models, in: Quattrochi, D. A. and Goodchild, M. F. (Eds.): Scale in Remote Sensing and GIS, Boca Raton, FL, pp. 13-26
- Bian, L. and Butler, R. (1999): Comparing Effects of Aggregation Methods on Statistical and Spatial Properties of Simulated Spatial Data, Photogramm. Eng. Remote Sens., Vol 65, No. 1, pp. 73-84
- Binaghi, E. (1997): Fuzzy contextual classification of multisource remote sensing images. IEEE Transactions on Geosciences and Remote Sensing, Vol. 35 Iss. 2; pp. 326-339

- Blackburn, G.A. (1998): Quantifying Chlorophylls and Carotenoids at Leaf and Canopy Scales: An Evaluation of Some Hyperspectral Approaches, *Remote Sens. Environ.*, Vol.66, Iss. 3, pp.273-285
- Blöschl, G. (1996): *Scale and Scaling in Hydrology*, Wien
- Blöschl, G. and Sivapalan, M. (1995): Scale issues in hydrological modelling: A review. *Hydrological Processes*, 9 (3/4): 251-290
- Booch, G., Rumbaugh, J. and Jacobson, I., (2005): *The Unified Modelling Language User Guide – 2nd Edition*, Reading
- Braswell, B.H., Hagen, S.C., Froking, S.E., Salas, W.A. (2003): A multivariable approach for mapping sub-pixel land cover distributions using MISR and MODIS: Application in the Brazilian Amazon region, *Remote Sens. Environ.*, Vol. 87, pp. 243-256
- Braun, M. (1998): *Fuzzy Logic gestützte Landnutzungsklassifizierung von LANDSAT-TM Hochgebirgsszenen am Beispiel des Toce-Einzugsgebiets in Piemonte/Norditalien*, Diplomarbeit, unpublished
- Bronstein, I. N., Semendjajew, K. A., Musiol, G., Mühlig, H. (2001): *Taschenbuch der Mathematik*, Frankfurt a.M.
- Bruneau, P., Gascuel-Oudou, C., Robin, P., Merot, Ph. and Beven K. (1995): Sensitivity to space and time resolution of a hydrological model using digital elevation data, *Hydrological Processes*, Vol. 9, pp. 69-81
- Bundesministerium für Umwelt, Naturschutz und Reaktorsicherheit (BMU) (Eds.) (2003): *Hydrologischer Atlas von Deutschland*, Berlin, (available online at: <http://had.bafg.de:8080/>)
- Burrough, P. A. (1989): Fuzzy mathematical methods for soil survey and land evaluation, *Journal of Soil Science*, 40, pp. 477-492
- Campbell, J.B. (1996): *Introduction to Remote Sensing*, London
- Cao, C.Y. and Lam, N.S.-N., (1996): Understanding the scale and resolution effects in remote sensing and GIS, in: pp. 57–72
- Carlson, T.N. and Ripley, D.A. (1997): On the Relation between NDVI, Fractional Vegetation Cover, and Leaf Area Index, *Remote Sens. Environ.*, Vol. 62, pp. 241-252
- Chen, J. M. and Cihlar, J. (1996): Retrieving leaf area indexes of boreal conifer forests using Landsat TM images. *Remote Sens. Environ.*, Vol. 55, Iss. 2, pp. 153–162
- Chen, J.M (1999): Spatial Scaling of a Remotely Sensed Surface Parameter by Contexture, *Remote Sens. Environ.*, Vol. 69, pp. 30-42
- Chen, J.M. and Black T.A. (1996): Defining leaf area index for non-flat leaves, *Plant Cell Environ.*, Vol. 15, pp. 421-429
- Civanlar, M. R. and Trussel, H. J. (1986): Constructing membership functions using statistical data, *Fuzzy Sets and Systems* 18, 1-13
- Cohen, W. B., Maiersperger, T. K., Yang, Z., Gower, S. T., Turner, D. P., Ritts, W. D., Berterretche, M. and Running, S. W. (2003): Comparison of land cover and LAI estimates derived from ETM+ and MODIS for four sites in North America: a quality assessment of 2000/2001 provisional MODIS products, *Remote Sens. Environ.*, Vol. 88, pp. 233-255

- Colombo, S., Chica-Olmo, M., Abarca, F., Eva, H. (2004): Variographic analysis of tropical forest cover from multi-scale remotely sensed imagery, *ISPRS Journal of Photogrammetry & Remote Sensing*, Vol. 58, pp. 330-341
- Combal, B., Baret, F., Poilvé, H., Polvérini, U. (2001): Using multispectral reflectance to retrieve LAI and chlorophyll content of maize and soybean, *Proceedings of the 8th International Symposium "Physical measurements and signature in remote sensing"*, Aussois, CNES, pp. 499-504
- Csillag, F. (1997): Quadrees: Hierarchical Multiresolution Data Structures for Analysis of Digital Images, in: Quattrochi, D.A. and Goodchild, M.F. (Eds.), *Scale in Remote Sensing and GIS*, Boca Raton, FL, pp. 247-272
- Curran, P.J. (1989): Remote Sensing of Foliar Chemistry, *Remote Sens. Environ.*, Vol. 30, pp. 271-278
- Curran, P.J., Foody, G.M. and van Gardingen, P.R. (1997): Scaling-up, in: Van Gardingen, P. R., Foody G. M., and Curran P. J. (1997): *Scaling-up from cell to landscape*. pp. 1-5, Cambridge
- D'Urso, G., Dini, L., Vuolo, F., Alonso, L., Guanter, L. (2004): Retrieval of Leaf Area Index by Inverting Hyper-Spectral Multi-Angular Chris/Proba Data from SPARC 2003, *Proc. of the 2nd CHRIS/Proba Workshop*, ESA/ESRIN, Frascati, Italy, 28-30 April (ESA SP-578)
- De Cola, L. (1997): Multiresolution Covariation Among Landsat and AVHRR Vegetation Indices, in: Quattrochi, D.A. and Goodchild, M.F. (Eds.), *Scale in Remote Sensing and GIS*, Boca Raton, FL, pp. 73-91
- DeFries, R.S., Townshend, J.R., Los, S.O. (1997): Scaling Land Cover Heterogeneity for Global Atmosphere-Biosphere Models, in: Quattrochi, D.A. and Goodchild, M.F. (Eds.), *Scale in Remote Sensing and GIS*, Boca Raton, FL, pp. 231-246
- Demircan, A. (1995): Die Nutzung fernerkundlich bestimmter Pflanzenparameter zur flächenhaften Modellierung von Ertragsbildung und Verdunstung, *Münchener Geographische Abhandlungen*, B20, p178
- Demircan, A. and Mauser, W., (1996): Bestimmung der aktuellen trockenen Biomasse und Ertragsschätzung von Getreide und Mais aus Satellitenbilddaten (Landsat5-TM), S.209-260, in: Hartl et al. *MLR-Ostalb-Projekt, Einsatz von Satellitendaten zur parzellenscharfen Bestimmung der Bodennutzung und Ertragsermittlung*, Abschlussbericht, ONr.4189.41
- Department of Mathematics and Computer Science South Dakota School of Mines and Technology (2004): *MODIS Reprojection Tool User's Manual*, USGS EROS Data Center
- Ellenberg, H. (1996): *Vegetation Mitteleuropas mit den Alpen in ökologischer, dynamischer und historischer Sicht*, 5. Auflage, Stuttgart
- Elterman, L. (1964): Rayleigh and Extinction Coefficients to 50km for the Region 0.27μ to 0.55μ , *Applied Optics*, Vol. 3, No 10, pp. 1139-1147
- Emerson, C.W., Lam, N.S-N. and Quattrochi, D.A. (1999): Multi-Scale Fractal Analysis of Image Texture and Pattern, *Photogramm. Eng. Remote Sens.*, Vol. 65, Iss. 1, pp. 51-61
- Eurimage (2005): *Multi-Mission Satellite Data: Products and Services*, Eurimage Products and Services Guide, (available online at: www.eurimage.com)

- Fang, H. and Liang, S. (2005): A hybrid inversion method for mapping leaf area index from MODIS data: experiments and application to broadleaf and needleleaf canopies, *Remote Sens. Environ.*, Vol. 94, pp. 405-424
- Fourty, Th., Baret, F., Jacquemoud, S., Schmuck, G. and Verdebout, J. (1996): Leaf optical properties with explicit description of its biochemical composition: Direct and inverse problems, *Remote Sens. Environ.*, Vol. 56, Iss. 12, 104-117
- Friedl, M.A. (1997): Examining the Effects of Sensor Resolution and Sub-Pixel Heterogeneity on Spectral Vegetation Indices: Implications for Biophysical Modeling, in: Quattrochi, D. A. and Goodchild, M. F. (Eds.): *Scale in Remote Sensing and GIS*, Boca Raton, FL, pp. 113-140
- Friedl, M.A., Davis, F.W., Michaelsen, J. and Moritz, M.A. (1995): Scaling and Uncertainty in the Relationship between NDVI and Land Surface Biophysical Variables: An Analysis Using a Scene Simulation Model and Data from FIFE, *Remote Sens. Environ.*, Vol. 54, pp. 233-246
- Früh, B., Schippers, J.W., Pfeiffer, A. and Wirth, V. (2006): A pragmatic approach for downscaling precipitation in alpine complex terrain, *Meteorologische Zeitschrift*, Vol. 15, No. 3, pp. 1-16
- Gamma, E., Helm, R., Johnson, R. and Vlissides, J. (1995): *Design Patterns – Elements of Reusable Object-Oriented Software*, Reading
- Garrigues, S., Allard, D., Weiss, M., Baret, F., Marni, S. and Jeanjean, H. (2002): Influence of spatial heterogeneity and scaling on leaf area index estimates from remote sensing data, in: Sobrino, J.A. (Ed.): *Proceedings of the First International Symposium on Recent Advances in Quantitative Remote Sensing*, Auditori de Torrent, Spain, 16-20 September 2002
- Gausman, H.W. (1974): Leaf reflectance of Near-Infrared. *Photogramm. Eng. Remote Sens.*, Vol. 40, pp.183-191
- Gausman, H.W. (1977): Reflectance of Leaf Components, *Remote Sens. Environ.*, Vol. 6, pp.1-9
- Goel, N. S. (1989): Inversion of Canopy Reflectance Models for Estimation of Biophysical Parameters from Reflectance Data, in: Asrar, G.(Ed.): *Theory and Applications of Optical Remote Sensing*, New York
- Goodchild, M.F. and Quattrochi, D.A. (1997): Scale, Multiscaling, Remote Sensing and GIS, in: Quattrochi, D. A. and Goodchild, M. F. (Eds.): *Scale in Remote Sensing and GIS*, Boca Raton, FL, pp. 1-11
- Govaerts, Y. M., Jacquemoud, S., Verstraete, M. M. and Ustin S. L. (1996): Three-dimensional radiation transfer modeling in a dicotyledon leaf, *Applied Optics*, Vol. 35, Iss. 33, pp. 6585-6598
- Gregoire, C., and Raffy, M., (1997): Elaboration of multispectral models for heterogeneous media: application to the LAI, *Remote Sens. Rev.*, Vol. 15, pp 223–234
- Gross, M.F., Hardisky, M.A. and Klemas, V. (1989): Applications to coastal wetlands vegetation, in: Asrar, G., Ed.: *Theory and applications of optical remote sensing*, New York, pp. 474– 490.
- Guenther, B., Xiong, X., Salomonson, V. V., Barnes, W. L. and Young, J. (2002): On-orbit performance of the Earth Observing System Moderate Resolution Imaging Spectrometer – first year of data, *Remote Sens. Environ.*, Vol. 83, Iss. 1-2, pp. 16-30

- Hake, G., Grünreich, D., Meng, L. (2002): Kartographie – Visualisierung raum-zeitlicher Informationen, Berlin
- Hay, G.J., Marceau, D.J., Dubé, P., Bouchard, A. (2001): A multiscale framework for landscape analysis : Object-specific analysis and upscaling, *Landscape Ecology*, Vol. 16, pp. 471-490
- Hay, G.J., Niemann, K.O. and Goodenough, D.G. (1997): Spatial Thresholds, Image Objects and Upscaling: A Multiscale Evaluation, *Remote Sens. Environ.*, Vol. 62, pp. 1-19
- Hintermaier-Erhard, G. and Zech, W. (1997): Wörterbuch der Bodenkunde – Systematik, Genese, Eigenschaften, Ökologie und Verbreitung von Böden, Stuttgart
- Herrmann, S. (2002): Wie kommt die Landwirtschaft aufs Proxel? In: 12. ÖGA Jahrestagung "Armut und Reichtum im ländlichen Raum", Wien, 26.–27.09.2002
- Heywood D. I., Cornelius, S. and Carver, S. (1998): An Introduction to Geographical Information Systems, New York
- Holzhauser, J. (2002): Möglichkeiten und Grenzen bei der Bestimmung des Blattflächenindex mit dem LI-COR LAI-2000 am Beispiel von Weizen und Mais, Master Thesis at the Chair for Geography and Geographical Remote Sensing, LMU München, unpublished
- Hootsmans, R. M. (1996): Fuzzy sets and series analysis for visual decision support in spatial data exploration, *Nederlandse Geografische Studies* 202, Utrecht
- Horler, D. N. H., Dockray, M. and Barber, J. (1983): The Red Edge of Plant Leaf Reflectance, *Int. J. Remote Sens.*, Vol. 4, Iss. 2, pp. 273-288
- Hu, Z., and Islam, S. (1997): A Framework for Analysing and Designing Scale Invariant Remote Sensing Algorithms, *IEEE Transactions on Geoscience and Remote Sensing*, Vol. 35, Iss. 3, pp. 747-755
- Huete, A. R. (1988): A Soil-Adjusted Vegetation Index (SAVI), *Remote Sens. Environ.*, Vol. 25, pp. 295-309
- Huete, A. R., Jackson, R. D., and Post, D. F. (1985): Spectral Response of a Plant Canopy With Different Soil Backgrounds, *Remote Sens. Environ.*, Vol. 17, pp. 37-53
- Huete, A., Didan, K., Mura, T., Rodriguez, E. P., Gao, X. and Ferreira, L. G. (2002): Overview of the radiometric and biophysical performance of the MODIS vegetation indices, *Remote Sens. Environ.*, Vol. 83, Iss. 1-2, pp. 195-213
- Huete, A., Justice, C. and van Leeuwen, W. (1999): MODIS Vegetation Index, Algorithm Theoretical Basis Document (ATDB) Version 3, University of Arizona (online at: http://modis.gsfc.nasa.gov/data/atbd/atbd_mod13.pdf)
- Hurcom, S. J., Harrison, A. R. and Taberner, M. (1996): Assessment of Biophysical Vegetation Properties Through Spectral Decomposition Techniques, *Remote Sens. Environ.*, Vol. 56, Iss. 3, pp. 203-214
- Itten, K. I. and Meyer, P. (1993): Geometric and radiometric Correction of TM Data of Mountainous Forested Areas, *IEEE Transactions on Geoscience and Remote Sensing*, Vol. 31, Iss. 4
- Itten, K. I., Meyer, P., Kellenberger, T., Leu, R., Sandmeier, St., Bitter, P. and Seidel, K. (1992): Correction of the Impact of Topography and Atmosphere on Landsat-TM Forest Mapping of Alpine Regions, *Remote Sensing Series* Vol. 18, University of Zürich

- Jacquemoud, S. and Ustin, S. L. (2001): Leaf Optical Properties: A State of the Art, in: Proc. 8th Int. Symp. Physical Measurements and Signatures in Remote Sensing, Aussois (F), pp. 223-231
- Jacquemoud, S., and Baret, F. (1990): PROSPECT: a model of leaf optical properties spectra, *Remote Sens. Environ.*, Vol. 34, pp. 75-91
- Jerz, Hermann (1993): *Das Eiszeitalter in Bayern - Erdgeschichte, Gesteine, Wasser, Boden. Geologie von Bayern II*, Stuttgart
- Ju, J., Gopal, S., Kolaczyk, E.D. (2005): On the choice of spatial and categorial scale in remote sensing land cover classification, *Remote Sens. Environ.*, Vol. 96, pp. 62-77
- Justice, C. O. and Townshend, J. R. G. (2002): Special issue on the moderate resolution imaging spectroradiometer (MODIS): a new generation of land surface monitoring, *Remote Sens. Environ.*, Vol. 83, Iss. 1-2, pp. 1-2
- Justice, C. O., Townshend, J. R. G., Vermote, E. F., Masuoka, E., Wolfe, R. E., Saleous, N., Roy, D. P. and Morisette, J. T. (2002): An overview of MODIS land data processing and product status, *Remote Sens. Environ.*, Vol. 83, Iss. 1-2, pp. 3-15
- Justice, C. O., Vermote, E., Townshend, J.R.G., Defries, R., Roy, D.P., Hall, D.K., Salomonson, V.V., Privette, J.L., Riggs, G., Strahler, A., Lucht, W., Myneni, R.B., Knyazikhin, Y., Running, S.W., Nemani, R.R., Zhengming, W., Huete, A.R., van Leeuwen, W., Wolfe, R.E., Giglio, L., Muller, J.-P., Lewis, P., and Barnsley, M.J. (1998): The Moderate Resolution Imaging Spectroradiometer (MODIS): Land Remote Sensing for Global Change Research, *IEEE Trans. Geosci. Remote Sensing*, Vol. 36, No. 4
- Kellenberger, T.W. (2001): Upscaling of spectrally derived land-surface parameters, *International Symposium on Physical Measurements & Signatures in Remote Sensing, Aussois 2001*, pp. 111-116
- King, M. D. and Greenstone R. (1999): *1999 EOS Reference Handbook – A Guide to NASA’s Earth Science Enterprise and the Earth Observing System*, NASA
- King, M. D., Closs, J., Spangler, S., Greenstone, R., Wharton, S. and Myers, M. (Eds.) (2004): *EOS Data Products Handbook – Volume 1*, NASA Goddard Space Flight Center, Greenbelt, MA
- Knauss, W. and Klein, L. (2000): *HDF-EOS Library User’s Guide for the ECS Project, Volume 1: Overview and Examples*, Technical Paper, Upper Marlboro, Maryland
- Kneizys, F. X., Shettle, E. P., Abreu, L. W., Chetwynd, J. H., Anderson, G. P., Gallery, W. O., Selby, J. E. A. and Clough, S. A. (1988): *Users guide to LOWTRAN 7*, Optical/Infrared Technology Division, Air Force Geophysics Laboratory, Hanscom AFB, MA
- Kneubühler, M. (2002): Spectral Assessment of Crop Phenology Based on Spring Wheat and Winter Barley, *Remote Sensing Series 38*, Zürich
- Knyazikhin, Y, Martonchik, J.V., Myneni, R. B, Diner, D. J. and Running, S.W. (1998): Synergistic algorithm for estimating vegetation canopy leaf area index and fraction of absorbed photosynthetically active radiation from MODIS and MISR data, *J. Geophys. Res.*, Vol. 103, No. D24 pp. 32,257-32,275
- Knyazikhin, Y., Glassy, J., Privette, J. L., Tian, Y., Lotsch, A., Zhang, Y., Wang, Y., Morisette, J. T., Votava, P., Myneni, R.B., Nemani, R. R. and Running, S. W. (1999): MODIS Leaf Area Index (LAI) and Fraction of Photosynthetically Active

- Radiation Absorbed by Vegetation (FPAR) Product (MOD15) Algorithm Theoretical Basis Document, <http://eosps0.gsfc.nasa.gov/atbd/modistables.html>.
- Knyazikhin, Y., Martonchik, J.V., Diner, D.J., Myneni, R.B., Verstraete, M., Pinty, B. and Gobron, N. (1998): Estimation of vegetation canopy leaf area index and fraction of absorbed photosynthetically active radiation from atmosphere-corrected MISR data, *J. Geophys. Res.*, Vol. 103, No. D24 pp. 32,239-32,256
- Kraak, M.-J. and Ormeling, F. (2003): *Cartography – Visualization of Geospatial Data*, Harlow
- Kuntze, H., Roeschmann, G. and Schwerdtfeger, G. (1994): *Bodenkunde*, Stuttgart
- Kuusk, A. (1991): The hot spot effect in plant canopy reflectance, in: Myneni R. B. and Ross J. (Eds.), *Photon-Vegetation Interactions: Applications in Optical Remote Sensing and Plant Ecology*, New York, pp. 9-44
- Lakshmi, V., Albertson, J. and Schaake J. (Eds.) (2001): *Land Surface Hydrology, Meteorology, and Climate: Observation and Modeling*, AGU, Washington
- Lam, N. (1983): Spatial Interpolation Methods: A Review, *The American Cartographer*, Vol. 10, No. 2, pp. 129-149
- Lam, N., Catts, D., Quattrochi, D., Brown, D., and McMaster, R. (2004): Chapter 4 – Scale, in: McMaster R.B. and Ustry E.L. (Eds.): *A Research Agenda for Geographic Information Science*. Boca Raton, FL, pp. 93-128
- Lam, N., Quattrochi, D. (1992): On the Issues of Scale, Resolution and Fractal Analysis in the Mapping Sciences, *The Professional Geographer*, Vol. 44, Iss. 1, pp. 88–98
- Lam, N., Quattrochi, D.A., Qiu, H.L. and Zhao, W. (1998): Environmental assessment and monitoring with image characterization and modeling system using multiscale remote sensing data. *Applied Geographic Studies*, Vol. 2, Iss. 2, pp. 77–93
- Lammers, R.B., Band, L.E. and Tague, C.L. (1997): Scaling behaviour of watershed processes, in: Van Gardingen, P. R., Foody, G. M. and Curran, P. J. (Eds.): *Scaling-up from cell to landscape*, Cambridge, pp. 295-318
- Land Processes DAAC, USGS Center for Earth Resources Observation and Science (EROS) (2006): MODIS Reprojection Tool Swath (MRTSwath) User's Manual, Version 2.1
- Lenz, V, Scharfenberg, H.-J., and Wendt, H. (2006): GLOWA-Danube Technical Release No. 017, Software Documentation: Biological, unpublished
- Levin, S.A. (1992): The Problem of Pattern and Scale in Ecology, *Ecology*, Vol. 73, No. 6 , pp. 1943-1967
- Li-Cor, Inc. (1992): LAI-2000 Plant Canopy Analyzer, Operating Manual, Lincoln, NE
- Liang, S. L., Fang, H. L., Chen, M. Z, Shuey, C. J., Walthall, C., Daughtry, C., Morisette, J. T., Schaaf, C. B. and Strahler, A. H. (2002): Validating MODIS land surface reflectance and albedo products: methods and preliminary results, *Remote Sens. Environ.*, Vol. 83, Iss. 1-2, pp. 149-162
- Lillesand, T.M. and Kiefer. R.W. (2000): *Remote Sensing and Image Interpretation*. The 4 th Edition. New York, 724 pp.
- Liu, H.Q. and Huete, A.R. (1995): A feedback based modification of the NDVI to minimize canopy background atmospheric noise, *IEEE Trans. Geosci. Remote Sens.*, Vol. 33, pp. 457-465

- Liu, W. and Wu, E.Y. (2005): Comparison of non-linear mixture models: sub-pixel classification, *Remote Sens. Environ.*, Vol. 93, pp. 145-154
- Lobell, D.B. and Asner, G.P. (2004): Cropland distributions from temporal unmixing of MODIS data, *Remote Sens. Environ.*, Vol. 93, pp. 412-422
- Longley, P.A., Goodchild, M.F., Maguire, D.J., Rhind, D.W. (Eds.) (1999): *Geographical Information Systems Volume 1: Principles and Technical Issues*, New York
- Ludwig, R., Bach, H., Grüner, V. and Mauser, W. (1998): The Use of Imaging Spectrometer Data to Determine Vegetation Parameters for SVAT-Modelling, *Proceedings of the EARSel Workshop on Imaging Spectroscopy*, pp. 263 – 270
- Ludwig, R., Mauser, W., Niemeyer, S., Colgan, A., Stolz, R., Escher-Vetter, H., Kuhn, M., Reichstein, M., Tenhunen, J., Kraus, A., Ludwig, M., Barth, M. and Hennicker, R. (2003a): Web-based modeling of water, energy and matter fluxes to support decision making in mesoscale catchments – the integrative perspective of GLOWA-Danube, in: *Physics and Chemistry of the Earth*, Vol. 28, pp. 621 - 634
- Ludwig, R., Probeck, M. and Mauser, W. (2003b): Mesoscale water balance modelling in the Upper Danube watershed using sub-scale land cover information derived from NOAA-AVHRR imagery and GIS-techniques, *Physics and Chemistry of the Earth*, Vol. 28, pp. 1351-1364
- Ludwig, R., Reichert, D. and Mauser, W. (2003c): Distributed Modeling of Water and Energy Fluxes in Mesoscale Catchments using the Concept of Geocomplexes, *Geophysical Research Abstracts*, Vol. 5, 03820, European Geophysical Society
- Lymburner, L., Beggs, P. J. and Jacobson, C. R. (2000): Estimation of Canopy-Average Surface-Specific Leaf Area Using Landsat TM Data, *Photogramm. Eng. Remote Sens.*, Vol. 66, No. 2, pp. 183-191
- Marceau, J.D. (1999): The scale issue in social and natural sciences, *Can. J. Remote Sens.* 1999, Vol 25, No. 4, pp. 347-356
- Marceau, J.D., and Hay, G.J. (1999): Remote sensing contributions to the scale issue, *Can. J. Remote Sens.*, Vol. 25, Iss. 4, pp. 357-366
- Mauser, W. (1989): Die Verwendung hochauflösender Satellitendaten in einem Geographischen Informationssystem zur Modellierung von Flächenverdunstung und Bodenfeuchte, *Habilitationsschrift*, Albert-Ludwigs-Universität, Freiburg i. Br.
- Mauser, W. (2000): GLOWA-Danube – integrative techniques, scenarios and strategies regarding global changes of the water cycle, a project within the framework of GLObal Change of the WAtercycle (GLOWA), an initiative of the German Ministry for Research and Education (BMBF) conducted by the Danube Competence Network, GLOWA-DANUBE Project Description Umbrella, Munich
- Mauser, W. (2002): GLOWA-Danube Technical Release No. 003, *Software Documentation: MeteoStationsData*, unpublished
- Mauser, W. and Ludwig, R. (2002): A research concept to develop integrative techniques, scenarios and strategies regarding global changes of the water cycle, in: M. Beniston (Ed.): *Climatic Change: Implications for the hydrological cycle and for water management*, *Advances in Global Change Research* 10, pp. 171-188
- Mauser, W. and Schädlich, S. (1998): Modelling the spatial distribution of evapotranspiration on different scales using remote sensing data, in: *J. of Hydrology*, Vols. 212-213, pp. 250-267

- Mausser, W. and Bach, H. (1993): FAP Flächendaten-Analyseprogramm. Ein interaktives Programm zur Bearbeitung von Vektor- und Rasterdaten (unpublished). University of Munich
- Mausser, W., Rast, M. and Bach, H. (1999): Remote Sensing – What will we get? in: Tenhunen, J.D. and Kabat, P. (Eds): Integrating Hydrology, Ecosystem Dynamics and Biogeochemistry in Complex Landscapes, New York
- Moorcroft, P.R., Hurtt, G.C. and Pacala, S.W. (2001): A method for scaling vegetation dynamics: The ecosystem demography model (ED), *Ecological Monographs*, Vol. 71, Iss. 4, pp. 557-586
- Myneni R. B. and Ross J. (Eds.) (1991): Photon-Vegetation Interactions: Applications in Optical Remote Sensing and Plant Ecology, New York
- Myneni, R. B, Asrar, G. and Edward, T. K. (1989): The Theory of Photon Transport in Leaf Canopies, in: Asrar, G. (Ed): Theory and Applications of Optical Remote Sensing, New York
- Myneni, R. B., Hall, F. G., Sellers, P. J., and Marshak, A. L. (1995): The interpretation of spectral vegetation indices, *IEEE Trans. Geosci. Remote Sensing*, Vol. 33, pp. 481-486
- Myneni, R. B., Nemani, R. R., Running, S. W. (1997): Estimation of global leaf area index and absorbed PAR using radiative transfer models. *IEEE Trans. Geosc. Rem. Sens.*, 35, No. 6, pp. 1380-1393
- NASA (2006): Landsat 7 Science Data Users Handbook, <http://landsathandbook.gsfc.nasa.gov/handbook.html>
- National Center for Supercomputing Applications, NCSA (2003): HDF User's Guide, HDF 4 Release 2.0, December 2003, University of Illinois
- Nebiker, S. (1997): Spatial Raster Data Management for Geo-Information Systems – A Database Perspective, IGP Mitteilung Nr. 63, Dissertation ETH No. 12374, Zürich
- Niemeyer, S. (2002a): GLOWA-Danube Technical Release No. 007, Software Documentation: RadiationBalance, unpublished
- Niemeyer, S. (2002b): GLOWA-Danube Technical Release No. 008, Software Documentation: Surface, unpublished
- Nishihama, M., Wolfe, R. E., Solomon, D., Patt, F., Blanchette, J., Fleig, A. J. and Masuoka, E. (1997): MODIS Level 1A Earth Location: Algorithm Theoretical Basis Document, Version 3.0, SDST-092, Lab. Terrestrial Phys. Greenbelt, MD: NASA Goddard Space Flight Center
- Oliver, M.A. (2001): Determining the Spatial Scale of Variation in Environmental Properties using the Variogram, in: Tate, N: J., and Atkinson, P. M. (Eds.): Modelling Scale in Geographical Information Science, Chichester, UK, pp. 193-219
- Openshaw, S. (1984): The Modifiable Areal Unit Problem, *Concepts and Techniques in Modern Geography (CATMOG)*, No. 38, 40p
- Oppelt, N. (2002): Monitoring of Plant Chlorophyll and Nitrogen Status Using the Airborne Imaging Spectrometer AVIS, Dissertation, Ludwig-Maximilians Universität, München (available online)
- Parkinson, C. L. and Greenstone, R. (Eds.) (2000): EOS Data Products Handbook - Volume 2, NASA Goddard Space Flight Center, Greenbelt, MA

- Pax-Lenney, M. and Woodcock, C.E. (1997) : The effect of Spatial Resolution on the Ability to Monitor the Status of Agricultural Lands, *Remote Sens. Environ.*, Vol. 61, pp. 210-220
- Peterson, D. L. and Running, S. W. (1989): Applications in Forest Science and Management, in: Asrar, G.(Ed.): *Theory and Applications of Optical Remote Sensing*, New York
- Price, J.C. (2003): Comparing MODIS and ETM+ data for regional and global land classification, *Remote Sens. Environ.*, Vol. 86, pp. 491-499
- Privette, J. L., Myneni, R. B., Knyazikhin, Y., Mukelabai, M., Roberts, G., Tian, Y., Wang, Y. and Leblanc, S. G. (2002): Early spatial and temporal validation of MODIS LAI product in the southern Africa Kalahari, *Remote Sens. Environ.*, Vol. 83, Iss. 1-2, pp. 232-243
- Proy, C., Tanré, D. and Deschamps, P. Y. (1989): Evaluation of Topographic Effects in Remotely Sensed Data, *Remote Sens. Environ.*, Vol. 30, pp. 21-32
- Quattrochi, D. A. (1993): The need for a lexicon of scale terms in integrating remote sensing data with geographic information systems, *J. Geogr.*, 93 (5), 206
- Quattrochi, D. A. and Goodchild, M. F. (Eds.) (1997): *Scale in Remote Sensing and GIS*, Boca Raton, FL
- Quinn, K. (2001): The Newton Raphson Algorithm for Function Optimization, <http://www.stat.washington.edu/quinn/classes/536/notes/Newton.pdf>
- Rahman, H. and Dedieu, G. (1994): SMAC: a simplified method for the atmospheric correction of satellite measurements in the solar spectrum, *Int. J. Remote Sens.*, 15, No. 1, pp.123-143
- Reichert, D., Ludwig, R. and Mauser, W. (2003): Subskalige Modellierung hydrologischer Prozesse in mesoskaligen Einzugsgebieten, in: Hennrich, K., Rode, M. and Bronstert, A. (Hrsg.): *6. Workshop zur großskaligen Modellierung in der Hydrologie – Flussgebietsmanagement*, Kassel, pp. 21-32
- Reichert, D., Ludwig, R. and Mauser, W. (2004a): Flächenverteilte Modellierung der Wasserflüsse in einem mesoskaligen Einzugsgebiet – Ergebnisse mit dem Skalierungsansatz „Geokomplexe“, in: Ludwig, R., Reichert, D. and Mauser, W. (Eds.): *7. Workshop zur großskaligen Modellierung in der Hydrologie – Neue Methodische Ansätze zur Modellierung der Wasser- und Stoffumsätze in großen Einzugsgebieten*, Kassel, pp. 74-85
- Reichert, D., Ludwig, R. and Mauser, W. (2004b): Sub-grid Hydrological Catchment Modelling using Geocomplexes, *Geophysical Research Abstracts*, Vol. 6, 07655, SRef-ID: 1607-7962/gra/EGU04-A-07655, European Geosciences Union
- Rigaux, R., Scholl, M. and Voisard, A. (2002): *Spatial Databases With Application to GIS*, San Francisco
- Rojas, F., Schowengerdt, R. A., Biggar, S. F. (2002): Early results on the characterization of the Terra MODIS spatial response, *Remote Sens. Environ.*, Vol. 83, pp. 50-61
- Ross, J. K. (1981): *The Radiation Regime and Architecture of Plant Stands*, Kluwer Boston, Hingham, MA
- Russel, G. and Van Gardingen, P.R. (1997): Problems with using models to predict regional crop production, in: Van Gardingen, P. R., Foody G. M. and Curran P. J. (Eds.): *Scaling-up from cell to landscape*, Cambridge, pp. 273-294

- RZD, Regionale Zusammenarbeit der Donauländer (1986): Die Donau und ihr Einzugsgebiet. Eine hydrologische Monographie. Teil 1: Texte, Teil 2: Tabellen, Teil 3: Karten, Bayerisches Landesamt für Wasserwirtschaft, Munich
- Sandmeier, S. R. (1995): A Physically-Based Radiometric Correction Model - Correction of Atmospheric and Illumination Effects in Optical Satellite Data of Rugged Terrain, Remote Sensing Series, Vol. 26, Universität Zürich.
- Schipper, J.W. (2005): Downscaling of Precipitation in the Upper Danube Catchment Area, Dissertation, Ludwig-Maximilians Universität, München (available online)
- Schneider, D.C. (1994): Quantitative Ecology. Spatial and Temporal Scaling, San Diego, CA
- Schneider, K. (2003): Assimilating remote sensing data into a land-surface process model, Int. J. Remote Sens., Vol. 24, No. 14, pp. 2959-2980
- Schultz, G.A. and Engman, E.T. (Eds.) (2000): Remote Sensing in Hydrology and Water Management, Berlin
- Schuster, H., Zarate, M., Krimly, T. and Herrmann, S. (2004) Räumliche Disaggregation statistischer Daten unter Verwendung Geographischer Informationssysteme – erste Ergebnisse, in: 9. Internationales Symposium zur Rolle der Informations- und Kommunikationstechnologien in der und für die räumliche Planung sowie zu den Wechselwirkungen zwischen realem und virtuellem Raum, CORP 2004, GEO MULTIMEDIA 04, 24.-27.02.2004, Wien
- Scurlock, J. M. O., Asner, G. P., and Gower, S. T. (2001a): Global Leaf Area Index Data from Field Measurements, 1932-2000, Data set, Oak Ridge National Laboratory Distributed Active Archive Center, Oak Ridge, TN, (available online at <http://www.daac.ornl.gov>)
- Scurlock, J. M. O., Asner, G. P., and Gower, S. T. (2001b): Worldwide Historical Estimates and Bibliography of Leaf Area Index, 1932-2000, ORNL Technical Memorandum TM-2001/268, Oak Ridge National Laboratory, Oak Ridge, TN
- Simic, A., Chen, J.M., Liu, J. and Csillag, F. (2004): Spatial scaling of net primary productivity using subpixel information, Remote Sens. Environ., Iss. 93, pp. 246-258
- Song, C. (2005): Spectral mixture analysis for subpixel vegetation fractions in the urban environment: How to incorporate endmember variability?, Remote Sens. Environ., Vol. 95, pp. 248-263
- Spanner, M.A., Peterson, D.L., Hall, M.J., Wrigley, R.C., Card, D.H. and Running, S.W. (1984): Atmospheric effects on the remote sensing estimation of forest leaf area index. Proc. 18th Int. Symp. Remote Sens. Environ., Paris, France, pp. 1295-1308
- Spanner, M.A., Pierce, L.L., Peterson, D.L. and Running S.W. (1990): Remote sensing of temperate coniferous forest leaf area index – The influence of canopy closure, understory vegetation and background reflectance, Int. J. Remote Sens., Vol. 11, No. 1, pp. 85-111
- Stevens, S. (1946): On the theory of scales of measurement, Science 103, pp. 677-680
- Stewart, J. B., Engman E. T., Feddes R. A. and Kerr Y., (Eds.) (1996): Scaling up in Hydrology Using Remote Sensing, Chichester
- Stolz R., Strasser, G. and Mauser, W., (1999): A knowledge based multisensoral and multitemporal approach for land use classification in rugged terrain using LANDSAT TM and ERS SAR data, in: Cecchi G., Engman, E. and E Zilioli, E.

- (Eds.): Proceedings of the EUROPTO Conference on Remote Sensing for Earth Science Applications, Florence 1999, SPIE Publications 3868, pp.195-206
- Stolz, R. (1998): Die Verwendung der Fuzzy Logic Theorie zur wissensbasierten Klassifikation von Fernerkundungsdaten - Ein methodischer Ansatz zur Verbesserung von Landnutzungsklassifikationen in mesoskaligen heterogenen Räumen, dargestellt am Einzugsgebiet der Ammer, Münchner Geographische Abhandlungen, Band B 26.
- Stolz, R., Braun, M., Probeck, M., Weidinger, R. and Mauser, W. (2005): Land use Classification in complex terrain: The role of ancillary knowledge, EARSeL eProceedings 4, pp. 94-105
- Strahler, A., Muchoney, D., Borak, J., Friedl, M., Gopal, S., Lambin, E. and Moody, A. (1999): MODIS Land Cover Product Algorithm Theoretical Basis Document (ATBD), Version 5.0, MODIS Land Cover and Land Cover Change, Boston, MA (available online at: http://modis.gsfc.nasa.gov/data/atbd/atbd_mod12.pdf)
- Strasser, U., Schaedlich, S., Taschner, S., Mauser, W. (1999): Regionalization of evapotranspiration modelling using multitemporal spectral unmixing of NOAA/AVHRR data, IAHS Publications, Nr. 254, pp. 131-136
- Stuckens, J., Coppin, P. R. and Bauer, M. E. (2000): Integrating contextual information with per-pixel classification for improved land cover classification. Remote Sens. Environ., Vol. 71, pp. 282-296
- Sun, W., Heidt, V., Gong, P. and Xu, G. (2003): Information fusion for rural land-use classification with high-resolution satellite imagery. IEEE Transaction on Geoscience and Remote Sensing, Vol. 41, Iss. 4, pp. 883-890
- Tanré, D., Deroo, C., Duhaut, P., Herman, M. and Morcrette, J. J. (1990): Description of a computer code to simulate the satellite signal in the solar spectrum: the 5S code, Int. J. Remote Sens., 11, pp. 659-668
- Tanré, D., Deschamps, P., Duhaut, P. and Herman, M. (1987): Adjacency Effect Produced by the Atmospheric Scattering in Thematic Mapper Data, J. Geophys. Res., Vol. 92, Iss. D10, pp. 12000-12006
- Tate, N: J., and Atkinson, P. M. (Eds.) (2001): Modelling Scale in Geographical Information Science, Chichester, UK
- Teillet, P. M. (1986): Image correction for radiometric effects in remote sensing, Int. J. Remote Sens., Vol. 7, Iss. 12, pp. 1637-1651
- Thomas, S. C. and Winner, W. E. (2000): Leaf area index of an old-growth Douglas-fir forest estimated from direct structural measurements in the canopy, Can. J. For. Res., Vol 30, pp. 1922-1930
- Tian, Y., Wang, Y., Zhang, Y., Knyazikhin, Y., Bogaert, J. and Myneni, R.B. (2002): Radiative transfer based scaling of LAI retrievals from reflectance data of different resolutions, Remote Sens. Environ., Vol. 84, pp. 143-159
- Tian, Y., Woodcock, C.E., Wang, Y., Privette, J.L., Shabanov, N.V., Zhou, L., Zhang, Y., Buermann, W., Dong, J., Veikkanen, B., Häme, T., Andersson, K., Ozdogan, M., Knyahikhin, Y. and Myneni, R.B. (2002a): Multiscale analysis and validation of the MODIS LAI product I. Uncertainty Assessment, Remote Sens. Environ., Vol. 83, pp. 414-430
- Tian, Y., Woodcock, C.E., Wang, Y., Privette, J.L., Shabanov, N.V., Zhou, L., Zhang, Y., Buermann, W., Dong, J., Veikkanen, B., Häme, T., Andersson, K., Ozdogan, M.,

- Knyazikhin, Y. and Myneni, R.B. (2002b): Multiscale analysis and validation of the MODIS LAI product II. Sampling strategy, *Remote Sens. Environ.*, Vol. 83, pp. 431-441
- Tian, Y., Zhang, Y., Knyazikhin, Y., Myneni, R.B., Glassy, J.M., Dedieu, G. and Running, S.W. (2000): Prototyping of MODIS LAI and FPAR Algorithm with LASUR and LANDSAT Data, *IEEE Trans. Geosc. Rem. Sens.*, Vol. 38, No. 5, pp. 2387-2401
- Torgerson, W. S., (1958): *Theory and Methods of Scaling*, New York
- Townshend, J. R. G. and Justice, C. O. (2002): Towards operational monitoring of terrestrial systems by moderate-resolution remote sensing, *Remote Sens. Environ.*, Vol. 83, Iss. 1-2, pp. 351-359
- Treitz, P. (2001): Variogram analysis of high spatial resolution remote sensing data: An examination of boreal forest ecosystems, *Int. J. Remote Sens.*, Vol. 22, Iss. 18, pp. 3895-3900
- Treitz, P. and Howarth, P. (2000): High Spatial Resolution Remote Sensing Data for Forest Ecosystem Classification, *Remote Sens. Environ.*, Vol. 72., pp. 268-289
- Troller, G. N., Isaacman, A. and Solomonson, V. (2003): MODIS Level 1B Product User's Guide, MCST Document # PUB-01-U-0202- REV B, NASA Goddard Space Flight Center, Greenbelt, MD
- Turner, D. P., Cohen, W. B., Kennedy, R. E., Fassnacht, K. S. and Briggs, J. M. (1999): Relationships between Leaf Area Index and Landsat TM Spectral Vegetation Indices across Three Temperate Zone Sites, *Remote Sens. Environ.*, Vol. 70, Iss. 1, pp. 52-68
- Turner, M. G., Dale V. H. and Gardner R. H. (1989): Predicting across scales: theory development and testing. *Landscape Ecol.*, Vol. 3, pp. 245-252
- U.S. Geological Survey (USGS)/ EROS Data Center (EDC) (1999): Landsat 7 System Zero-R Distribution Product Data Format Control Book, Volume 5, Book 1, Revision 6, October 1999
- U.S. Geological Survey (USGS)/ EROS Data Center (EDC) (2000): Level 1 Product Output Files Data Format Control Book, Volume 5, Book 2, Revision 4, January 2000
- Van Gardingen, P. R., Foody G. M. and Curran P. J. (1997): *Scaling-up from cell to landscape*. pp 386, Cambridge
- Van Leeuwen, W. J. D. and Huete, A. R. (1996): Effects of Standing Litter on the Biophysical Interpretation of Plant Canopies with Spectral Indices. *Remote Sensing of Environment*, Vol.55, pp.123-138
- Verhoef, W. (1984): Light Scattering by Leaf Layers With Application to Canopy Reflectance Modelling: The SAIL Model, *Remote Sens. Environ.*, Vol. 16, pp. 125-141
- Verhoef, W. and Bach, H. (2003): Simulation of hyperspectral and directional radiance images using coupled biophysical and atmospheric radiative transfer models, *Remote Sens. Environ.*, Vol. 87, pp. 23-41
- Vermote, E. F., El Saleous, N. Z. and Justice, C. O. (2002): Atmospheric correction of MODIS data in the visible to middle infrared: first results, *Remote Sens. Environ.*, Vol. 83, Iss. 1-2, pp. 97-111
- Vermote, E. F. and Vermeulen, A. (1999): Atmospheric correction algorithm: spectral reflectances (MOD09). Algorithm Theoretical Background Document, NASA

- contract NAS5-96062, University of Maryland, Dept of Geography, (available online at: http://modis.gsfc.nasa.gov/data/atbd/atbd_mod08.pdf)
- Verstraete, M. M., Pinty, B. and Myneni, R. B. (1996): Potential and Limitations of Information Extraction on the Terrestrial Biosphere from Satellite Remote Sensing. *Remote Sens. Environ.*, Vol. 58, Iss. 2, pp. 201-214
- Walford, N. (2002): *Geographical Data – Characteristics and Sources*, New York
- Wang, Q., Tenhunen, J., Dinh, N.Q., Reichstein, M., Otieno, D., Granier, A., Pilegarrrd, K. (2005): Evaluation of seasonal variation of MODIS derived leaf area index at two European deciduous broadleaf forest sites, *Remote Sens. Environ.*, Vol. 96, pp. 475-484
- Wang, Y., Woodcock, C. E., Buermann, W., Stenberg, P., Voipio, P., Smolander, H., Häme, T., Tian, Y., Hu, J., Knyazikhin, Y., and Myneni, R. B. (2004): Evaluation of the MODIS LAI algorithm at a coniferous forest site in Finland, *Remote Sens. Environ.*, Vol. 91, Iss. 1, pp. 114-127
- Weiss, M. and Baret, F. (1999): Evaluation of Canopy Biophysical Variable Retrieval Performances from the Accumulation of Large Swath Satellite Data, *Remote Sens. Environ.*, Vol. 70, pp. 293-306
- Welles, J. M. (1990): Some Indirect Methods of Estimating Canopy Structure, *Remote Sensing Reviews*, Vol. 5, Iss. 1, pp. 31-43
- Welles, J. M. and Norman, J. M. (1991): Instrument for Indirect Measurement of Canopy Architecture, *Agronomy Journal*, Vol. 83, Iss. 5. pp. 818-825
- Wessman, C.A., Aber, J.D., Peterson, D.L. and Melillo, J.M. (1988): Foliar Analysis Using Near Infrared Reflectance Spectroscopy, *Can. J. Forest. Res.*, Vol.18, pp. 6-11
- Winkler, S. (1980): *Einführung in die Pflanzenökologie*, 2. Aufl., Stuttgart
- Wolfe, R. E., Nishihama, M., Fleig, A. J., Kuyper, J. A., Roy, D. P., Storey, J. C., Patt, F. S. (2002): Achieving sub-pixel geolocation accuracy in support of MODIS land science, *Remote Sens. Environ.*, Vol. 83, pp. 31-49
- Woodcock, C. E. and Strahler, A. H. (1987): The factor of scale in remote sensing, *Remote Sens. Environ.*, Vol. 21, Iss. 3, pp. 311-332
- Woodcock, C.E., Strahler, A.H., and Jupp, D.L.B (1988a): Th use of variograms in remote sensing: Part I. Scene models and simulated images, *Remote Sens. Environ.*, Vol. 25, pp. 323-348
- Woodcock, C.E., Strahler, A.H., and Jupp, D.L.B (1988b): Th use of variograms in remote sensing: Part II. Real digital images, *Remote Sens. Environ.*, Vol. 25, pp. 349-379
- Woolley, J. T. (1971): Reflectance and transmittance of light by leaves, *Plant Physiology*, Vol. 47, Iss. 5, pp. 656-662
- Wu, J. (1999): Hierarchy and scaling: extrapolating information along a scaling ladder, *Can. J. of Remote Sens.*, Vol. 25, pp. 367-380
- Wu, J., Jones K. B., Li, H. and Loucks, O. L. (Eds.) (2006): *Scaling and Uncertainty Analysis in Ecology: Methods and Applications*, New York.
- Wu, J. and Li, H. (2006): Concepts of Scale and Scaling, in: Wu, J., Jones K. B., Li, H., and Loucks, O. L. (Eds.) (2006): *Scaling and Uncertainty Analysis in Ecology: Methods and Applications*, New York

- Wu, J. and Qi, Y. (2000): Dealing with scale in landscape analysis: An overview, *Geographic Information Sciences* Vol. 6, No. 1, pp.1-5
- Zadeh, L. A. (1965): Fuzzy Sets. *Information Control* 8, pp. 338-353
- Zawadzki, J., Cieszewski, C.J., Zasada, M. and Lowe, R.C. (2005): Applying geostatistics for investigations of forest ecosystems using remote sensing imagery, *Silva Fennica*, Vol. 39, Iss. 4, pp. 599–617
- Zeidler, E. (Ed.)(1996): *Teubner-Taschenbuch der Mathematik, Teil 1*, Leipzig
- Zhang, Y., Tian, Y., Knyazikhin, Y., Martonchick, J.V., Diner, D.J., Leroy, M. and Myneni, R.B. (2000): Prototyping of MISR LAI and FPAR Algorithm with POLDER Data over Africa, *IEEE Trans. Geosc. Rem. Sens.*, Vol. 38, No. 5, pp. 2402-2418
- Zimmermann, H.-J. (1987): *Fuzzy Sets, Decision Making and Expert Systems*, Boston
- Zimmermann, H.-J., (1991): *Fuzzy set theory and its applications*, 2nd Ed., Boston.

Appendix

Appendix 1: MODIS Data Levels

Raw data	-	Data in their original packets, as received from the observer.
Level 0	-	Raw instrument data at original resolution, time ordered, with duplicate packets removed.
Level 1A	-	Reconstructed unprocessed instrument/payload data at full resolution; any and all communications artifacts (e.g. synchronization frames, communications headers) removed.
Level 1B	-	Level 1A data that have been processed to sensor units and radiometrically corrected and geolocated.
Level 2	-	Derived geophysical variables at the same resolution and location as the Level 1 source data.
Level 3	-	Variables mapped on uniform space-time grid scales, usually with some completeness and consistency.
Level 4	-	Model output or results from analyses of lower level data (i.e., variables derived from multiple measurements).

Taken from the Parameter Data Product Glossary web page at Goddard Earth Sciences (GES) Data and Information Services Center (DISC), GES DAAC

Appendix 2: Software

This Appendix summarizes the coding work conducted for this study. The purpose and object-oriented layout of the software is documented. It comprises a codec for access to the FAP file format in the java programming language. An object oriented structure was sought to provide simple programming interfaces for arbitrary manipulation of FAP format files. This codec is used in the software for reflectance segmentation and for a converter to transform HDF Scientific datasets to the FAP format.

Codec FapPicIO

This java package contains a codec for reading and writing data to and from FAP *.pic files providing a flexible interface to file information and data extraction. The structure is designed to allow processing of FAP format files by usage and/or implementation of existing interfaces. It contains the packages `iggf.io`, `iggf.io.pic` and `iggf.io.pic.example`. Its main concept is an inheritance tree of which the main classes are `PicFile`, `Band`, `Pixel` and `Scan`. All are implementations of the `PicElement` interface to provide a common basis for iteration operations and the manipulation of instances of `PicElement` (see Figure A1).

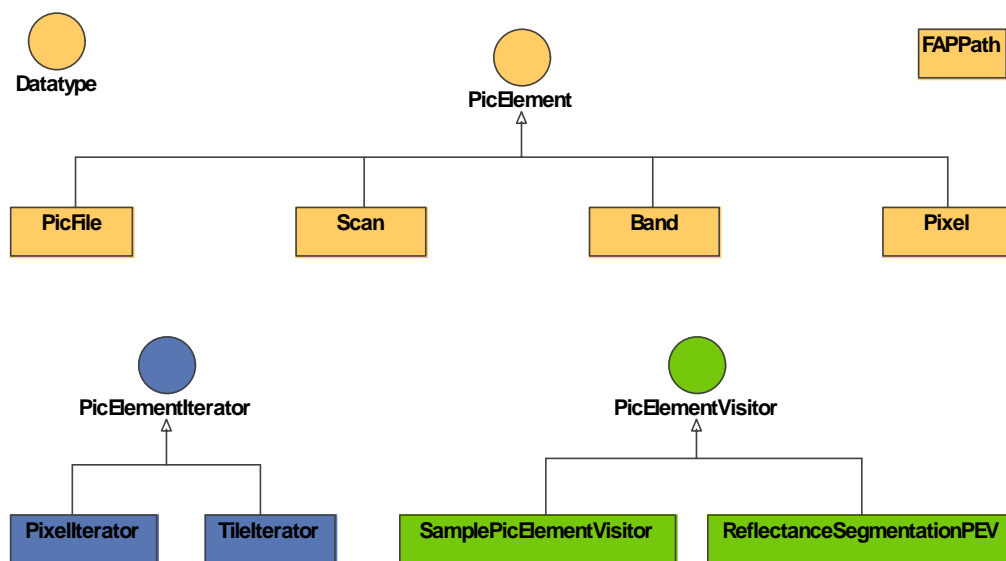


Figure A1: UML Class diagram of the FapPicIO codec, Iterators and Visitors.

The IO-Operations are based on the `java.nio` package for execution speed. Each `PicElement` is backed by one or more instances of type `java.nio.ByteBuffer` so that operations for data reading and writing can be performed by effective operating system's native I/O operations. For information on using the `ByteBuffer` class see the Java language API.

While the `PicFile` class abstracts the full physical file and provides primary access to all information, `Band`, `Scan` and `Pixel` are portions of the file and associated with a `PicFile`

object. A `Band` is one horizontal layer in the file and stores the layers header information (e.g. name, data type, data type size, position in file) and data. A `Pixel` is the stack of the values of all bands or a portion of them at one unique raster position. A `Scan` is an arbitrary rectangular subset of the `PicFile` containing a selection of the bands of the file. The `PicFile` class interface provides access to metadata and its `PicElements`. The key I/O functionality is implemented in a method to retrieve or insert a `Scan` object specified by position and size as well as a selection of `Bands`. The overloaded `PicFile.getScan()` method provides access to common “scans” such as the data of all bands of one full row.

This method is accessed when using the Iterator pattern (Gamma et al., 1995) to iterate over the collection of a `PicElement`. The implementations of the `PicElementIterator` interface provide functionality to iterate over the pixels of a `PicFile`, a `Scan` or a `Band` (`PixelIterator`) or over equally sized square tiles returned as instances of `Scan` of the underlying `PicFile` (`TileIterator`). The core functionality to process `PicFileElements` is provided as a Visitor-pattern (Gamma, et al., 1995). `PicElements` can interact with implementations of `PicElementsVisitor`. A `PicElementVistor` is designed to perform operations on a `PicElement` (visit it). It may be used to consecutively process each `Pixel` or `Scan` returned by either `PicElementIterator`. Two implementations of `PicElementVistor` are shown in Figure A1.

To provide functionality for reading ancillary data from ASCII-files, the abstract `DataBuilder` class from the `iggf.io` package is provided (Builder-pattern). The `DataBuilders` functionality of extracting ASCII file records as strings can be extended to build any desired data structure such as implemented in the `PixelBuilderFloat` extension of `DataBuilder` to produce instances of `Pixel` from a text file. The package also contains a class with the static functionality to read out the FAP path set on a system (`FAPPath`).

Details on the implementation and usage are given in the javadoc documentation and in the code of the package `iggf.io.pic.example`.

Reflectance Segmentation

The algorithm for reflectance segmentation is realized as an implementation of `PicElementVisitor`, the `ReflectanceSegmentationPEV`. It uses a number of other classes for the calculations (see Figure A2). The main computations are carried out by implementations of an interface `Function` to compute Gaussian function values (`GaussFunction`), the area weighted sum of land cover reflectances (`LandcoverReflectanceSum`) and the function that is optimized in the Newton-Raphson method (`OptimizationFunction`). The `Function` interface provides access to retrieve the derivative `Function` objects of the functions which are required in the Newton-Raphson method. The `ReflectanceSegmentationPEV` reads initial `GaussFunctions` parameters from file via a `GaussFunctionBuilder`. The computation of reflectance segmentation and selection of the final best result is conducted within the visitor based on the input from the visited `Pixel`. Output is stored to a new `Pixel` that can be retrieved from the `ReflectanceSegmentationPEV`-object after the visit.

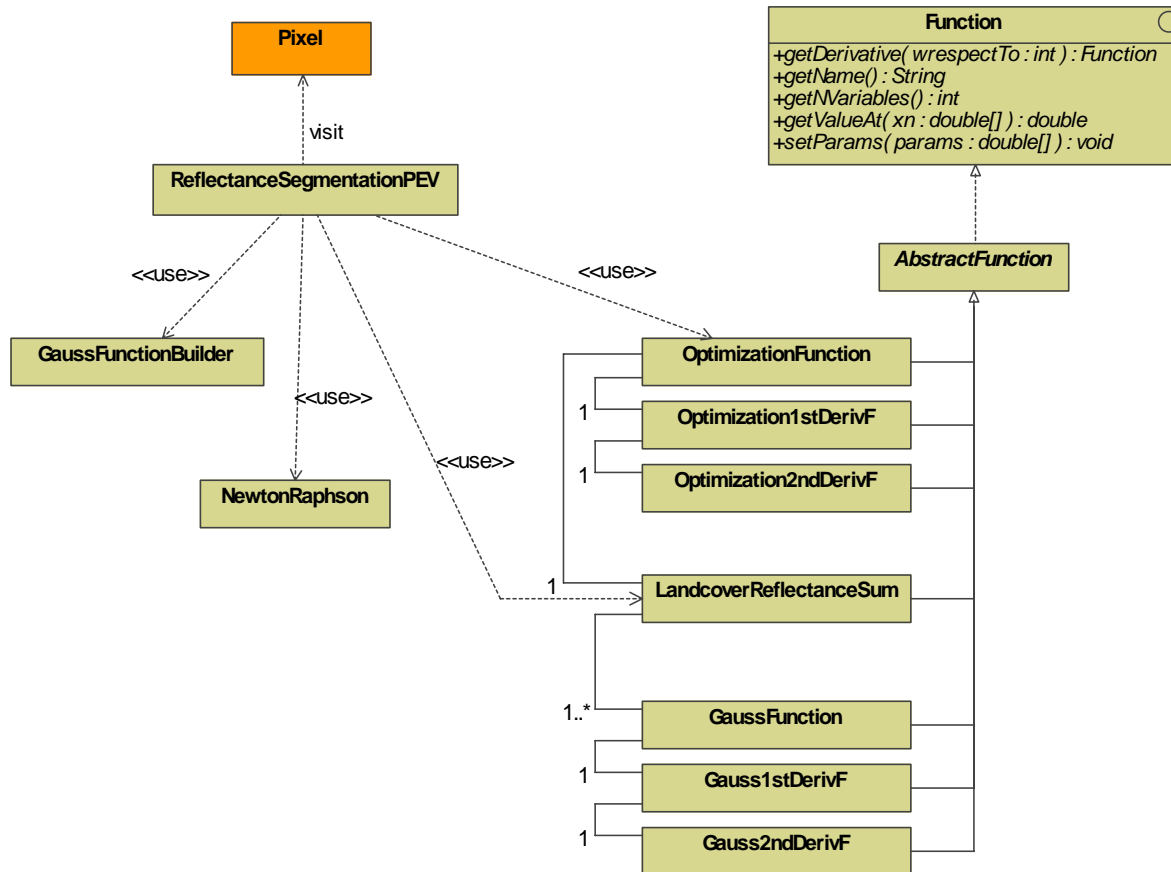


Figure A2: UML Class diagram of the algorithm for reflectance segmentation implemented as *ReflectanceSegmentationPEV*.

The matrix computations within the *NewtonRaphson* class are based on the software from the Colt project (Copyright © 1999 CERN - European Organization for Nuclear Research, see copyright and permission notice below). The `cern.colt.matrix*` package from the Colt library and the `cern.jet.math*` package from the Jet library contain the components that are in use in the optimization iteration. The version of the library is Colt 1.2.0 from September 2004 which was still the latest at the time of this writing and is available on the Internet at <http://dsd.lbl.gov/~hoschek/colt/>. The `colt.jar` archive is required in the classpath for the execution of reflectance segmentation.

Colt License Agreement - Packages `cern.colt*`, `cern.jet*`, `cern.clhep`

Copyright (c) 1999 CERN - European Organization for Nuclear Research.

Permission to use, copy, modify, distribute and sell this software and its documentation for any purpose is hereby granted without fee, provided that the above copyright notice appear in all copies and that both that copyright notice and this permission notice appear in supporting documentation. CERN makes no representations about the suitability of this software for any purpose. It is provided "as is" without expressed or implied warranty.

Converter HDF2FAP/HDF2PIC

The FAPPicIO library is used in two versions of a tool to convert a selection of the scientific datasets (SDS) contained in a HDF file to bands of files in the FAP format. HDF2FAP has a simple graphical interface to select SDS and dump them to either FAP format or flat binary files (see Figure A3). The HDF2PIC version is a command line tool for the same purpose allowing batch conversion of HDF files (Figure A4).

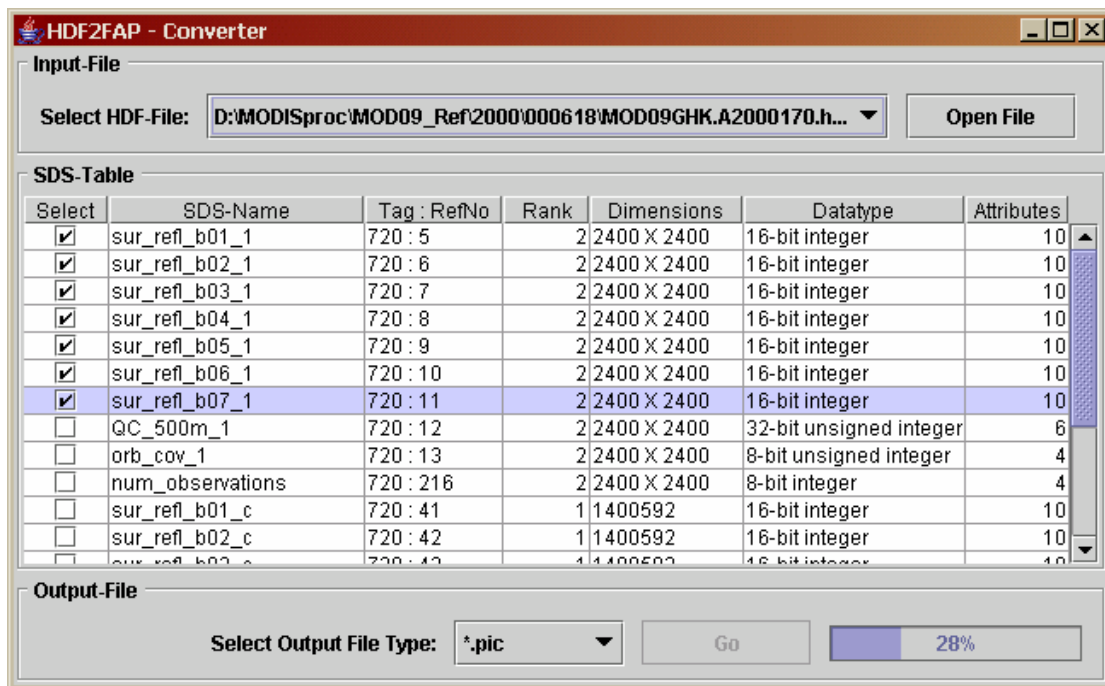


Figure A3: HDF2FAP converter, surface reflectance bands 1-7 of a MOD09 Reflectance file selected for conversion.

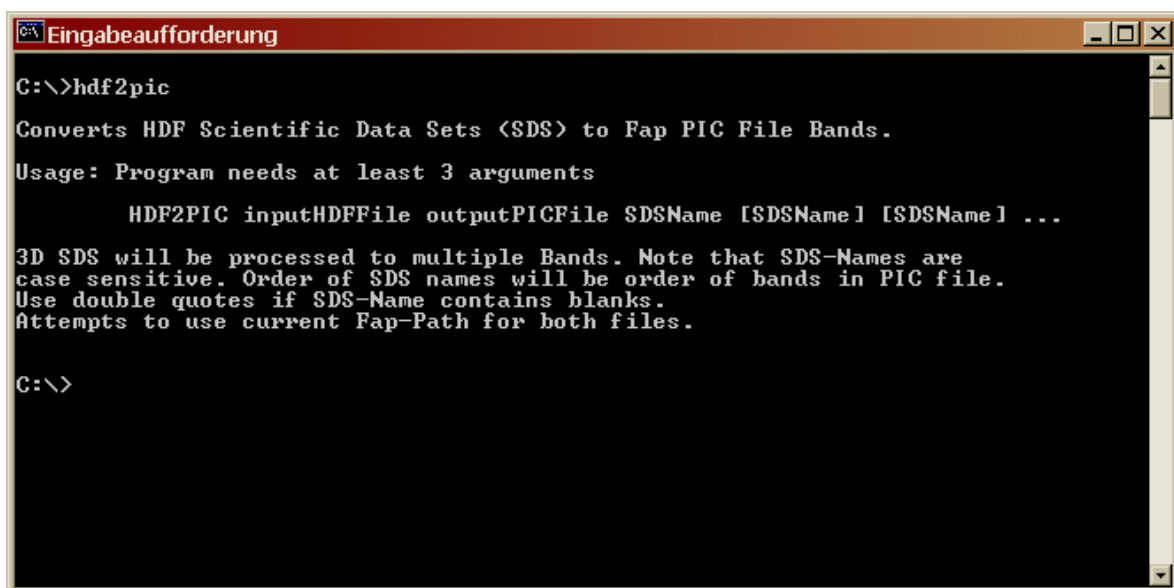


Figure A4: HDF2PIC converter, help displayed when no arguments are provided.

Appendix 3: LAI Measurements

Needleleaf forest:

Date	DOY	Measurements							mean	stddev	min	max
Needleleaf forest Oberbrunn 2002, old stand												
03.05.2002	123	4.11	3.91	3.80	3.79	3.88			6.24	0.21	6.06	6.58
15.05.2002	135	4.72	4.67	4.56	4.43	4.97			7.47	0.32	7.09	7.95
23.05.2002	143	4.37	4.12	3.99	4.17	4.39			6.73	0.27	6.38	7.02
Needleleaf forest Oberbrunn 2002, young stand												
03.05.2002	123	4.65	5.26	4.56	4.85	4.65			7.67	0.45	7.30	8.42
15.05.2002	135	4.95	5.21	4.92	4.69	4.03			7.62	0.72	6.45	8.34
23.05.2002	143	5.35	5.00	4.42	4.44	5.18			7.80	0.68	7.07	8.56
Needleleaf forest Reißmühlenweg 2003, old stand												
30.04.2003	120	3.26	3.47	3.29	3.31	3.46	3.34	3.54	5.37	0.16	5.22	5.55
12.05.2003	132	3.30	3.29	3.38	3.32	3.35	3.33		5.32	0.06	5.26	5.41
11.08.2003	223	2.95	3.57	2.77	3.00	3.16			4.94	0.48	4.43	5.71
10.09.2003	253	3.31	3.49	3.68	3.69	3.60	3.32	3.86	5.69	0.25	5.30	5.90
Needleleaf forest Bocksfeld 2003, young stand												
30.04.2003	120	3.67	3.83	3.91	4.01	4.19	4.23		6.28	0.31	5.87	6.70
12.05.2003	132	4.57	4.26	4.11	4.14	4.09	4.45	4.43	6.77	0.32	6.54	7.31
11.08.2003	223	3.90	4.00	4.08	4.11	4.15	4.34		6.48	0.16	6.24	6.64
10.09.2003	253	4.43	4.70	4.84	4.59	4.99	5.03		7.54	0.35	7.09	7.98

Deciduous forest:

Date	DOY	Measurements							mean	stddev	min	max	
Deciduous forest Neuhöchstadt 2002, old stand													
26.04.2002	116	1.32	1.49	1.45	1.53	1.49			1.46	0.08	1.32	1.53	
03.05.2002	123	2.36	2.56	2.72	2.30	2.41	2.68	2.56	2.68	2.53	0.16	2.3	2.72
14.05.2002	134	4.78	4.47	4.96	4.86	5.29			4.87	0.30	4.47	5.29	
23.05.2002	143	5.27	5.46	5.35	5.02	5.43			5.31	0.18	5.02	5.46	
Deciduous forest Meiling 2002, old stand													
26.04.2002	116	1.71	1.78	1.59	1.63	1.59			1.66	0.08	1.59	1.78	
03.05.2002	123	3.10	2.95	2.95	2.78	2.80			2.92	0.13	2.78	3.1	
15.05.2002	135	3.69	4.78	4.63	5.05	4.52			4.53	0.51	3.69	5.05	
23.05.2002	143	4.72	5.43	5.79	5.85	5.19			5.40	0.46	4.72	5.85	
Deciduous forest Meiling 2002, young stand													
26.04.2002	116	1.56	1.93	2.01	1.81	1.68			1.80	0.18	1.56	2.01	
03.05.2002	123	2.28	2.27	2.40	2.58	2.55	2.49		2.43	0.13	2.27	2.58	
15.05.2002	135	4.92	4.97	4.67	4.47	4.39			4.68	0.26	4.39	4.97	
23.05.2002	143	6.26	5.99	5.64	5.48	5.33			5.74	0.38	5.33	6.26	
Deciduous forest Mühltalerleiten 2003, old stand													
30.04.2003	120	1.95	2.12	2.51	2.83	2.76	2.98	1.73	2.41	0.48	1.73	2.98	
12.05.2003	132	4.98	4.92	3.19	3.10	3.20	2.94	2.94	3.61	0.92	2.94	4.98	
23.05.2003	143	3.01	3.13	3.05	4.30	4.85	4.47		3.80	0.83	3.01	4.85	
03.09.2003	246	3.28	3.09	3.29	4.53	4.61			3.76	0.74	3.09	4.61	
10.09.2003	253	2.69	2.52	2.46	3.87	4.08	3.87		3.25	0.77	2.46	4.08	
Deciduous forest Weiherbuchet 2003, old stand													
30.04.2003	120	2.93	2.98	2.89	2.66	3.23	2.56	3.11	2.97	2.92	0.22	2.56	3.23
12.05.2003	132	4.28	4.68	5.44	4.52	6.38	6.03		5.22	0.86	4.28	6.38	
23.05.2003	143	5.00	5.00	4.38	5.37	4.68	4.80		4.87	0.34	4.38	5.37	
03.09.2003	246	4.15	4.31	4.34	3.88	4.49			4.23	0.23	3.88	4.49	
10.09.2003	253	3.95	4.06	4.14	3.71	3.94			3.96	0.16	3.71	4.14	

Winter grain

erroneous measurements are in brackets and omitted in the statistics:

Date	DOY	Measurements Plot 1				Measurements Plot 2				Measurements Plot 3				mean	stddev	min	max
Winter wheat DLR, 2002																	
03.05.2002	123	1.93	1.88	1.78	2.23	2.57	2.74	2.00	2.08	1.73	2.56	2.51	1.70	2.14	0.368	1.70	2.74
14.05.2002	134	4.13	4.10	4.35	4.15	3.23	3.34	3.76	3.58	2.56	2.54	2.81	3.00	3.46	0.646	2.54	4.35
23.05.2002	143	4.43	4.15	3.92	4.12	3.52	3.52	4.14	4.01	3.14	3.24	3.49	3.31	3.75	0.427	3.14	4.43
29.05.2002	149	5.20	5.09	4.45	5.32	3.69	3.72	3.80	3.88	3.72	3.63	3.94	4.03	4.21	0.641	3.63	5.32
05.06.2002	156	4.36	4.32	4.42	4.44	4.36	4.54	4.36	4.32	4.31	3.95	4.37	4.27	4.34	0.140	3.95	4.54
17.06.2002	168	4.69	4.05	4.11	4.19	3.69	3.80	3.70	3.55	4.11	3.28	3.40	3.56	3.84	0.399	3.28	4.69
27.06.2002	178	3.74	3.69	4.06	3.85	4.26	4.30	4.02	4.01	3.51	3.78	3.54	3.72	3.87	0.258	3.51	4.30
11.07.2002	192	3.53	4.02	3.96	3.58	3.42	3.39	3.16	3.02	2.97	3.02	3.16	3.20	3.37	0.352	2.97	4.02
22.07.2002	203	2.77	2.99	3.03	2.97	2.44	2.59	2.49	2.43	2.75	2.95	2.59	2.52	2.71	0.229	2.43	3.03
08.08.2002	220	2.70	2.68	2.69	2.66	2.77	2.77	2.92	2.84	2.26	2.23	2.32	2.17	2.58	0.263	2.17	2.92
Winter wheat Mitterwies, 2002																	
03.05.2002	123	2.03	1.82	2.02	1.73	1.76	1.94	1.98	1.95	1.71	1.78	1.72	1.85	1.86	0.121	1.71	2.03
14.05.2002	134	3.01	2.88	2.80	2.38	2.95	3.16	2.53	2.59	2.62	2.52	2.9	2.72	2.76	0.233	2.38	3.16
23.05.2002	143	2.97	2.94	3.11	2.99	3.27	3.28	3.36	3.23	3.32	3.21	3.23	3.08	3.17	0.143	2.94	3.36
29.05.2002	149	3.37	3.56	3.55	3.47	3.46	3.61	3.59	3.54	2.79	3.23	3.09	3.38	3.39	0.244	2.79	3.61
05.06.2002	156	[4,14]	5.00	5.00	5.18	4.52	4.21	3.76	3.95	4.21	3.98	3.27	3.39	4.22	0.645	3.27	5.18
17.06.2002	168	3.70	4.73	4.41	4.60	5.12	4.37	4.33	4.61	4.05	4.46	4.42	4.21	4.42	0.352	3.70	5.12
27.06.2002	178	4.14	4.17	4.29	4.23	3.84	3.46	4.19	3.99	4.04	3.87	3.76	3.57	3.96	0.267	3.46	4.29
11.07.2002	192	3.17	3.51	3.69	3.69	3.5	3.44	3.52	3.66	3.34	3.27	3.25	3.28	3.44	0.181	3.17	3.69
22.07.2002	203	2.43	2.48	2.66	2.37	2.66	2.82	2.63	2.59	2.46	2.27	2.15	2.91	2.54	0.220	2.15	2.91
08.08.2002	220	2.10	2.28	1.88	1.91	2.3	2.34	2.34	2.26	2.35	2.36	2.72	2.78	2.30	0.267	1.88	2.78
Winter wheat Stürzer, 2002																	
03.05.2002	123	1.67	1.82	2.09	1.87	1.99	1.87	2.08	2.20	2.21	2.06	2.20	1.72	1.98	0.189	1.67	2.21
15.05.2002	135	3.43	3.54	3.84	3.68	3.76	4.07	3.40	3.45	2.21	2.06	2.64	2.65	3.23	0.665	2.06	4.07
23.05.2002	143	3.22	3.21	3.06	3.06	3.84	3.82	3.96	4.39	3.33	2.73	2.97	3.28	3.41	0.488	2.73	4.39
29.05.2002	149	3.92	4.12	3.99	3.90	3.95	4.00	4.42	4.38	3.42	3.42	3.41	3.71	3.89	0.344	3.41	4.42
05.06.2002	156	3.85	3.76	3.55	3.38					3.27	3.29	3.39	3.31	3.48	0.223	3.27	3.85
17.06.2002	168	4.51	4.59	4.42	4.30	5.13	5.14	5.26	5.28	3.92	3.06	3.24	3.24	4.34	0.816	3.06	5.28
27.06.2002	178	4.14	3.99	3.90	3.90	4.82	4.65	4.58	4.71	3.48	3.90	4.63	3.77	4.21	0.447	3.48	4.82
11.07.2002	192	3.47	3.52	3.34	3.52	3.67	3.82	3.80	3.95	3.52	3.64	2.97	3.14	3.51	0.265	2.97	3.95
23.07.2002	204	3.47	3.19	4.03	4.13	2.32	2.45	2.31	2.69	2.66	2.72	2.61	2.56	3.00	0.635	2.31	4.13
08.08.2002	220	2.11	2.14	2.43	2.79	2.31	2.03	2.00	1.69	2.86	2.79	2.37	2.53	2.34	0.363	1.69	2.86
Winter wheat Stürzer, 2003																	
23.04.2003	113	0.60	0.54	0.74	0.51	0.47	0.43	0.23	0.22	0.18	0.15	0.10	0.23	0.37	0.207	0.10	0.74
06.05.2003	126	1.15	1.28	1.59	1.57	1.96	1.69	1.94	2.06	1.23	1.15	0.92	1.24	1.48	0.373	0.92	2.06
19.05.2003	139	3.32	3.39	3.38	3.57	2.62	2.70	3.17	3.20	2.45	2.58	2.35	2.40	2.93	0.45	2.35	3.57
02.06.2003	153	4.16	4.29	4.57	4.52	5.17	5.03	5.13	5.12	4.62	4.51	4.25	4.12	4.62	0.395	4.12	5.17
16.06.2003	167	5.67	[3,87]	5.43	4.99	5.10	5.00	5.17	5.13	4.44	4.57	4.21	4.23	4.90	0.48	4.21	5.67
08.07.2003	189	3.78	3.77	3.99	3.89	3.74	3.48	3.36	3.34	3.17	3.22	3.54	3.50	3.57	0.267	3.17	3.99
28.07.2003	209	3.84	3.74	3.11	3.30	2.57	2.27	2.69	2.44	3.10	3.02	2.85	2.98	2.99	0.478	2.27	3.84
Triticale Stürzer, 2003																	
23.04.2003	113	0.49	0.18	0.30	0.49	0.46	0.44	0.67	0.65	0.89	0.98	0.97	1.09	0.59	0.266	0.18	0.98
06.05.2003	126	1.84	[0,23]	1.47	1.40	1.76	1.74	1.50	1.66	1.95	1.95	2.04	2.09	1.73	0.221	1.40	2.04
19.05.2003	139	2.40	2.27	2.27	2.32	2.23	2.25	2.77	2.83	2.39	2.23	2.72	2.58	2.43	0.232	2.23	2.83
02.06.2003	153	3.75	3.76	3.85	3.69	3.54	3.38	3.72	3.57	3.82	3.73	3.72	3.63	3.68	0.137	3.38	3.85
16.06.2003	167	4.34	4.55	4.41	4.36	3.14	3.12	3.50	3.50	3.38	3.38	3.91	3.65	3.78	0.546	3.12	4.55
08.07.2003	189	2.38	2.39	2.15	2.16	2.60	2.63	2.73	2.77	2.66	2.69	2.95	3.03	2.56	0.254	2.15	2.95

Date	DOY	Measurements Plot 1						Measurements Plot 2						Measurements Plot 3									
29.04.2004	120	1.67	1.73	1.58	1.65	1.60	1.55							1.87	1.84								
06.05.2004	127	1.81	1.86	1.44	1.36			2.34	2.35	2.60	2.07	1.92		2.34	2.23	1.85	1.75						
13.05.2004	134	3.40	2.96	3.12	3.37			3.89	3.95	3.16	[2.87]	3.03		2.21	2.36	[2.61]	2.44	2.36					
25.05.2004	146	3.21	3.43	3.43	3.52	3.49	3.77	4.14	4.31	3.87	3.79	4.29	4.26	[4,22]	[4,43]	[4,67]	[4,66]	[5,14]	[5,22]	[5,33]	[5,43]		
01.06.2004	153	3.01	3.29	3.58	3.55			3.46	3.28	3.53	3.45			3.97	3.73	4.16	4.14						
07.06.2004	159	3.28	3.36	3.86	3.76	4.41	4.24	4.08	4.37	4.53	4.73	4.94	4.67	[5,36]	[4,38]	[5,39]	[5,51]	[6,07]	[5,52]	[4,42]	[4,89]		
11.06.2004	163	4.59	4.55	3.79	3.48			4.97	4.90	[5,82]	[5,70]	5.35	5.23	4.45	4.51	4.48	4.53						
17.06.2004	169	5.50	5.80	5.39	5.49			5.75	6.07	5.55	5.16			5.27	5.28	5.60	5.32						
24.06.2004	176	4.12	4.43	4.94	5.11			5.08	5.22	4.35	4.27			[5,95]	[6,00]	[6,64]	[6,77]						
05.07.2004	187							4.92	4.96	5.33													
15.07.2004	197	5.03	5.00	4.41	4.25	4.56	4.66	4.80	4.80	4.76	4.65			5.61	5.56	6.38	6.45	5.65	5.65				
22.07.2004	204	5.18	5.39	5.30	5.50			4.67	4.60	4.64	4.84			5.30	5.64	5.09	4.99						
29.07.2004	211	5.18	5.22	5.25	5.32			4.82	4.72	4.96	5.08			4.56	4.56	4.83	4.78						
05.08.2004	218	4.78	4.62	4.80	4.63			3.33	3.28	3.40	3.41			4.07	4.05	4.12	4.30						
12.08.2004	225	4.22	4.29	4.22	4.37			3.84	3.92	3.78	3.83			4.21	4.37	4.11	3.95						
19.08.2004	231	3.03	3.01	2.86	2.78			3.09	3.21	3.28	3.25			3.06	3.25	3.31	3.32						

Date	DOY	Measurements Plot 4						Measurements Plot 5						mean	stddev	min	max
29.04.2004	120	0.99	1.01	1.05	0.90			0.75	1.10	1.73	1.65			1.42	0.38	0.75	1.87
06.05.2004	127	1.85	1.67	1.51	1.32	1.40	1.78	2.18	1.90	2.59	2.10	2.34		1.94	0.38	1.32	2.60
13.05.2004	134	2.44	2.36	2.26	2.08			2.27	2.62	2.58	2.97	2.35	2.45	2.76	0.54	2.08	3.95
25.05.2004	146	3.29	3.42	3.64	3.54	3.52	3.50	3.90	4.08	3.88	3.83	4.23	4.02	3.77	0.34	3.21	4.31
01.06.2004	153	3.13	3.10	3.11	3.11			5.12	4.93	5.06	[5,42]	4.63		3.77	0.69	3.01	5.12
07.06.2004	159	4.45	4.58	4.48	4.53	3.81	3.99	4.87	4.74	4.86	4.76	4.84	4.61	4.36	0.47	3.28	4.94
11.06.2004	163	4.58	4.38	4.31	4.42			4.24	4.30	4.51	4.68			4.51	0.42	3.48	5.35
17.06.2004	169	4.83	4.79	4.05	4.28			4.89	5.07	4.91	5.29			5.21	0.49	4.05	6.07
24.06.2004	176	5.68	5.64	5.35	5.21			5.40	5.39	5.28	5.33			5.05	0.49	4.12	5.68
05.07.2004	187	5.04	5.24	4.86	4.71			4.87	5.35	4.91	5.31			5.05	0.22	4.71	5.35
15.07.2004	197	4.48	4.38	4.32	4.38			4.97	4.94	5.06	5.05			4.99	0.61	4.25	6.45
22.07.2004	204	[2,98]	[3,10]	[3,15]	[3,31]			4.21	4.26	4.02	4.00			4.85	0.53	4.00	5.64
29.07.2004	211	4.20	4.30	4.22	4.32			3.99	4.07	[4,59]	[4,52]			4.69	0.43	3.99	5.32
05.08.2004	218	3.50	3.54	3.72	3.76			3.84	3.76	3.92	3.93			3.94	0.48	3.28	4.80
12.08.2004	225	3.68	3.63	3.64	3.91			3.76	3.79	3.86	3.76			3.96	0.25	3.63	4.37
19.08.2004	231	3.35	3.41	3.47	3.48			3.42	3.38	3.33	3.36			3.23	0.20	2.78	3.48

Maize

erroneous measurements are in brackets and omitted in the statistics:

Date	DOY	Measurements Plot 1				Measurements Plot 2				Measurements Plot 3				mean	stddev	min	max				
Maize Argelsried, 2003																					
16.06.2003	167	2.11	2.16	2.23	2.22	2.10	2.07	2.05	2.08			2.25	2.34	2.25	2.24			2.18	0.09	2.05	2.34
09.07.2003	190	3.97	3.97	4.16	4.25	4.03	4.19	4.23	4.19			4.32	4.31	4.22	3.98			4.15	0.13	3.97	4.32
28.07.2003	209	3.84	3.73	3.76	3.88	2.63	2.75	2.78	4.13			3.09		4.29	4.07			3.54	0.61	2.63	4.29
11.08.2003	223	2.95	2.90	2.89	2.91	4.09	4.06					2.31	2.42					3.07	0.67	2.31	4.09
Maize Teifenbrunn, 2003																					
16.06.2003	167	1.01	1.02	0.86	0.87	1.77	1.62	1.86	1.82			1.31	1.43	1.22	1.19			1.33	0.37	0.86	1.86
08.07.2003	189	2.32	2.36	2.58	2.56	2.65	2.74	2.82	2.69			2.88	3.12	3.04	2.96			2.73	0.25	2.32	3.12
28.07.2003	209	2.50	2.66	2.81	2.78	3.05	2.58	2.51	2.14			3.36	3.32	3.56	3.77			2.92	0.49	2.14	3.77
11.08.2003	223	1.51	1.48			1.69	1.65					2.50	2.61					1.91	0.51	1.48	2.61
28.08.2003	240	1.65	1.61	1.96	2.08	1.45	1.38	1.56	1.57			1.62	1.55	1.49	1.48			1.62	0.20	1.38	2.08
10.09.2003	253	1.51	1.46	1.39	1.44	1.48	1.42	1.64	1.67			1.77	1.78	1.68	1.70			1.58	0.14	1.39	1.78
Maize DLR, 2002																					
17.06.2002	168	1.07	1.1	0.99	0.92	0.82	0.96	0.86	0.83			0.80	0.83	0.74	0.79			0.89	0.12	0.74	1.10
27.06.2002	178	2.59	2.53	2.5	2.85	2.46	2.48	2.31	2.33			3.38	3.36	3.25	3.22			2.77	0.42	2.31	3.38
12.07.2002	193	[0,9]	[0,66]	[1,74]	[0,55]	[0]	[0]	[0]	[0]	[0,29]	[1,1]	4.30	4.08	4.19	4.07			4.16	0.11	4.07	4.30
23.07.2002	204	4.03	4.24	3.85	3.82	4.08	3.92	4.71	4.73			3.36	4.35	3.26	3.45	4.00	3.40	3.94	0.47	3.26	4.73
08.08.2002	220	4.45	4.45	3.65	3.79	3.54	3.61	3.87	3.87			4.56	4.34	5.09	5.18			4.20	0.56	3.54	5.18
21.08.2002	233	3.95	4.46	4.53	4.72							5.79	5.20	4.80	4.73			4.77	0.54	3.95	5.79
Maize St. Gilgen, 2002																					
17.06.2002	168	0.93	0.97	0.9	0.87	0.9	0.88	0.9	0.87			1.04	1.22	1.41	1.49	1.48	0.97	1.06	0.24	0.87	1.49
27.06.2002	178	2.25	2.38	2.17	2.21	2.36	2.42	2.34	2.5			2.1	2.21	2.33	2.33			2.30	0.11	2.10	2.50
12.07.2002	193	3.52	4.21	3.39	2.74	3.91	3.83	3.63	3.56			3.12	3.18	2.97	2.95			3.48	0.40	2.95	4.21
23.07.2002	204	3.24	3.39	3.24	2.94	3.65	3.67	3.59	3.4			3.72	3.5	3.6	3.56			3.46	0.23	2.94	3.72
08.08.2002	220	3.6	3.47	3.16	3.21	3.32	3.24	3.28	3.3			2.94	2.84	3.42	3.34			3.26	0.22	2.84	3.60
21.08.2002	233	3.41	3.35	3.14	3.22	3.22	3.28	3.52	3.64			4.04	4.01	4.7	4.31			3.65	0.50	3.14	4.70
Maize Wastian, 2002																					
17.06.2002	168	0.63	0.58	0.65	0.6	0.6	0.74	0.77	0.93			0.59	0.58	0.68	0.70			0.67	0.10	0.58	0.93
27.06.2002	178	1.92	1.85	1.74	1.61	1.28	1.27	1.57	1.51			1.46	1.50	1.44	1.53			1.56	0.20	1.27	1.92
11.07.2002	192	3.4	3.38	3.49	3.15	2.76	2.94	2.92	2.57			3.26	3.19	2.66	2.68			3.03	0.32	2.57	3.49
23.07.2002	204	3.56	3.16	3.42	3.14	3.34	3.2	3.32	3.32			4.27	3.56	3.75	4.31	4.00	3.68	3.57	0.39	3.14	4.31
08.08.2002	220	3.92	4.04	4.02	3.88	3.31	3.08	3.1	3.22			3.58	3.70	3.49	3.64			3.58	0.35	3.08	4.04
21.08.2002	233	3.73	3.68	3.39	3.53	4.03	4.25	3.59	3.34			3.56	3.45	3.43	3.23			3.60	0.29	3.23	4.25

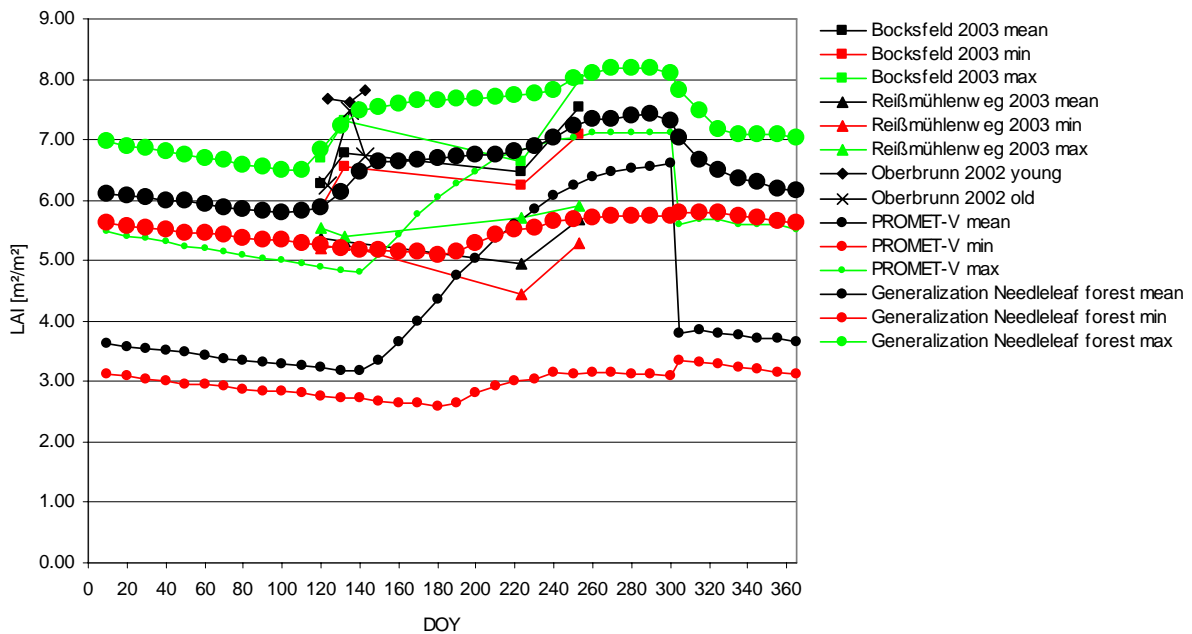
Maize Argelsried, 2004																									
Date	DOY	Measurements Plot 1								Measurements Plot 2								Measurements Plot 3							
17.06.2004	169	0.23	0.30	0.33	0.30													0.36	0.35	0.43	0.36				
24.06.2004	176	0.56	0.55	0.59	0.61					0.51	0.61	0.84	0.68	0.54	0.60			0.73	0.78	0.83	0.76				
01.07.2004	183	1.14	1.09	1.05	1.04					1.43	1.42	1.35	1.37					1.75	1.70	1.69	1.68				
15.07.2004	197	2.42	2.42	2.45	2.48					2.57	2.50	2.27	2.29	2.28	2.28			2.53	2.62	2.87	2.80	2.79	2.74		
22.07.2004	204	2.90	2.80	2.90	3.07					3.27	3.02	3.04	2.80					3.48	3.10	3.15	3.08				
29.07.2004	211	3.34								3.28	3.45	4.06	3.40	4.55	3.40			3.91	4.73	3.79	3.86				
05.08.2004	218	3.61	3.50	3.61	3.60					4.26	4.22	4.29	4.02					4.05	4.28	3.94	4.16				
12.08.2004	225	4.34	4.15	3.90	3.93					4.47	4.38	4.30	4.16					3.81	3.76	3.88	3.76				
19.08.2004	232	3.45	3.47	3.36	3.45					3.88	3.97	4.19	4.24					3.43	3.38	3.16	3.18				
26.08.2004	239	3.60	3.65	3.35	3.45													4.19	4.12	3.94	3.91				
02.09.2004	246	3.70	3.78	3.74	3.71					4.09	4.06	4.15	4.06							3.84	3.83	4.01	3.92		
09.09.2004	253	3.58	3.63	3.55	3.49					3.95	4.02	3.99	3.99							3.91	3.97	3.88	3.73		
16.09.2004	260	3.18	3.16	3.08	3.03	3.34	3.30	3.30	3.37	3.29	3.36	3.63	3.76	3.63	3.65	3.35	3.31	3.27	3.25	3.47	3.54	3.74	3.71	3.75	3.70
23.09.2004	267	2.94		3.00	3.01	2.91	2.78			3.22	3.30	2.96	3.32	2.51	2.87			3.12	3.18	3.47	3.42				
30.09.2004	274	2.91	2.89	2.80	2.77					2.94	2.93	3.15	3.13					3.41	3.35	3.55	3.41				

Maize Argelsried, 2004 (continued)																									
Date	DOY	Measurements Plot 4								Measurements Plot 5								mean	stddev	min	max				
17.06.2004	169									0.38	0.4	0.4	0.4					0.35	0.06	0.23	0.43				
24.06.2004	176	0.88	0.88	0.9	0.83					0.81	0.76	0.68	0.68					0.71	0.12	0.51	0.90				
01.07.2004	183	1.46	1.39	1.39	1.31					1.54	1.44	1.55	1.64					1.42	0.22	1.04	1.75				
15.07.2004	197	2.67	2.57	2.72	2.79	2.83	2.8			2.38	2.25	2.28	2.27					2.53	0.21	2.25	2.87				
22.07.2004	204	3.07	2.92	3.14	2.94					3.17	3.2	3.36	3.24					3.08	0.18	2.80	3.48				
29.07.2004	211	3.99	3.39	3.58	3.30					3.80	3.52	3.66	4.09					3.74	0.41	3.28	4.73				
05.08.2004	218	3.99	3.87	3.79	3.62					3.79	3.48	3.47	3.3					3.84	0.31	3.30	4.29				
12.08.2004	225	3.5	3.56	3.48	3.43					4.28	3.99	4.11	4.48					3.98	0.34	3.43	4.48				
19.08.2004	232	3.73	3.54	3.73	3.74					3.90	4.00	3.49	3.58					3.64	0.31	3.16	4.24				
26.08.2004	239	3.01	2.98	3.06	3.04					3.18	3.26	3.34	3.40					3.47	0.40	2.98	4.19				
02.09.2004	246	3.14	3.1	2.99	2.89					3.49	3.56	3.51	3.50					3.65	0.38	2.89	4.15				
09.09.2004	253									3.27	3.24	3.30	3.27					3.67	0.29	3.24	4.02				
16.09.2004	260	1.98	2.04	2.20	2.23	2.11	2.19	2.44	2.32	3.38	3.33	3.41	3.50	3.29	3.40	3.33	3.37	3.17	0.53	1.98	3.76				
23.09.2004	267	1.90	1.93	1.89	2.06					2.65	2.93	3.02	3.02	3.02	3.12			2.86	0.46	1.89	3.47				
30.09.2004	274	1.83	1.83	1.79	1.82					2.97	2.93	2.86	2.92					2.81	0.55	1.79	3.55				

Appendix 4: Generalized Seasonal Development of LAI

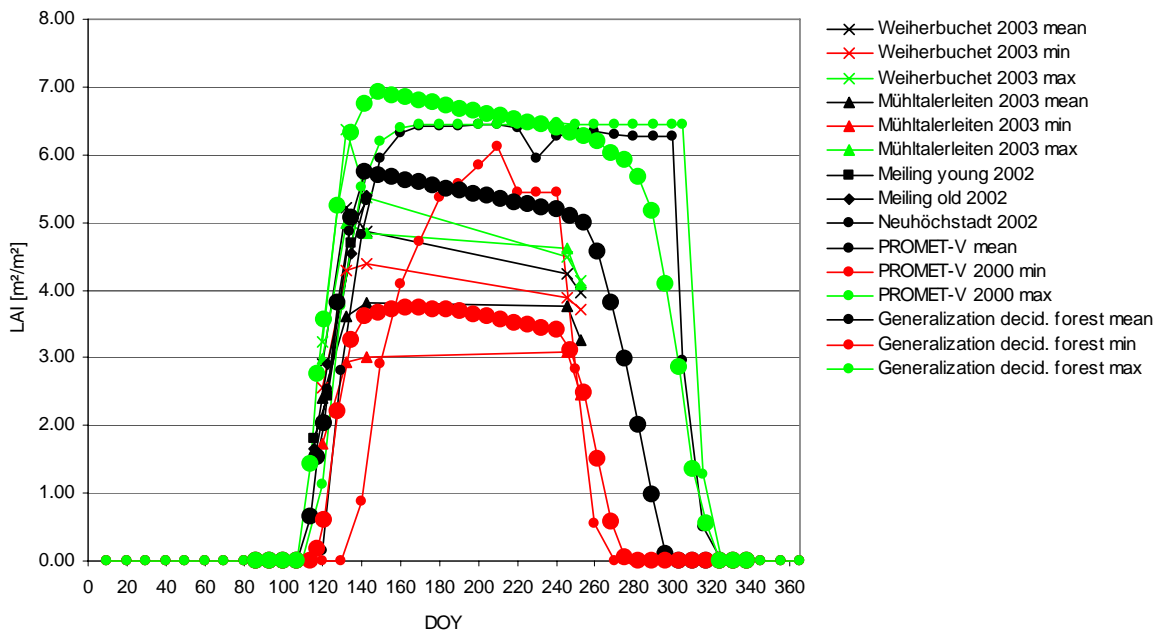
The following plots and tables provide the generalizations of mean, minimum and maximum LAI estimated from the host of available LAI data. The generalization of the land cover type of mixed forest was approximated from the needleleaf forest and the deciduous forest generalizations. With the assumption of equal portions of both tree types in mixed forest the mean from the two forest types was taken as the generalization for mixed forest. No plot and values are provided for this land cover type.

Needleleaf Forest



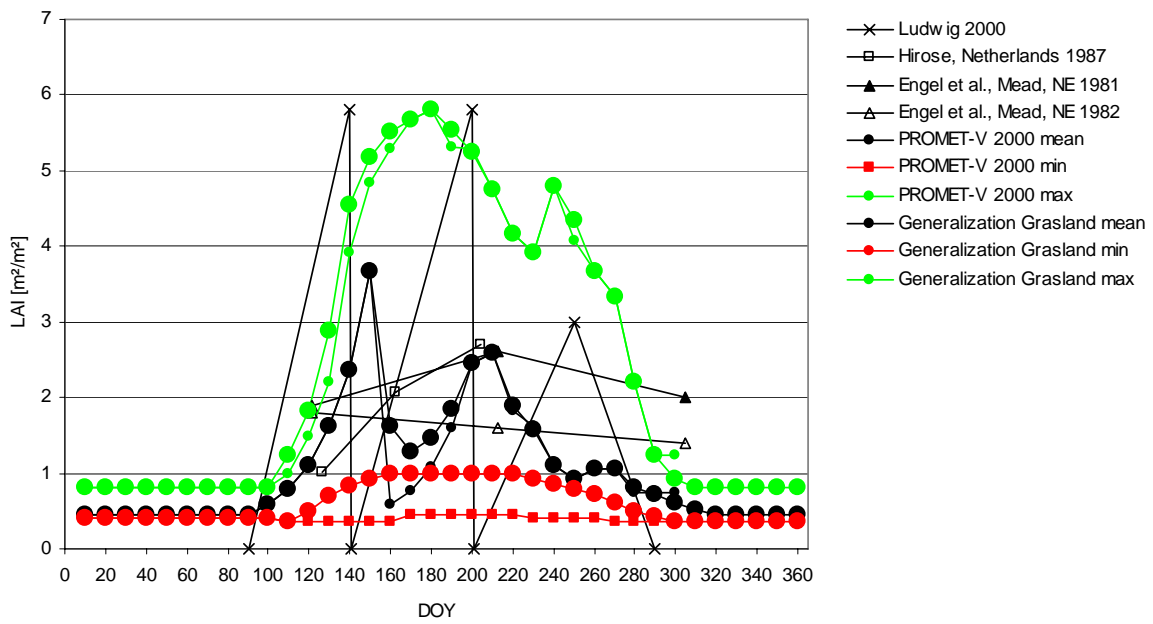
Needleleaf forest Generalization											
doy	mean	min	max	doy	mean	min	max	doy	mean	min	max
1	6.16	5.62	7.02	130	6.12	5.20	7.22	260	7.33	5.70	8.10
10	6.12	5.62	6.98	140	6.47	5.17	7.49	270	7.35	5.73	8.18
20	6.07	5.58	6.90	150	6.63	5.18	7.54	280	7.40	5.73	8.18
30	6.04	5.54	6.86	160	6.63	5.14	7.60	290	7.43	5.75	8.18
40	6.00	5.50	6.82	170	6.66	5.14	7.65	300	7.30	5.75	8.10
50	5.98	5.46	6.74	180	6.68	5.10	7.65	305	7.03	5.78	7.83
60	5.93	5.46	6.70	190	6.71	5.14	7.67	315	6.67	5.80	7.49
70	5.88	5.42	6.66	200	6.76	5.30	7.67	325	6.50	5.78	7.18
80	5.86	5.38	6.58	210	6.76	5.42	7.70	335	6.35	5.74	7.10
90	5.83	5.34	6.54	220	6.80	5.50	7.73	345	6.30	5.70	7.10
100	5.79	5.34	6.50	230	6.90	5.54	7.75	355	6.20	5.66	7.10
110	5.83	5.30	6.50	240	7.03	5.66	7.83	365	6.16	5.62	7.02
120	5.88	5.26	6.84	250	7.22	5.68	8.02				

Deciduous Forest



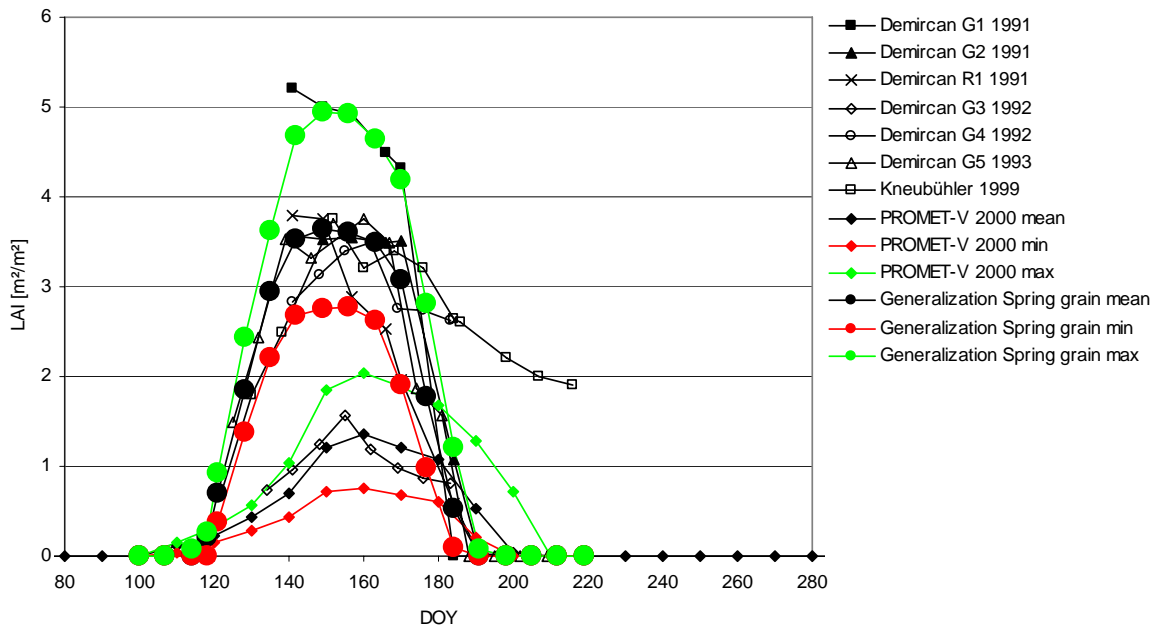
Deciduous forest Generalization											
doy	mean	min	max	doy	mean	min	max	doy	mean	min	max
86	0.00	0.00	0.00	170	5.58	3.73	6.80	261	4.56	1.51	6.20
93	0.00	0.00	0.00	177	5.54	3.70	6.76	268	3.80	0.57	6.03
100	0.00	0.00	0.00	184	5.50	3.72	6.72	277	2.98	0.04	5.92
107	0.00	0.00	0.00	191	5.46	3.68	6.68	282	2.00	0.00	5.67
114	0.65	0.00	1.43	198	5.42	3.64	6.64	289	0.97	0.00	5.17
118	1.54	0.18	2.76	205	5.38	3.60	6.60	296	0.11	0.00	4.09
121	2.04	0.60	3.55	212	5.34	3.56	6.56	303	0.00	0.00	2.87
128	3.80	2.20	5.24	219	5.30	3.52	6.52	310	0.00	0.00	1.36
135	5.06	3.26	6.31	226	5.26	3.48	6.48	317	0.00	0.00	0.54
142	5.74	3.60	6.74	233	5.22	3.44	6.44	324	0.00	0.00	0.00
149	5.70	3.66	6.92	240	5.18	3.40	6.40	331	0.00	0.00	0.00
156	5.66	3.70	6.88	247	5.09	3.12	6.31	338	0.00	0.00	0.00
163	5.62	3.73	6.84	254	5.00	2.48	6.28				

Grassland



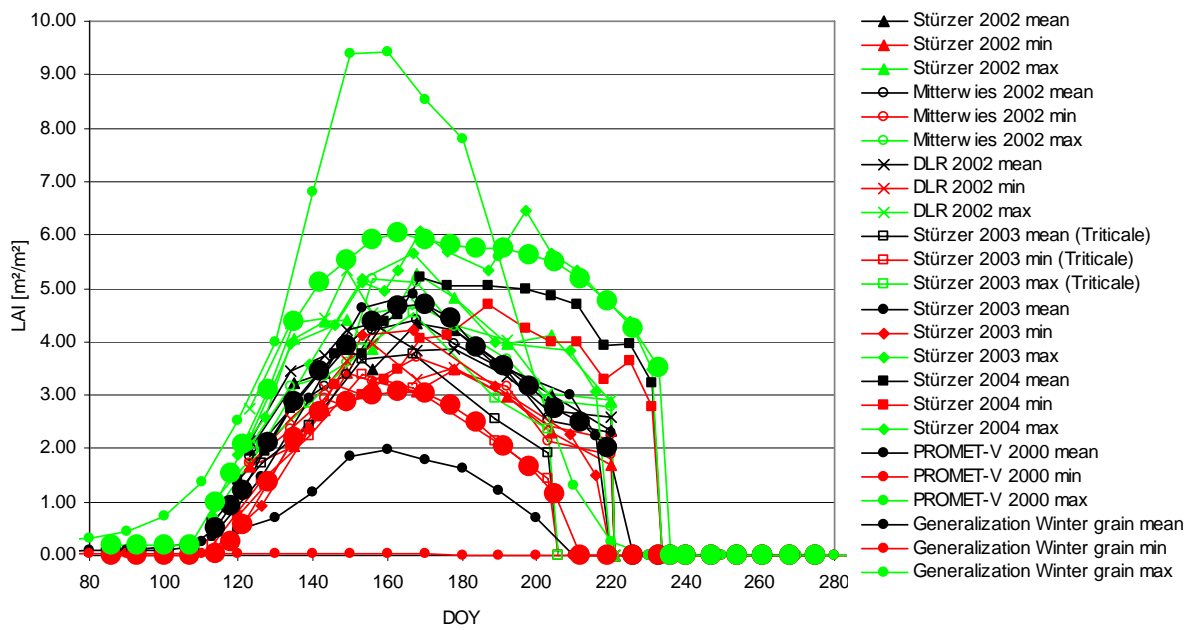
Grasland Generalization											
doy	mean	min	max	doy	mean	min	max	doy	mean	min	max
1	0.44	0.40	0.80	130	1.63	0.69	2.87	260	1.05	0.73	3.68
10	0.44	0.40	0.80	140	2.36	0.83	4.54	270	1.06	0.60	3.32
20	0.44	0.40	0.80	150	3.66	0.92	5.17	280	0.80	0.49	2.20
30	0.44	0.40	0.80	160	1.61	1.00	5.51	290	0.71	0.43	1.24
40	0.44	0.40	0.80	170	1.28	1.00	5.68	300	0.60	0.36	0.92
50	0.44	0.40	0.80	180	1.46	1.00	5.80	310	0.51	0.36	0.80
60	0.44	0.40	0.80	190	1.85	1.00	5.54	320	0.44	0.36	0.80
70	0.44	0.40	0.80	200	2.46	1.00	5.25	330	0.44	0.36	0.80
80	0.44	0.40	0.80	210	2.59	1.00	4.76	340	0.44	0.36	0.80
90	0.45	0.40	0.80	220	1.89	1.00	4.16	350	0.44	0.36	0.80
100	0.59	0.40	0.80	230	1.57	0.92	3.92	360	0.44	0.36	0.80
110	0.78	0.36	1.24	240	1.09	0.85	4.80	260	1.05	0.73	3.68
120	1.10	0.49	1.83	250	0.92	0.79	4.35				

Spring Grain



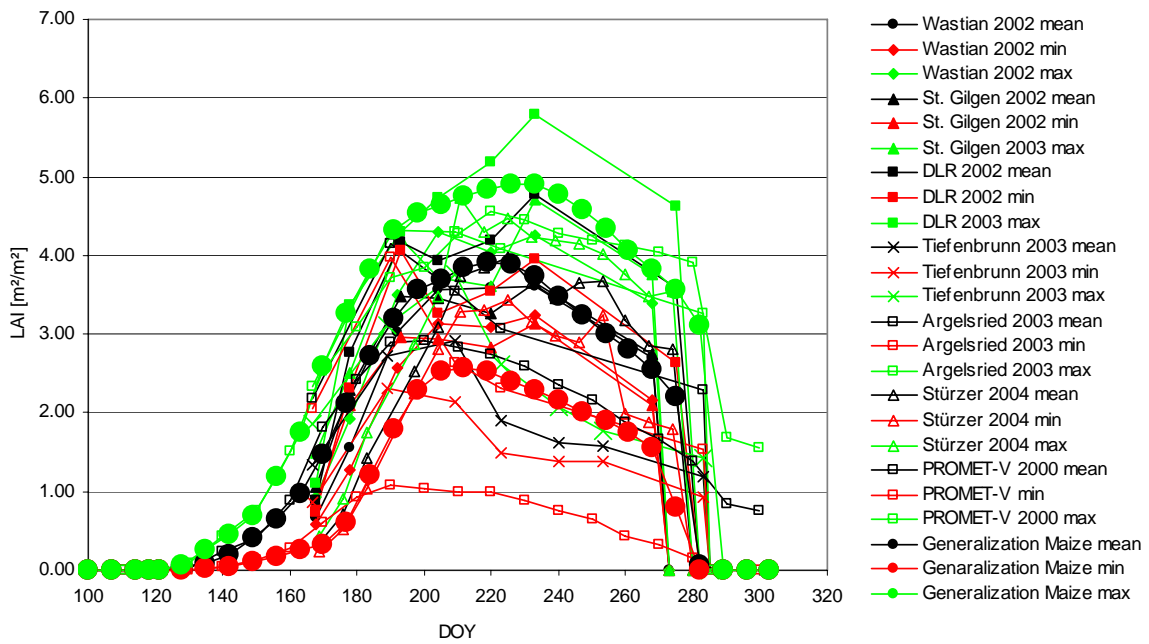
Spring Grain Generalization							
doy	mean	min	max	doy	mean	min	max
100	0.00	0.00	0.00	163	3.49	2.62	4.64
107	0.00	0.00	0.00	170	3.08	1.91	4.18
114	0.00	0.00	0.07	177	1.78	0.99	2.81
118	0.20	0.00	0.26	184	0.53	0.09	1.20
121	0.70	0.37	0.92	191	0.00	0.00	0.07
128	1.85	1.38	2.44	198	0.00	0.00	0.00
135	2.95	2.20	3.63	205	0.00	0.00	0.00
142	3.52	2.68	4.68	212	0.00	0.00	0.00
149	3.65	2.75	4.94	219	0.00	0.00	0.00
156	3.60	2.77	4.92				

Winter Grain



Winter Grain Generalization											
doy	mean	min	max	doy	mean	min	max	doy	mean	min	max
1	0.10	0.00	0.20	177	4.44	2.80	5.82	275	0.00	0.00	0.00
86	0.10	0.00	0.20	184	3.89	2.48	5.75	282	0.00	0.00	0.00
93	0.10	0.00	0.20	191	3.56	2.04	5.75	289	0.00	0.00	0.00
100	0.10	0.00	0.20	198	3.15	1.67	5.63	296	0.00	0.00	0.00
107	0.15	0.00	0.20	205	2.74	1.15	5.48	303	0.10	0.00	0.20
114	0.52	0.04	1.00	212	2.48	0.00	5.17	310	0.10	0.00	0.20
118	0.93	0.26	1.53	219	2.00	0.00	4.75	317	0.10	0.00	0.20
121	1.22	0.56	2.07	226	0.00	0.00	4.25	324	0.10	0.00	0.20
128	2.11	1.38	3.10	233	0.00	0.00	3.50	331	0.10	0.00	0.20
135	2.89	2.20	4.37	236	0.00	0.00	0.00	338	0.10	0.00	0.20
142	3.44	2.68	5.10	240	0.00	0.00	0.00	345	0.10	0.00	0.20
149	3.93	2.89	5.52	247	0.00	0.00	0.00	352	0.10	0.00	0.20
156	4.37	3.00	5.90	254	0.00	0.00	0.00	359	0.10	0.00	0.20
163	4.67	3.07	6.05	261	0.00	0.00	0.00	365	0.10	0.00	0.20
170	4.70	3.04	5.90	268	0.00	0.00	0.00				

Maize



Maize Generalization												
doy	mean	min	max	doy	mean	min	max	doy	mean	min	max	
86	0.00	0.00	0.00	163	0.98	0.25	1.76	247	3.24	2.01	4.57	
93	0.00	0.00	0.00	170	1.47	0.33	2.60	254	3.00	1.91	4.34	
100	0.00	0.00	0.00	177	2.11	0.60	3.26	261	2.80	1.76	4.07	
107	0.00	0.00	0.00	184	2.72	1.22	3.82	268	2.56	1.55	3.82	
114	0.00	0.00	0.00	191	3.20	1.79	4.32	275	2.20	0.80	3.57	
118	0.00	0.00	0.00	198	3.57	2.30	4.53	282	0.06	0.00	3.12	
121	0.00	0.00	0.00	205	3.69	2.53	4.65	289	0.00	0.00	0.00	
128	0.04	0.00	0.06	212	3.85	2.58	4.76	296	0.00	0.00	0.00	
135	0.09	0.03	0.25	219	3.91	2.53	4.84	303	0.00	0.00	0.00	
142	0.20	0.04	0.45	226	3.88	2.39	4.90	247	3.24	2.01	4.57	
149	0.40	0.11	0.70	233	3.73	2.28	4.90	254	3.00	1.91	4.34	
156	0.64	0.17	1.18	240	3.47	2.16	4.78	261	2.80	1.76	4.07	

Appendix 5: Reflectance Probability Functions

The functions that were used in the reflectance segmentation prototyping and application are listed in the following tables. They contain the contents of the files that were read by the software for reflectance segmentation. First the functions that were derived directly from the high-resolution reflectance data are given (used in the prototyping and the application to coincident data of high and low resolution doy 170/171, 2000). The second table summarizes the functions that were generated from the GeoSAIL simulations of reflectances. They were used in the reflectance segmentation of the 19 MODIS scenes of 2003.

Reflectance Probability Gaussian Function Parameters for DOY 171, 2000 (generated from high resolution reflectance histograms)	
RED	NIR
# k3 - Parameters for 3 param Gauss function $a \cdot \exp(-.5 \cdot ((x-x0)/b)^2)$, DOY 171 (from fits to high res histograms)	# k4 - Parameters for 3 param Gauss function $a \cdot \exp(-.5 \cdot ((x-x0)/b)^2)$, DOY 171 (from fits to high res histograms)
# land cover type, a, x0, b	# land cover type, a, x0, b
Deciduous, 0.916009848765501, 0.026972877532762, 0.009290284653843	Deciduous, 0.906720883146173, 0.396638760519374, 0.063146059912161
Mixed Forest, 0.943244118752844, 0.020822279789494, 0.007007655772883	Mixed Forest, 0.952875841836687, 0.253237828421860, 0.058681932455725
Coniferous, 0.958186545410539, 0.022047329555344, 0.008372575873238	Coniferous, 0.903726249713775, 0.185082401930564, 0.031099787628804
Grassland, 0.908945797880119, 0.051524606695294, 0.021932331428066	Grassland, 0.818790472978434, 0.387338791298971, 0.082788500540283
Summercereals, 0.614573859764575, 0.035119001005268, 0.012441441143867	Summercereals, 1.034794840269490, 0.448807157304024, 0.033524909314332
Wintercereals, 0.963803953208957, 0.028431421042494, 0.008876930983400	Wintercereals, 0.860384140305015, 0.380917006709728, 0.057114661833012
Maize, 0.960875045204768, 0.043468548992129, 0.015285994224823	Maize, 0.865994355178323, 0.359503639189477, 0.035304455689847
Rock, 0.879742776080572, 0.125587645480524, 0.067445657811590	Rock, 0.995001685494205, 0.261116193588741, 0.068872416570309
Soil, 0.776590204414268, 0.147582280504454, 0.041459034624869	Soil, 0.828718992056425, 0.317648370690618, 0.067155723404204
Urban, 0.872273724761920, 0.089376044870024, 0.033573239985266	Urban, 0.915678852836465, 0.247493093668613, 0.044377835838129
Snow, 0.964109614398773, 0.424754724491972, 0.192778173027072	Snow, 0.989611898315982, 0.445017393220418, 0.131588002756347
Water, 0.597639978395613, 0.012043722079445, 0.016003608057608	Water, 1.022848677464220, 0.009691636089728, 0.005577309148914

Reflectance Probability Gaussian Functions for the 2003 MODIS time series		
DOY	RED	NIR
091	# doy 91 # Parameter for Gauss-Function: name, a, μ , sigma Deciduous, 1, 0.1536, 0.00001 Mixed Forest, 1, 0.0326, -0.0012 Coniferous, 1, 0.025, -0.000475 Grasland, 1, 0.0976, -0.007125 Spring Grain, 1, 0.1536, 0.00001 Winter Grain, 1, 0.1423, -0.0054 Maize, 1, 0.1536, 0.00001 Rock, 1, 0.125490819, 0.067977773 Bare Soil, 1, 0.148090847, 0.042050528 Urban, 1, 0.089063198, 0.033701723 Snow and Ice, 1, 0.424729869, 0.194526916 Water, 1, 0.012074216, 0.015997301	# doy 91 # Parameter for Gauss-Function: name, a, μ , sigma Deciduous, 1, 0.2123, 0.00001 Mixed Forest, 1, 0.2403, 0.00135 Coniferous, 1, 0.1715, -5.24999999999998E-04 Grasland, 1, 0.2681, 0.010625 Spring Grain, 1, 0.2123, 0.00001 Winter Grain, 1, 0.2178, 0.002775 Maize, 1, 0.2123, 0.00001 Rock, 1, 0.260757632, 0.069086984 Bare Soil, 1, 0.318273003, 0.067003789 Urban, 1, 0.249085185, 0.045946432 Snow and Ice, 1, 0.44491274, 0.132559209 Water, 1, 0.009699672, 0.005585239
098	# doy 98 # Parameter for Gauss-Function: name, a, μ , sigma Deciduous, 1, 0.1562, 0.00001 Mixed Forest, 1, 0.0343, -0.0013 Coniferous, 1, 0.0262, -0.00055 Grasland, 1, 0.0915, -0.007275 Spring Grain, 1, 0.1562, 0.00001 Winter Grain, 1, 0.1451, -0.005325 Maize, 1, 0.1562, 0.00001 Rock, 1, 0.125490819, 0.067977773 Bare Soil, 1, 0.148090847, 0.042050528 Urban, 1, 0.089063198, 0.033701723 Snow and Ice, 1, 0.424729869, 0.194526916 Water, 1, 0.012074216, 0.015997301	# doy 91 # Parameter for Gauss-Function: name, a, μ , sigma Deciduous, 1, 0.2123, 0.00001 Mixed Forest, 1, 0.2403, 0.00135 Coniferous, 1, 0.1715, -5.24999999999998E-04 Grasland, 1, 0.2681, 0.010625 Spring Grain, 1, 0.2123, 0.00001 Winter Grain, 1, 0.2178, 0.002775 Maize, 1, 0.2123, 0.00001 Rock, 1, 0.260757632, 0.069086984 Bare Soil, 1, 0.318273003, 0.067003789 Urban, 1, 0.249085185, 0.045946432 Snow and Ice, 1, 0.44491274, 0.132559209 Water, 1, 0.009699672, 0.005585239
105	# doy 105 # Parameter for Gauss-Function: name, a, μ , sigma Deciduous, 1, 0.1587, 0.00001 Mixed Forest, 1, 0.0359, -0.001425 Coniferous, 1, 0.0273, -6.00000000000001E-04 Grasland, 1, 0.0843, -0.009525 Spring Grain, 1, 0.1587, 0.00001 Winter Grain, 1, 0.1441, -0.005225 Maize, 1, 0.1587, 0.00001 Rock, 1, 0.125490819, 0.067977773 Bare Soil, 1, 0.148090847, 0.042050528 Urban, 1, 0.089063198, 0.033701723 Snow and Ice, 1, 0.424729869, 0.194526916 Water, 1, 0.012074216, 0.015997301	# doy 105 # Parameter for Gauss-Function: name, a, μ , sigma Deciduous, 1, 0.2192, 0.00001 Mixed Forest, 1, 0.2398, 1.22499999999999E-03 Coniferous, 1, 0.1728, -6.49999999999998E-04 Grasland, 1, 0.2932, 0.014575 Spring Grain, 1, 0.2192, 0.00001 Winter Grain, 1, 0.2259, 0.0025 Maize, 1, 0.2192, 0.00001 Rock, 1, 0.260757632, 0.069086984 Bare Soil, 1, 0.318273003, 0.067003789 Urban, 1, 0.249085185, 0.045946432 Snow and Ice, 1, 0.44491274, 0.132559209 Water, 1, 0.009699672, 0.005585239
107	# doy 107 # Parameter for Gauss-Function: name, a, μ , sigma Deciduous, 1, 0.1594, 0.00001 Mixed Forest, 1, 0.0363, -0.001425 Coniferous, 1, 0.0277, -0.000625 Grasland, 1, 0.0822, -0.010225 Spring Grain, 1, 0.1594, 0.00001 Winter Grain, 1, 0.1434, -5.22499999999999E-03 Maize, 1, 0.1594, 0.00001 Rock, 1, 0.125490819, 0.067977773 Bare Soil, 1, 0.148090847, 0.042050528 Urban, 1, 0.089063198, 0.033701723 Snow and Ice, 1, 0.424729869, 0.194526916 Water, 1, 0.012074216, 0.015997301	# doy 107 # Parameter for Gauss-Function: name, a, μ , sigma Deciduous, 1, 0.2201, 0.00001 Mixed Forest, 1, 0.2398, 1.22499999999999E-03 Coniferous, 1, 0.1731, -6.75000000000002E-04 Grasland, 1, 0.2972, 0.016175 Spring Grain, 1, 0.2201, 0.00001 Winter Grain, 1, 0.2274, 2.44999999999999E-03 Maize, 1, 0.2201, 0.00001 Rock, 1, 0.260757632, 0.069086984 Bare Soil, 1, 0.318273003, 0.067003789 Urban, 1, 0.249085185, 0.045946432 Snow and Ice, 1, 0.44491274, 0.132559209 Water, 1, 0.009699672, 0.005585239

Reflectance Probability Gaussian Functions for the 2003 MODIS time series		
DOY	RED	NIR
125	# doy 125 # Parameter for Gauss-Function: name, a, μ , sigma Deciduous, 1, 0.0319, -0.00805 Mixed Forest, 1, 0.0295, -0.00235 Coniferous, 1, 0.0303, -0.001125 Grasland, 1, 0.0577, -0.0126 Spring Grain, 1, 0.0728, -0.02665 Winter Grain, 1, 0.059, -0.012075 Maize, 1, 0.1624, -9.24999999999995E-04 Rock, 1, 0.125490819, 0.067977773 Bare Soil, 1, 0.148090847, 0.042050528 Urban, 1, 0.089063198, 0.033701723 Snow and Ice, 1, 0.424729869, 0.194526916 Water, 1, 0.012074216, 0.015997301	# doy 125 # Parameter for Gauss-Function: name, a, μ , sigma Deciduous, 1, 0.3054, 0.016725 Mixed Forest, 1, 0.2493, 2.124999999999999E-03 Coniferous, 1, 0.1753, -1.124999999999999E-03 Grasland, 1, 0.3533, 0.0314 Spring Grain, 1, 0.315, 0.027725 Winter Grain, 1, 0.3105, 0.01855 Maize, 1, 0.2281, 2.750000000000004E-04 Rock, 1, 0.260757632, 0.069086984 Bare Soil, 1, 0.318273003, 0.067003789 Urban, 1, 0.249085185, 0.045946432 Snow and Ice, 1, 0.44491274, 0.132559209 Water, 1, 0.009699672, 0.005585239
139	# doy 139 # Parameter for Gauss-Function: name, a, μ , sigma Deciduous, 1, 0.0249, -0.00155 Mixed Forest, 1, 0.0275, -0.00145 Coniferous, 1, 0.0313, -0.001475 Grasland, 1, 0.0448, -0.01005 Spring Grain, 1, 0.0383, -0.032575 Winter Grain, 1, 0.0358, -0.004175 Maize, 1, 0.1528, -0.00745 Rock, 1, 0.125490819, 0.067977773 Bare Soil, 1, 0.148090847, 0.042050528 Urban, 1, 0.089063198, 0.033701723 Snow and Ice, 1, 0.424729869, 0.194526916 Water, 1, 0.012074216, 0.015997301	# doy 139 # Parameter for Gauss-Function: name, a, μ , sigma Deciduous, 1, 0.34, 0.00835 Mixed Forest, 1, 0.2532, 0.001175 Coniferous, 1, 0.1764, -0.001475 Grasland, 1, 0.4103, 0.0412 Spring Grain, 1, 0.4119, 0.053575 Winter Grain, 1, 0.3775, 0.022175 Maize, 1, 0.2366, 0.0029 Rock, 1, 0.260757632, 0.069086984 Bare Soil, 1, 0.318273003, 0.067003789 Urban, 1, 0.249085185, 0.045946432 Snow and Ice, 1, 0.44491274, 0.132559209 Water, 1, 0.009699672, 0.005585239
153	# doy 153 # Parameter for Gauss-Function: name, a, μ , sigma Deciduous, 1, 0.0253, -0.001375 Mixed Forest, 1, 0.0281, -0.00145 Coniferous, 1, 0.0323, -0.0016 Grasland, 1, 0.0418, -0.008475 Spring Grain, 1, 0.0355, -0.031375 Winter Grain, 1, 0.0307, -0.0031 Maize, 1, 0.1242, -0.01445 Rock, 1, 0.125490819, 0.067977773 Bare Soil, 1, 0.148090847, 0.042050528 Urban, 1, 0.089063198, 0.033701723 Snow and Ice, 1, 0.424729869, 0.194526916 Water, 1, 0.012074216, 0.015997301	# doy 153 # Parameter for Gauss-Function: name, a, μ , sigma Deciduous, 1, 0.3377, 7.350000000000002E-03 Mixed Forest, 1, 0.253, 0.001 Coniferous, 1, 0.1777, -0.0016 Grasland, 1, 0.4423, 0.041625 Spring Grain, 1, 0.3824, 0.045425 Winter Grain, 1, 0.4148, 0.02305 Maize, 1, 0.2537, 8.500000000000001E-03 Rock, 1, 0.260757632, 0.069086984 Bare Soil, 1, 0.318273003, 0.067003789 Urban, 1, 0.249085185, 0.045946432 Snow and Ice, 1, 0.44491274, 0.132559209 Water, 1, 0.009699672, 0.005585239
173	# doy 173 # Parameter for Gauss-Function: name, a, μ , sigma Deciduous, 1, 0.0256, -0.001325 Mixed Forest, 1, 0.0286, -0.001475 Coniferous, 1, 0.0329, -0.00175 Grasland, 1, 0.0603, -0.007825 Spring Grain, 1, 0.0404, -0.024375 Winter Grain, 1, 0.0319, -0.0025 Maize, 1, 0.0644, -0.023125 Rock, 1, 0.125490819, 0.067977773 Bare Soil, 1, 0.148090847, 0.042050528 Urban, 1, 0.089063198, 0.033701723 Snow and Ice, 1, 0.424729869, 0.194526916 Water, 1, 0.012074216, 0.015997301	# doy 173 # Parameter for Gauss-Function: name, a, μ , sigma Deciduous, 1, 0.3294, 0.0055 Mixed Forest, 1, 0.2512, 5.749999999999992E-04 Coniferous, 1, 0.1784, -0.0017 Grasland, 1, 0.3528, 0.041625 Spring Grain, 1, 0.3087, 0.0211 Winter Grain, 1, 0.4577, 0.023925 Maize, 1, 0.3026, 0.025675 Rock, 1, 0.260757632, 0.069086984 Bare Soil, 1, 0.318273003, 0.067003789 Urban, 1, 0.249085185, 0.045946432 Snow and Ice, 1, 0.44491274, 0.132559209 Water, 1, 0.009699672, 0.005585239

Reflectance Probability Gaussian Functions for the 2003 MODIS time series		
DOY	RED	NIR
196	# doy 196 # Parameter for Gauss-Function: name, a, μ , sigma Deciduous, 1, 0.0251, -0.001275 Mixed Forest, 1, 0.0278, -0.00135 Coniferous, 1, 0.0314, -0.00155 Grasland, 1, 0.0455, -0.00775 Spring Grain, 1, 0.169, 0.00225 Winter Grain, 1, 0.0355, -0.00455 Maize, 1, 0.0322, -0.006075 Rock, 1, 0.125490819, 0.067977773 Bare Soil, 1, 0.148090847, 0.042050528 Urban, 1, 0.089063198, 0.033701723 Snow and Ice, 1, 0.424729869, 0.194526916 Water, 1, 0.012074216, 0.015997301	# doy 196 # Parameter for Gauss-Function: name, a, μ , sigma Deciduous, 1, 0.3192, 4.724999999999999E-03 Mixed Forest, 1, 0.2477, 3.249999999999999E-04 Coniferous, 1, 0.1765, -0.00155 Grasland, 1, 0.407, 0.040625 Spring Grain, 1, 0.233, -0.05355 Winter Grain, 1, 0.3897, 0.0408 Maize, 1, 0.3809, 0.025575 Rock, 1, 0.260757632, 0.069086984 Bare Soil, 1, 0.318273003, 0.067003789 Urban, 1, 0.249085185, 0.045946432 Snow and Ice, 1, 0.44491274, 0.132559209 Water, 1, 0.009699672, 0.005585239
201	# doy 201 # Parameter for Gauss-Function: name, a, μ , sigma Deciduous, 1, 0.0249, -0.00125 Mixed Forest, 1, 0.0275, -0.001275 Coniferous, 1, 0.0308, -0.0014 Grasland, 1, 0.0437, -0.0077 Spring Grain, 1, 0.1683, 0.03005 Winter Grain, 1, 0.0365, -0.0054 Maize, 1, 0.0307, -0.004775 Rock, 1, 0.125490819, 0.067977773 Bare Soil, 1, 0.148090847, 0.042050528 Urban, 1, 0.089063198, 0.033701723 Snow and Ice, 1, 0.424729869, 0.194526916 Water, 1, 0.012074216, 0.015997301	# doy 201 # Parameter for Gauss-Function: name, a, μ , sigma Deciduous, 1, 0.317, 0.004875 Mixed Forest, 1, 0.2469, 3.500000000000003E-04 Coniferous, 1, 0.1758, -0.001475 Grasland, 1, 0.419, 0.04015 Spring Grain, 1, 0.232, -0.0348 Winter Grain, 1, 0.3738, 0.045375 Maize, 1, 0.3883, 0.023875 Rock, 1, 0.260757632, 0.069086984 Bare Soil, 1, 0.318273003, 0.067003789 Urban, 1, 0.249085185, 0.045946432 Snow and Ice, 1, 0.44491274, 0.132559209 Water, 1, 0.009699672, 0.005585239
215	# doy 215 # Parameter for Gauss-Function: name, a, μ , sigma Deciduous, 1, 0.0243, -0.00115 Mixed Forest, 1, 0.0264, -0.0011 Coniferous, 1, 0.0291, -0.00115 Grasland, 1, 0.0448, -0.007525 Spring Grain, 1, 0.1655, 0.030475 Winter Grain, 1, 0.0394, -0.033675 Maize, 1, 0.0281, -0.003825 Rock, 1, 0.125490819, 0.067977773 Bare Soil, 1, 0.148090847, 0.042050528 Urban, 1, 0.089063198, 0.033701723 Snow and Ice, 1, 0.424729869, 0.194526916 Water, 1, 0.012074216, 0.015997301	# doy 215 # Parameter for Gauss-Function: name, a, μ , sigma Deciduous, 1, 0.3111, 5.249999999999999E-03 Mixed Forest, 1, 0.2446, 4.249999999999995E-04 Coniferous, 1, 0.1738, -0.0013 Grasland, 1, 0.4075, 0.037525 Spring Grain, 1, 0.2283, -0.027775 Winter Grain, 1, 0.3345, 0.055925 Maize, 1, 0.4011, 0.02435 Rock, 1, 0.260757632, 0.069086984 Bare Soil, 1, 0.318273003, 0.067003789 Urban, 1, 0.249085185, 0.045946432 Snow and Ice, 1, 0.44491274, 0.132559209 Water, 1, 0.009699672, 0.005585239
219	# doy 219 # Parameter for Gauss-Function: name, a, μ , sigma Deciduous, 1, 0.0241, -0.001125 Mixed Forest, 1, 0.0261, -0.001075 Coniferous, 1, 0.0285, -0.0011 Grasland, 1, 0.0472, -0.00745 Spring Grain, 1, 0.1646, 0.030375 Winter Grain, 1, 0.041, -0.0334 Maize, 1, 0.0276, -0.00375 Rock, 1, 0.125490819, 0.067977773 Bare Soil, 1, 0.148090847, 0.042050528 Urban, 1, 0.089063198, 0.033701723 Snow and Ice, 1, 0.424729869, 0.194526916 Water, 1, 0.012074216, 0.015997301	# doy 219 # Parameter for Gauss-Function: name, a, μ , sigma Deciduous, 1, 0.3096, 5.374999999999999E-03 Mixed Forest, 1, 0.244, 4.250000000000002E-04 Coniferous, 1, 0.1733, -0.00125 Grasland, 1, 0.3923, 0.036475 Spring Grain, 1, 0.227, -0.0275 Winter Grain, 1, 0.3184, 0.05375 Maize, 1, 0.4033, 0.025425 Rock, 1, 0.260757632, 0.069086984 Bare Soil, 1, 0.318273003, 0.067003789 Urban, 1, 0.249085185, 0.045946432 Snow and Ice, 1, 0.44491274, 0.132559209 Water, 1, 0.009699672, 0.005585239

Reflectance Probability Gaussian Functions for the 2003 MODIS time series		
DOY	RED	NIR
225	# doy 225 # Parameter for Gauss-Function: name, a, μ , sigma Deciduous, 1, 0.0238, -0.0011 Mixed Forest, 1, 0.0256, -0.001025 Coniferous, 1, 0.0276, -0.001025 Grasland, 1, 0.0499, -0.0078 Spring Grain, 1, 0.1631, 0.030125 Winter Grain, 1, 0.07, -0.032875 Maize, 1, 0.0271, -0.00365 Rock, 1, 0.125490819, 0.067977773 Bare Soil, 1, 0.148090847, 0.042050528 Urban, 1, 0.089063198, 0.033701723 Snow and Ice, 1, 0.424729869, 0.194526916 Water, 1, 0.012074216, 0.015997301	# doy 225 # Parameter for Gauss-Function: name, a, μ , sigma Deciduous, 1, 0.3074, 0.005525 Mixed Forest, 1, 0.2433, 4.750000000000003E-04 Coniferous, 1, 0.1724, -0.0012 Grasland, 1, 0.3782, 0.036475 Spring Grain, 1, 0.225, -0.025625 Winter Grain, 1, 0.2062, 0.049775 Maize, 1, 0.4023, 0.0286 Rock, 1, 0.260757632, 0.069086984 Bare Soil, 1, 0.318273003, 0.067003789 Urban, 1, 0.249085185, 0.045946432 Snow and Ice, 1, 0.44491274, 0.132559209 Water, 1, 0.009699672, 0.005585239
235	# doy 235 # Parameter for Gauss-Function: name, a, μ , sigma Deciduous, 1, 0.0234, -0.000975 Mixed Forest, 1, 0.0247, -0.0009 Coniferous, 1, 0.0261, -0.00085 Grasland, 1, 0.0572, -0.008475 Spring Grain, 1, 0.1603, 0.029675 Winter Grain, 1, 0.1603, -0.02795 Maize, 1, 0.0264, -0.00335 Rock, 1, 0.125490819, 0.067977773 Bare Soil, 1, 0.148090847, 0.042050528 Urban, 1, 0.089063198, 0.033701723 Snow and Ice, 1, 0.424729869, 0.194526916 Water, 1, 0.012074216, 0.015997301	# doy 235 # Parameter for Gauss-Function: name, a, μ , sigma Deciduous, 1, 0.3042, 0.005825 Mixed Forest, 1, 0.2424, 5.750000000000006E-04 Coniferous, 1, 0.171, -0.001075 Grasland, 1, 0.3502, 0.039575 Spring Grain, 1, 0.2212, -0.0234 Winter Grain, 1, 0.2212, 0.010675 Maize, 1, 0.3869, 0.03175 Rock, 1, 0.260757632, 0.069086984 Bare Soil, 1, 0.318273003, 0.067003789 Urban, 1, 0.249085185, 0.045946432 Snow and Ice, 1, 0.44491274, 0.132559209 Water, 1, 0.009699672, 0.005585239
247	# doy 247 # Parameter for Gauss-Function: name, a, μ , sigma Deciduous, 1, 0.0229, -0.000925 Mixed Forest, 1, 0.0238, -8.000000000000001E-04 Coniferous, 1, 0.0244, -6.999999999999999E-04 Grasland, 1, 0.0678, -0.009075 Spring Grain, 1, 0.1565, 0.029 Winter Grain, 1, 0.1565, 0.00001 Maize, 1, 0.0257, -0.00295 Rock, 1, 0.125490819, 0.067977773 Bare Soil, 1, 0.148090847, 0.042050528 Urban, 1, 0.089063198, 0.033701723 Snow and Ice, 1, 0.424729869, 0.194526916 Water, 1, 0.012074216, 0.015997301	# doy 247 # Parameter for Gauss-Function: name, a, μ , sigma Deciduous, 1, 0.2979, 0.010125 Mixed Forest, 1, 0.241, 0.001925 Coniferous, 1, 0.1698, -9.750000000000004E-04 Grasland, 1, 0.3202, 0.0419 Spring Grain, 1, 0.2162, -0.0202 Winter Grain, 1, 0.2162, 0.00001 Maize, 1, 0.3595, 0.0318 Rock, 1, 0.260757632, 0.069086984 Bare Soil, 1, 0.318273003, 0.067003789 Urban, 1, 0.249085185, 0.045946432 Snow and Ice, 1, 0.44491274, 0.132559209 Water, 1, 0.009699672, 0.005585239
258	# doy 258 # Parameter for Gauss-Function: name, a, μ , sigma Deciduous, 1, 0.0228, -0.00105 Mixed Forest, 1, 0.0234, -0.001075 Coniferous, 1, 0.023, -6.000000000000001E-04 Grasland, 1, 0.0641, -0.00955 Spring Grain, 1, 0.1527, 0.02835 Winter Grain, 1, 0.1527, 0.00001 Maize, 1, 0.0251, -0.002575 Rock, 1, 0.125490819, 0.067977773 Bare Soil, 1, 0.148090847, 0.042050528 Urban, 1, 0.089063198, 0.033701723 Snow and Ice, 1, 0.424729869, 0.194526916 Water, 1, 0.012074216, 0.015997301	# doy 258 # Parameter for Gauss-Function: name, a, μ , sigma Deciduous, 1, 0.2789, 0.027475 Mixed Forest, 1, 0.2359, 0.00795 Coniferous, 1, 0.1691, -8.499999999999997E-04 Grasland, 1, 0.3246, 0.040575 Spring Grain, 1, 0.2111, -0.0181 Winter Grain, 1, 0.2111, 0.00001 Maize, 1, 0.3378, 0.029475 Rock, 1, 0.260757632, 0.069086984 Bare Soil, 1, 0.318273003, 0.067003789 Urban, 1, 0.249085185, 0.045946432 Snow and Ice, 1, 0.44491274, 0.132559209 Water, 1, 0.009699672, 0.005585239

Reflectance Probability Gaussian Functions for the 2003 MODIS time series		
DOY	RED	NIR
262	# doy 262 # Parameter for Gauss-Function: name, a, μ , sigma Deciduous, 1, 0.0229, -0.00115 Mixed Forest, 1, 0.0234, -0.001225 Coniferous, 1, 0.0226, -0.00055 Grasland, 1, 0.0625, -0.00995 Spring Grain, 1, 0.1513, 0.02805 Winter Grain, 1, 0.1513, 0.00001 Maize, 1, 0.0249, -0.002425 Rock, 1, 0.125490819, 0.067977773 Bare Soil, 1, 0.148090847, 0.042050528 Urban, 1, 0.089063198, 0.033701723 Snow and Ice, 1, 0.424729869, 0.194526916 Water, 1, 0.012074216, 0.015997301	# doy 262 # Parameter for Gauss-Function: name, a, μ , sigma Deciduous, 1, 0.2633, 0.0332 Mixed Forest, 1, 0.2312, 0.01035 Coniferous, 1, 0.1689, -7.999999999999995E-04 Grasland, 1, 0.3272, 0.040475 Spring Grain, 1, 0.2092, -0.016875 Winter Grain, 1, 0.2092, 0.00001 Maize, 1, 0.3309, 0.02905 Rock, 1, 0.260757632, 0.069086984 Bare Soil, 1, 0.318273003, 0.067003789 Urban, 1, 0.249085185, 0.045946432 Snow and Ice, 1, 0.44491274, 0.132559209 Water, 1, 0.009699672, 0.005585239
265	# doy 265 # Parameter for Gauss-Function: name, a, μ , sigma Deciduous, 1, 0.0231, -0.001225 Mixed Forest, 1, 0.0236, -0.001325 Coniferous, 1, 0.0223, -0.0005 Grasland, 1, 0.062, -0.010375 Spring Grain, 1, 0.1502, 0.027775 Winter Grain, 1, 0.1502, 0.00001 Maize, 1, 0.0248, -0.00235 Rock, 1, 0.125490819, 0.067977773 Bare Soil, 1, 0.148090847, 0.042050528 Urban, 1, 0.089063198, 0.033701723 Snow and Ice, 1, 0.424729869, 0.194526916 Water, 1, 0.012074216, 0.015997301	# doy 265 # Parameter for Gauss-Function: name, a, μ , sigma Deciduous, 1, 0.2476, 0.0363 Mixed Forest, 1, 0.226, 0.01175 Coniferous, 1, 0.1689, -7.749999999999998E-04 Grasland, 1, 0.3276, 0.0409 Spring Grain, 1, 0.2078, -0.0156 Winter Grain, 1, 0.2078, 0.00001 Maize, 1, 0.3249, 0.02925 Rock, 1, 0.260757632, 0.069086984 Bare Soil, 1, 0.318273003, 0.067003789 Urban, 1, 0.249085185, 0.045946432 Snow and Ice, 1, 0.44491274, 0.132559209 Water, 1, 0.009699672, 0.005585239
290	# doy 290 # Parameter for Gauss-Function: name, a, μ , sigma Deciduous, 1, 0.0252, -0.029625 Mixed Forest, 1, 0.026, -0.0009 Coniferous, 1, 0.0203, -0.000275 Grasland, 1, 0.0724, -0.009575 Spring Grain, 1, 0.1413, 0.00001 Winter Grain, 1, 0.1413, 0.00001 Maize, 1, 0.1413, 0.00001 Rock, 1, 0.125490819, 0.067977773 Bare Soil, 1, 0.148090847, 0.042050528 Urban, 1, 0.089063198, 0.033701723 Snow and Ice, 1, 0.424729869, 0.194526916 Water, 1, 0.012074216, 0.015997301	# doy 290 # Parameter for Gauss-Function: name, a, μ , sigma Deciduous, 1, 0.1421, 0.0148 Mixed Forest, 1, 0.1846, -0.003675 Coniferous, 1, 0.1685, -4.749999999999996E-04 Grasland, 1, 0.2946, 0.02165 Spring Grain, 1, 0.1959, 0.00001 Winter Grain, 1, 0.1959, 0.00001 Maize, 1, 0.1959, 0.00001 Rock, 1, 0.260757632, 0.069086984 Bare Soil, 1, 0.318273003, 0.067003789 Urban, 1, 0.249085185, 0.045946432 Snow and Ice, 1, 0.44491274, 0.132559209 Water, 1, 0.009699672, 0.005585239

Appendix 6: Pixel by Pixel Analysis of LAI from reflectance segmentation

This appendix lists all 64 pixel of each of the 240m scale validation sites, the Hochstadt and the Gut Huell area. All the land cover types sharing the pixel are listed (majority type in bold print). For each land cover type, the area fraction, the true reflectances of the truth dataset and the result from the reflectance segmentation, the relative error in each band, the LAI derived from the truth dataset and the reflectance segmentation, is given. This latter section shows the subscale fractional information for each cover type and evaluates the error of reflectance segmentation. The subscale results from the LAI algorithms were summed to find LAI as a single value for the 240m pixel. That section of the tables compares 240m scale values. Sums of land cover specific LAI from the truth dataset (*LAI sum truth*) and from the reflectance segmentation (*LAI sum refseg*) are provided along with majority LAI computed under the assumption of a homogeneous pixel. Relative and absolute error of *LAI sum refseg* and *LAI majority* in relation to *LAI sum truth* are compared. At the bottom of the table mean and maximum errors of all pixels are given. (see Section 7.1.4)

Hochstadt area

(resolution 240m, row 193-200, col 313-320, one-based index)

Land Cover Type	Pixel row/col	area fraction	RED refseg	RED truth	NIR refseg	NIR truth	relErr RED [%]	relErr NIR [%]	LAI refseg [m ² /m ²]	LAI truth [m ² /m ²]	relErr LAI [%]	absErr LAI [m ² /m ²]	LAI sum refseg [m ² /m ²]	LAI sum truth [m ² /m ²]	LAI majority [m ² /m ²]	relErr LAI sum refseg [%]	relErr LAI sum majority [%]	absErr refseg [m ² /m ²]	absErr majority [m ² /m ²]
Mixed Forest	193/ 313	0.0500	0.0213	0.0332	0.2517	0.2910	35.8	13.5	8.20	5.95	37.8	2.3	1.65	1.40	0.95	17.9	32.1	0.25	0.45
Grassland	193/ 313	0.6170	0.1100	0.0800	0.3514	0.3919	37.5	10.3	0.55	1.15	52.2	0.6							
Winter Grain	193/ 313	0.2330	0.0320	0.0960	0.3744	0.3275	66.7	14.3	2.70	1.00	170.0	1.7							
Maize	193/ 313	0.0830	0.0473	0.0729	0.3586	0.2921	35.1	22.8	3.30	1.95	69.2	1.4							
Urban Fabric	193/ 313	0.0170	0.0930	0.1035	0.2472	0.2189	10.1	12.9	0.00	0.00	0.0	0.0							
Deciduous Forest	193/ 314	0.0160	0.0271	0.0297	0.3965	0.4478	8.8	11.5	5.20	5.30	1.9	0.1	2.35	2.30	1.40	2.2	39.1	0.05	0.90
Mixed Forest	193/ 314	0.0940	0.0212	0.0263	0.2525	0.2889	19.4	12.6	8.25	7.65	7.8	0.6							
Grassland	193/ 314	0.5780	0.0787	0.0723	0.3787	0.3859	8.9	1.9	1.15	1.30	11.5	0.2							
Winter Grain	193/ 314	0.1250	0.0293	0.0689	0.3800	0.3462	57.5	9.8	2.85	1.60	78.1	1.3							
Maize	193/ 314	0.1560	0.0470	0.0386	0.3590	0.3311	21.8	8.4	3.35	3.55	5.6	0.2							
Urban Fabric	193/ 314	0.0310	0.0928	0.0801	0.2473	0.2543	15.9	2.8	0.00	0.00	0.0	0.0							
Grassland	193/ 315	0.4530	0.0276	0.0782	0.3911	0.3975	64.7	1.6	2.65	1.20	120.8	1.5	1.85	1.60	1.10	15.6	31.3	0.25	0.50
Winter Grain	193/ 315	0.1410	0.0272	0.0899	0.3814	0.3506	69.7	8.8	2.90	1.20	141.7	1.7							
Maize	193/ 315	0.4060	0.1564	0.0782	0.3601	0.3637	100.0	1.0	0.65	2.25	71.1	1.6							
Mixed Forest	193/ 316	0.2030	0.0210	0.0206	0.2563	0.2526	1.9	1.5	8.45	8.45	0.0	0.0	3.70	3.70	1.95	0.0	47.3	0.00	1.75
Grassland	193/ 316	0.3750	0.0562	0.0542	0.3987	0.3929	3.7	1.5	1.70	1.75	2.9	0.1							
Spring Grain	193/ 316	0.0780	0.0354	0.0426	0.4491	0.4393	16.9	2.2	2.80	2.60	7.7	0.2							
Winter Grain	193/ 316	0.0310	0.0284	0.0367	0.3813	0.3743	22.6	1.9	2.85	2.55	11.8	0.3							
Maize	193/ 316	0.3120	0.0453	0.0452	0.3612	0.3738	0.2	3.4	3.40	3.45	1.4	0.1							
Mixed Forest	193/ 317	0.7810	0.0191	0.0190	0.2440	0.2456	0.5	0.7	8.80	8.85	0.6	0.0	7.50	7.55	8.30	0.7	9.9	0.05	0.75
Grassland	193/ 317	0.0160	0.0511	0.0391	0.3869	0.4057	30.7	4.6	1.80	2.25	20.0	0.5							
Spring Grain	193/ 317	0.1090	0.0343	0.0452	0.4483	0.4419	24.1	1.4	2.85	2.50	14.0	0.4							
Winter Grain	193/ 317	0.0160	0.0283	0.0393	0.3807	0.4044	28.0	5.9	2.85	2.55	11.8	0.3							
Maize	193/ 317	0.0780	0.0426	0.0289	0.3591	0.3440	47.4	4.4	3.50	4.05	13.6	0.6							
Mixed Forest	193/ 318	0.6030	0.0706	0.0217	0.2691	0.2752	225.3	2.2	1.10	8.70	87.4	7.6	1.20	5.60	1.65	78.6	70.5	4.40	3.95
Grassland	193/ 318	0.0950	0.0425	0.0879	0.3923	0.3829	51.6	2.5	2.10	1.00	110.0	1.1							
Spring Grain	193/ 318	0.0320	0.0341	0.0435	0.4490	0.4129	21.6	8.7	2.85	2.50	14.0	0.4							
Winter Grain	193/ 318	0.0320	0.0279	0.0545	0.3817	0.3690	48.8	3.4	2.90	2.05	41.5	0.9							
Maize	193/ 318	0.0480	0.0413	0.0481	0.3599	0.3454	14.1	4.2	3.55	3.20	10.9	0.4							
Rock	193/ 318	0.0630	0.0679	0.2373	0.2634	0.2851	71.4	7.6	0.00	0.00	0.0	0.0							
Bare Soil	193/ 318	0.1110	0.1074	0.2003	0.3214	0.2945	46.4	9.1	0.00	0.00	0.0	0.0							
Urban Fabric	193/ 318	0.0160	0.0859	0.1977	0.2477	0.2532	56.6	2.2	0.00	0.00	0.0	0.0							
Grassland	193/ 319	0.3590	0.2084	0.0514	0.3987	0.3949	305.4	1.0	0.10	1.85	94.6	1.8	0.70	1.15	0.00	39.1	100.0	0.45	1.15
Winter Grain	193/ 319	0.1880	0.0273	0.0601	0.3837	0.3623	54.6	5.9	2.90	1.85	56.8	1.1							
Maize	193/ 319	0.0470	0.0426	0.0474	0.3597	0.3721	10.1	3.3	3.50	3.40	2.9	0.1							
Rock	193/ 319	0.0160	0.1203	0.2257	0.2614	0.3111	46.7	16.0	0.00	0.00	0.0	0.0							
Bare Soil	193/ 319	0.3910	0.0905	0.2145	0.3258	0.3360	57.8	3.0	0.00	0.00	0.0	0.0							
Deciduous Forest	193/ 320	0.0160	0.0267	0.0330	0.3958	0.4553	19.1	13.1	5.25	5.00	5.0	0.3	2.05	1.90	1.90	7.9	0.0	0.15	0.00
Grassland	193/ 320	0.2970	0.0283	0.0658	0.3615	0.4034	57.0	10.4	2.55	1.50	70.0	1.1							
Spring Grain	193/ 320	0.1410	0.0316	0.0402	0.4468	0.4399	21.4	1.6	2.90	2.65	9.4	0.3							
Winter Grain	193/ 320	0.4690	0.0926	0.0629	0.3615	0.3355	47.2	7.7	1.20	1.70	29.4	0.5							
Maize	193/ 320	0.0780	0.0405	0.0593	0.3582	0.3550	31.7	0.9	3.60	2.85	26.3	0.8							

Land Cover Type	Pixel (row/col)	area fraction	RED refseg	RED truth	NIR refseg	NIR truth	relErr RED [%]	relErr NIR [%]	LAI refseg [m ² /m ²]	LAI truth [m ² /m ²]	relErr LAI [%]	absErr LAI [m ² /m ²]	LAI sum refseg [m ² /m ²]	LAI sum truth [m ² /m ²]	LAI majority [m ² /m ²]	relErr LAI sum refseg [%]	relErr LAI sum majority [%]	absErr refseg [m ² /m ²]	absErr majority [m ² /m ²]
Grassland	194/ 313	0.6560	0.0572	0.0644	0.3967	0.3835	11.2	3.4	1.70	1.45	17.2	0.3	1.20	1.00	1.20	20.0	20.0	0.20	0.20
Winter Grain	194/ 313	0.0160	0.0284	0.0861	0.3810	0.3244	67.0	17.4	2.85	1.15	147.8	1.7							
Maize	194/ 313	0.0160	0.0435	0.0729	0.3595	0.3437	40.3	4.6	3.45	2.30	50.0	1.2							
Urban Fabric	194/ 313	0.3120	0.0957	0.0763	0.2487	0.2803	25.4	11.3	0.00	0.00	0.00	0.0							
Grassland	194/ 314	0.5470	0.0747	0.0574	0.4617	0.4435	30.1	4.1	1.50	1.85	18.9	0.4	1.60	1.35	1.45	18.5	7.4	0.25	0.10
Winter Grain	194/ 314	0.2660	0.0302	0.0920	0.3981	0.3374	67.2	18.0	2.85	1.10	159.1	1.8							
Maize	194/ 314	0.0160	0.0437	0.0302	0.3598	0.3109	44.7	15.7	3.45	3.85	10.4	0.4							
Urban Fabric	194/ 314	0.1720	0.1064	0.0676	0.2542	0.4103	57.4	38.0	0.00	0.00	0.00	0.0							
Mixed Forest	194/ 315	0.1090	0.0196	0.0232	0.2582	0.3235	15.5	20.2	9.00	9.45	4.8	0.4	3.10	2.85	2.25	8.8	21.1	0.25	0.60
Grassland	194/ 315	0.3590	0.1016	0.0562	0.4200	0.4229	81.1	0.7	3.50	1.80	94.4	1.7							
Spring Grain	194/ 315	0.0470	0.0335	0.0548	0.4495	0.4295	38.9	4.7	2.85	2.25	26.7	0.6							
Winter Grain	194/ 315	0.4380	0.0914	0.0481	0.3998	0.3819	90.0	4.7	1.35	2.25	40.0	0.9							
Maize	194/ 315	0.0470	0.0411	0.0654	0.3602	0.3726	37.2	3.3	3.60	2.75	30.9	0.9							
Mixed Forest	194/ 316	0.4530	0.0217	0.0286	0.2799	0.2799	24.1	0.0	8.85	6.75	31.1	2.1	5.05	4.25	6.05	18.8	42.4	0.80	1.80
Grassland	194/ 316	0.4530	0.0601	0.0546	0.4406	0.4456	10.1	1.1	1.75	1.95	10.3	0.2							
Winter Grain	194/ 316	0.0470	0.0285	0.0282	0.3835	0.3728	1.1	2.9	2.85	2.85	0.0	0.0							
Maize	194/ 316	0.0470	0.0439	0.0307	0.3605	0.3228	43.0	11.7	3.45	3.90	11.5	0.5							
Deciduous Forest	194/ 317	0.2060	0.0000	0.0231	0.4124	0.4548	100.0	9.3	9.90	6.15	61.0	3.8	10.35	7.75	10.50	33.5	35.5	2.60	2.75
Mixed Forest	194/ 317	0.6030	0.0000	0.0188	0.2932	0.2758	100.0	6.3	12.50	9.80	27.6	2.7							
Grassland	194/ 317	0.1110	0.0000	0.0263	0.4020	0.4091	100.0	1.7	4.05	2.75	47.3	1.3							
Spring Grain	194/ 317	0.0160	0.0000	0.0191	0.4491	0.4026	100.0	11.5	4.05	3.25	24.6	0.8							
Winter Grain	194/ 317	0.0480	0.0000	0.0215	0.3839	0.3949	100.0	2.8	4.05	3.15	28.6	0.9							
Maize	194/ 317	0.0160	0.0000	0.0195	0.3598	0.4161	100.0	13.5	5.80	4.75	22.1	1.1							
Mixed Forest	194/ 318	0.0490	0.0201	0.0194	0.2549	0.3131	3.6	18.6	8.70	10.50	17.1	1.8	3.25	2.40	1.55	35.4	35.4	0.85	0.85
Grassland	194/ 318	0.2950	0.0077	0.0554	0.4077	0.4018	86.1	1.5	3.65	1.75	108.6	1.9							
Spring Grain	194/ 318	0.0490	0.0329	0.0361	0.4493	0.4135	8.9	8.7	2.90	2.70	7.4	0.2							
Winter Grain	194/ 318	0.4260	0.0189	0.0442	0.3949	0.3819	57.2	3.4	3.25	2.35	38.3	0.9							
Maize	194/ 318	0.0660	0.0391	0.0415	0.3603	0.3666	5.8	1.7	3.65	3.60	1.4	0.0							
Rock	194/ 318	0.0980	0.5913	0.2596	0.2658	0.3171	127.8	16.2	0.00	0.00	0.00	0.0							
Bare Soil	194/ 318	0.0160	0.1396	0.1560	0.3183	0.3907	10.5	18.5	0.00	0.00	0.00	0.0							
Grassland	194/ 319	0.5000	0.0446	0.0711	0.3873	0.3878	37.3	0.1	2.00	1.30	53.8	0.7	1.95	1.30	0.85	50.0	34.6	0.65	0.45
Winter Grain	194/ 319	0.3120	0.0277	0.0580	0.3809	0.3578	52.2	6.5	2.90	1.90	52.6	1.0							
Maize	194/ 319	0.0160	0.0433	0.0360	0.3595	0.3670	20.3	2.0	3.50	3.85	9.1	0.4							
Rock	194/ 319	0.0780	0.6200	0.2449	0.2611	0.3297	153.2	20.8	0.00	0.00	0.00	0.0							
Bare Soil	194/ 319	0.0940	0.1429	0.2145	0.3176	0.3330	33.4	4.6	0.00	0.00	0.00	0.0							
Grassland	194/ 320	0.3750	0.1983	0.0788	0.3499	0.3754	151.6	6.8	0.05	1.10	95.5	1.1	2.40	1.30	1.40	84.6	7.7	1.10	0.10
Winter Grain	194/ 320	0.5470	0.0006	0.0814	0.3549	0.3358	99.3	5.7	4.00	1.30	207.7	2.7							
Maize	194/ 320	0.0630	0.0350	0.0552	0.3583	0.3436	36.6	4.3	3.85	2.90	32.8	1.0							
Rock	194/ 320	0.0160	0.0840	0.0449	0.2600	0.3718	87.1	30.1	0.00	0.00	0.00	0.0							
Grassland	195/ 313	0.1720	0.0515	0.0783	0.4201	0.3243	34.2	29.5	1.95	0.90	116.7	1.1	0.40	0.20	0.00	100.0	100.0	0.20	0.20
Winter Grain	195/ 313	0.0160	0.0284	0.0950	0.3823	0.3167	70.1	20.7	2.85	0.95	200.0	1.9							
Maize	195/ 313	0.0160	0.0434	0.0654	0.3600	0.3185	33.6	13.0	3.50	2.40	45.8	1.1							
Bare Soil	195/ 313	0.0310	0.1476	0.1041	0.3215	0.3298	41.8	2.5	0.00	0.00	0.00	0.0							
Urban Fabric	195/ 313	0.7660	0.0901	0.0841	0.2894	0.3128	7.1	7.5	0.00	0.00	0.00	0.0							
Grassland	195/ 314	0.0780	0.0516	0.0544	0.4067	0.4158	5.1	2.2	1.90	1.85	2.7	0.0	0.15	0.15	0.00	0.0	100.0	0.00	0.15
Winter Grain	195/ 314	0.0160	0.0284	0.1099	0.3827	0.2956	74.2	29.5	2.85	0.65	338.5	2.2							
Bare Soil	195/ 314	0.0160	0.1476	0.1071	0.3202	0.3589	37.8	10.8	0.00	0.00	0.00	0.0							
Urban Fabric	195/ 314	0.8910	0.0937	0.0928	0.3110	0.3111	1.0	0.0	0.00	0.00	0.00	0.0							
Mixed Forest	195/ 315	0.1430	0.0204	0.0251	0.2673	0.3085	18.7	13.4	8.95	8.50	5.3	0.4	2.45	2.15	1.85	14.0	14.0	0.30	0.30
Grassland	195/ 315	0.3970	0.0404	0.0496	0.4654	0.3729	18.5	24.8	2.40	1.80	33.3	0.6							
Spring Grain	195/ 315	0.0320	0.0348	0.0323	0.4498	0.4542	7.7	1.0	2.80	2.90	3.4	0.1							
Winter Grain	195/ 315	0.0160	0.0283	0.0386	0.3824	0.3996	26.7	4.3	2.85	2.60	9.6	0.3							
Maize	195/ 315	0.0320	0.0430	0.0327	0.3606	0.3501	31.5	3.0	3.50	3.90	10.3	0.4							
Urban Fabric	195/ 315	0.3810	0.0643	0.0547	0.2690	0.3492	17.6	23.0	0.00	0.00	0.00	0.0							
Mixed Forest	195/ 316	0.2740	0.0211	0.0210	0.2569	0.2804	0.5	8.4	8.40	9.10	7.7	0.7	3.65	3.85	1.85	5.2	51.9	0.20	2.00
Grassland	195/ 316	0.6450	0.0580	0.0612	0.4047	0.4007	5.2	1.0	1.70	1.60	6.2	0.1							
Maize	195/ 316	0.0810	0.0438	0.0237	0.3598	0.3141	84.8	14.5	3.45	4.20	17.9	0.8							
Deciduous Forest	195/ 317	0.0160	0.0271	0.0256	0.3963	0.4640	5.9	14.6	5.20	5.90	11.9	0.7	2.20	2.15	1.25	2.3	41.9	0.05	0.90
Mixed Forest	195/ 317	0.1090	0.0215	0.0205	0.2514	0.2450	4.9	2.6	8.10	8.25	1.8	0.2							
Grassland	195/ 317	0.6250	0.0911	0.0780	0.3664	0.3761	16.8	2.6	0.85	1.15	26.1	0.3							
Winter Grain	195/ 317	0.1720	0.0302	0.0702	0.3781	0.3397	57.0	11.3	2.80	1.55	80.6	1.3							
Maize	195/ 317	0.0780	0.0458	0.0635	0.3590	0.3611	27.9	0.6	3.35	2.70	24.1	0.7							
Grassland	195/ 318	0.5780	0.0210	0.0732	0.37														

Land Cover Type	Pixel (row/col)	area fraction	RED refseg	RED truth	NIR refseg	NIR truth	relErr RED [%]	relErr NIR [%]	LAI refseg [m ² /m ²]	LAI truth [m ² /m ²]	relErr LAI [%]	absErr LAI [m ² /m ²]	LAI sum refseg [m ² /m ²]	LAI sum truth [m ² /m ²]	LAI majority [m ² /m ²]	relErr LAI sum refseg [%]	relErr LAI sum majority [%]	absErr refseg [m ² /m ²]	absErr majority [m ² /m ²]
Mixed Forest	196/ 315	0.0490	0.0210	0.0403	0.2529	0.1910	47.9	32.4	8.35	2.00	317.5	6.4	1.70	1.40	1.20	21.4	14.3	0.30	0.20
Grassland	196/ 315	0.7050	0.0799	0.0699	0.3792	0.3934	14.3	3.6	1.10	1.35	18.5	0.3							
Winter Grain	196/ 315	0.1310	0.0292	0.0765	0.3802	0.3653	61.8	4.1	2.85	1.50	90.0	1.4							
Maize	196/ 315	0.0490	0.0444	0.0443	0.3594	0.3529	0.2	1.8	3.45	3.40	1.5	0.1							
Bare Soil	196/ 315	0.0490	0.1546	0.1518	0.3172	0.2811	1.8	12.8	0.00	0.00	0.0	0.0							
Water	196/ 315	0.0160	0.0123	0.0326	0.0096	0.2187	62.3	95.6	0.00	0.00	0.0	0.0							
Grassland	196/ 316	0.6250	0.1005	0.0770	0.4223	0.4138	30.5	2.1	0.95	1.30	26.9	0.4	1.60	1.45	1.30	10.3	10.3	0.15	0.15
Winter Grain	196/ 316	0.3440	0.0328	0.0727	0.3900	0.4040	54.9	3.5	2.75	1.75	57.1	1.0							
Maize	196/ 316	0.0310	0.0446	0.0743	0.3598	0.3761	40.0	4.3	3.45	2.45	40.8	1.0							
Grassland	196/ 317	0.2190	0.0506	0.0726	0.3889	0.3736	30.3	4.1	1.85	1.25	48.0	0.6	2.20	2.05	1.80	7.3	12.2	0.15	0.25
Spring Grain	196/ 317	0.0160	0.0350	0.0451	0.4488	0.4141	22.4	8.4	2.80	2.45	14.3	0.4							
Winter Grain	196/ 317	0.3910	0.0938	0.0564	0.3822	0.3845	66.3	0.6	1.25	2.05	39.0	0.8							
Maize	196/ 317	0.3750	0.0427	0.0685	0.3599	0.3678	37.7	2.1	3.50	2.60	34.6	0.9							
Maize	196/ 318	1.0000	0.0583	0.0583	0.3449	0.3450	0.0	0.0	2.80	2.80	0.0	0.0	2.80	2.80	2.80	0.0	0.0	0.00	0.00
Grassland	196/ 319	0.1720	0.0119	0.0526	0.4113	0.4082	77.4	0.8	3.40	1.85	83.8	1.6	3.05	2.55	2.30	19.6	9.8	0.50	0.25
Spring Grain	196/ 319	0.0160	0.0340	0.0362	0.4491	0.4362	6.1	3.0	2.85	2.75	3.6	0.1							
Winter Grain	196/ 319	0.4840	0.0890	0.0440	0.4130	0.4122	102.3	0.2	1.45	2.45	40.8	1.0							
Maize	196/ 319	0.3280	0.0081	0.0532	0.3678	0.3711	84.8	0.9	5.30	3.15	68.3	2.2							
Mixed Forest	196/ 320	0.0630	0.0208	0.0240	0.2529	0.3018	13.3	16.2	8.40	8.65	2.9	0.3	2.10	1.90	1.25	10.5	34.2	0.20	0.65
Grassland	196/ 320	0.5080	0.0515	0.0938	0.3832	0.3725	45.1	2.9	1.80	0.85	111.8	1.0							
Spring Grain	196/ 320	0.1110	0.0351	0.0488	0.4486	0.4283	28.1	4.7	2.80	2.40	16.7	0.4							
Winter Grain	196/ 320	0.2540	0.1525	0.0444	0.3799	0.4124	243.5	7.9	0.55	2.45	77.6	1.9							
Maize	196/ 320	0.0630	0.0434	0.1077	0.3594	0.3167	59.7	13.5	3.50	1.20	191.7	2.3							
Grassland	197/ 313	0.7190	0.0722	0.0651	0.3729	0.3763	10.9	0.9	1.25	1.40	10.7	0.2	1.70	1.60	1.50	6.2	6.3	0.10	0.10
Winter Grain	197/ 313	0.2500	0.0296	0.0474	0.3785	0.3749	37.6	1.0	2.80	2.25	24.4	0.6							
Maize	197/ 313	0.0310	0.0439	0.0638	0.3593	0.3096	31.2	16.1	3.45	2.35	46.8	1.1							
Grassland	197/ 314	0.7500	0.0737	0.0715	0.3780	0.3767	3.1	0.3	1.25	1.25	0.0	0.0	1.60	1.60	1.45	0.0	9.4	0.00	0.15
Winter Grain	197/ 314	0.2340	0.0295	0.0354	0.3795	0.3825	16.7	0.8	2.80	2.65	5.7	0.2							
Maize	197/ 314	0.0160	0.0436	0.0626	0.3594	0.3729	30.4	3.6	3.45	2.80	23.2	0.7							
Grassland	197/ 315	0.8750	0.0795	0.0794	0.3909	0.3909	0.1	0.0	1.15	1.15	0.0	0.0	1.35	1.35	1.30	0.0	3.7	0.00	0.05
Winter Grain	197/ 315	0.1250	0.0290	0.0294	0.3811	0.3815	1.4	0.1	2.85	2.85	0.0	0.0							
Mixed Forest	197/ 316	0.0160	0.0209	0.0450	0.2532	0.2726	53.6	7.1	8.40	3.35	150.7	5.1	1.60	1.55	1.30	3.2	16.1	0.05	0.25
Grassland	197/ 316	0.6610	0.0936	0.0903	0.3874	0.3812	3.7	1.6	0.90	0.95	5.3	0.0							
Spring Grain	197/ 316	0.2100	0.0394	0.0318	0.4488	0.4662	23.9	3.7	2.70	2.95	8.5	0.3							
Winter Grain	197/ 316	0.0970	0.0294	0.0503	0.3809	0.4087	41.6	6.8	2.85	2.30	23.9	0.6							
Maize	197/ 316	0.0160	0.0439	0.0729	0.3595	0.3732	39.8	3.7	3.45	2.50	38.0	1.0							
Grassland	197/ 317	0.1090	0.0641	0.0835	0.4215	0.4136	23.2	1.9	1.60	1.15	39.1	0.5	2.25	2.25	2.55	0.0	13.3	0.00	0.30
Spring Grain	197/ 317	0.0940	0.0385	0.0423	0.4536	0.4659	9.0	2.6	2.75	2.65	3.8	0.1							
Winter Grain	197/ 317	0.0310	0.0290	0.0378	0.3855	0.4178	23.3	7.7	2.85	2.65	7.5	0.2							
Maize	197/ 317	0.7660	0.0862	0.0826	0.4030	0.4013	4.4	0.4	2.30	2.35	2.1	0.1							
Deciduous Forest	197/ 318	0.0310	0.0273	0.0329	0.3960	0.4722	17.0	16.1	5.15	5.15	0.0	0.0	3.70	2.40	2.80	54.2	16.7	1.30	0.40
Grassland	197/ 318	0.2500	0.2055	0.0551	0.3793	0.3879	273.0	2.2	0.10	1.70	94.1	1.6							
Winter Grain	197/ 318	0.0310	0.0288	0.0344	0.3804	0.3835	16.3	0.8	2.85	2.65	7.5	0.2							
Maize	197/ 318	0.6880	0.0121	0.0663	0.3554	0.3487	81.7	1.9	5.05	2.55	98.0	2.5							
Grassland	197/ 319	0.6410	0.0817	0.0785	0.3473	0.3322	4.1	4.5	0.95	0.95	0.0	0.0	1.60	1.55	1.40	3.2	9.7	0.05	0.15
Spring Grain	197/ 319	0.0780	0.0363	0.0328	0.4480	0.4290	10.7	4.4	2.80	2.85	1.8	0.1							
Winter Grain	197/ 319	0.2660	0.0304	0.0398	0.3730	0.4126	23.6	9.6	2.75	2.60	5.8	0.2							
Maize	197/ 319	0.0160	0.0438	0.0392	0.3593	0.4003	11.7	10.2	3.45	3.85	10.4	0.4							
Mixed Forest	197/ 320	0.3440	0.0221	0.0234	0.2721	0.2774	5.6	1.9	8.50	8.20	3.7	0.3	4.75	4.65	2.60	2.2	44.1	0.10	2.05
Grassland	197/ 320	0.0940	0.0551	0.0611	0.3976	0.3636	9.8	9.4	1.75	1.45	20.7	0.3							
Spring Grain	197/ 320	0.0160	0.0353	0.0330	0.4490	0.4362	7.0	2.9	2.80	2.85	1.8	0.1							
Winter Grain	197/ 320	0.3590	0.0307	0.0268	0.3996	0.4179	14.6	4.4	2.85	3.00	5.0	0.2							
Maize	197/ 320	0.1880	0.0470	0.0490	0.3632	0.3366	4.1	7.9	3.35	3.10	8.1	0.3							
Grassland	198/ 313	0.0470	0.0424	0.0389	0.3909	0.4431	9.0	11.8	2.10	2.40	12.5	0.3	2.85	2.55	2.35	11.8	7.8	0.30	0.20
Spring Grain	198/ 313	0.0630	0.0311	0.0326	0.4496	0.4424	4.6	1.6	2.95	2.85	3.5	0.1							
Winter Grain	198/ 313	0.6410	0.0066	0.0442	0.4046	0.4002	85.1	1.1	3.75	2.40	56.3	1.4							
Maize	198/ 313	0.2500	0.1515	0.0555	0.3630	0.3661	173.0	0.8	0.75	3.05	75.4	2.3							
Grassland	198/ 314	0.7500	0.0794	0.0706	0.3721	0.3715	12.5	0.2	1.10	1.25	12.0	0.2	1.55	1.45	1.35	6.9	6.9	0.10	0.10
Spring Grain	198/ 314	0.0470	0.0356	0.0408	0.4486	0.4382	12.7	2.4	2.80	2.60	7.7	0.2							
Winter Grain	198/ 314	0.1560	0.0293	0.0679	0.3794	0.3788	56.8	0.2	2.85	1.75	62.9	1.1							
Maize	198/ 314	0.0470	0.0443	0.0516	0.3593	0.3813	14.1	5.8	3.45	3.25	6.2	0.2							
Grassland	198/ 315	0.8910	0.0625	0.0605	0.3986	0.3997	3.3	0.3	1.55	1.60	3.1	0.1	1.70	1.70	1.65	0.0	2.9	0.00	0.05
Winter Grain	198/ 315	0.0780	0.0285	0.0537	0.3813	0.3584	46.												

Land Cover Type	Pixel (row/col)	area fraction	RED refseg	RED truth	NIR refseg	NIR truth	relErr RED [%]	relErr NIR [%]	LAI refseg [m ² /m ²]	LAI truth [m ² /m ²]	relErr LAI [%]	absErr LAI [m ² /m ²]	LAI sum refseg [m ² /m ²]	LAI sum truth [m ² /m ²]	LAI majority [m ² /m ²]	relErr LAI sum refseg [%]	relErr LAI sum majority [%]	absErr refseg [m ² /m ²]	absErr majority [m ² /m ²]
Mixed Forest	199/ 313	0.1090	0.0201	0.0222	0.2749	0.2344	9.5	17.3	9.30	7.35	26.5	2.0	4.95	3.00	3.10	65.0	3.3	1.95	0.10
Needleleaf Forest	199/ 313	0.0160	0.0219	0.0171	0.1859	0.1923	28.1	3.3	10.20	12.50	18.4	2.3							
Grassland	199/ 313	0.2340	0.0369	0.0648	0.6716	0.3502	43.1	91.8	2.90	1.30	123.1	1.6							
Winter Grain	199/ 313	0.2810	0.0947	0.0438	0.0246	0.3628	116.2	93.2	6.00	2.30	160.9	3.7							
Maize	199/ 313	0.3590	0.0326	0.0540	0.3883	0.3453	39.6	12.5	4.05	2.95	37.3	1.1							
Mixed Forest	199/ 314	0.2030	0.0212	0.0226	0.2496	0.2417	6.2	3.3	8.15	7.45	9.4	0.7	4.35	4.65	1.75	6.5	62.4	0.30	2.90
Needleleaf Forest	199/ 314	0.1560	0.0225	0.0196	0.1843	0.1940	14.8	5.0	9.65	12.50	22.8	2.9							
Grassland	199/ 314	0.4840	0.0613	0.0615	0.3703	0.3829	0.3	3.3	1.50	1.50	0.0	0.0							
Winter Grain	199/ 314	0.0630	0.0286	0.0374	0.3798	0.3739	23.5	1.6	2.85	2.55	11.8	0.3							
Maize	199/ 314	0.0940	0.0443	0.0393	0.3589	0.2989	12.7	20.1	3.45	3.30	4.5	0.2							
Mixed Forest	199/ 315	0.2660	0.0226	0.0231	0.0000	0.2472	2.2	100.0	12.50	7.45	67.8	5.1	6.75	3.65	2.90	84.9	20.5	3.10	0.75
Grassland	199/ 315	0.1560	0.0618	0.0491	0.0000	0.3944	25.9	100.0	0.00	1.90	100.0	1.9							
Winter Grain	199/ 315	0.0310	0.0287	0.0271	0.0000	0.4227	5.9	100.0	6.00	3.00	100.0	3.0							
Maize	199/ 315	0.5470	0.0609	0.0644	0.0000	0.3122	5.4	100.0	6.00	2.35	155.3	3.7							
Grassland	199/ 316	0.1090	0.0584	0.0416	0.3964	0.4025	40.4	1.5	1.65	2.15	23.3	0.5	2.70	2.65	3.40	1.9	28.3	0.05	0.75
Spring Grain	199/ 316	0.0160	0.0354	0.0331	0.4490	0.4211	6.9	6.6	2.80	2.80	0.0	0.0							
Winter Grain	199/ 316	0.3910	0.0324	0.0320	0.3963	0.4131	1.2	4.1	2.75	2.80	1.8	0.0							
Maize	199/ 316	0.4840	0.0583	0.0626	0.3668	0.3528	6.9	4.0	2.95	2.70	9.3	0.3							
Spring Grain	199/ 317	0.0470	0.0356	0.0425	0.4493	0.4129	16.2	8.8	2.80	2.50	12.0	0.3	2.75	2.70	2.75	1.9	1.9	0.05	0.05
Winter Grain	199/ 317	0.9530	0.0341	0.0337	0.4113	0.4131	1.2	0.4	2.75	2.75	0.0	0.0							
Needleleaf Forest	199/ 318	0.0160	0.0223	0.0327	0.1849	0.1714	31.8	7.9	9.85	4.10	140.2	5.8	2.20	2.10	2.10	4.8	0.0	0.10	0.00
Winter Grain	199/ 318	0.9840	0.0493	0.0491	0.3494	0.3497	0.4	0.1	2.10	2.10	0.0	0.0							
Mixed Forest	199/ 319	0.2340	0.0180	0.0243	0.2308	0.2207	25.9	4.6	8.80	6.20	41.9	2.6	3.75	4.80	2.40	21.9	50.0	1.05	2.40
Needleleaf Forest	199/ 319	0.2030	0.0843	0.0208	0.1796	0.1796	305.3	2.6	0.05	10.05	99.5	10.0							
Spring Grain	199/ 319	0.2340	0.0253	0.0341	0.4414	0.4507	25.8	2.1	3.10	2.85	8.8	0.3							
Winter Grain	199/ 319	0.3280	0.0222	0.0507	0.3511	0.3546	56.2	1.0	3.00	2.05	46.3	1.0							
Mixed Forest	199/ 320	0.4530	0.0000	0.0187	0.2673	0.2725	100.0	1.9	12.50	9.75	28.2	2.8	9.80	8.15	9.60	20.2	17.8	1.65	1.45
Needleleaf Forest	199/ 320	0.2190	0.0000	0.0150	0.1869	0.1811	100.0	3.2	12.50	12.50	0.0	0.0							
Grassland	199/ 320	0.0160	0.0000	0.0233	0.3883	0.4040	100.0	3.9	4.05	2.85	42.1	1.2							
Spring Grain	199/ 320	0.1720	0.0000	0.0323	0.4505	0.4340	100.0	3.8	4.05	2.85	42.1	1.2							
Winter Grain	199/ 320	0.0940	0.0000	0.0238	0.3836	0.4062	100.0	5.6	4.05	3.10	30.6	1.0							
Maize	199/ 320	0.0470	0.0000	0.0212	0.3600	0.3477	100.0	3.5	5.80	4.50	28.9	1.3							
Deciduous Forest	200/ 313	0.0310	0.0265	0.0264	0.4018	0.4456	0.4	9.8	5.30	5.65	6.2	0.4	10.60	9.90	9.95	7.1	0.5	0.70	0.05
Mixed Forest	200/ 313	0.5940	0.0166	0.0197	0.3380	0.3311	15.7	2.1	12.05	10.75	12.1	1.3							
Needleleaf Forest	200/ 313	0.2340	0.0196	0.0180	0.1944	0.1969	8.9	1.3	12.50	12.50	0.0	0.0							
Grassland	200/ 313	0.0630	0.0471	0.0347	0.4051	0.4422	35.7	8.4	2.00	2.55	21.6	0.6							
Spring Grain	200/ 313	0.0310	0.0344	0.0361	0.4502	0.4446	4.7	1.3	2.85	2.75	3.6	0.1							
Winter Grain	200/ 313	0.0160	0.0282	0.0142	0.3830	0.3587	98.6	6.8	2.85	3.35	14.9	0.5							
Maize	200/ 313	0.0310	0.0424	0.0238	0.3611	0.3741	78.2	3.5	3.55	4.45	20.2	0.9							
Deciduous Forest	200/ 314	0.1560	0.0289	0.0246	0.4075	0.4768	17.5	14.5	5.05	6.10	17.2	1.1	4.75	5.15	3.50	7.8	32.0	0.40	1.65
Mixed Forest	200/ 314	0.3120	0.0230	0.0220	0.2720	0.3014	4.5	9.8	8.20	9.30	11.8	1.1							
Grassland	200/ 314	0.1090	0.0592	0.0683	0.4004	0.3321	13.3	20.6	1.65	1.15	43.5	0.5							
Winter Grain	200/ 314	0.0160	0.0286	0.0348	0.3818	0.3654	17.8	4.5	2.85	2.60	9.6	0.3							
Maize	200/ 314	0.4060	0.0574	0.0571	0.3683	0.3381	0.5	8.9	3.00	2.80	7.1	0.2							
Maize	200/ 315	1.0000	0.0736	0.0736	0.3163	0.3163	0.0	0.0	2.10	2.10	0.0	0.0	2.10	2.10	2.10	0.0	0.0	0.00	0.00
Grassland	200/ 316	0.0630	0.0580	0.0792	0.3694	0.3336	26.8	10.7	1.55	0.95	63.2	0.6	1.80	1.85	2.05	2.7	10.8	0.05	0.20
Spring Grain	200/ 316	0.0630	0.0372	0.0409	0.4458	0.4350	9.0	2.5	2.75	2.60	5.8	0.2							
Winter Grain	200/ 316	0.0470	0.0292	0.0541	0.3745	0.3902	46.0	4.0	2.80	2.10	33.3	0.7							
Maize	200/ 316	0.8280	0.0855	0.0823	0.3163	0.3189	3.9	0.8	1.75	1.85	5.4	0.1							
Grassland	200/ 317	0.1250	0.0219	0.0658	0.3937	0.3895	226.6	1.1	0.10	1.45	93.1	1.4	2.75	2.30	2.30	19.6	0.0	0.45	0.00
Spring Grain	200/ 317	0.1250	0.0325	0.0433	0.4498	0.4281	24.9	5.1	2.90	2.55	13.7	0.4							
Winter Grain	200/ 317	0.7030	0.0211	0.0443	0.3980	0.4022	52.4	1.0	3.15	2.40	31.3	0.8							
Maize	200/ 317	0.0470	0.0420	0.0619	0.3599	0.3650	32.1	1.4	3.55	2.80	26.8	0.8							
Mixed Forest	200/ 318	0.2030	0.0697	0.0376	0.2420	0.2380	85.4	1.7	0.80	3.65	78.1	2.9	2.00	2.55	1.90	21.6	25.5	0.55	0.65
Needleleaf Forest	200/ 318	0.0310	0.0253	0.0186	0.1846	0.1791	36.0	3.1	8.05	12.10	33.5	4.1							
Spring Grain	200/ 318	0.0160	0.0387	0.0331	0.4485	0.4359	16.9	2.9	2.70	2.85	5.3	0.2							
Winter Grain	200/ 318	0.7500	0.0485	0.0577	0.3419	0.3435	15.9	0.5	2.10	1.85	15.5	0.3							
Mixed Forest	200/ 319	0.7810	0.0184	0.0190	0.2354	0.2367	3.2	0.5	8.80	8.60	2.3	0.2	9.15	9.30	8.15	1.6	12.4	0.15	1.15
Needleleaf Forest	200/ 319	0.2190	0.0210	0.0189	0.1836	0.1790	11.1	2.6	10.60	11.85	10.5	1.3							
Mixed Forest	200/ 320	0.2190	0.0195	0.0169	0.2582	0.2568	15.4	0.5	9.05	10.05	10.0	1.0	11.70	11.95	12.50	2.1	4.6	0.25	0.55
Needleleaf Forest	200/ 320	0.7810	0.0153	0.0161	0.1900	0.1904	5.0	0.2	12.50	12.50	0.0	0.0							
						Mean	40.3	8.9			36.2	0.8				22.0	25.8	0.48	0.65
						Max	305.4	100.0			470.0	10.							

Gut Huell area

(resolution 240m, row 177-184, col 325-333, one-based index)

Land Cover Type	Pixel row/col	area fraction	RED refseg	RED truth	NIR refseg	NIR truth	relErr RED [%]	relErr NIR [%]	LAI refseg [m ² /m ²]	LAI truth [m ² /m ²]	relErr LAI [%]	absErr LAI [m ² /m ²]	LAI sum refseg [m ² /m ²]	LAI sum truth [m ² /m ²]	LAI majority [m ² /m ²]	relErr LAI sum refseg [%]	relErr LAI sum majority [%]	absErr refseg [m ² /m ²]	absErr majority [m ² /m ²]
Grassland	177/ 325	0.0630	0.0515	0.0597	0.3737	0.3104	13.7	20.4	1.75	1.25	40.0	0.50	2.10	1.50	1.45	40.0	3.4	0.60	0.05
Winter Grain	177/ 325	0.7810	0.0284	0.0674	0.2998	0.3061	57.9	2.1	2.60	1.45	79.3	1.15	2.25	2.25	2.25	0.0	0.0	0.00	0.00
Maize	177/ 325	0.1090	0.3435	0.0622	0.3551	0.3381	452.3	5.0	0.00	2.65	100.0	2.65	2.35	2.30	2.30	2.2	0.0	0.05	0.00
Urban Fabric	177/ 325	0.0470	0.0893	0.0845	0.2445	0.2642	5.7	7.5	0.00	0.00	0.00	0.00	2.25	2.25	2.25	0.0	0.0	0.00	0.00
Winter Grain	177/ 326	1.0000	0.0406	0.0406	0.3179	0.3179	0.0	0.0	2.25	2.25	0.00	0.00	2.25	2.25	2.25	0.0	0.0	0.00	0.00
Grassland	177/ 327	0.0630	0.0582	0.0593	0.3862	0.3654	1.9	5.7	1.60	1.50	6.7	0.10	2.35	2.30	2.30	2.2	0.0	0.05	0.00
Winter Grain	177/ 327	0.8750	0.0439	0.0429	0.3734	0.3746	2.3	0.3	2.35	2.35	0.0	0.00	2.35	2.30	2.30	2.2	0.0	0.05	0.00
Maize	177/ 327	0.0630	0.0467	0.0593	0.3593	0.3638	21.2	1.2	3.35	2.90	15.5	0.45	2.90	2.90	2.90	0.0	0.0	0.00	0.00
Winter Grain	177/ 328	1.0000	0.0302	0.0301	0.4286	0.4285	0.3	0.0	2.90	2.90	0.00	0.00	2.90	2.90	2.90	0.0	0.0	0.00	0.00
Grassland	177/ 329	0.0160	0.0526	0.0646	0.3879	0.3040	18.6	27.6	1.80	1.10	63.6	0.70	2.55	2.50	2.55	2.0	2.0	0.05	0.05
Spring Grain	177/ 329	0.0160	0.0354	0.0532	0.4489	0.4732	33.5	5.1	2.80	2.40	16.7	0.40	2.55	2.50	2.55	2.0	2.0	0.05	0.05
Winter Grain	177/ 329	0.9530	0.0399	0.0394	0.3978	0.4006	1.3	0.7	2.55	2.55	0.0	0.00	2.55	2.50	2.55	2.0	2.0	0.05	0.05
Maize	177/ 329	0.0160	0.0440	0.0450	0.3596	0.2487	2.2	44.6	3.45	2.65	30.2	0.80	2.55	2.50	2.55	2.0	2.0	0.05	0.05
Mixed Forest	177/ 330	0.0330	0.0206	0.0372	0.2530	0.2727	44.6	7.2	8.50	4.65	82.8	3.85	2.30	1.60	1.40	43.8	14.3	0.70	0.20
Grassland	177/ 330	0.1480	0.0438	0.0692	0.3860	0.3990	36.7	3.3	2.05	1.40	46.4	0.65	2.30	1.60	1.40	43.8	14.3	0.70	0.20
Spring Grain	177/ 330	0.0980	0.0334	0.0591	0.4486	0.4347	43.5	3.2	2.85	2.15	32.6	0.70	2.30	1.60	1.40	43.8	14.3	0.70	0.20
Winter Grain	177/ 330	0.3440	0.0255	0.0595	0.3794	0.3846	57.1	1.4	2.95	1.95	51.3	1.00	2.30	1.60	1.40	43.8	14.3	0.70	0.20
Maize	177/ 330	0.1310	0.0401	0.0572	0.3592	0.3648	29.9	1.5	3.60	2.95	22.0	0.65	2.30	1.60	1.40	43.8	14.3	0.70	0.20
Bare Soil	177/ 330	0.0980	0.4471	0.1596	0.3170	0.3039	180.1	4.3	0.00	0.00	0.00	0.00	2.30	1.60	1.40	43.8	14.3	0.70	0.20
Urban Fabric	177/ 330	0.1480	0.0713	0.1202	0.2471	0.2528	40.7	2.3	0.00	0.00	0.00	0.00	2.30	1.60	1.40	43.8	14.3	0.70	0.20
Mixed Forest	177/ 331	0.0160	0.0208	0.0291	0.2539	0.3340	28.5	24.0	8.45	7.95	6.3	0.50	2.85	2.55	2.50	11.8	2.0	0.30	0.05
Grassland	177/ 331	0.0310	0.4302	0.0308	0.3903	0.6039	1298.8	35.4	0.00	3.00	100.0	3.00	2.85	2.55	2.50	11.8	2.0	0.30	0.05
Spring Grain	177/ 331	0.4530	0.0351	0.0478	0.4559	0.4439	26.6	2.7	2.85	2.45	16.3	0.40	2.85	2.55	2.50	11.8	2.0	0.30	0.05
Winter Grain	177/ 331	0.5000	0.0284	0.0416	0.4038	0.3988	31.7	1.3	2.90	2.50	16.0	0.40	2.85	2.55	2.50	11.8	2.0	0.30	0.05
Deciduous Forest	177/ 332	0.0350	0.0000	0.0179	0.3957	0.4240	100.0	6.7	9.90	6.65	48.9	3.25	9.65	7.90	9.70	22.2	18.6	1.75	1.80
Mixed Forest	177/ 332	0.3510	0.0000	0.0194	0.5492	0.2652	100.0	107.1	12.50	9.30	34.4	3.20	9.65	7.90	9.70	22.2	18.6	1.75	1.80
Needleleaf Forest	177/ 332	0.2810	0.0000	0.0118	0.1842	0.1661	100.0	10.9	12.50	12.50	0.00	0.00	9.65	7.90	9.70	22.2	18.6	1.75	1.80
Grassland	177/ 332	0.0700	0.0000	0.0305	0.3856	0.5285	100.0	27.0	4.05	2.85	42.1	1.20	9.65	7.90	9.70	22.2	18.6	1.75	1.80
Spring Grain	177/ 332	0.0350	0.0000	0.0442	0.4485	0.4444	100.0	0.9	4.05	2.55	58.8	1.50	9.65	7.90	9.70	22.2	18.6	1.75	1.80
Winter Grain	177/ 332	0.1930	0.0000	0.0380	0.0942	0.3975	100.0	76.3	4.05	2.60	55.8	1.45	9.65	7.90	9.70	22.2	18.6	1.75	1.80
Maize	177/ 332	0.0350	0.0000	0.0232	0.3592	0.2867	100.0	25.3	5.80	4.15	39.8	1.65	9.65	7.90	9.70	22.2	18.6	1.75	1.80
Winter Grain	178/ 325	1.0000	0.0502	0.0502	0.3590	0.3591	0.0	0.0	2.10	2.10	0.00	0.00	2.10	2.10	2.10	0.0	0.0	0.00	0.00
Winter Grain	178/ 326	1.0000	0.0325	0.0324	0.3481	0.3480	0.3	0.0	2.60	2.60	0.00	0.00	2.60	2.60	2.60	0.0	0.0	0.00	0.00
Mixed Forest	178/ 327	0.3750	0.0231	0.0286	0.2795	0.3576	19.2	21.8	8.35	8.60	2.9	0.25	4.80	4.85	2.75	1.0	76.4	0.05	2.10
Grassland	178/ 327	0.0310	0.0534	0.0389	0.3917	0.3844	37.3	1.9	1.75	2.20	20.5	0.45	4.80	4.85	2.75	1.0	76.4	0.05	2.10
Winter Grain	178/ 327	0.5940	0.0344	0.0316	0.4204	0.3715	8.9	13.2	2.75	2.70	1.9	0.05	4.80	4.85	2.75	1.0	76.4	0.05	2.10
Mixed Forest	178/ 328	0.2660	0.0197	0.0359	0.6594	0.4047	45.1	62.9	12.50	7.85	59.2	4.65	5.10	3.95	2.55	29.1	54.9	1.15	1.40
Grassland	178/ 328	0.0780	0.2157	0.0408	0.3562	0.4169	428.7	14.6	0.05	2.25	97.8	2.20	5.10	3.95	2.55	29.1	54.9	1.15	1.40
Spring Grain	178/ 328	0.1250	0.0334	0.0553	0.4407	0.4057	39.6	8.6	2.85	2.15	32.6	0.70	5.10	3.95	2.55	29.1	54.9	1.15	1.40
Winter Grain	178/ 328	0.4840	0.0252	0.0387	0.2710	0.4090	34.9	33.7	2.65	2.60	1.9	0.05	5.10	3.95	2.55	29.1	54.9	1.15	1.40
Maize	178/ 328	0.0470	0.0425	0.0432	0.3561	0.3653	1.6	2.5	3.50	3.50	0.00	0.00	5.10	3.95	2.55	29.1	54.9	1.15	1.40
Spring Grain	178/ 329	0.4530	0.0000	0.0482	0.4488	0.4170	100.0	7.6	4.05	2.35	72.3	1.70	4.05	2.40	2.45	68.8	2.0	1.65	0.05
Winter Grain	178/ 329	0.5470	0.0000	0.0425	0.3809	0.4072	100.0	6.5	4.05	2.50	62.0	1.55	4.05	2.40	2.45	68.8	2.0	1.65	0.05
Winter Grain	178/ 330	0.9520	0.0332	0.0351	0.3731	0.3730	5.4	0.0	2.65	2.60	1.9	0.05	2.60	2.55	2.60	2.0	1.9	0.05	0.05
Maize	178/ 330	0.0320	0.0439	0.0388	0.3594	0.3504	13.1	2.6	3.45	3.65	5.5	0.20	2.60	2.55	2.60	2.0	1.9	0.05	0.05
Bare Soil	178/ 330	0.0160	0.1493	0.0390	0.3174	0.3561	282.8	10.9	0.00	0.00	0.00	0.00	2.60	2.55	2.60	2.0	1.9	0.05	0.05
Spring Grain	178/ 331	0.1410	0.0381	0.0483	0.4480	0.4062	21.1	10.3	2.70	2.30	17.4	0.40	2.50	2.55	2.55	2.0	0.0	0.05	0.00
Winter Grain	178/ 331	0.8590	0.0377	0.0360	0.3673	0.3742	4.7	1.8	2.50	2.60	3.8	0.10	2.50	2.55	2.55	2.0	0.0	0.05	0.00
Mixed Forest	178/ 332	0.3440	0.0241	0.0213	0.2620	0.2601	13.1	0.7	7.55	8.45	10.7	0.90	5.15	5.80	2.60	11.2	123.1	0.65	3.20
Needleleaf Forest	178/ 332	0.1250	0.0237	0.0190	0.1859	0.1856	24.7	0.2	9.05	12.30	26.4	3.25	5.15	5.80	2.60	11.2	123.1	0.65	3.20
Winter Grain	178/ 332	0.4840	0.0359	0.0402	0.3926	0.3966	10.7	1.0	2.65	2.50	6.0	0.15	5.15	5.80	2.60	11.2	123.1	0.65	3.20
Maize	178/ 332	0.0470	0.0456	0.0346	0.3599	0.3339	31.8	7.8	3.40	3.75	9.3	0.35	5.15	5.80	2.60	11.2	123.1	0.65	3.20
Mixed Forest	179/ 325	0.1250	0.0224	0.0218	0.2528	0.2372	2.8	6.6	7.85	7.55	4.0	0.30	3.20	3.25	2.35	1.5	38.3	0.05	0.90
Needleleaf Forest	179/ 325	0.0310	0.0226	0.0182	0.1850	0.1864	24.2	0.8	9.65	12.50	22.8	2.85	3.20	3.25	2.35	1.5	38.3	0.05	0.90
Grassland	179/ 325	0.0160	0.0535	0.0357	0.3872	0.3863	49.9	0.2	1.75	2.30	23.9	0.55	3.20	3.25	2.35	1.5	38.3	0.05	0.90
Spring Grain	179/ 325	0.0310	0.0364	0.0405	0.4487	0.4142	10.1	8.3	2.80	2.55	9.8	0.25	3.20	3.25	2.35	1.5	38.3	0.05	0.90
Winter Grain	179/ 325	0.7970	0.0453	0.0457	0.3782	0.3820	0.9	1.0	2.30	2.30	0.00	0.00	3.20	3.25	2.35	1.5	38.3	0.05	0.90
Grassland	179/ 326	0.0160	0.0539	0.0587	0.3880	0.4209	8.2	7.8	1.75	1.75	0.0	0.00	2.20	2.15	2.20	2.3	2.3	0.05	0.05
Spring Grain	179/ 326	0.0310	0.0367	0.0631	0.4490	0.4041	41.8	11.1	2.75	1.95	41.0	0.80	2.20	2.15	2.20	2.3	2.3	0.05	0.05
Winter Grain	179/ 326	0.9380	0.0525	0.0514	0.4001	0.4010	2.1	0.2	2.20	2.20	0.0	0.00	2.20	2.15	2.20	2.3	2.3	0.05	0.05
Maize	179/ 326	0.0160	0.0446	0.0552	0.3596	0.3659	19.2	1.7</											

Land Cover Type	Pixel row/col	area fraction	RED refseg	RED truth	NIR refseg	NIR truth	relErr RED [%]	relErr NIR [%]	LAI refseg [m ² /m ²]	LAI truth [m ² /m ²]	relErr LAI [%]	absErr LAI [m ² /m ²]	LAI sum refseg [m ² /m ²]	LAI sum truth [m ² /m ²]	LAI majority [m ² /m ²]	relErr LAI sum refseg [%]	relErr LAI sum majority [%]	absErr refseg [m ² /m ²]	absErr majority [m ² /m ²]
Mixed Forest	179/ 330	0.6410	0.0251	0.0215	0.2775	0.2759	16.7	0.6	7.70	8.80	12.5	1.10	5.90	6.55	7.80	9.9	16.0	0.65	1.25
Grassland	179/ 330	0.0160	0.0525	0.0461	0.3885	0.3892	13.9	0.2	1.80	2.00	10.0	0.20							
Spring Grain	179/ 330	0.0160	0.0354	0.0428	0.4490	0.4158	17.3	8.0	2.80	2.50	12.0	0.30							
Winter Grain	179/ 330	0.2970	0.0316	0.0397	0.3915	0.3989	20.4	1.9	2.80	2.55	9.8	0.25							
Maize	179/ 330	0.0310	0.0444	0.0412	0.3599	0.3410	7.8	5.5	3.45	3.50	1.4	0.05							
Mixed Forest	179/ 331	0.1410	0.0201	0.0254	0.2488	0.2588	20.9	3.9	8.55	7.05	21.3	1.50	3.40	2.75	2.00	23.6	37.5	0.65	0.75
Grassland	179/ 331	0.1410	0.2153	0.0775	0.3786	0.3863	177.8	2.0	0.05	1.20	95.8	1.15							
Winter Grain	179/ 331	0.6090	0.0236	0.0544	0.3629	0.3634	56.6	0.1	3.00	2.00	50.0	1.00							
Maize	179/ 331	0.1090	0.0409	0.0392	0.3582	0.3330	4.3	7.6	3.60	3.50	2.9	0.10							
Mixed Forest	179/ 332	0.7500	0.0188	0.0206	0.2835	0.2837	8.7	0.1	10.00	9.35	7.0	0.65	8.20	7.75	9.35	5.8	17.1	0.45	1.60
Grassland	179/ 332	0.0310	0.0507	0.0418	0.3898	0.4198	21.3	7.1	1.85	2.20	15.9	0.35							
Spring Grain	179/ 332	0.0160	0.0349	0.0291	0.4490	0.4701	19.9	4.5	2.80	3.05	8.2	0.25							
Winter Grain	179/ 332	0.1720	0.0277	0.0244	0.3874	0.3868	13.5	0.2	2.90	3.00	3.3	0.10							
Maize	179/ 332	0.0310	0.0430	0.0305	0.3599	0.3172	41.0	13.5	3.50	3.85	9.1	0.35							
Mixed Forest	180/ 325	0.2030	0.0674	0.0245	0.2689	0.2801	175.1	4.0	1.25	7.95	84.3	6.70	2.55	3.85	2.35	33.8	63.8	1.30	1.50
Needleleaf Forest	180/ 325	0.0470	0.0293	0.0209	0.1861	0.1831	40.2	1.6	6.25	10.65	41.3	4.40							
Spring Grain	180/ 325	0.0630	0.0683	0.0502	0.4503	0.4377	36.1	2.9	2.00	2.35	14.9	0.35							
Winter Grain	180/ 325	0.6410	0.0345	0.0525	0.4279	0.4253	34.3	0.6	2.80	2.25	24.4	0.55							
Maize	180/ 325	0.0470	0.0667	0.0390	0.3608	0.3695	71.0	2.4	2.60	3.70	29.7	1.10							
Mixed Forest	180/ 326	0.2660	0.0923	0.0285	0.2797	0.2912	223.9	3.9	0.50	7.10	93.0	6.60	2.25	3.55	2.35	36.6	51.1	1.30	1.20
Grassland	180/ 326	0.0160	0.0515	0.0295	0.3904	0.4146	74.6	5.8	1.80	2.65	32.1	0.85							
Spring Grain	180/ 326	0.0940	0.0351	0.0493	0.4518	0.4452	28.8	1.5	2.80	2.40	16.7	0.40							
Winter Grain	180/ 326	0.6250	0.0284	0.0539	0.4400	0.4355	47.3	1.0	3.00	2.25	33.3	0.75							
Mixed Forest	180/ 327	1.0000	0.0293	0.0292	0.3509	0.3508	0.3	0.0	8.30	8.30	0.0	0.00	8.30	8.30	8.30	0.0	0.0	0.00	0.00
Mixed Forest	180/ 328	0.8440	0.0239	0.0249	0.2866	0.2892	4.0	0.9	8.30	8.05	3.1	0.25	8.15	8.25	7.80	1.2	5.8	0.10	0.45
Needleleaf Forest	180/ 328	0.1090	0.0226	0.0181	0.1862	0.1889	24.9	1.4	9.75	12.50	22.0	2.75							
Grassland	180/ 328	0.0310	0.0526	0.0511	0.3897	0.3370	2.9	15.6	1.80	1.60	12.5	0.20							
Maize	180/ 328	0.0160	0.0437	0.0233	0.3597	0.3078	87.6	16.9	3.45	4.20	17.9	0.75							
Mixed Forest	180/ 329	0.2340	0.0200	0.0206	0.2556	0.2451	2.9	4.3	8.80	8.25	6.7	0.55	11.60	11.50	12.50	0.9	8.0	0.10	1.00
Needleleaf Forest	180/ 329	0.7660	0.0182	0.0181	0.1872	0.1905	0.6	1.7	12.50	12.50	0.0	0.00							
Mixed Forest	180/ 330	0.9690	0.0242	0.0238	0.2508	0.2519	1.7	0.4	7.20	7.35	2.0	0.15	7.15	7.30	7.20	2.1	1.4	0.15	0.10
Needleleaf Forest	180/ 330	0.0160	0.0221	0.0203	0.1850	0.1923	8.9	3.8	10.00	11.85	15.6	1.85							
Winter Grain	180/ 330	0.0160	0.0285	0.0602	0.3808	0.3071	52.7	24.0	2.85	1.60	78.1	1.25							
Mixed Forest	180/ 331	0.2810	0.1676	0.0251	0.2439	0.2655	567.7	8.1	0.00	7.35	100.0	7.35	1.50	2.70	0.90	44.4	200.0	1.20	1.80
Grassland	180/ 331	0.4840	0.0515	0.0985	0.3555	0.3550	47.7	0.1	1.70	0.70	142.9	1.00							
Winter Grain	180/ 331	0.1720	0.0284	0.1315	0.3755	0.3556	78.4	5.6	2.85	0.65	338.5	2.20							
Maize	180/ 331	0.0630	0.0434	0.0362	0.3587	0.3206	19.9	11.9	3.45	3.60	4.2	0.15							
Mixed Forest	180/ 332	0.7810	0.0193	0.0204	0.2931	0.2913	5.4	0.6	10.05	9.60	4.7	0.45	10.15	10.20	9.25	0.5	10.3	0.05	0.95
Needleleaf Forest	180/ 332	0.2190	0.0214	0.0174	0.1882	0.1944	23.0	3.2	10.70	12.50	14.4	1.80							
Mixed Forest	181/ 325	0.5470	0.0217	0.0233	0.3136	0.3115	6.9	0.7	9.70	9.10	6.6	0.60	9.35	9.85	8.25	5.1	19.4	0.50	1.60
Needleleaf Forest	181/ 325	0.3750	0.0229	0.0190	0.1967	0.1951	20.5	0.8	10.35	12.50	17.2	2.15							
Grassland	181/ 325	0.0160	0.0517	0.0262	0.3907	0.4011	97.3	2.6	1.80	2.75	34.5	0.95							
Spring Grain	181/ 325	0.0160	0.0352	0.0422	0.4493	0.4457	16.6	0.8	2.80	2.60	7.7	0.20							
Winter Grain	181/ 325	0.0470	0.0285	0.0475	0.3858	0.4217	40.0	8.5	2.85	2.40	18.8	0.45							
Deciduous Forest	181/ 326	0.0310	0.0276	0.0232	0.4004	0.4434	19.0	9.7	5.15	6.05	14.9	0.90	6.70	6.60	7.65	1.5	13.7	0.10	1.05
Mixed Forest	181/ 326	0.7970	0.0310	0.0315	0.3382	0.3375	1.6	0.2	7.60	7.45	2.0	0.15							
Grassland	181/ 326	0.0160	0.0534	0.0294	0.3906	0.3042	81.6	28.4	1.75	2.25	22.2	0.50							
Winter Grain	181/ 326	0.1250	0.0309	0.0358	0.3935	0.4158	13.7	5.4	2.80	2.70	3.7	0.10							
Maize	181/ 326	0.0310	0.0453	0.0278	0.3607	0.2899	62.9	24.4	3.40	3.85	11.7	0.45							
Mixed Forest	181/ 327	0.9530	0.0248	0.0254	0.3102	0.3124	2.4	0.7	8.60	8.50	1.2	0.10	8.55	8.55	8.45	0.0	1.2	0.00	0.10
Needleleaf Forest	181/ 327	0.0310	0.0222	0.0168	0.1856	0.1906	32.1	2.6	9.95	12.50	20.4	2.55							
Maize	181/ 327	0.0160	0.0437	0.0203	0.3598	0.2154	115.3	67.0	3.45	3.90	11.5	0.45							
Mixed Forest	181/ 328	0.9690	0.0267	0.0274	0.3634	0.3649	2.6	0.4	9.25	9.10	1.6	0.15	9.05	8.95	9.10	1.1	1.6	0.10	0.15
Maize	181/ 328	0.0310	0.0443	0.0218	0.3607	0.3155	103.2	14.3	3.45	4.35	20.7	0.90							
Mixed Forest	181/ 329	0.7500	0.0184	0.0194	0.2513	0.2501	5.2	0.5	9.25	8.85	4.5	0.40	9.50	9.60	8.55	1.0	12.3	0.10	1.05
Needleleaf Forest	181/ 329	0.2340	0.0209	0.0175	0.1849	0.1875	19.4	1.4	10.80	12.50	13.6	1.70							
Winter Grain	181/ 329	0.0160	0.0283	0.0328	0.3808	0.3954	13.7	3.7	2.85	2.75	3.6	0.10							
Mixed Forest	181/ 330	0.5970	0.0205	0.0211	0.2502	0.2578	2.8	2.9	8.45	8.45	0.0	0.00	7.40	7.75	4.80	4.5	61.5	0.35	2.95
Needleleaf Forest	181/ 330	0.1940	0.0219	0.0178	0.1848	0.1881	23.0	1.8	10.10	12.50	19.2	2.40							
Grassland	181/ 330	0.0650	0.2180	0.1174	0.3866	0.3538	85.7	9.3	0.05	0.50	90.0	0.45							
Winter Grain	181/ 330	0.1130	0.0283	0.0699	0.3803	0.3416	59.5	11.3	2.85	1.55	83.9	1.30							
Maize	181/ 330	0.0320	0.0434	0.0604	0.3594	0													

Appendix 7: Gallery of results from reflectance segmentation / LAI algorithm

Reflectances

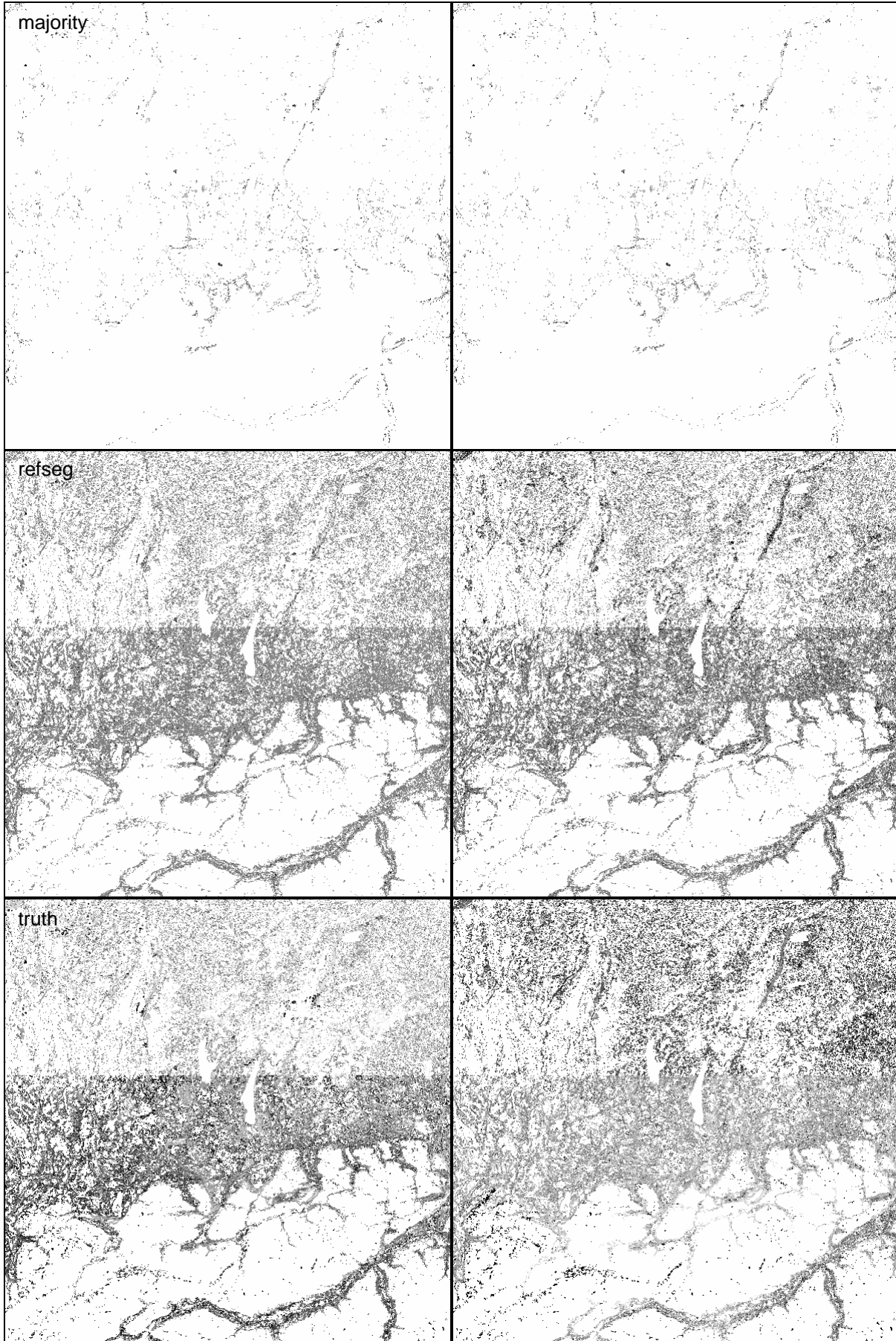
[next page]

Reflectance of LCT1: Deciduous Forest



RED

NIR

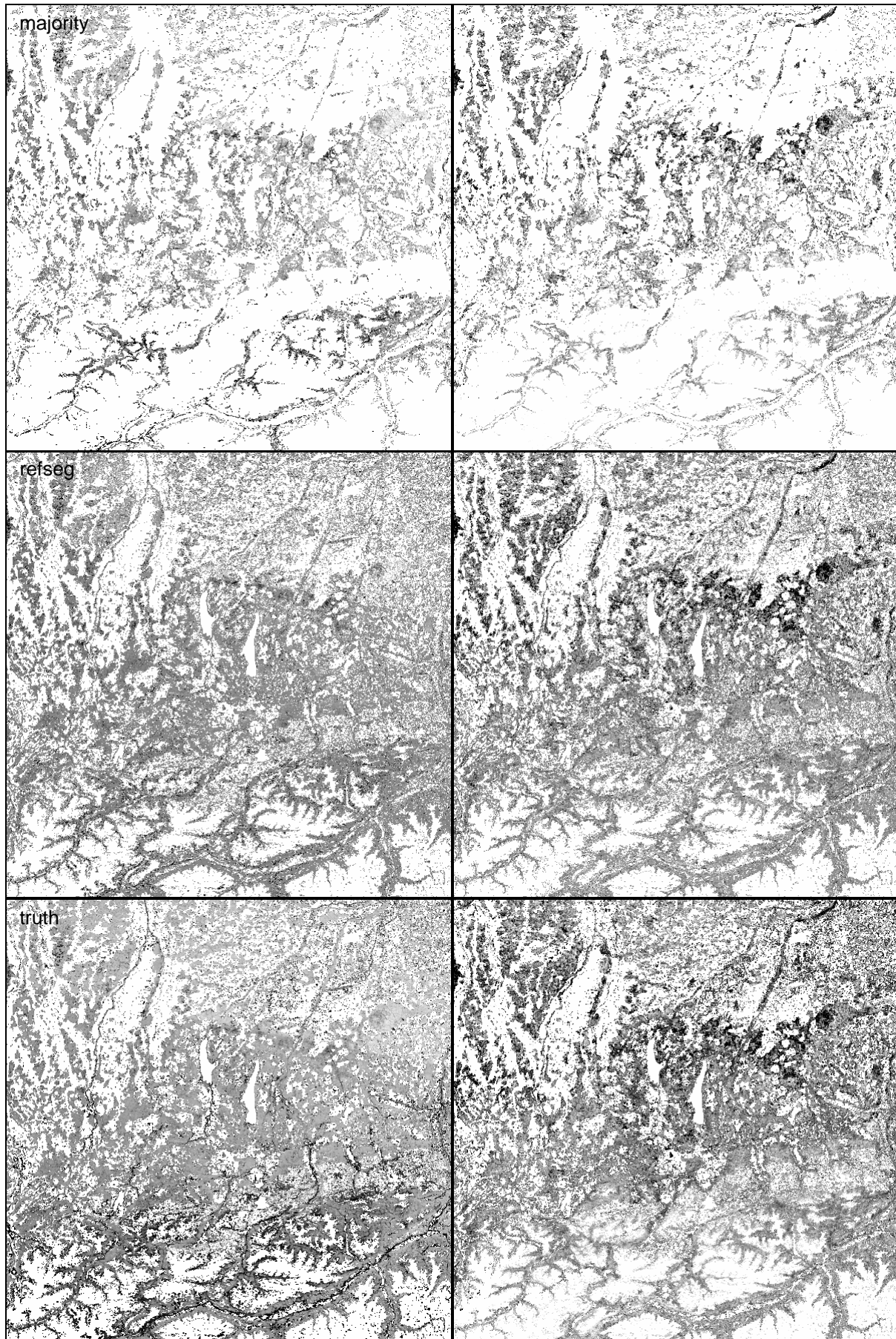


Reflectance of LCT2: Mixed Forest



RED

NIR

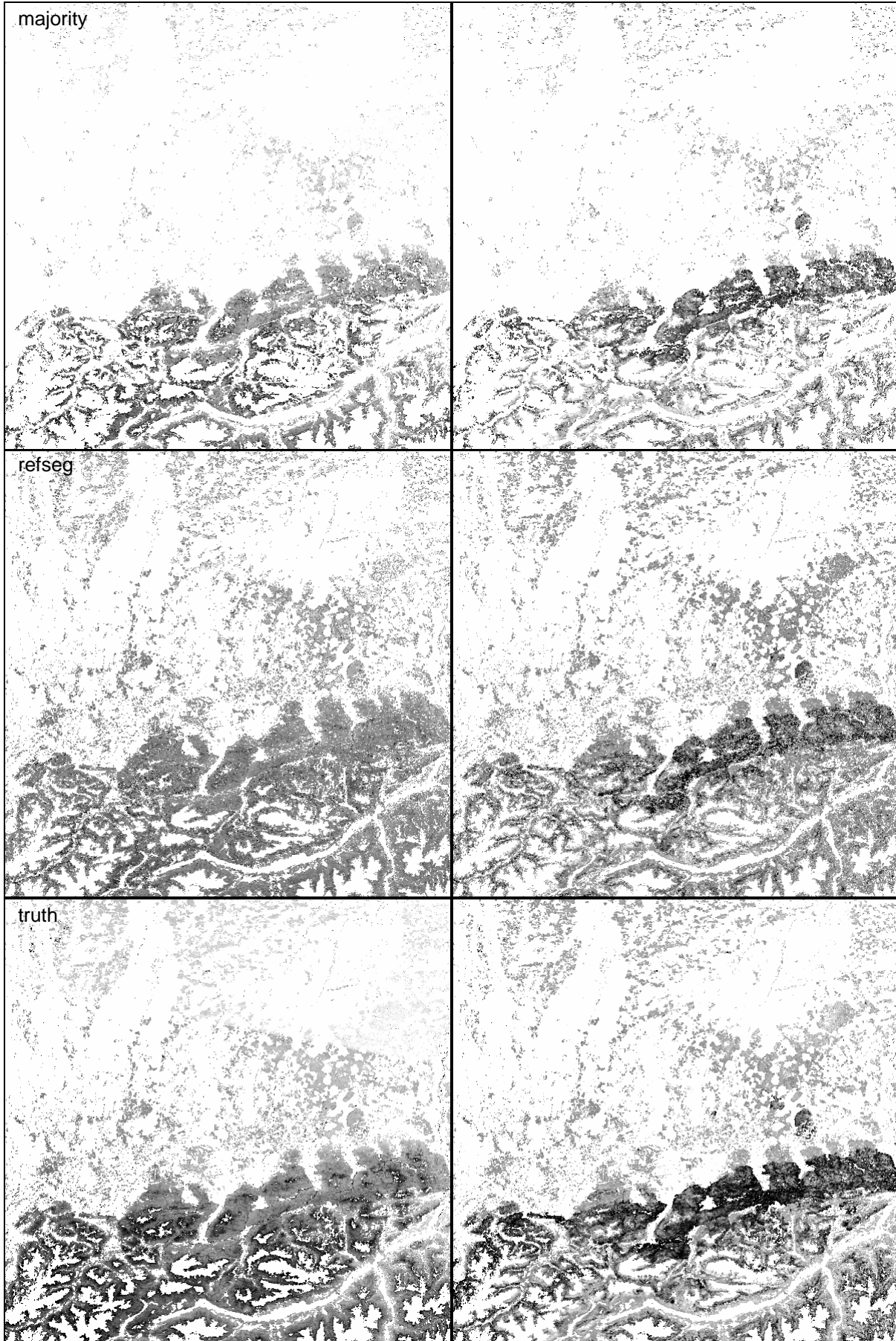


Reflectance of LCT3: Needleleaf Forest



RED

NIR

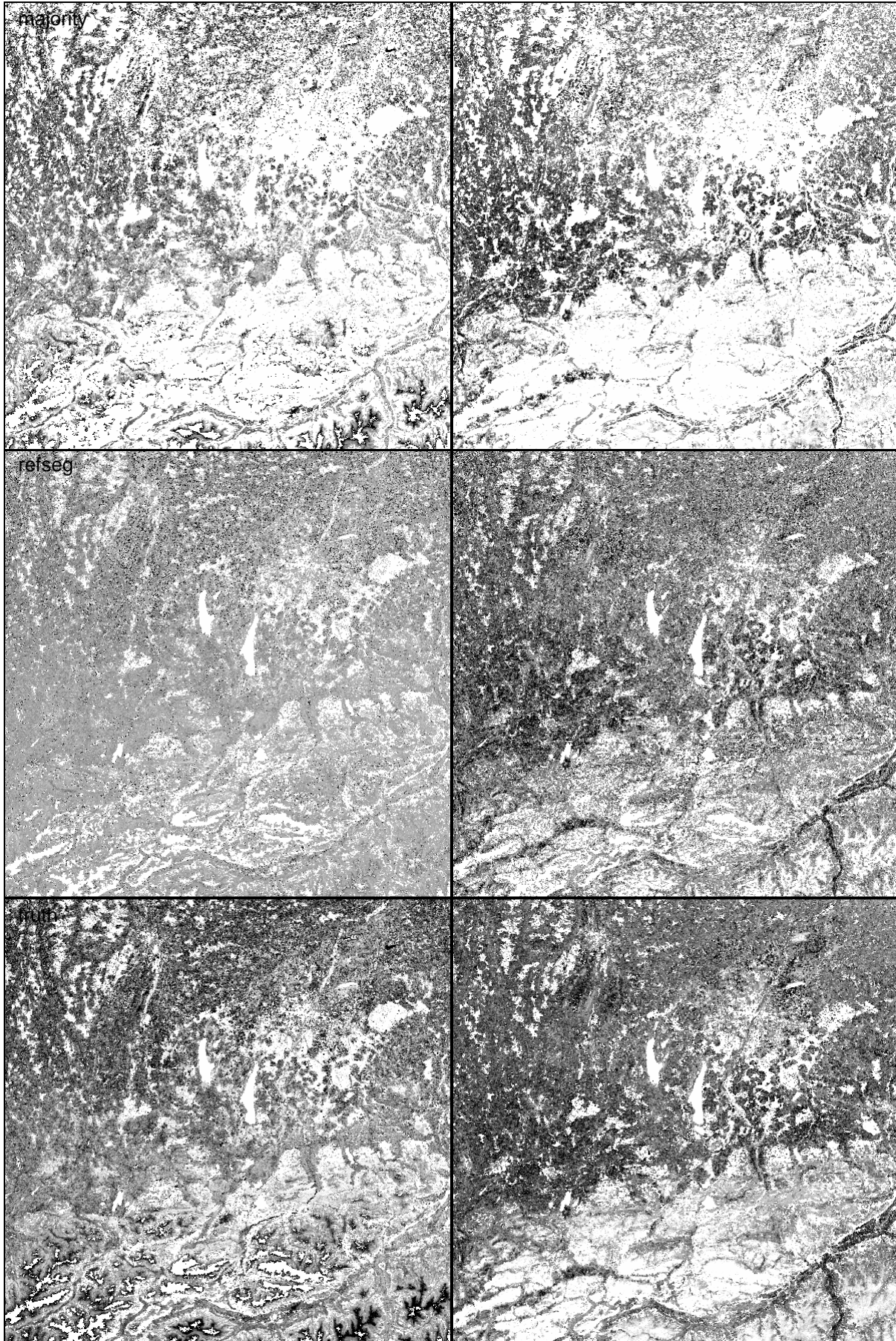


Reflectance of LCT4: Grassland



RED

NIR

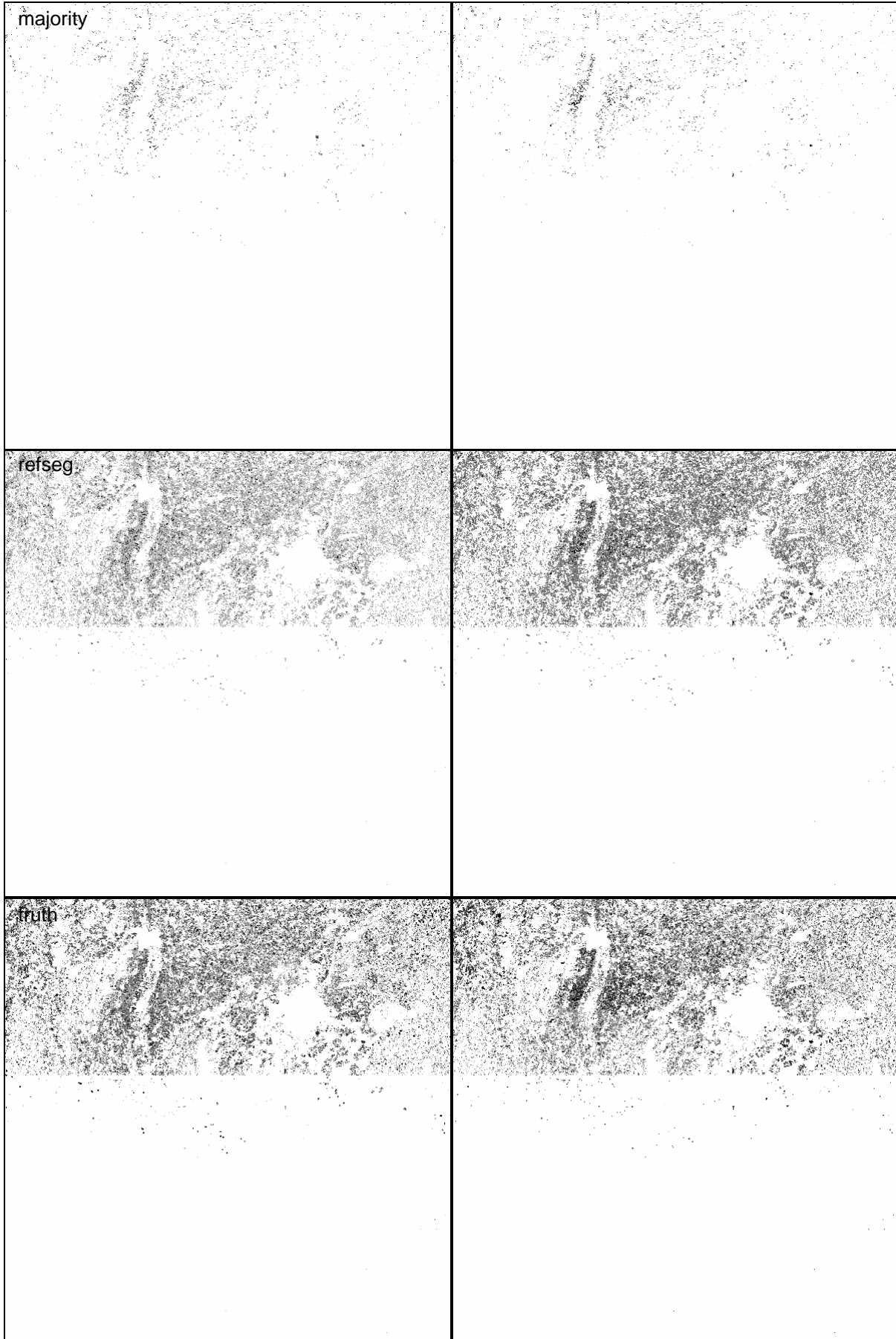


Reflectance of LCT5: Spring Grain



RED

NIR

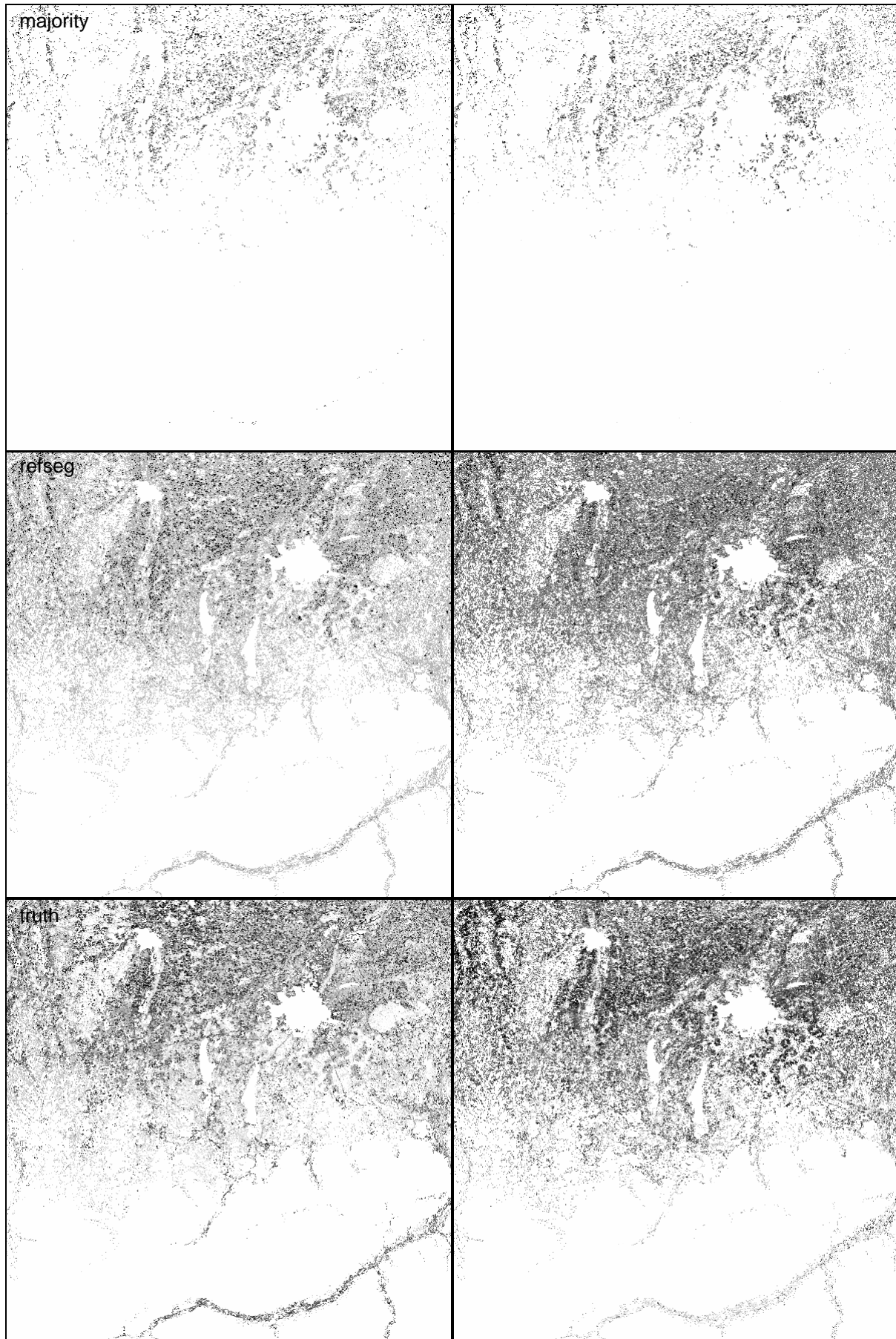


Reflectance of LCT6: Winter Grain



RED

NIR

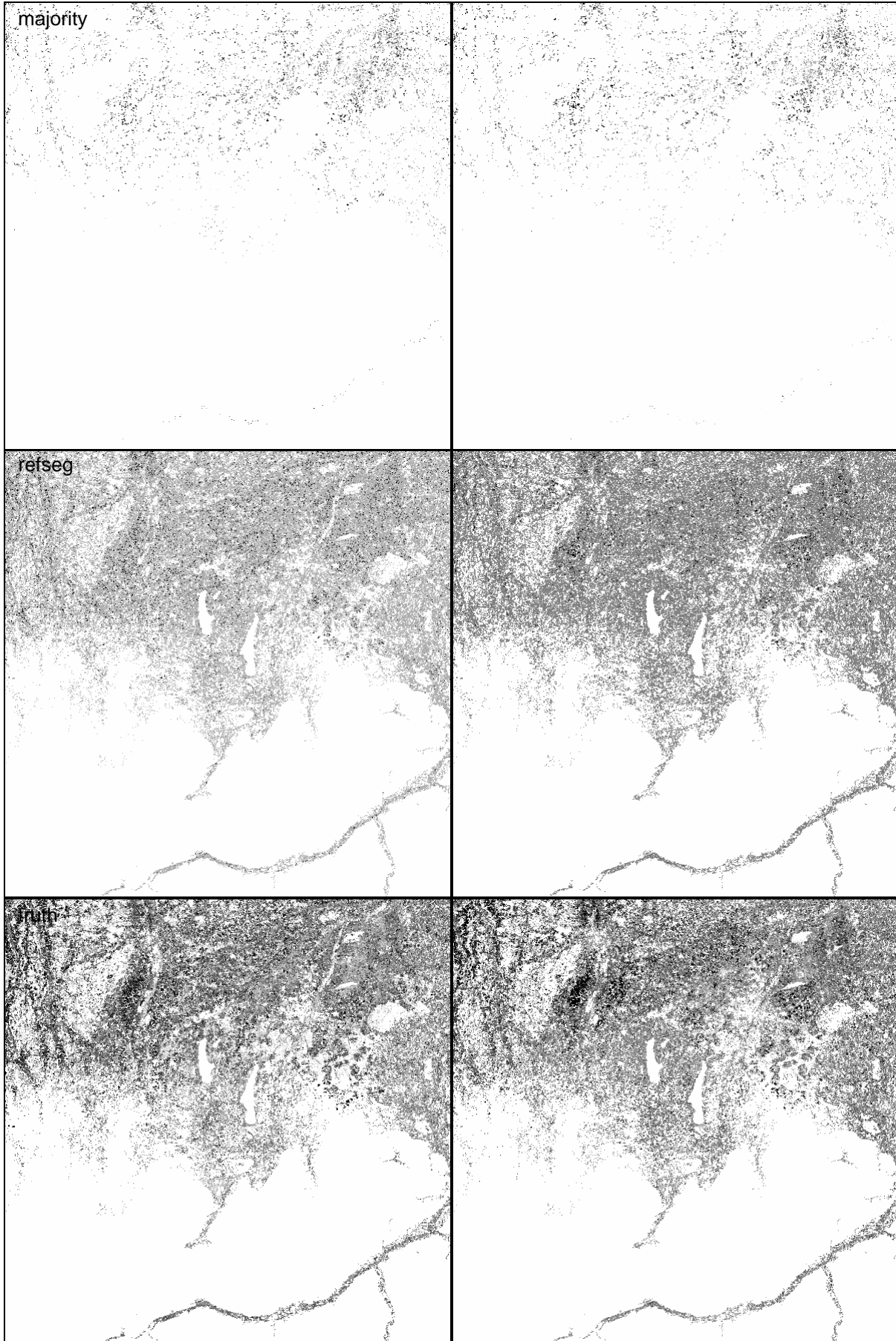


Reflectance of LCT7: Maize



RED

NIR

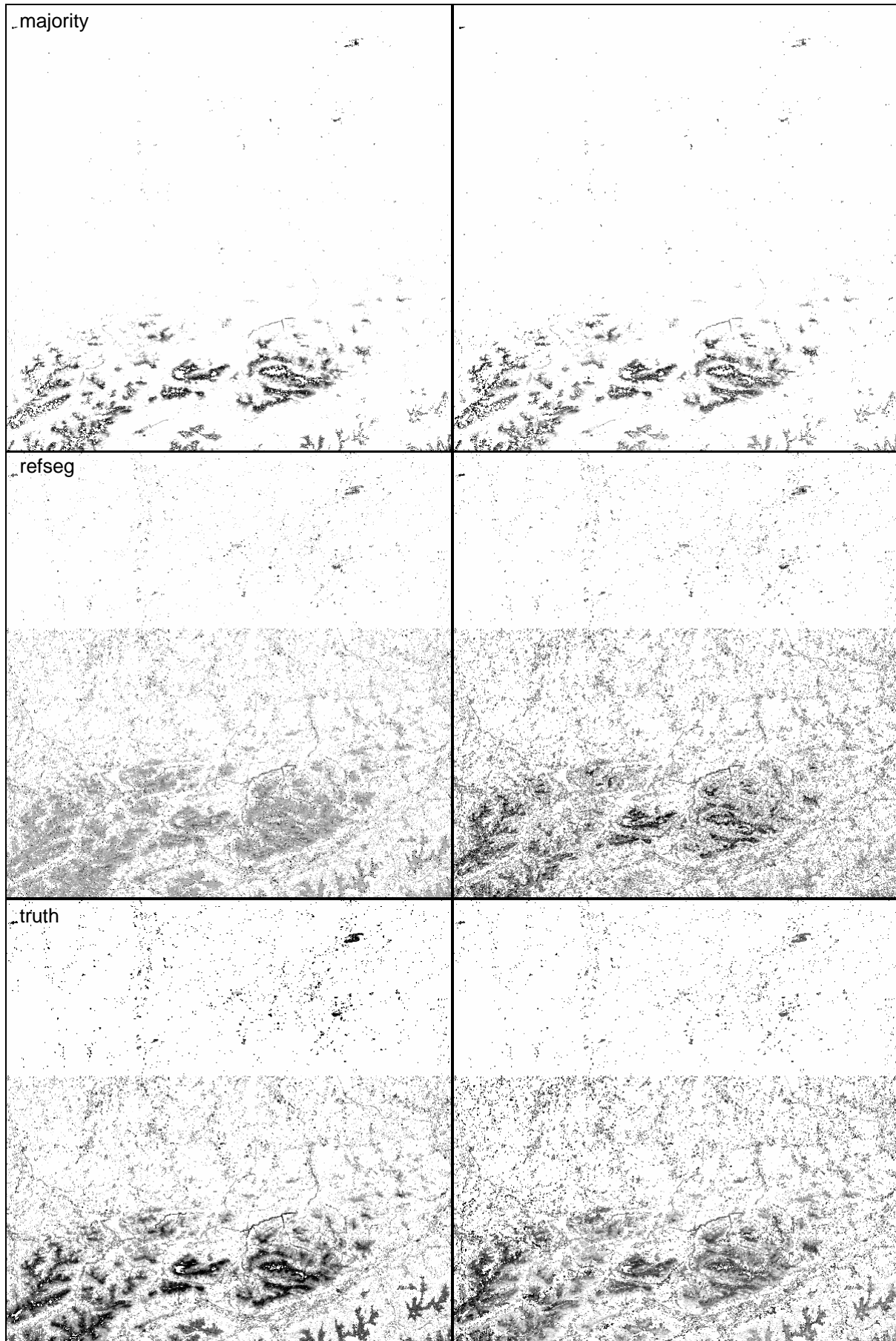


Reflectance of LCT8: Rock



RED

NIR

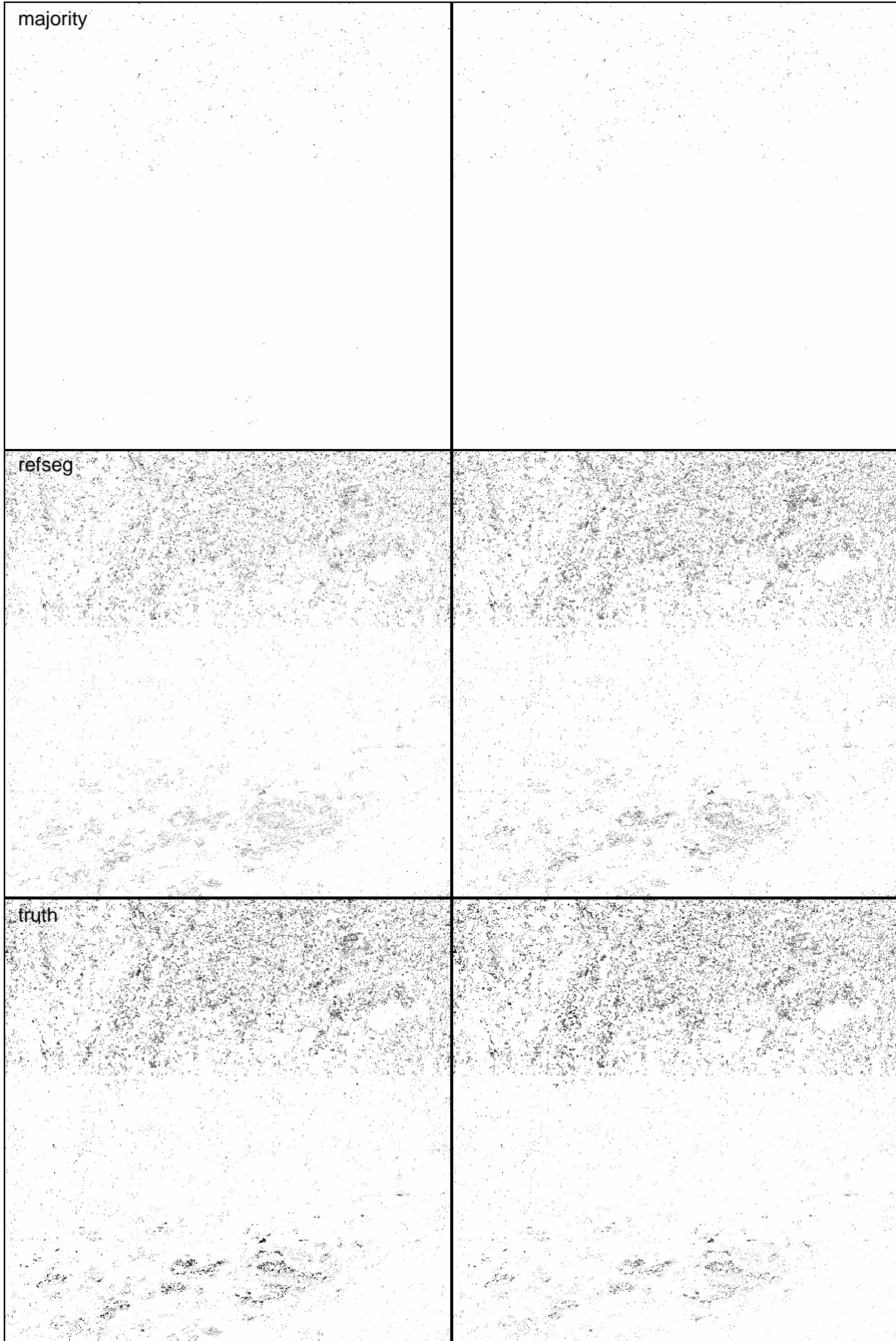


Reflectance of LCT9: Bare Soil



RED

NIR

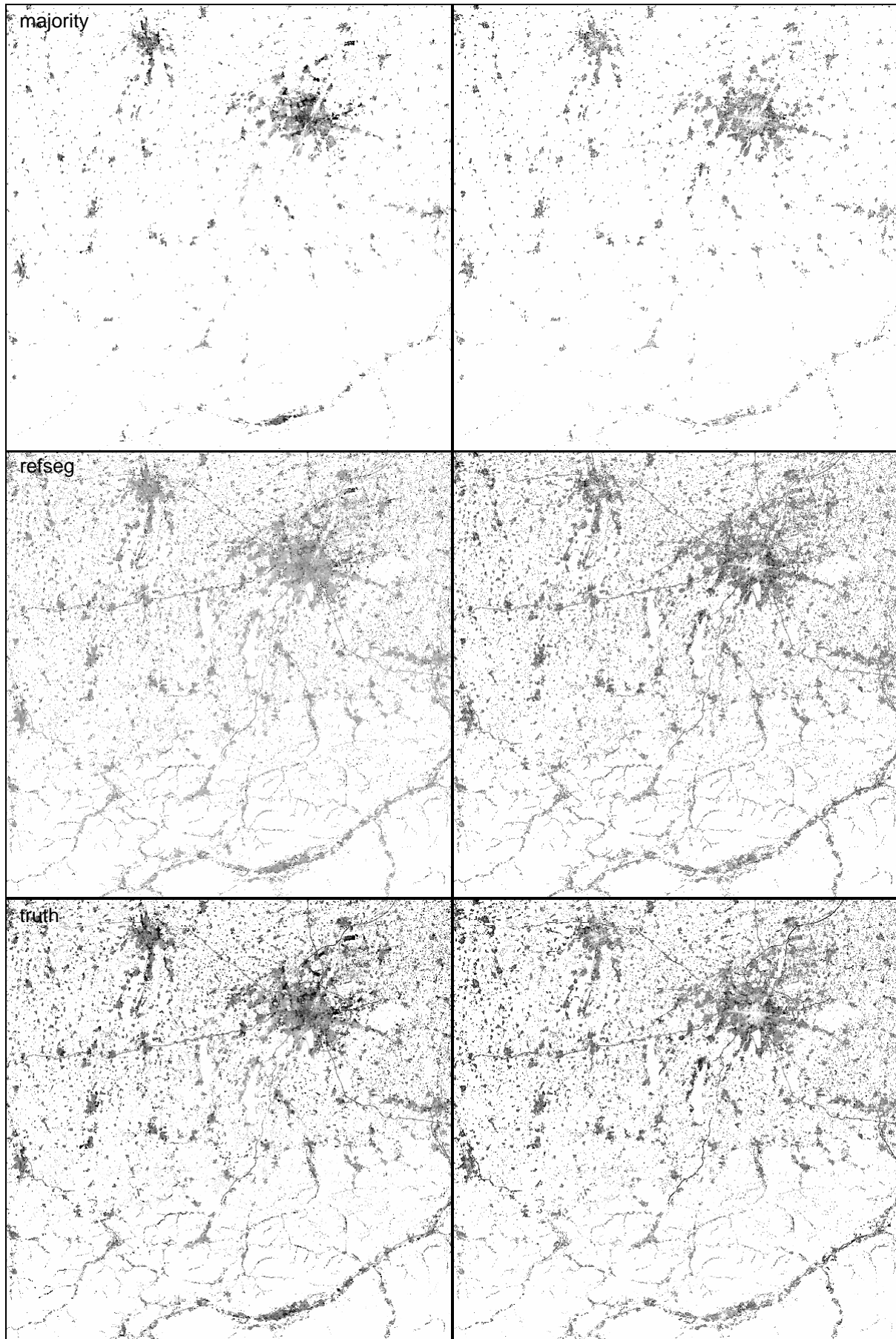


Reflectance of LCT10: Urban Fabric



RED

NIR

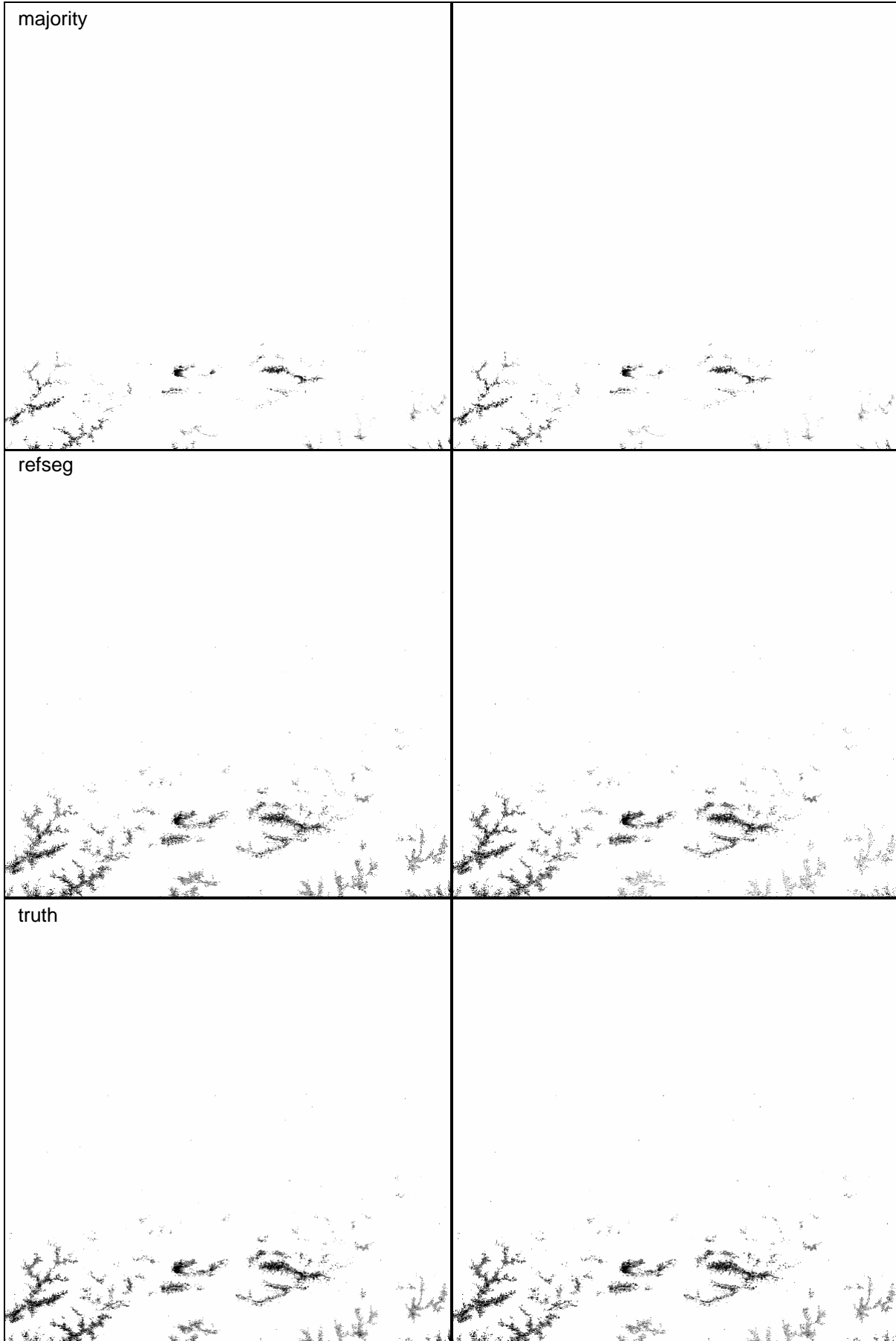


Reflectance of LCT11: Snow and Ice



RED

NIR

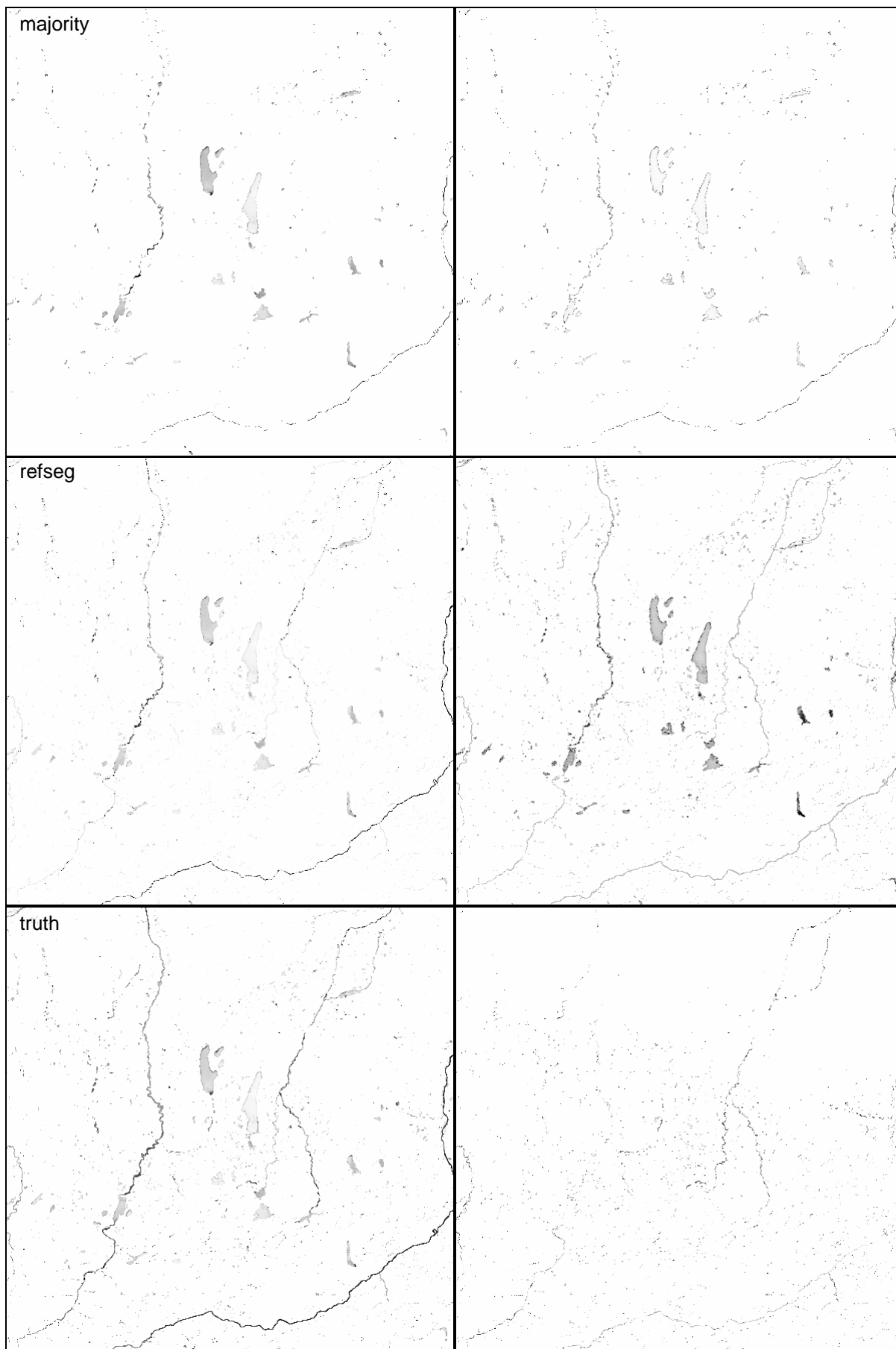


Reflectance of LCT12: Water



RED

NIR

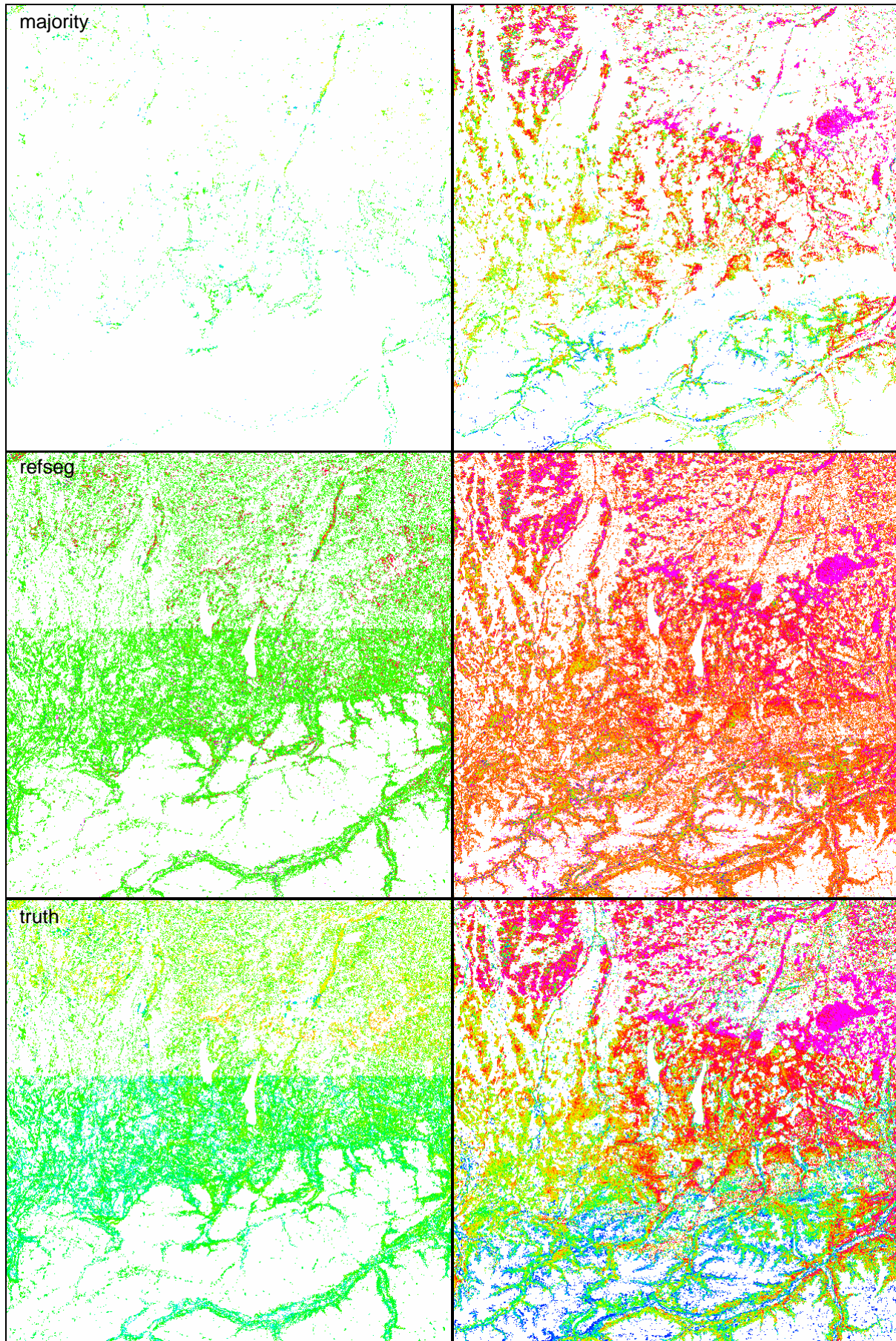


LAI

[next page]

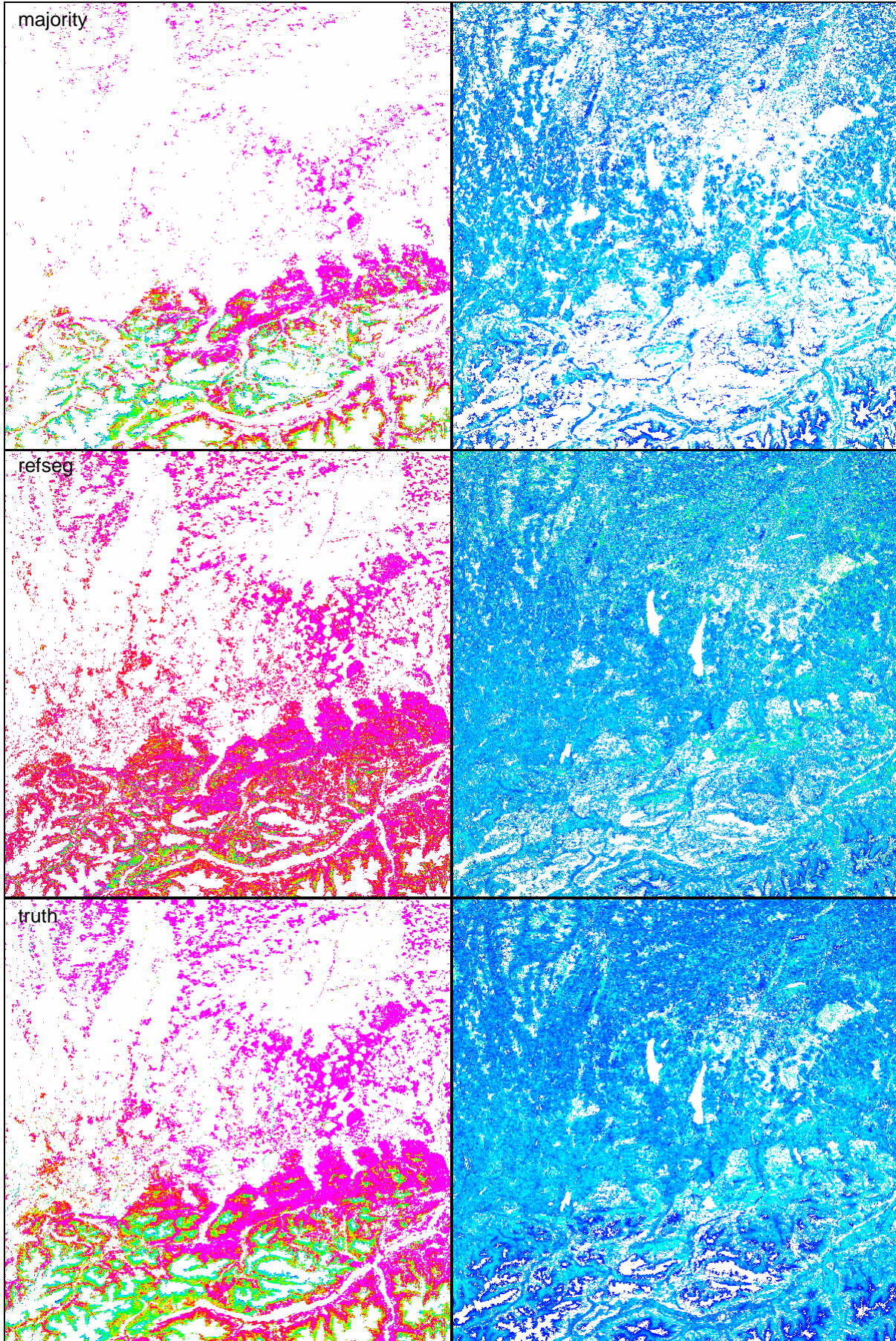
LAI of LCT 1: Deciduous Forest

LAI of LCT 2: Mixed Forest



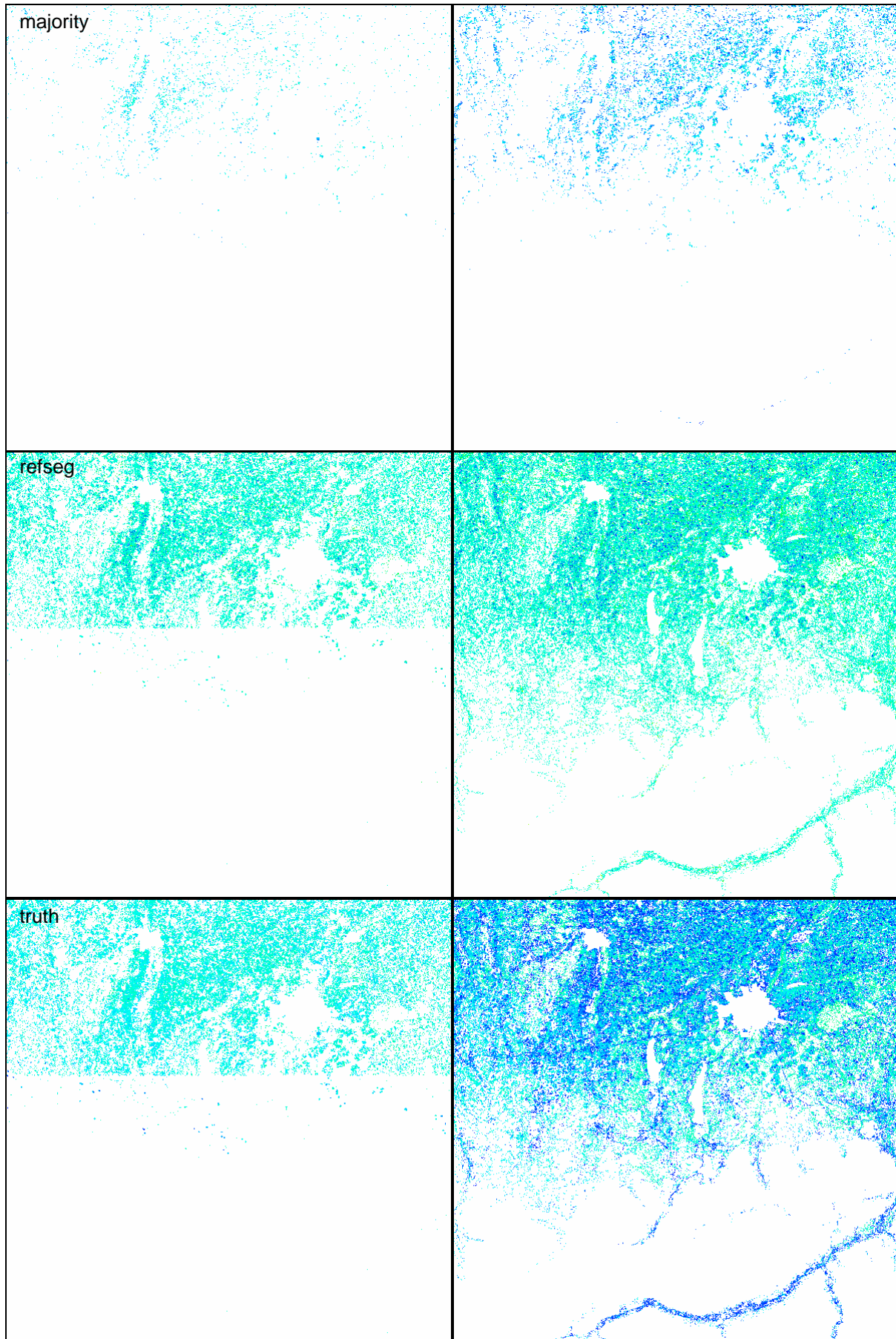
LAI of LCT 3: Needleleaf Forest

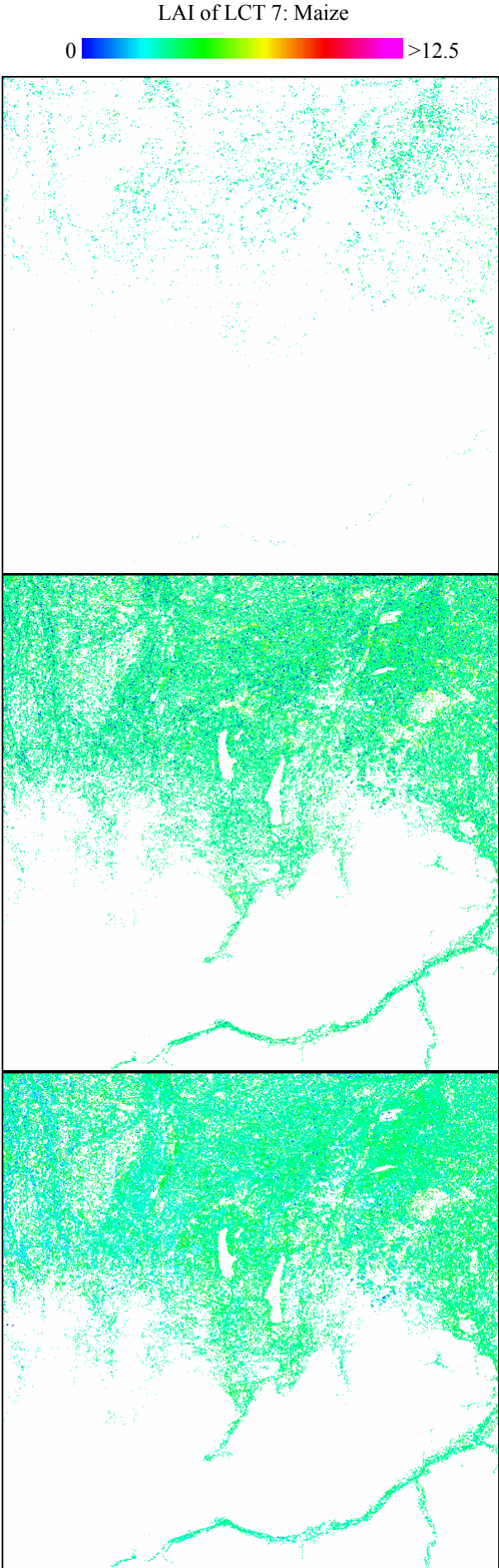
LAI of LCT 4: Grassland



LAI of LCT 5: Spring Grain

LAI of LCT 6: Winter Grain





Curriculum Vitae

Personal

Name : Marko Braun
Date of Birth : January 16th, 1969
Place of Birth : Haunstetten, now Augsburg
Nationality : German

Education

1975 – 1979 : Primary School in Steppach and Diedorf (Germany)
1979 – 1989 : Justus von Liebig Gymnasium Neusäß, Highschool (Germany)
1985 – 1986 : Abilene Cooper Highschool, Abilene TX (USA), Diploma
1990 – 1991 : Study of Philosophy, University of Augsburg (Germany)
1991 – 1998 : Study of Geography, University of Augsburg (Germany)
Subsidiary Subjects: Politics, Spanish, Remote Sensing
Diploma Thesis: Fuzzy Logic Based Land Cover Classification of
LANDSAT TM High Mountain Scenes in the Toce Catchment in
Piemonte/Northern Italy

Career

1998 – 2000 : Freelance Professional at Vista Remote Sensing in Geosciences
(Munich); mapping of nitrate stress, precision farming and
GIS-Integration
1999 - 2000 : Freelance Professional at the Chair of Geography and
Geographical Remote Sensing, University of Munich;
geometric and radiometric processing of Landsat TM data for
GIS-Integration
2000 : Scientific Researcher at the Chair of Geography and
Geographical Remote Sensing, University of Munich;
Validation of digital elevation models from SRTM interferometry
for hydrological modelling
2001 – 2004 : Scientific Researcher at the Chair of Geography and
Geographical Remote Sensing, University of Munich; Ph.D. Student
in the GLOWA-Danube project
2004 – 2006 : Freelance Professional Trainer for computer applications and
programming, finishing of Dissertation
since 12/2006 : Scientific Researcher at the Chair of Geography and
Geographical Remote Sensing, University of Munich;
Integrative catchment modeling in the context of climate change –
Comparison of Problems, Research and solutions in Quebec and
Bavaria